

Frequency tunable terahertz quantum cascade lasers

Iman Kundu

*Submitted in accordance with the requirements for the degree of
Doctor of Philosophy*

The University of Leeds
School of Electronic and Electrical Engineering

July 2014

The candidate confirms that the work submitted is his/her own, except where work which has formed part of jointly authored publications has been included. The contribution of the candidate and the other authors to this work has been explicitly indicated below. The candidate confirms that appropriate credit has been given within the thesis where reference has been made to the work of others.

Devices fabricated in Chapter 2 were used in the following journal:

“Detection of terahertz frequency radiation via the photothermoelastic response of zincblende crystals”, Paul Dean, Aziati H. Awang, Iman Kundu, Raed Alhathloul, Suraj P. Khanna, Lianhe H. Li, Andrew Burnett, Edmund H. Linfield, A. Giles Davies, Journal of the Optical Society of America B, Vol. 30, Issue 12, Pages 3151–3160, 2013.

Iman Kundu and R. Alhathloul fabricated the THz QCL devices, which were subsequently used in the application developed by P. Dean, A. H. Awang and A. Burnett. L. H. Li grew in the QCL material using MBE. E. H. Linfield and A. G. Davies supervised the project.

Chapter 5 is based on the following journal:

“Discrete Vernier tuning in terahertz quantum cascade lasers using coupled cavities”, Iman Kundu, Paul Dean, Alexander Valavanis, Li Chen, Lianhe Li, John E. Cunningham, Edmund H. Linfield, A. Giles Davies, Optics Express, Vol. 22, Issue 13, Pages 16595-16605, 2014.

Iman Kundu was involved in the simulation, fabrication and characterisation of THz QCL devices used in this study and data analysis. P. Dean and A. Valavanis verified the data and proofread the manuscript. L. Chen performed the FIB milling of packaged THz QCL chips. L. H. Li grew in the QCL material using MBE. J. E. Cunningham, E. H. Linfield and A. G. Davies supervised the project and proofread the manuscript.

This copy has been supplied on the understanding that it is copyright material and that no quotation from the thesis may be published without proper acknowledgement.

© 2014 The University of Leeds and Iman Kundu

The right of Iman Kundu to be identified as Author of this work has been asserted by him in accordance with the Copyright, Designs and Patents Act 1988.

To the four pillars of my life –

Maa, Sreem, Koyel and Sushanta Mamu

“The only true wisdom is in knowing you know nothing.”

Socrates

Acknowledgements

First and foremost, I would like to thank the almighty God for all the blessings and strength through this amazing journey.

I would like to express my sincere gratitude to my supervisors, Prof. Edmund H. Linfield and Prof. A. Giles Davies, for giving me the opportunity to work in their world-leading research team and help me realise my dream of studying for a PhD degree! I sincerely thank them both for the enormous mentoring, support and supervision during the tenure of my PhD studies. I would also like to sincerely thank Prof. John E. Cunningham for his valuable advice during the supervision meetings.

I would take this opportunity to acknowledge the University of Leeds for funding my studies. I also acknowledge the support received from the Engineering and Physical Sciences Research Council (EPSRC), UK (COTS programme EP/J017671/1, and EP/J002356/1); the ERC (NOTES and TOSCA programmes); the Royal Society; and, the Wolfson Foundation during the various phases of this project.

I would like to thank the members of staff and students at the Institute of Microwaves and Photonics, School of Electronic and Electrical Engineering, University of Leeds. I am particularly grateful to Dr. Paul Dean and Dr. Alexander Valavanis for the many thought provoking discussions, and their enormous contribution to the development of this project. Without your help this project would not have been possible!

I would also like to thank Dr. Raed Al-Hathloul, Dr. Mohammed Salih and Dr. Mohamed Shahrizan bin Mohd Ibrahim for their valuable comments during the fabri-

cation of THz QCLs, and to Dr. Lianhe Li and Dr. Suraj P. Khanna for providing quality MBE-grown THz QCL wafers.

I also extend my sincere gratitude to Dr. D. Paul. Steenson, Dr. Li Chen, Dr. Vaidotas Mišeikis, Dr. Mark Rosamond, Mr. Geoff Butterworth, Mr. Jordan Thomas and Mr. John Harrington (Institute of Materials Research, University of Leeds) for their valuable training and support during cleanroom processing, electron beam lithography and focussed ion beam milling techniques.

I acknowledge the support from Dr. Alexander Vanavanis and Dr. Leon J. M. Lever for their assistance during finite element modelling. I sincerely acknowledge the tremendous effort out forth by many to proof-read this thesis – Prof. Edmund H. Linfield, Prof. A. Giles Davies, Dr. Paul Dean, Dr. Alexander Valavanis, Dr. Joshua R. Freeman, Dr. Divyang K. Mistry, Mr. James Keeley and Mr. David R. Bacon.

I would also like to thank Ms. Louise Redmonds, Mrs. Sue Hobson, Mrs. Clair Atkinson and Mrs. Anna de Jong for their tremendous administrative support and for arranging my travels to conferences!

I express my gratitude to my past and present fellow PhD colleagues: Mr. Siddhant Chowdhury, Ms. Reshma A. Mohandas, Mr. Manoj Kumar, Mr. Dong Rui, Ms. Julie Zhu, Mr. Viktor Doychinov, Dr. Aziati H. Awang and Dr. Kamila Noor Saat, for the endless discussions on QCLs, and sharing the laughter and agony that is associated with research.

Last, but not the least, I would like to acknowledge the tremendous support I received from my family during this crucial phase of my life – to my Mum and sister, who have always encouraged me to work hard, and to my beautiful wife Sreemoti, who has been a pillar of support through many years now. Sreem, it has been quite an experience as well as an achievement to be able to complete our PhDs simultaneously, without losing our sanity! I hope my Dad, grandpa and granny would be really proud that I could make their wish come true. Hope you all are watching this from the Heavens above! Lastly, thanks to Mr. Pradip Pan, my mentor in high school, who have shaped my intellect during my formative years and with whom I have shared many days of love and hate!

Abstract

Terahertz (THz) quantum cascade lasers (QCLs) are compact solid-state sources of coherent radiation operating in the far-infrared (FIR) range of the electromagnetic spectrum. THz QCL ridge waveguides are typically Fabry-Pérot (FP) cavities and exhibit characteristic multiple-mode emission. However, widely tunable single-mode (SM) THz QCLs are ideally suited to many THz-sensing applications, such as trace gas detection, atmospheric observations and security screening. Tunable THz QCLs are also highly desirable for techniques like heterodyne mixing and self-mixing interferometry. SM emission from THz QCLs has been demonstrated using distributed feedback (DFB) cavities, photonic lattices (PLs) and photonic crystals (PhCs). Tunable THz QCLs have also been demonstrated using various techniques, such as external coupled mirrors, variation of growth parameters, deposition of nitrogen gas and dielectric materials, and aperiodic PLs.

In this study, SM emission from THz QCLs is obtained from PLs patterned with electron beam lithography (EBL). This lithography based processing has the advantage of integrated device processing. Spectral performance of the PLs was simulated using finite element modelling (FEM) and coupled mode theory. A frequency stopband centred at the characteristic Bragg frequency was computed with emission predicted outside this stopband. Spectral emission of experimentally fabricated devices was observed outside the stopband, as was predicted from simulations.

The design of the THz QCLs with PL was modified to investigate frequency tunability by depleting carriers under the PL metallised sections using a three-section device. A bulk Drude model was used to simulate the variation of refractive index as a function of carrier concentration. The PLs were deposited such that they form a Schottky junction and

a thin depletion layer at the active material interface. The PLs were driven with an independent external electrical connection. An electrical model was designed, which explained the experimentally observed behaviour. This electrical model was used to calculate the depletion layer and the redistribution of carriers under the PL. The resulting variation in the refractive index was computed using FEM. A 15–20 GHz shift in the Bragg frequency was predicted using the Drude model. The frequency stopband was also predicted to reduce from ~ 90 GHz to ~ 77 GHz with carrier depletion and a ~ 5 –6 GHz shift in the stopband band edge was predicted. In an exemplar device, a tuning of 15 GHz was observed. A change in spectral power density (SPD) amongst modes was observed in all other devices.

A different approach towards the realisation of a frequency tunable THz QCLs was adopted based on two-coupled cavities. This design was based on a Vernier selection rule and promised a wide band tuning from a small refractive index perturbation. One of the two cavities formed the lasing section, while the other formed a tuning section. A thermal tuning mechanism based on a localised Joule heating was used to tune frequency of the coupled-cavity. THz QCLs with coupled-cavities were modelled using transfer matrices and a bulk thermal model. Two devices were designed to exhibit a blue shift in frequency when the shorter of the coupled-cavities acted as a tuning element. The frequency spacing of the devices were ~ 15 and ~ 25 GHz respectively. The devices were also optimised such that a reversal in tuning direction is observed by swapping the functions of the lasing and tuning cavities. A monotonic discrete frequency hopping with a blue shift of ~ 50 and ~ 85 GHz was observed from the two devices. A red shift in frequency was also observed as the lasing and tuning cavities were swapped. Additionally, since the tuning element is isolated from the lasing section, the power emission of the lasing section was unaffected by the tuning current.

The coupled cavity designs were further optimised to disrupt the monotonic frequency hopping to obtain a quasi-continuous frequency tuning. Unlike, the discrete tuning design, this detuned design required variation of current at the lasing and tuning cavities simultaneously, along with a variation in heat sink temperature. Spectral behaviour was modelled using the same transfer matrices, bulk thermal mode and coupled mode theory. Closely spaced discrete tuning over a range of ~ 67 and 100 GHz was observed from two devices, with continuous tuning of ~ 5 GHz observed at certain dominant modes. Continuous tuning was also investigated using coupled-cavities with an integrated PL. A continuous tun-

ing of ~ 3 GHz was observed from experimental devices. Unlike the detuned coupled cavity devices, the power emission from these devices were unaffected by the tuning current. However, these devices are limited by a low tuning range.

Table of contents

Acknowledgements.....	ix
Abstract.....	xi
Table of contents.....	xv
List of publications.....	xix
List of abbreviations.....	xxiii
List of symbols.....	xxv
List of figures	xxix
List of tables	xli
Chapter 1 Introduction.....	1
1.1 Terahertz frequency spectrum.....	1
1.2 Interband and intersubband semiconductor lasers.....	2
1.3 Quantum cascade laser.....	5
1.3.1 Operation of QCLs	6
1.3.2 Development of QCLs	9
1.3.2.1 Mid-IR QCL active region design.....	9
1.3.2.2 Mid-IR QCL waveguides.....	12
1.3.2.3 THz QCL active region design	15
1.3.2.4 THz QCL waveguides	20
1.4 Single mode emission from THz QCLs	22
1.4.1 DFB/DBR lasers	22
1.4.2 Photonic crystals.....	25
1.5 Thesis outline.....	27
Chapter 2 Fabrication and characterisation of single-metal THz QCLs.....	29
2.1 Introduction	29
2.2 Fabrication of THz QCL with single-metal waveguide	29
2.2.1 Sample cleaning and edge bead removal.....	31
2.2.2 Mesa etching using wet chemicals to form laser ridge.....	32
2.2.3 Deposition of ohmic side contacts	35
2.2.4 Annealing of ohmic side contacts.....	37
2.2.5 Deposition of ohmic top contacts	38
2.2.6 Deposition of cladding metal.....	39

2.2.7 Substrate etching and metallisation.....	40
2.2.8 Sintering of top ohmic contact	41
2.2.9 Cleaving, soldering and packaging of laser ridges	41
2.2.10 Electron beam lithography.....	45
2.2.11 Focussed ion beam milling.....	46
2.3 Characterisation of THz QCLs.....	47
2.3.1 Experimental setup	47
2.3.1.1 Optical setup	48
2.3.1.2 Electrical setup.....	49
2.4 Experimental results from a reference device from L1007	51
2.5 Summary	53
Chapter 3 THz QCLs with one-dimensional photonic lattice.....	55
3.1 Photonic lattice.....	55
3.2 Design and modelling of THz QCLs with PLs	57
3.2.1 PL design parameters	57
3.2.1.1 Finite element modelling of device cross sections.....	58
3.2.2 Stopband in a PL.....	61
3.2.3 Designing a PL with Bragg frequency at 2.80 THz	63
3.2.4 Final PL designs.....	65
3.3 Fabrication	66
3.4 Experimental results.....	70
3.4.1 Results from reference devices.....	70
3.4.2 Results from THz QCLs with PLs	72
3.4.2.1 Spectral characterisation	72
3.4.2.2 Electrical characteristics	77
3.5 Summary	78
Chapter 4 Three-section THz QCLs with electrically-controlled photonic lattices	81
4.1 Introduction	81
4.1.1 Frequency tunable THz QCLs	83
4.2 Device design and operating principle	86
4.3 Tuning refractive index by changing carrier concentration.....	87
4.3.1 Variation of refractive index with doping.....	87
4.3.2 Depletion of carrier at PL grating	88
4.4 Fabrication	91
4.5 Experimental setup	93
4.6 Experimental results.....	94
4.6.1 Electrical characterisation	94
4.6.1.1 Floating PL section	95
4.6.1.2 PL section with a bias	98
4.6.1.2.1 Stopband in the PL with a depletion layer	101
4.6.2 Spectral characterisation	103
4.7 Summary	107
Chapter 5 Discrete Vernier tuning using coupled cavity QCLs	109
5.1 Introduction	109
5.2 Theory of coupled cavity QCLs	111
5.2.1 Modelling using scattering and transmission matrices.....	113
5.2.1.1 Modelling coupled cavity QCLs	117
5.2.1.2 Modelling tuning of refractive index with temperature	119

5.2.1.3 Current induced Joule heating of tuning section	120
5.3 Designing coupled cavity QCLs.....	123
5.3.1 Design 1: Mode hopping between adjacent modes	123
5.3.2 Design 2: Mode hopping between alternate modes	124
5.4 Fabrication	126
5.5 Experimental setup	128
5.6 Experimental results.....	130
5.6.1 Electrical characterisation.....	130
5.6.1.1 THz power stability	131
5.6.2 Spectral characterisation.....	132
5.6.2.1 Device 5A: Design 1	132
5.6.2.1.1 Shorter cavity as the tuning section	132
5.6.2.1.2 Longer cavity as the tuning section	134
5.6.2.2 Device 5B: Design 2	136
5.6.2.2.1 Shorter cavity as the tuning section	136
5.6.2.2.2 Longer cavity as the tuning section	137
5.7 Summary	138
Chapter 6 Continuous tuning using coupled cavity QCLs	141
6.1 Introduction	141
6.2 Quasi-continuous tuning using detuned coupled cavity QCLs.....	143
6.2.1 Theory of detuned coupled cavity QCLs.....	143
6.2.1.1 Detuned coupled cavity design	145
6.2.2 Fabrication	149
6.2.3 Experimental setup	149
6.2.4 Experimental results.....	150
6.2.4.1 Design 1: Device 6A.....	151
6.2.4.2 Design 2: Device 6B	155
6.2.5 Discussion	157
6.3 Continuous frequency tuning using photonic lattice.....	157
6.3.1 Theory and modelling of coupled cavity QCLs with PL.....	158
6.3.1.1 Modelling of coupled cavity QCLs with PL.....	159
6.3.1.2 Design 3: Coupled cavity devices with a uniform PL	162
6.3.1.3 Design 4: Coupled cavity devices with $\lambda/4$ -shifted PL	163
6.3.2 Fabrication	164
6.3.3 Experimental results.....	166
6.3.3.1 Uniform PL: Device 5B-PL	166
6.3.3.2 $\lambda/4$ -shifted PL: Device 6B-PL	167
6.4 Summary	168
Chapter 7 Conclusion and future work.....	169
7.1 SM emission from THz QCLs with PLs	169
7.2 Frequency tunable THz QCL through carrier depletion	170
7.3 THz QCLs using a coupled cavity	172
7.4 Future Work.....	173
References	177

List of publications

The following journal and conference papers were published by the author during the course of the present work. The underlined work denotes first-authorship.

Journal papers

- Paul Dean, Aziati H. Awang, Iman Kundu, Raed Alhathloul, Suraj P. Khanna, Lianhe H. Li, Andrew Burnett, Edmund H. Linfield, A. Giles Davies, “Detection of terahertz frequency radiation via the photothermoelastic response of zincblende crystals”, Journal of the Optical Society of America B, Vol. 30, Issue 12, Pages 3151 – 3160, 2013.
 - THz QCLs fabricated in Chapter 2 was used the journal.
 - Iman Kundu, Paul Dean, Alexander Valavanis, Craig A. Evans, Lianhe Li, John E. Cunningham, Edmund H. Linfield, A. Giles Davies, “Electrical modelling of multiple segment terahertz quantum cascade laser”. [In Preparation].
 - Chapter 4 is based on this work.
 - Iman Kundu, Paul Dean, Alexander Valavanis, Li Chen, Lianhe Li, John E. Cunningham, Edmund H. Linfield, A. Giles Davies, “Discrete Vernier tuning in terahertz quantum cascade lasers using coupled cavities”, Optics Express, Vol. 22, Issue 13, Pages 16595-16605, 2014.
 - Chapter 5 is based on this work.
-

Conference presentations

- Iman Kundu, Paul Dean, Alexander Valavanis, Li Chen, Lianhe Li, John E. Cunningham, Edmund H. Linfield, A. Giles Davies, “Discrete Vernier tuning in terahertz quantum cascade lasers using coupled cavities”, International Quantum Cascade Lasers School and Workshop 2014, Policoro (Matera), Italy, 2014. (Accepted for an oral presentation)
 - Iman Kundu, Paul Dean, Alexander Valavanis, Li Chen, Lianhe Li, John E. Cunningham, Edmund H. Linfield, A. Giles Davies, “Discrete Vernier tuning with constant output power in terahertz quantum cascade lasers using coupled cavities”, UK Semiconductors 2014, Sheffield, UK, 2014. (Oral presentation)
 - Iman Kundu, Paul Dean, Lianhe H. Li, Alexander Valavanis, Suraj P. Khanna, Craig A. Evans, John E. Cunningham, Edmund H. Linfield, A. Giles Davies, “Three-section terahertz quantum cascade lasers with externally biased photonic lattices”, European Cooperation in Science and Technology (COST), MPNS COST Action Training School – MP1204 TERA-MIR Radiation: Materials, Generation, Detection and Applications, Cortona, Italy, 2013. (Poster presentation)
 - Paul Dean, Aziati H. Awang, Raed Alhathloul, Iman Kundu, Suraj P. Khanna, Lianhe H. Li, Edmund H. Linfield, A. Giles Davies, “Thermo-optic detection of quantum cascade laser radiation in the range ~ 2.2 - 2.9 THz using a ZnTe crystal”, International Conference on Infrared, Millimeter, and Terahertz Waves (IRMMW–THz), 2012.
 - Iman Kundu, Paul Dean, Lianhe H. Li, Alexander Valavanis, Suraj P. Khanna, John E. Cunningham, Edmund H. Linfield, A. Giles Davies, “Terahertz quantum cascade lasers with externally biased photonic lattices for electronic tuning”, International Quantum Cascade Lasers School and Workshop 2012, Baden near Vienna, Austria, 2012. (Oral presentation)
-

- Aziati H. Awang, Paul Dean, Raed Alhathloul, Iman Kundu, Suraj P. Khanna, Lianhe H. Li, Edmund H. Linfield, A. Giles Davies, “Thermo-optic detection of quantum cascade laser radiation in the range ~ 2.2 - 2.9 THz using a ZnTe crystal”, International Quantum Cascade Lasers School and Workshop 2012, Baden near Vienna, Austria, 2012. (Poster presentation)
 - Iman Kundu, Paul Dean, Lianhe H. Li, Alexander Valavanis, Suraj P. Khanna, John E. Cunningham, Edmund H. Linfield, A. Giles Davies, “Terahertz quantum cascade lasers with externally biased photonic lattices for electronic tuning”, MITEPHO Summer School on THz Systems and Applications, London, UK, 2012. (Oral presentation)
 - Iman Kundu, Paul Dean, Lianhe H. Li, Alexander Valavanis, Suraj P. Khanna, John E. Cunningham, Edmund H. Linfield, A. Giles Davies, “Terahertz quantum cascade lasers with externally biased photonic lattices for electronic tuning”, UK Semiconductors 2012, Sheffield, UK, 2012. (Poster presentation)
 - Aziati H. Awang, Paul Dean, Raed Alhathloul, Iman Kundu, Suraj P. Khanna, Lianhe H. Li, Edmund H. Linfield, A. Giles Davies, “Thermo-optic detection of quantum cascade laser radiation in the range ~ 2.2 - 2.9 THz using a ZnTe crystal”, UK Semiconductors 2012, Sheffield, UK, 2012. (Oral presentation)
-

List of abbreviations

APL	Aperiodic photonic lattice
BTC	Bound-to-continuum
CW	Continuous wave
IV	Current-voltage
DI	De-ionised
DBR	Distributed Bragg reflector
DFB	Distributed feedback
EA	Electro-absorption
EBL	Electron beam lithography
FP	Fabry-Pérot
FEM	Finite element modelling
FIB	Focussed ion beam
FTIR	Fourier transform infrared
IPA	Isopropyl alcohol
LI	Light-current
LIV	Light-current-voltage
LO	Longitudinal optical
MIBK	Methyl isobutyl ketone
mid-IR	Mid-infrared
MBE	Molecular beam epitaxy
PhC	Photonic crystal
PL	Photonic lattice
PMMA	Poly(methyl methacrylate)
QCL	Quantum cascade laser
QW	Quantum well

SG–DBR	Sampled grating distributed Bragg reflector
SEM	Scanning electron microscopy
S	Scattering matrix
SI	Semi–insulating
SISP	Semi–insulating surface plasmon
SMSR	Side mode suppression ratio
SM	Single mode
SPD	Spectral power density
SL	Super lattice
SP	Surface plasmon
THz	Terahertz
T	Transmission matrix
UV	Ultra–violet

List of symbols

Fundamental constants

$k = 1.38 \times 10^{-23} \text{ J/K}$	Boltzmann constant
$e = 1.6 \times 10^{-19} \text{ C}$	Elementary charge
$h = 6.63 \times 10^{-34} \text{ J/s}$	Planck constant
$c = 3 \times 10^8 \text{ m/s}$	Speed of light in vacuum
$\varepsilon_0 = 8.85 \times 10^{-12} \text{ F/m}$	Vacuum permittivity

Photonic lattice (PL) symbols

f_{BR}	Bragg frequency
λ_{BR}	Bragg wavelength
Γ	Confinement of optical mode in gain medium
κ	Coupling coefficient
δ	Detuning factor
n_{eff}	Effective refractive index
n_g	Group refractive index
Δf_{BR}	Photonic bandgap / bandwidth of stopband
γ	PL duty cycle
Λ	PL pitch / optical lattice constant
α_{wg}	Waveguide loss
α_m	Mirror loss

Material symbols

AlSb	Aluminium antimonide
AlGaAs	Aluminium gallium arsenide
AlInAs	Aluminium indium arsenide
As	Arsenic
Cu	Copper
Ga	Gallium
GaAs	Gallium arsenide
GaAsSb	Gallium arsenide antimonide
GaInAs	Gallium indium arsenide
Ge	Germanium
Au	Gold
He	Helium
H₂O₂	Hydrogen peroxide
In	Indium
InAs	Indium arsenide
InP	Indium phosphide
<i>n</i>-GaAs	<i>n</i> -doped gallium arsenide
Ni	Nickel
N	Nitrogen
Si	Silicon
H₂SO₄	Sulfuric acid
Ti	Titanium
H₂O	Water

Material properties

ϕ_{bn}	Barrier heights
ϕ_{bi}	Built-in potential
m_e^*	Effective mass of electron in conduction band
χ	Electron affinity
ε_s	Permittivity of semiconductor material
ϕ	Work function

Thermal properties

R_{Th}^*	Normalised thermal resistance
T	Temperature
R_{Th}	Thermal resistance

List of figures

Figure 1.1: Position of THz range in the electromagnetic spectrum. Taken from ref. [5]...	2
Figure 1.2: Schematic representation of: (a) absorption, (b) spontaneous emission and (c) stimulated emission. [Modified from ref. [16]].	3
Figure 1.3: Schematic representation of: (a) interband optical transition between conduction band and valence band, (b) interband optical transition between subbands in the conduction and valence band, and (c) intersubband optical transition between subbands in the conduction band.	5
Figure 1.4: Schematic representation of: (a) intersubband optical transitions in an active module of a QCL, (b) cascading of electron through multiple active modules in a QCL. Adapted from ref. [19].	6
Figure 1.5: Schematic representation of a QCL with three-level lasing levels. Adapted from [20].	7
Figure 1.6: Conduction band of the first demonstrated QCL. Moduli-squared of electron wavefunctions in the active region and the injector/extractor stage formed from a digitally graded alloy are shown. Taken from [26].	10
Figure 1.7: Conduction band of a QCL with: (a) Vertical optical transition. Taken from [30]. (b) Tapered funnel injector. Taken from [36].	11
Figure 1.8: Conduction band of a QCL based on: (a) a superlattice. Taken from [38]. (b) A chirped superlattice. Taken from [41].	12
Figure 1.9: Refractive index and mode profiles of the fundamental optical modes in a: (a) Plasmon enhanced waveguide. Taken from [50]. (b) SP waveguide. (Inset) Device cross-section. Taken from from [49].	14
Figure 1.10: The refractive index and mode profile of the fundamental optical mode in a GaAs/AlGaAs based QCL with plasmonic cladding. Taken from from [57].	15
Figure 1.11: Conduction band of the active region of the first demonstrated THz QCL. Minibands of energy levels, shown in grey, allows injection of electrons into the upper lasing state 2, and extraction of electrons from the lower lasing state 1 to the next upper lasing state. Taken from [15].	16
Figure 1.12: Conduction band of the first demonstrated THz QCL with LO phonon depopulation. A vertical optical transition takes place between levels 5 and 4.	

Level 4 and 3 are in resonance, from where electrons relax to levels 2 and 1 through LO phonons. Taken from [72].....	18
Figure 1.13: Conduction band of a THz QCL design with a BTC optical transition and LO phonon depopulation. Taken from [81].....	19
Figure 1.14: (Left) Schematic representations and (right) optical mode intensity profiles of THz QCLs with: (a) Single-metal and (b) double-metal waveguides. Taken from ref. [66].	20
Figure 1.15: (a) Illustration of a microcavity LC resonator. Taken from [103]. (b) Illustration of a metamaterial based transmission line. Taken from ref. [104]. Both designs are based on a THz QCL with double-metal waveguide.	21
Figure 1.16: (a) Schematic diagram of a THz QCL cavity with DFB gratings. (b) Transmission spectrum (black) from a DFB grating with Bragg frequency at 2.50 THz (red). The DFB grating introduces a stop band centred at the Bragg frequency.....	23
Figure 1.17: Schematic diagram of a THz QCL cavity with a DBR grating.	24
Figure 1.18: Optical image of a PhC from a double metal THz QCL with hexagonal geometry. Arrays of air gaps are evident on the device surface allowing perturbation of the dielectric constant of the top cladding and outcoupling of light. Taken from [118].....	26
Figure 1.19: (a) Schematic diagram of a THz QCL with PhC (top) without side absorber, and (bottom) with side absorber. The top doped epilayer is removed along the device edge to form the side absorber. Taken from [118]. (b) Optical images of a PhC with optimised Q factor (left) without π -phase shifter, (right) with π -phase shifter. Taken from [120].....	26
Figure 2.1: Illustration of a sample after laser ridge etching.....	33
Figure 2.2: Optical microscopy of a sample after development of resist for mesa laser ridge definition. The cross marks along the sides served as alignment marks for subsequent lithography steps. The horizontal marks served as visual aid to measure device length during cleaving. The dark 'dot' in the sample is a oval defect, typical in MBE grown samples.	34
Figure 2.3: Optical microscopy of a sample after etching. Sloped sidewall along the length of the ridge is evident from the thick dark features.....	34
Figure 2.4: Illustration of a sample after deposition of ohmic side contact.	35
Figure 2.5: Optical microscopy of a sample after development of photoresist for side contact deposition.	36
Figure 2.6: Optical microscopy of a sample after lift-off of side contact deposition.	36
Figure 2.7: Optical microscopy of a sample after annealing of ohmic side contacts.	37
Figure 2.8: Illustration of a sample after deposition of ohmic side contact.	38
Figure 2.9: Optical microscopy of a sample during top ohmic contact deposition: (a) after development of photoresist, and (b) after metal lift-off.....	39
Figure 2.10: Illustration of a sample after deposition of cladding metal.....	39

Figure 2.11: Optical microscopy of a sample during cladding metal deposition: (a) after development of photoresist, and (b) after metal lift-off.....	40
Figure 2.12: (a) Schematic of a fabricated THz QCL chip with three 6 mm long laser ridges. Samples were diced along the dotted lines to obtain three individual laser ridges, which were subsequently cleaved to obtain Fabry–Pérot cavities. (b) Schematic of cleaving of a diced laser ridge. The diced laser chips were cleaved along the dotted lines. During manual cleaving, a small crack was introduced at the edge of the diced laser, whereas during automated scribing process, a 500 μm long line was scribed from the edge into the sample.	42
Figure 2.13: (a–d) SEM of cleaved facets using automated scriber.	43
Figure 2.14: Schematic diagram of packaging of two THz QCL devices (labelled as device ‘ <i>Top</i> ’ and device ‘ <i>Bottom</i> ’) on a Cu block.	43
Figure 2.15: Optical microscopy of a QCL device after packaging and wire bonding.....	45
Figure 2.16: Optical microscopy of a sample patterned with EBL: (a) after resist development, (b) after lift-off. Unwanted metal was found shorting grating features due to poor lift-off.	46
Figure 2.17: Scanning electron microscopy of an alignment mark patterned using FIB milling.	47
Figure 2.18: Schematic diagram of experimental setup for characterising LIV of a standard QCL device.	50
Figure 2.19: Schematic diagram of experimental setup for characterising spectra of a standard QCL device.	50
Figure 2.20: (a) LIV recorded from a reference device at different heat sink temperatures. (b) Threshold current density obtained from fig. (a) is plotted as a function of heat sink temperature. (c) Peak emission power plotted as a function of heat sink temperature. All data are obtained from the device L1007-S1-D1.	52
Figure 2.21: (a) Spectra obtained at various drive currents at a heat sink temperature of 4 K. (b) Spectra obtained at a drive current of 1.14 A at various heat sink temperatures. All data are obtained from the device L1007-S1-D1.	52
Figure 3.1: (a) Schematic diagram of THz QCLs cavities with PL grating. (b) Photonic bandgap in a one-dimensional PL with 2- μm deep etched unmetallised sections.....	56
Figure 3.2: Schematic diagram of longitudinal cross section of grating pitch Λ , comprising metallised and unmetallised sections.	57
Figure 3.3: Device cross-section of the metallised section modelled in COMSOL Multiphysics®: (a) Complete view of the model, (b) magnified view of the active region.	59
Figure 3.4: Device cross-section of the metallised section of the PL modelled in COMSOL Multiphysics®: after triangular mesh optimisation.	60
Figure 3.5: Computed optical mode at 2.77 THz using FEM. Contour of power distribution is plotted at: (a) metallised and (b) unmetallised sections.	60
Figure 3.6: Dispersion curve in a PL. The detuning factor is plotted as a function of the propagation constant. A stopband is observed centred at Bragg frequency.	63

Figure 3.7: Simulated stopband in a PL with a Bragg frequency at 2.80 THz. The bandwidth of the stopband was calculated as ~ 90 GHz.....	65
Figure 3.8: (a) Illustration and (b) optical microscopy from a fabricated device after top ohmic contact deposition with a central gap. (c) Illustration and (d) optical microscopy of a fabricated device after deposition of Ti/Au cladding metal with a central gap.	68
Figure 3.9: (a) Illustration of a PL grating deposited at the central gap. (b) Optical microscopy from a fabricated device after the development of resist following EBL patterning of PL grating. (c) Magnified view after the development of EBL resist. ...	69
Figure 3.10: (a) Optical microscopy from a fabricated device after development of resist following EBL patterning of PL grating. (b) Magnified view.....	69
Figure 3.11: Spectra obtained from a reference device labelled L701-S2-B. (a) Spectra obtained at different drive currents with a heat sink temperature of 4 K. (b) Spectra obtained at different heat sink temperatures with a drive current of 1.96 A.....	71
Figure 3.12: (a) LIV characteristics from a reference device labelled L701-S2-B at a heat sink temperature of 14 K. (b) Threshold current density is plotted as a function of heat sink temperature for the same reference device.	71
Figure 3.13: (a) Spectra obtained from device 3B with $f_{BR} = 2.80$ THz. (b) The emission was observed at the edge of the stopband.	72
Figure 3.14: Spectra obtained from devices: (a) 3G and (c) 3H, both with $f_{BR} = 2.88$ THz. (b, d) The emission was observed at the edge of the stopband.	73
Figure 3.15: Spectra obtained from devices: (a) 3C and (c) 3D both with $f_{BR} = 2.81$ THz. (b, d) The emission was observed at the edge of the stopband.	74
Figure 3.16: Spectra obtained from devices: (a) 3F [$f_{BR} = 2.84$ THz] (c) 3A [$f_{BR} = 2.77$ THz] (e) 3E [$f_{BR} = 2.82$ THz]. (b, d, f) Emission was observed at the edge of the stopband.	75
Figure 3.17: Summary of emission frequency for all devices as a function of grating pitch measured in real samples. The Bragg frequency and the stopband edges calculated from the grating pitch are also shown. Multiple mode emission is shown as black and red triangles. Emission is always observed beyond the stopband edge. Multiple devices were tested with grating pitch at $\Lambda = 14.72$ & 15.08 μm	76
Figure 3.18: (a) Spectra from device 3A. A SM emission with an SMSR of more than 20 dB was observed. (b) Spectra from device 3H: with a drive current of 3.24 A at different heat sink temperatures.	77
Figure 3.19: (a) LIV characteristics from the device 3H obtained at different heat sink temperatures. (b) Threshold current density from device 3A plotted as a function of heat sink temperature.	78
Figure 4.1: Schematic diagram of a single-chip optical laser with SG-DBRs on either side of gain section. Phase between the SG-DBRs and the gain section is controlled through a phase matching section. A semiconductor optical amplifier and an EA modulator are integrated in the chip for amplification and modulation of the emitted radiation. Light is collected from the direction marked with an arrow. Figure taken from ref. [165].	82

- Figure 4.2: (a) Illustration of a THz QCL with PL with bond pads and side rail. All grating sites are connected to two bond pads through the side rails. (b) Wire bonding of the device. The PLs are connected with bond wires that enable application of independent bias to the PL. (c) Schematic diagram of depletion layer formed under the metallised section of the grating. 86
- Figure 4.3: Refractive index (red) and the corresponding Bragg frequency (blue) for $\Lambda = 15.25 \mu\text{m}$ as a function of carrier concentration of active material calculated using Drude model. QCL active material simulated as bulk $\text{Al}_{0.15}\text{Ga}_{0.85}\text{As}$. Average doping of QCL material is indicated with an arrow. Doping varied between (a) 10^{14} - 10^{20} cm^{-3} (b) 9.5×10^{15} - $2.5 \times 10^{16} \text{ cm}^{-3}$ 88
- Figure 4.4: Energy band diagram of: (a) metal and semiconductor. Metal–semiconductor interface at different conditions: (b) equilibrium and (c) with a reverse bias. Image adapted from [180]. 89
- Figure 4.5: (a) Illustration of a PL with contact pads and side rail. (b) Optical microscopy of a fabricated device. PL and outer cavity sections are illustrated in the image. (b) SEM image of a device after wire bonding. Separate wire bonds were applied to the PL section. 92
- Figure 4.6: Schematic diagram of the experimental setup to obtain LIV data with: (a) a floating PL section (no applied bias on the PL section), (b) a reverse bias applied to the PL section. Both pulse generators are gated to a square wave function generator (not shown). 94
- Figure 4.7: LIV obtained from device 4A, without any bias applied to the PL section. Voltage across the outer sections (red) and the PL section (blue), and the THz output power (green) are plotted as a function of current across the outer sections. 95
- Figure 4.8: (a) Equivalent circuit model describing the observed electrical characteristics of three–section QCL with PL. (b) Cross–talk voltage in PL (blue) as the current through the outer sections is varied. Both experimental (solid) and simulated (dashed) cross–talk voltage are plotted. (c) Experimental and (d) simulated capacitive decay observed at the PL section when the bias at the outer sections is switched off. All experimental data are obtained from device 4A. 97
- Figure 4.9: LIV obtained from device 4A, with a bias applied to the PL section. Device parameters, like threshold current density and output power remain unaffected by the applied bias on the PL section. Voltage measured at the PL section is also plotted. ... 98
- Figure 4.10: Simulated voltage at the PL section as a function of current at the outer sections, with different bias applied to the PL section. The cross–talk from the outer sections increases the voltage at the PL section. 99
- Figure 4.11: (a) Depletion layer formed under the PL metallised section (with different bias at the PL section) as a function of the bias at the outer sections. (b) Change in the carrier concentration is plotted as a function of the bias to the outer sections, for different bias applied to the PL section. (c) Variation of refractive index corresponding to the change in carrier concentration in (b). 100
- Figure 4.12: (a) LIV with a floating gate (no applied bias on the PL section) recorded at various heat sink temperatures. (b–d) Variation of device parameters – voltage (black), power (blue) and current (green) at the outer sections, and current at the PL section (red) as a function of bias applied to the PL section. Outer sections are biased at

(b) threshold, (c) peak power and (d) maximum applied bias. Device parameters are unaffected by the bias applied to the PL section.....	101
Figure 4.13: Computed optical mode of a PL metallised section with a depletion layer (2.77 THz) using FEM.....	102
Figure 4.14: Dispersion curve in the PL section. A stopband with bandwidth (Δf_{BR}) is observed centred at the Bragg frequency (f_{BR}). (a) PL with a no applied bias (floating gate), (b) PL with a depletion region formed in the metallised section.	102
Figure 4.15: (a) Emission spectra from the device 4A obtained with a floating PL section and at a heat sink temperature of 4 K. Spectra are vertically offset and are shown in colour coded for a range of current applied to the outer sections. (b) Emission was observed at the centre of stopband at the Bragg frequency calculated in Figure 4.14 (a).....	103
Figure 4.16: Emission spectra from device 4A at a heat sink temperature of 4 K, with a bias of (a) 2 V and (b) 6 V applied to the PL. Spectra are vertically offset and are shown in colour coded for a range of current applied to the outer section. (c) Simulated Bragg frequency (red) and stopband (yellow) in the PL with depleted carriers under grating calculated in Figure 4.14 (a). Emission (black) was observed at the shifted Bragg frequency.....	104
Figure 4.17: Emission spectra from device 4B at different drive current at outer section with (a) floating PL (4 K), (c) bias of 9 V applied to the PL section. (b) Emission was observed beyond the edge of the stopband. (d) Spectra under different PL bias with an outer section current of 2.21 A. Spectra are vertically offset and are colour coded for a range of applied to the outer section.	105
Figure 4.18: Emission spectra at different drive currents at the outer section from devices (a, b) 4C, (c, d) 4D and (e, f) 4E, at a heat sink temperature of 4 K: (a, c, e) with a floating PL section, and (b, d, f) with a bias of 9 V applied on the PL section.....	106
Figure 5.1: Schematic illustration of a coupled cavity THz QCL with a single-plasmon waveguide containing separate lasing and tuning section, which are separated by an air gap.....	112
Figure 5.2: Schematic diagram of a coupled-cavity laser modelled as a four-mirror system. The tuning section and the air gap section together form an external cavity. Emitted radiation is collected from the front facet of the lasing section as indicated by the arrow. The reflectivity of the rear facet of the lasing section is approximated as the effective reflectivity from the external cavity.....	113
Figure 5.3: Schematic diagram of a multi-port network used to describe S matrices. Adapted from [106].....	114
Figure 5.4: (a) Schematic diagram of a two-port network used to describe the T matrices. (b) Schematic diagram of a cascading of two-port networks. Adapted from [106]..	114
Figure 5.5: (a) Schematic diagram of a dielectric interface between two materials with effective refractive indices n_1 and n_2 . Owing to the difference in refractive index, a part of the wave is reflected back (r_1 and r_2), as illustrated with curved arrows, and part is transmitted (t). (b) Schematic diagram of a transmission line of length L with no discontinuity in the material with an effective refractive index n	115

- Figure 5.6: (a) Magnitude and (b) phase of the reflectivity calculated for a 4-mm long loss-less laser cavity with mirror reflectivity of 0.56 (red) and 0.9 (blue). 116
- Figure 5.7: Schematic diagram of a coupled cavity QCL. Two FP cavities of length L_1 and L_2 formed the lasing and the tuning sections respectively, and were separated by an air gap of length L_g . The effective refractive index of the lasing and the tuning sections are n_1 and n_2 respectively. The reflectivity and the transmission at the laser facets are indicated as r_n and t_n respectively. Radiation is collected from the front facet of the lasing section as indicated by the arrow. 117
- Figure 5.8: (a) Spectra obtained from a reference device from wafer L701 at 7 K. Multiple FP modes were observed between 2.70 and 2.85 THz. (b) Computed optical mode at 2.75 THz using finite element modelling of the device cross section with an effective refractive index of 3.62. The intensity distribution of the optical field is represented as a colour map with red being most intense and dark blue being least intense. 118
- Figure 5.9: Simulated normalised transmission in a 2.45-mm-long lasing section (blue), and in a 2.30-mm-long tuning section with a 13- μ m wide air gap section (red). The length of each section is selected such that the longitudinal modes coincide at a resonant frequency of 2.745 THz (bottom panel). 119
- Figure 5.10: (a) Spectra obtained from a reference device from wafer L701 at different heat-sink temperatures. (b) Modes exhibit a red shift of 4 GHz as the heat sink temperature was increased from 7 K to 70 K. 120
- Figure 5.11: (a) Peak output measured in the lockin amplifier as a function of heat sink temperature and duty cycle. (b) Change in temperature as a function of duty cycle and input tuning power. 121
- Figure 5.12: Simulated normalized transmission in the lasing section (blue) and in the tuning sections (red) of the device. The length of each section is selected such that the longitudinal modes coincide at a resonant frequency of 2.745 THz (bottom panel). Illustration of the shift in the resonant frequency as the refractive index of the tuning section is perturbed (middle and top panel). The dominant mode of the coupled cavity, indicated by a black arrow in each case, shifts to a higher frequency. 122
- Figure 5.13: Simulated transmission spectra of design 1 as a function of heat-induced shift of longitudinal modes in the tuning section only. (a) blue shift of frequency induced by heating the shorter cavity, (b) red shift of frequency induced by heating the longer cavity. 124
- Figure 5.14: Simulated transmission spectra of design 2 as a function of the heat-induced shift of longitudinal modes in the tuning section only. (a) blue shift of frequency induced by heating the shorter cavity, (b) red shift of frequency induced by heating the longer cavity. 125
- Figure 5.15: Schematic illustration of the packaging and physical connection scheme of a coupled cavity THz QCL. 126
- Figure 5.16: Scanning electron microscopy of a THz QCL ridge (a) before and (b) after FIB milling. Etch marks to determine precise cavity lengths are visible above the etched air gap. 127
- Figure 5.17: Scanning electron microscopy of (a) FIB milled facet, (b) scribed facet and (c) FIB milled facet at higher magnification. Redeposition of the etched material along

the milled surface is evident at higher magnification. The milling process also resulted in vertical impressions along the surface of the milled facet..... 128

Figure 5.18: Schematic diagram of the experimental setup for measuring spectra from a coupled cavity QCL..... 129

Figure 5.19: Schematic diagram of a wide tuning pulse and the resulting temperature profile at the tuning section. Time-resolved sampling of the laser performance is achieved by systematically varying the delay between the wide tuning pulse and the narrow laser pulse over the duration of the thermal transients..... 130

Figure 5.20: LIV characteristics obtained at different heat-sink temperatures after FIB milling (device 5A): (a) longer and (b) shorter sections of comparable lengths. (c) LIV characteristics obtained before FIB milling. 131

Figure 5.21: (a) Light–current (LI) characteristics of the lasing section. (b) Variation of the emitted power from the lasing section as a function of current in the tuning section. Data from device 5A..... 132

Figure 5.22: Experimental data obtained from device 5A, with tuning power applied to the short tuning section. (a) Spectral evolution and (b) weighted mean of spectral power density (SPD), as a function of the delay between the lasing and tuning pulses, as the former is scanned through the wider tuning pulse. The horizontal line in (b) shows the mean SPD when no current is applied to the tuning section, and serves as a reference. (c) Spectral evolution as tuning power amplitude varies. (d) Weighted mean of the SPD from experimental and simulated data shown in Figure 5.13 (a), as a function of tuning power. Error bars in the experimental data correspond to weighted standard deviation..... 134

Figure 5.23: Experimental data obtained from device 5A, with tuning power applied to the longer section. (a) Spectral evolution and (b) weighted mean of SPD, as a function of the delay between the lasing and tuning pulses, as the former is scanned through the wider tuning pulse. The horizontal line in (b) shows the mean SPD when no current is applied to the tuning section, and serves as a reference. (c) Spectral evolution with applied tuning power at the longer tuning section. (d) Weighted mean of the SPD as a function of the tuning power. Error bars in the experimental data correspond to weighted standard deviation. 136

Figure 5.24: Experimental data obtained from device 5B with the shorter cavity as the tuning section. (a) Blue-shift of spectrum and (b) the mean SPD with a constant lasing section current of 2.03 A, when the tuning power is varied in the shorter section. Error bars indicate weighted standard deviation of the spectral distribution. 137

Figure 5.25: Experimental data obtained from device 5B with the longer cavity as the tuning section. (a) Red shift of spectrum and (b) the mean SPD with a constant lasing-section current of 0.95 A, when the tuning power is varied in the shorter section. Error bars indicate weighted standard deviation of the spectral distribution. 138

Figure 6.1: Normalised transmission in a coupled cavity device with a 3.4-mm long lasing section (red), 1.5-mm long tuning section (blue) and a 16- μm wide air gap (design 2, Chapter 5). The coupled cavity has a resonant frequency of 2.755 THz when no tuning current is applied (bottom panel). Increasing the tuning current changes refractive index of the tuning section and shifts the alignment as indicated by arrows

- (top three panels, tuning current is increased to a maximum bias in the top panel). The shift of alignment results in partially aligned detuned states. The misalignments of the longitudinal modes are highlighted in coloured rectangle boxes. 144
- Figure 6.2: Normalised transmission in a detuned coupled cavity device with a 3.6 mm long lasing section (red) and 1.3 mm long tuning section (blue). The longitudinal modes at the lasing and tuning sections are partially aligned. The modes with maximum longitudinal mode overlap are marked with arrows. Increasing tuning current does not result in a monotonic shift in resonance. 145
- Figure 6.3: Normalised product of transmission at lasing and tuning section as a function of heating power. Results from a detuned coupled cavity design with a 3.0-mm long lasing section, 1.6-mm long tuning section and a 16- μ m wide air gap: (a) Heating power varied at the tuning section only. (b) Heating power varied at the lasing section only. Distribution of alignment is represented as a colour contour with red being complete alignment and dark blue being misalignment..... 146
- Figure 6.4: Schematic diagram of the variation of the current at the lasing and tuning section and the heat sink temperature used to simulate quasi-continuous tuning. . 147
- Figure 6.5: Normalised product of transmission at the lasing and the tuning section. Results from a detuned coupled cavity from L701 with a 3.0-mm long lasing section, 1.6-mm long tuning section and a 16- μ m wide air gap. Current at both the lasing and the tuning sections, and heat sink temperature are varied. Distribution of alignment is represented as a colour contour with red being complete alignment and dark blue being misalignment..... 147
- Figure 6.6: Normalised product of transmission at lasing and tuning section as a function of heating power. Results from a detuned coupled cavity design from L1007 with a 3.5-mm long lasing section, 1.2-mm long tuning section and a 16- μ m wide air gap: (a) Heating power varied at the tuning section only. (b) Heating power varied at the lasing section only. Distribution of alignment is represented as a colour contour with red being complete alignment and dark blue being misalignment. 148
- Figure 6.7: Normalised product of transmission at lasing and tuning section from a detuned coupled cavity from L1007 with a 3.5 mm long lasing section, 1.2 mm long tuning section and a 16 μ m air gap. Current at both lasing and tuning sections, and heat sink temperature are varied. Distribution of alignment is represented as a colour contour with red being complete alignment and dark blue being misalignment. 149
- Figure 6.8: Schematic diagram of experimental setup for measuring spectra from detuned coupled cavity QCLs. 150
- Figure 6.9: Spectra and the corresponding weighted mean of the SPD from detuned coupled cavity device 6A. Lasing section current of 1.73 A. Tuning section heated with: (a) 10 μ s and (b) 95 μ s wide pulses, and (c) with DC current. SPD is plotted as a function of the tuning section current is shown (b, d, f). The horizontal line shows the mean SPD when no current is applied to the tuning section, and serves as a reference. 152
- Figure 6.10: Spectra and the corresponding weighted mean of the SPD from detuned coupled cavity device 6A. Lasing section current of 2.29 A. Tuning section heated with: (a) 10 μ s and (b) 95 μ s wide pulses, and (c) with DC current. SPD is plotted as a function of the tuning section current is shown (b, d, f). The horizontal line shows

the mean SPD when no current is applied to the tuning section, and serves as a reference.	153
Figure 6.11: Scanning electron microscopy of damage to device 6A after high DC negative current operation. The electrical contacts to the device were shorted.....	154
Figure 6.12: Collated spectra from detuned coupled cavity device 6A.....	154
Figure 6.13: Spectra from detuned design 6B: at different lasing section bias and (tuning section pulse width): (a) 0.83 A (20 μ s), (b) 1.20 A (20 μ s), (c) 0.95 A (20 μ s), (d) 0.95 A (95 μ s), (e) 1.06 A (20 μ s), (f) 1.06 A (95 μ s), (g) 1.13 A (20 μ s), (h) 1.13 A (95 μ s).....	156
Figure 6.14: Collated spectra from detuned coupled cavity device 6B.....	157
Figure 6.15: Schematic illustration of a coupled cavity device with photonic lattice. Inset: Photonic lattice.....	158
Figure 6.16: A schematic diagram of longitudinal cross-section of a PL with a central $\lambda/4$ -shifted element. PL grating pitch Λ comprise of a metallised section of length L_u (with cladding metal and n^+ -doped contact), and an unmetallised section of length L_e (without cladding metal and n-doped contact). The central $\lambda/4$ -shifted element is realised by breaking the PL periodicity and by inserting an additional element of length L_u into the PL feature with cladding material.	161
Figure 6.17: Normalised transmission (black) in a: (a) uniform PL and (b) PL with a $\lambda/4$ -shifted element. The uniform PL introduces a stop band centred at Bragg frequency, whereas the $\lambda/4$ -shifted PL introduces a stop band with an additional peak at the Bragg frequency. Both the PLs have a same Bragg frequency (red) at 2.75 THz and have 2- μ m deep etched unmetallised sections.	162
Figure 6.18: Normalised transmission in the coupled cavity device 5B, with a PL centred at 2.73 THz. Distribution of alignment is represented as a colour contour with red being complete alignment and dark blue being misalignment.	163
Figure 6.19: Normalised transmission from detuned cavity design 2 (device 6B) with a $\lambda/4$ -shifted PL centred at 2.205 THz as a function of heating power at the tuning section.	164
Figure 6.20: Scanning electron microscopy of a coupled cavity device before FIB milling to etch PL. Devices were wire bonded on either side of a central region where PL would be milled at the lasing section.	164
Figure 6.21: Scanning electron microscopy after FIB milling of PL in device 5B-PL: (a) a shallow etched uniform PL, (b) shallow etch profile, (c) Deep etched $\lambda/4$ -shifted PL in device 6B-PL.	165
Figure 6.22: Spectra from device 5B-PL after uniform PL milling.	166
Figure 6.23: LIV characteristics obtained from device 5B-PL after $\lambda/4$ -shifted PL patterning. Emission from lasing section is obtained at different current at tuning section.	167
Figure 6.24: Collated spectra from device 6B-PL with a $\lambda/4$ -shifted PL at different lasing and tuning currents. (a) SM emission at 2.21 THz with an SMSR of 20 dB and (b) a continuous tuning of ~ 3 GHz.....	168

Figure 7.1: Illustration of a coupled cavity THz QCL with a wide aperture tuning section.	174
Figure 7.2: Illustration of a coupled cavity THz QCL with evanescent field coupled tuning sections.	174
Figure 7.3: Illustration of a coupled cavity THz QCL with evanescent field coupled SG- DFBs. The central section is tapered near the coupled sections to increase coupling.	175

List of tables

Table 2.1: MBE layer growth structure of L1007.....	31
Table 3.1: List of designed THz QCLs with PLs.	65
Table 3.2: MBE layer growth structure of L701.....	67
Table 3.3: List of fabricated THz QCLs with PLs.....	70
Table 4.1: List of fabricated THz QCLs electrically-controlled PLs.....	93
Table 5.1: List of processed coupled cavity THz QCLs.....	128
Table 6.1: List of processed detuned coupled cavity THz QCLs.	149
Table 6.2: List of processed coupled cavity THz QCLs with a PL.....	165

Chapter 1

Introduction

1.1 Terahertz frequency spectrum

The terahertz (THz) frequency range, also known as the far infra-red (FIR) range, comprises frequencies ranging from 300 GHz to 10 THz in the electromagnetic spectrum [1,2]. These frequencies are of immense interest to both academic and industrial communities due to a plethora of proposed applications including imaging [3], astronomy [4] and spectroscopy [5]. Indeed, the non-ionising properties of THz radiation and its absorption by water molecules can be exploited for medical imaging. In fact, medical imaging systems based on THz technology have been demonstrated for detection of cancerous tissues [6] as well as imaging of an extracted human tooth [7]. In addition, the ability of THz radiation to penetrate through clothing and packaging material has been harnessed to detect concealed weapons [8]. Excitation of molecular rotation and vibration in the THz range also forms the basis of spectroscopic and astronomical applications. This is particularly significant as interstellar dust and heavy molecules have vibrational and rotational spectra in the THz range [9]. Additionally, a significantly large proportion (98%) of all photons emitted since the Big Bang are in the THz and sub-millimetre range [4,10]. Furthermore, THz frequency has also been investigated for secure communication over a smaller footprint area, which exploits the water attenuation of THz radiation [11].

Owing to its relative position in the electromagnetic spectrum [Figure 1.1], THz sources have been designed using techniques prevalent in both microwave engineering and semiconductor based opto-electronics. For example, THz radiation has been generated from backward wave oscillators [12], photo conductive switches [3] and surface field acceleration in semiconductor surface [13]. Indeed, photo conductive switches are the basis for broad band THz time domain spectroscopy [3] and on-chip microscopic systems [14]. These sources do, however, have their inherent limitations. For many applications, particularly imaging and gas spectroscopy, a high power compact THz source emitting at a stable single frequency is required. Indeed, it has long been realised that terahertz frequencies have not been exploited fully, in comparison to the optical or the microwave frequencies, owing to the lack of a solid-state emitter. The absence of such a reliable solid state emitter operating in the THz frequencies is described in the literature as the “Terahertz Gap” [2].

However, in 2002 a compact solid-state source of THz radiation was realised – the THz *quantum cascade laser* (QCL) [15]. Since this first demonstration, the THz QCL has seen tremendous development. The following section briefly describes the basic operating principles for semiconductor lasers. Operation of QCLs and their development is discussed in section 1.3. Single mode emission, a highly desirable requirement in many spectroscopic applications and interferometric techniques, is then discussed in section 1.4, and the chapter is concluded with section 1.5, which outlines the structure of this thesis.

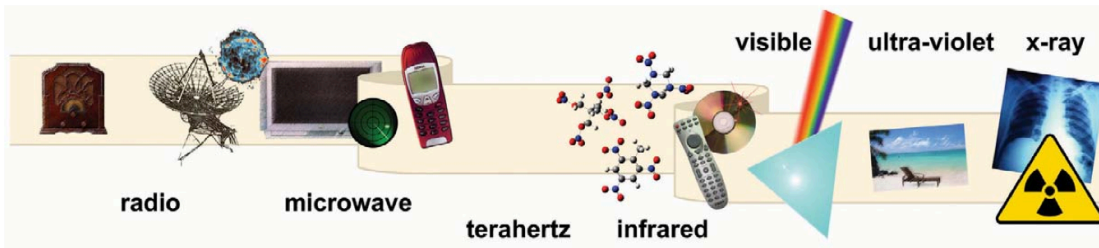


Figure 1.1: Position of THz range in the electromagnetic spectrum. Taken from ref. [5].

1.2 Interband and intersubband semiconductor lasers

The interaction between photons and electrons is governed by Planck’s relation. In a simple system with two electron energy levels, an electron at a lower energy state E_1 can be excited to an upper energy state E_2 by a photon, which has an energy $h\nu$ corresponding to the en-

energy difference between the two states. This is known as ‘*absorption*’ [Figure 1.2 (a)]. Conversely, an electron in the upper energy state E_2 can drop to the lower energy state E_1 and emit a photon with an energy corresponding to the energy $E_{21} = E_2 - E_1$. This is known as ‘*spontaneous emission*’ [Figure 1.2 (b)]. There also exists a third possibility, where a photon can interact with an electron at an upper energy state and result in ‘*stimulated emission*’ [Figure 1.2 (c)]. During stimulated emission, an electron in the upper energy E_2 state falls to the lower energy state E_1 and releases a photon with the same phase, frequency, polarisation and direction as the incident photon.

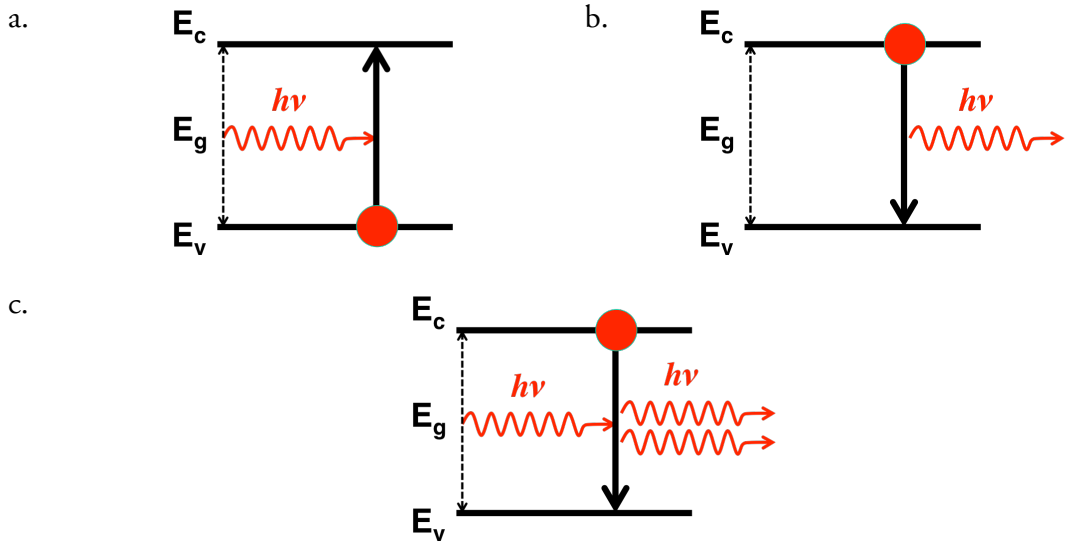


Figure 1.2: Schematic representation of: (a) absorption, (b) spontaneous emission and (c) stimulated emission. [Modified from ref. [16]].

In a semiconductor laser, electrons are ‘*pumped*’ to a higher energy state using either an external light source (‘*optical*’ pumping) or using an electrical current source (‘*electrical*’ pumping). This results in a non-equilibrium system where the majority of electrons are excited to a higher energy state (‘*upper lasing state*’) with very few electrons in the lower energy state (‘*lower lasing state*’) and is referred to as ‘*population inversion*’. An incident photon with the same energy as the difference between the upper and lower energy states would result in stimulated emission with strong coherence. The decayed electrons are then re-pumped to the upper lasing state using the external source and the process is repeated.

Another important aspect in the laser design is incorporation of a waveguide to confine the emitted photons within the gain material to induce further stimulated emission. This can be achieved by enclosing the gain material within a ‘*cladding*’ material whose die-

electric index is lower than the active material. The resulting refractive index contrast between the active material and the cladding material facilitates total internal reflection and radiation is guided through the gain medium. A semiconductor laser traditionally uses dielectric layers as cladding material in the z (growth) direction and cleaved facets are used as mirror faces in the x - y plane, which reflect photons back into the cavity and provide feedback to the structure.

In a conventional semiconductor laser, the conduction and valence bands constitute the upper and lower lasing states respectively. For example, a pn junction diode can be degenerately doped to move the Fermi level into the valence and conduction bands respectively. Population inversion is then achieved by forward biasing the diode. The frequency of the emitted radiation depends on the bandgap of the material. Such lasers are referred to as *interband* lasers after the nature of the lasing transition [Figure 1.3 (a)].

A different laser design, based on multiple quantum wells (QWs) makes it possible to tailor the energy of the lasing transition. QWs are realised by depositing thin layers of alternating semiconductor materials of different energy bandgaps to form a heterostructure. Unlike bulk semiconductors, electron states in a quantum well are quantised at discrete energy ‘*subbands*’ [17]. Moreover, the discrete energy levels can be engineered by varying the width of the quantum well. Thus, the lasing transition in quantum well lasers is tailored by the discrete energy subbands [18]. A schematic of interband transitions in a quantum well laser is shown in Figure 1.3 (b).

Bandgap engineering of interband transitions has enabled engineering of the frequency of optical transitions. It further enabled the possibilities of designing semiconductor lasers operating at lower frequencies, notably the mid-infrared (mid-IR) and FIR or THz range of the electromagnetic spectrum. However, the low frequency of these regions required lasing transition smaller than the bandgap of the semiconductor material system. This was achieved in a unipolar lasing transition where electrons would scatter between energy subbands in the conduction band itself, and led to the design of the QCL. Such lasers are known as ‘*intersubband*’ lasers due to the intersubband nature of the lasing transitions [Figure 1.3 (c)].

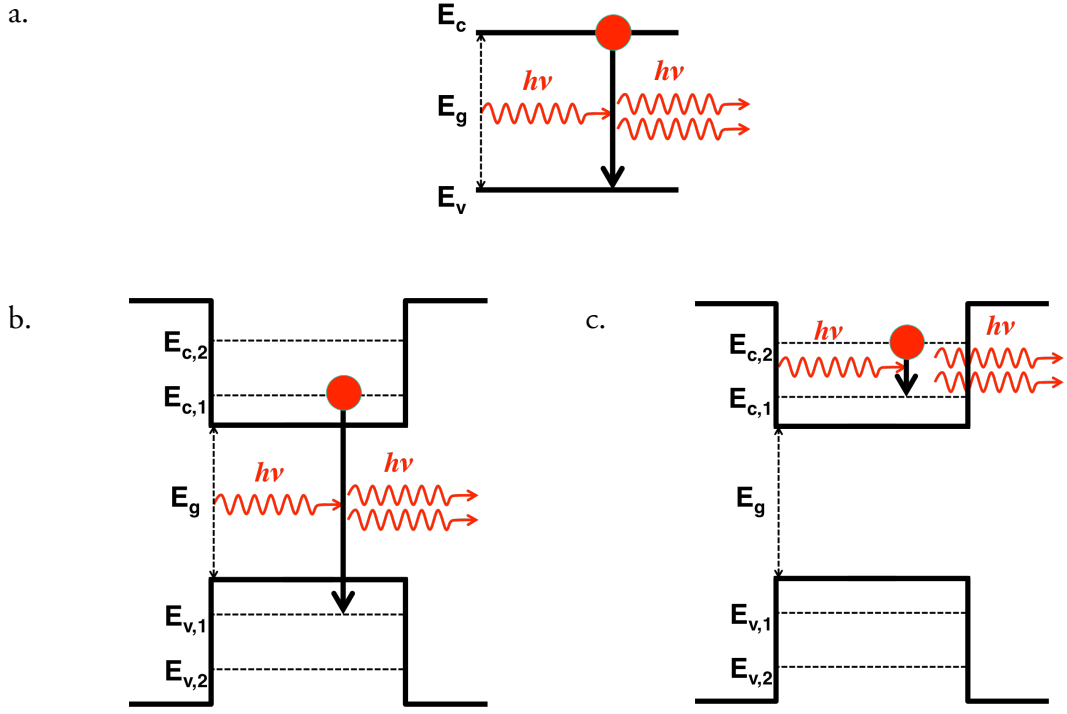


Figure 1.3: Schematic representation of: (a) interband optical transition between conduction band and valence band, (b) interband optical transition between subbands in the conduction and valence band, and (c) intersubband optical transition between subbands in the conduction band.

1.3 Quantum cascade laser

A QCL is an intersubband cascaded laser designed by coupling multiple quantum wells to form a ‘*superlattice*’ (SL), with discrete electron states in the quantum wells overlapping to form ‘*minibands*’ of energy. Fast scattering of electrons is possible in these minibands and they can be used to form the ‘*injector*’ and the ‘*extractor*’ stages in the QCL. On application of an electric field electrons are scattered into the upper lasing subband through the injector stage, whereupon an optical (mid-IR/THz) transition takes place and the electron relaxes to a lower lasing subband. Electrons are subsequently extracted from the lower lasing subband through the extractor miniband. The injector, optical transition and extractor stages form an ‘*active module*’ in a QCL [Figure 1.4 (a)]. A salient feature of the QCL is a periodic arrangement of active modules where an extractor stage scatters electrons to the injector stage of the next active module [Figure 1.4 (b)]. Thus, electrons ‘*cascade*’ down the active module stack and, in principle, emit a photon at each optical transition stage. Various QCL active region designs have been published in the literature, optimising various aspects of this device operation. This will be discussed in greater detail in section 1.3.2,

where the different scattering mechanism (e.g. phonon-assisted, electron–electron) occurring in the injector and extractor will be discussed. The operating principles of a QCL are discussed next.

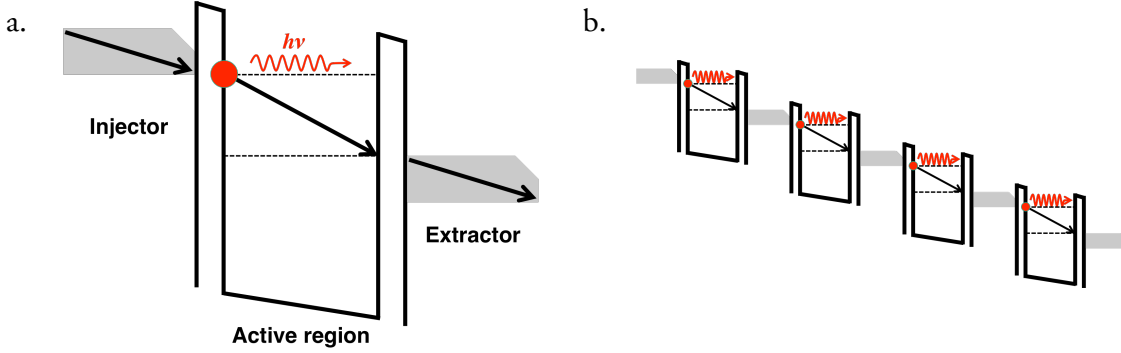


Figure 1.4: Schematic representation of: (a) intersubband optical transitions in an active module of a QCL, (b) cascading of electron through multiple active modules in a QCL. Adapted from ref. [19].

1.3.1 Operation of QCLs

The operation of a QCL can be explained most simply by modelling the active region as a three-level laser [Figure 1.5]. Electrons are injected into the upper lasing level 3. An optical transition occurs as an electron relaxes from upper lasing level 3 to level 2. Electrons then scatter from level 2 to level 1 and are extracted from level 1 through minibands. Assuming that all electrons are injected only into the upper lasing level 3 and are only extracted from level 1, for simplicity, the scattering rate equations at various levels can be described as:

$$\frac{\partial n_3}{\partial t} = \frac{\eta J_{in}}{e} + \frac{n_1}{\tau_{13}} + \frac{n_2}{\tau_{23}} - \frac{n_3}{\tau_{31}} - \frac{n_3}{\tau_{32}} \quad (1.1)$$

$$\frac{\partial n_2}{\partial t} = \frac{n_3}{\tau_{32}} + \frac{n_1}{\tau_{12}} - \frac{n_2}{\tau_{21}} - \frac{n_2}{\tau_{23}} \quad (1.2)$$

$$\frac{\partial n_1}{\partial t} = \frac{n_2}{\tau_{21}} + \frac{n_3}{\tau_{31}} - \frac{n_1}{\tau_{13}} - \frac{n_1}{\tau_{12}} - \frac{J_{out}}{e} \quad (1.3)$$

where η is the injection efficiency, n_i is the number of electrons in level i , e is the electronic charge, J is the current density and τ_{ij} is lifetime of the transition between initial subband i and final subband j . For a ‘cold’ system with no phonon (crystal lattice vibration) or thermal excitation of electrons to higher subbands, the above equations can be simplified further as:

$$\frac{\partial n_3}{\partial t} = \frac{J_{in}}{e} - \frac{n_3}{\tau_{31}} - \frac{n_3}{\tau_{32}} \quad (1.4)$$

$$\frac{\partial n_2}{\partial t} = \frac{n_3}{\tau_{32}} - \frac{n_2}{\tau_{21}} \quad (1.5)$$

$$\frac{\partial n_1}{\partial t} = \frac{n_2}{\tau_{21}} + \frac{n_3}{\tau_{31}} - \frac{J_{out}}{e} \quad (1.6)$$

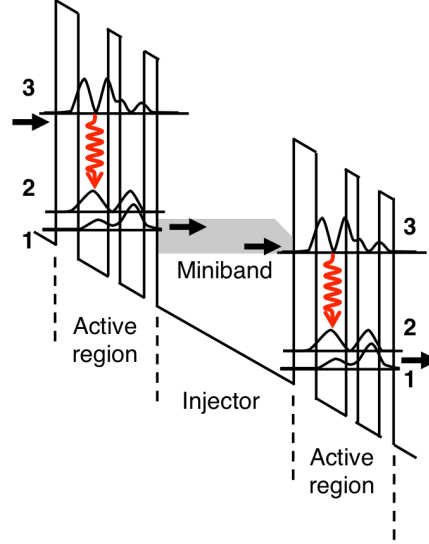


Figure 1.5: Schematic representation of a QCL with three-level lasing levels.
Adapted from [20].

At steady state, the time derivative equates to zero, and eq. (1.5) can be rearranged as:

$$\frac{n_3}{\tau_{32}} = \frac{n_2}{\tau_{21}} \quad (1.7)$$

The necessary conditions for population inversion ($n_3 > n_2$) can be derived from eq. (1.7) as $\tau_{32} > \tau_{21}$.

The gain coefficient in QCL is mathematically expressed as [20,21]:

$$g = \eta \tau_3 \left(1 - \frac{\tau_2}{\tau_{32}}\right) \frac{4\pi e z_{32}^2}{\lambda_0 \epsilon_0 n_{eff} L_p} \frac{1}{2\gamma_{32}} \quad (1.8)$$

where z_{32}^2 is the dipole matrix element, λ_0 is the wavelength in vacuum, ϵ_0 is the dielectric constant in vacuum, n_{eff} is the effective refractive mode index, L_p is the length of one period of the active module and injector/extractor stage, $2\gamma_{32}$ is the full-width-at-half maximum of spontaneous emission spectrum, and τ_3 and τ_2 are total upper and lower state life

times respectively. Lasing is observed when the gain in the structure exceeds the losses. The threshold current density, J_{Th} , then is expressed as [20]:

$$J_{Th} = \frac{\alpha_m + \alpha_w}{\Gamma g} \quad (1.9)$$

where Γ is the confinement of the optical mode in the active material, α_w is the waveguide loss and α_m is the mirror loss, which can be calculated from the Fresnel reflectivity of the laser facets, specifically, the mirror losses can be expressed as [20]:

$$\alpha_m = \frac{1}{L} \ln R \quad (1.10)$$

where L is the length of the laser cavity and R is the reflectivity, which can be expressed as [20]:

$$R = \left(\frac{n_{eff} - 1}{n_{eff} + 1} \right)^2 \quad (1.11)$$

The threshold current in QCLs exhibits an exponential rise with temperature and can be expressed as [20]:

$$J_{Th}(T) = J_0 \exp\left(\frac{T}{T_0}\right) \quad (1.12)$$

where J_0 is the threshold current at the characteristic temperature T_0 .

The slope efficiency, which is a measure of the increase in optical power per unit current above lasing threshold, can then be expressed as [20]:

$$\frac{\partial P}{\partial I} = \eta \frac{1}{2} \frac{h\nu}{e} N_p \frac{\alpha_m}{\alpha_m + \alpha_w} \left(1 - \frac{\tau_2}{\tau_{32}} \right) \quad (1.13)$$

where $h\nu$ is the energy of the emitted photon and N_p is the number of repetitions of active modules including injector/extractor stages.

The following section briefly describes the major milestones in the development of QCL technology.

1.3.2 Development of QCLs

1.3.2.1 Mid-IR QCL active region design

Unipolar intersubband transitions and population inversion in a cascaded structures were first proposed in the seminal paper by R. Kazarinov and R. Suris in 1971 [22]. However, in initial experiments lasing was not observed. This was later ascribed to be due to a lack of a uniform electric field in the designed structures [20]. Electron scattering and ultrafast relaxation through longitudinal-optical (LO) phonons, i.e. crystal lattice vibrations, were further challenges faced during the initial design of the quantum cascade structure. Indeed, it was believed that electron scattering through the non-radiative LO phonon would be dominant in a design where the optical transition is larger than the LO phonon energy [20]. A practical realisation of the cascaded design also required precise layers of high quality semiconductor material, which was a technological challenge at the time. However, with the development and optimisation of molecular beam epitaxy (MBE) the growth of complex quantum structures with atomic level precision became a reality [23–25].

The first successful unipolar intersubband laser was demonstrated in 1994 and operated in the mid-IR range of the electromagnetic spectrum at a wavelength of $4.2\ \mu\text{m}$ [26]. The QCL was grown using MBE in the GaInAs/AlInAs material system on an InP substrate. In this design, the extractor stage used LO phonons, which had initially been thought to be detrimental to optical transition, to depopulate lower lasing subbands [Figure 1.6]. The QCL operated in pulsed mode at cryogenic temperatures with a maximum operating temperature of 88 K and a peak power of $\sim 8\ \text{mW}$. In the design, the 3-QW active region with a diagonal optical transition was separated with a SL graded injector stage that supposedly prevented electric field inhomogeneity. However, subsequent demonstrations of QCLs without any injector proved otherwise [27,28]. Furthermore, reduction of doping in the injector stage reduced impurity scattering and lowered threshold current [29].

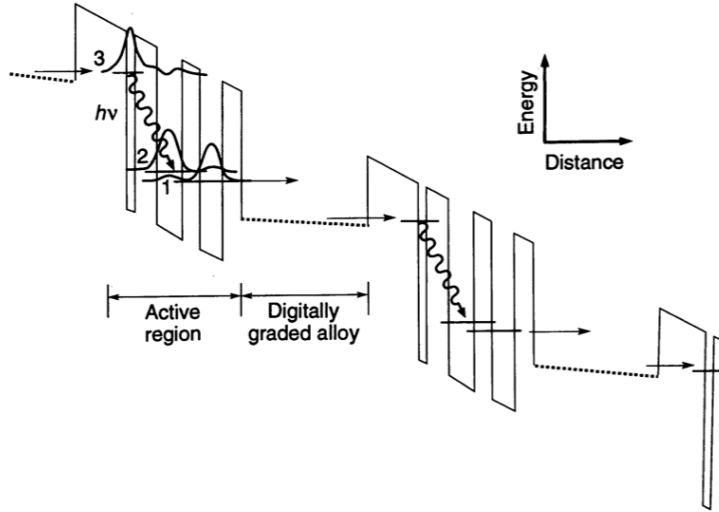


Figure 1.6: Conduction band of the first demonstrated QCL. Moduli-squared of electron wavefunctions in the active region and the injector/extractor stage formed from a digitally graded alloy are shown. Taken from [26].

Although the first QCL used a 3-QW design, active region designs with fewer QWs were also demonstrated. Shortly after the first demonstration, a 2-QW active region design with vertical optical transition was reported in ref. [30]. The conduction band of the design is shown in Figure 1.7 (a). The vertical optical transition offered advantages over the diagonal optical transition used in the first demonstration, such as narrower gain spectrum and lower threshold currents due to the reduced sensitivity to interface roughness and impurity fluctuations [31]. The 2-QW was optimised further to achieve continuous wave (CW) operation at 80 K [32], 110 K [33] and then at room temperature [34]. An active region design with 1-QW was also reported in ref. [35], which operated with a higher carrier lifetime in the lower lasing subband. However, the design did not match the superior temperature performance of the 2-QW based active region design. Meanwhile, an optimised low-doped 3-QW active region with a vertical optical transition and a ‘*funnel*’ injector stage [Figure 1.7 (b)], which featured a gradual decrease in injector/extractor miniband, resulted in the first high power (~ 200 mW) pulsed mode room temperature operation [36,37]. This tapered injector design effectively funnelled electrons into the ground state of the injector/extractor stage and into the upper lasing state of the next active module.

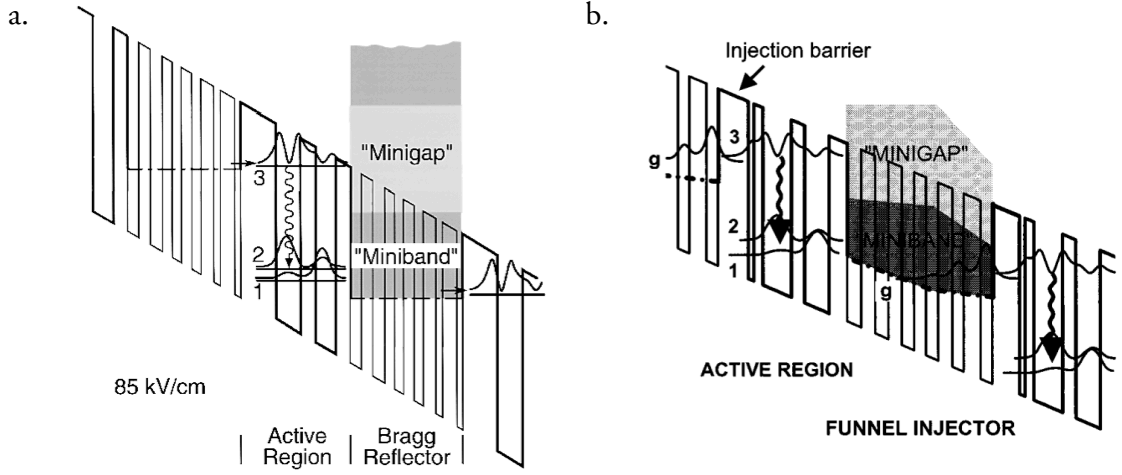


Figure 1.7: Conduction band of a QCL with: (a) Vertical optical transition. Taken from [30]. (b) Tapered funnel injector. Taken from [36].

All of the active regions discussed so far involved optical transitions between two localised discrete subbands in one or more QWs. A different active region design, based on a SL was reported in ref. [38]. In this design, the optical transition was obtained between two strongly coupled SLs with electrons scattering across a *minigap* formed between the SLs [Figure 1.8 (a)]. Thus, the emission frequency was proportional to the energy difference between the SL minibands. The strong coupling of electron energy states in the SL allowed a higher current density through the structure. However, the selectivity of electron injection in this design was compromised due to the broad miniband associated with the optical transition. Although a higher optical power was obtained from the SL based active regions, the uniformly doped active region used to obtain a uniform electric field resulted in increased impurity scattering and higher lasing threshold, which limited CW operation of the design [39]. The effect of the impurity scattering was also manifested in the broad electroluminescence spectrum [38]. The SL design was subsequently improved by using uniform doping of injector stages and undoped active regions [39]. This was further optimised by doping specific injector regions, which reduced the impurity scattering and lowered the lasing threshold [40]. However, the high doping in specific regions of the injector stage resulted in an increase in lasing threshold at elevated temperature. The undoped SL active region was further optimised by gradual decrease in well width in the direction of electron flow to form a ‘*chirped*’ SL [41], as shown in Figure 1.8 (b). The graded SL led to localised subbands, which formed a ‘*quasi-electric field*’. On application of an external field, the quasi-electric fields are compensated to form a uniform field in the structure. Lowering doping in this active region also improved the performance compared to a ‘*normal*’ SL design.

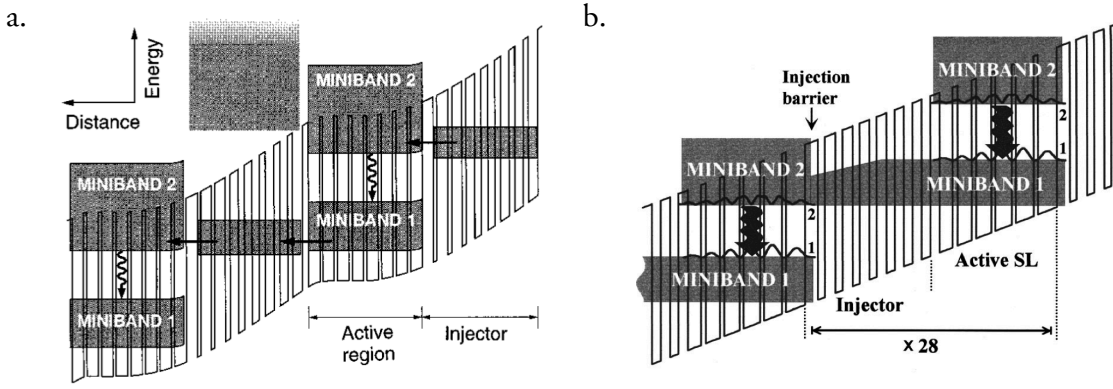


Figure 1.8: Conduction band of a QCL based on: (a) a superlattice. Taken from [38]. (b) A chirped superlattice. Taken from [41].

Another major milestone in the development of QCLs was the demonstration of lasing using a different material system. All initial QCL designs were grown using the GaInAs/AlInAs material system. However, a QCL based on the GaAs/Al_{0.33}Ga_{0.67}As material system was reported in ref. [42], although there is a superior conduction band discontinuity and lower effective mass in the established GaInAs/AlInAs material system [43]. In fact, the conduction band discontinuity in GaInAs/AlInAs system was reported to be ~520 meV [44,45], compared to value 290 meV observed in the first GaAs/Al_{0.33}Ga_{0.77}As based QCL [42,45]. However, GaAs/AlGaAs material system had an advantage over the InP based material system as it benefited from an established processing technology owing to the more commercial application of this material system at that time [46,47]. The adaptation to the GaAs/AlGaAs material system was crucial, however, for the development of the first FIR or THz QCL as a lower free carrier loss in THz regime was postulated due to the higher effective mass in this material system [45].

1.3.2.2 Mid-IR QCL waveguides

Section 1.3.2.1 described the development of mid-IR QCL active region design. This section describe the waveguides used in mid-IR QCLs, which are optimised to lower losses.

QCLs based on the GaInAs/AlInAs material system used an InP substrate, which had lower refractive index of ~3.10 than the active region [20,26,48]. Hence, an effective optical cladding at the bottom of the active region was obtained from the substrate itself [43]. The top cladding was realised through growing alternate layers of InGaAs/AlInAs using MBE forming a DBR stack. To compensate for the weak refractive index contrast between

the top cladding and the active layers, a thicker cladding layer was used for QCLs with wavelength between 8–15 μm [49]. The top cladding layers were also doped to facilitate current injection through the active layers, but this increased free carrier losses in the waveguide [50]. Waveguide losses are particularly severe for QCLs operating at wavelengths longer than $\sim 20 \mu\text{m}$, as the free carrier losses are proportional to the square of the wavelength [43,49]. The thicker cladding layers also posed a tremendous challenge for MBE growth.

In addition to the free carrier losses, another significant contributor to waveguide loss originated from coupling of the optical mode to a surface plasmon (SP) formed at the interface between the cladding and metallised contacts at the top [20]. SPs are electron oscillations at a material interface where the dielectric constants of the materials change polarity [51]. To reduce this additional waveguide loss, a waveguide based on SP was reported in ref. [49]. This waveguide, called the '*plasmon enhanced*' waveguide included a highly doped GaInAs layer between the active material and top metallisation to reduce unwanted coupling and increase confinement of the optical mode within the active material, but the additional highly doped GaInAs layer also increased the free-carrier losses in the waveguide [52,53]. However, it was subsequently shown that the lower skin-depth of the SPs in the metal at longer wavelengths ($\sim 17 \mu\text{m}$) results in lower free-carrier losses but an increase in the optical confinement [53,54]. The increased confinement and lower losses also improved the temperature performance of the laser [53]. The SP based waveguide was improved further to include SP based cladding at both top and bottom of the active material, which further lowered the waveguide losses [55]. The mode profiles of the fundamental optical mode in plasmon enhanced and SP based waveguides are shown in Figure 1.9.

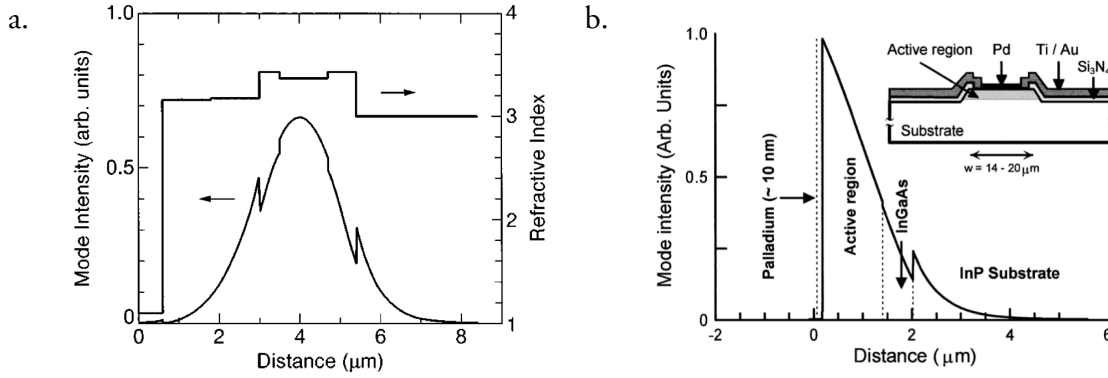


Figure 1.9: Refractive index and mode profiles of the fundamental optical modes in a: (a) Plasmon enhanced waveguide. Taken from [50]. (b) SP waveguide. (Inset) Device cross-section. Taken from [49].

Unlike for GaInAs/AlInAs QCLs on InP, the GaAs substrate used for GaAs/AlGaAs based QCLs does not give a large refractive index contrast with the active material [42]. Hence, the natural optical confinement obtained from the InP substrate in the former was not applicable for GaAs based devices. Instead, GaAs based QCLs used AlGaAs with high Al content as the cladding material. This reduced the cladding layer thickness while providing the required refractive index contrast [20,42]. However, the high Al content in the cladding proved detrimental to current transport due to the formation of deep level defects, which prompted an Al free cladding layer design [46,56]. Plasmonic cladding, using doped GaAs, was used in GaAs/AlGaAs based QCLs [57]. The refractive index profile and fundamental optical mode in a GaAs/AlGaAs QCL with doped GaAs cladding is shown in Figure 1.10. Plasmonic waveguides play a crucial role in the development of THz QCLs, which is discussed next.

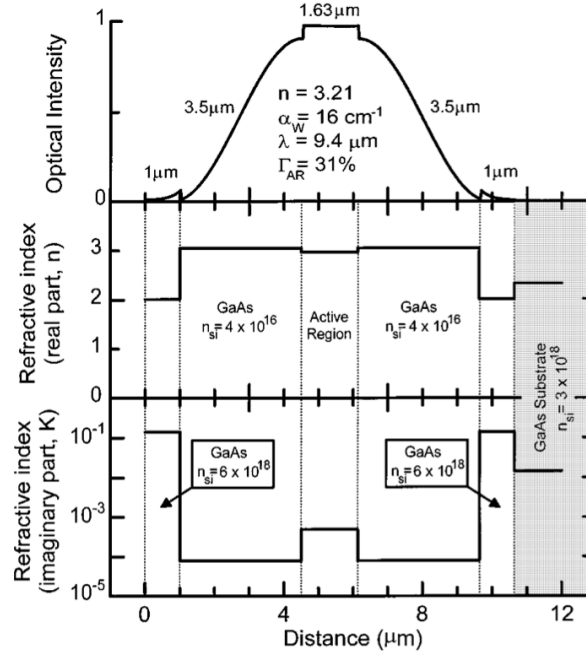


Figure 1.10: The refractive index and mode profile of the fundamental optical mode in a GaAs/AlGaAs based QCL with plasmonic cladding. Taken from [57].

1.3.2.3 THz QCL active region design

Operation of QCLs in the long wavelength (THz) range requires smaller energy separation between the upper and lower lasing states. This narrow energy separation poses a significant challenge to the efficient extract of electrons from the lower lasing state without depopulating the upper lasing state. Indeed, the energy separation of lasing states in THz QCLs is smaller than the LO phonon energy. Unlike mid-IR QCLs where electron transport is dominated by electron-phonon scattering, the lower optical transition energy and the absence of LO phonon interactions in THz QCLs entailed electron transport through elastic scattering processes, such as electron-electron scattering, impurity scattering and interface roughness scattering [43,58]. These inefficient transport properties in THz QCLs can result in hot electrons, which can acquire sufficient thermal excitation to relax through a non-radiative LO phonon transition [58–60]. Population inversion in THz QCLs is also affected by thermal back-filling of lower lasing states, and room temperature operation of THz QCLs has not yet been achieved because of these adverse thermal effects. The long wavelengths in the THz spectrum also increase free-carrier losses and render dielectric waveguides unsuitable for THz QCLs. Hence, development of THz QCLs required optimised waveguides based on surface plasmons.

The realisation of a THz QCL had to wait for almost a decade after the first mid-IR QCL and was first demonstrated in 2002 [15]. The reported THz QCL emitted a few milli-Watts of optical power at 4.4 THz and addressed many issues that hitherto had plagued the operation of QCL designs in the THz range. It featured a GaAs/AlGaAs chirped SL design to maintain population inversion [Figure 1.11]. The SL structure had wide minibands allowing efficient extraction of electrons and suppressing thermal backfilling, which was pivotal in achieving population inversion in the device. While the first THz QCL operated in pulsed mode to ~ 50 K, optimisation of the fabrication methodology and device geometry resulted in CW mode emission upto 35 K [61]. Further improvement in temperature performance (48 K) in CW mode was observed by reducing the contact stripes used for ohmic metallisation at the top of the ridge [62]. A similar chirped superlattice design was also modified to obtain even lower frequency emission at ~ 3.5 THz [63]. A 2 THz QCL with a chirped SL was subsequently reported in ref. [64].

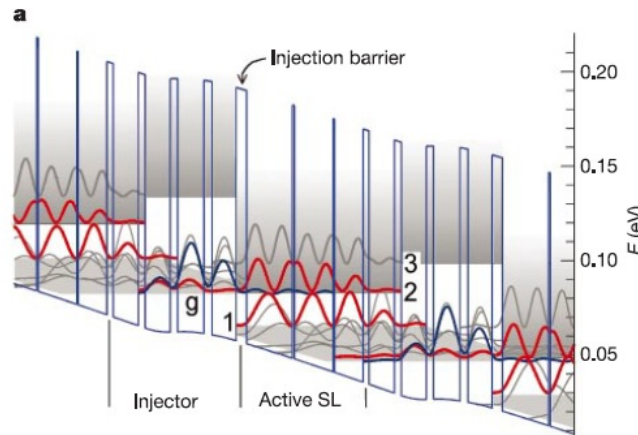


Figure 1.11: Conduction band of the active region of the first demonstrated THz QCL. Minibands of energy levels, shown in grey, allows injection of electrons into the upper lasing state 2, and extraction of electrons from the lower lasing state 1 to the next upper lasing state. Taken from [15].

THz QCLs with a different, ‘*bound-to-continuum*’ (BTC), active region were reported in [65]. The BTC active region design is similar to the chirped superlattice structure and involves extraction of electrons in the lower lasing state through a miniband. However, the upper lasing state incorporates a bound defect state resulting in a spatial diagonal radiative transition. This reduces non-radiative scattering of electrons from upper lasing states and improves lifetime of the upper state. As a result, BTC devices exhibited better tempera-

ture performance than their chirped SL counterparts [66]. The reported design exhibited a superior temperature performance and lased (pulsed) up to a temperature of 95 K [65]. A similar BTC active region was then used to observe emission at lower frequencies (higher wavelength) at 2.90 THz [67], 2.75 THz [68], 2.59 THz [68], 1.8 THz [69], and 1.6 THz [70]. The performance of BTC devices at lower frequency was also optimised to improve wall-plug efficiency and extraction from the lower lasing state [71].

The next major milestone in the development of THz QCL active region designs was the report of a radical new design involving a LO phonon based depopulation scheme [72]. The conduction band of the reported design is shown in Figure 1.12. The use of the high energy LO phonon (36 meV in GaAs) for depopulation resulted in lower thermal backfilling of the lower lasing states, a better control of population inversion and the subsequent higher temperature of operation. However, these devices require higher operating voltages. Although the first THz QCL with LO phonon active region exhibited a maximum operating temperature of 65 K, the temperature performance was improved significantly using a double-metal waveguide (to be discussed in section 1.3.2.4) [73]. Another advantage of the LO phonon active region over BTC or chirped SL active region is the simpler MBE growth due to the reduced number of QWs. The active region design was also simplified from a four-well design used in the first LO phonon THz QCL to a three-well design [74]. Thermal performance was further improved using a double LO phonon stage, which reduced thermal back filling [75]. Like the BTC design, LO phonon designs have also been used extensively to cover a broad frequency range, with emission observed at 3.8 THz [60], 3.2 THz [76], 3 THz [77], 2.1 THz [78], 1.9 THz [79] and 1.45 THz [80].

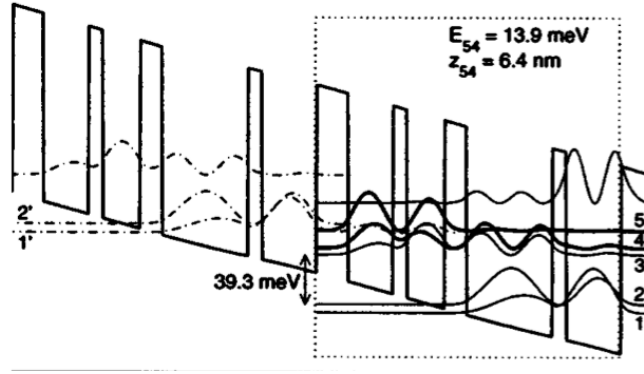


Figure 1.12: Conduction band of the first demonstrated THz QCL with LO phonon depopulation. A vertical optical transition takes place between levels 5 and 4. Level 4 and 3 are in resonance, from where electrons relax to levels 2 and 1 through LO phonons. Taken from [72].

Over recent years, BTC and LO phonon based active regions have become the dominant THz QCL designs. It was only natural that a design, which combined the advantages of both were merged in a single active region design. An active region with a BTC diagonal transition and a LO phonon based depopulation scheme was reported in ref. [81]. The conduction band of the reported design is shown in Figure 1.13. The design was robust to small variations in growth thickness and promised higher temperature operation. Emission between 2.8–3.2 THz was observed from the design with a maximum operating temperature of 160 K. This design was modified further to use a GaAs/AlGaAs material system with a 16% Al fraction (unlike the original 15% Al fraction) to obtain the highest power emission from a THz QCL, with 1 W output obtained from a single facet [82].

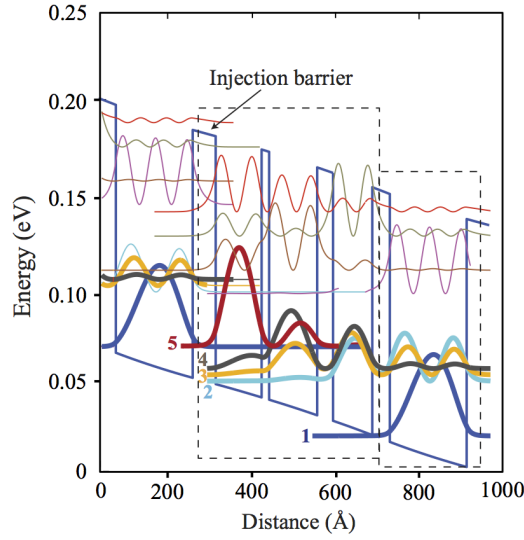


Figure 1.13: Conduction band of a THz QCL design with a BTC optical transition and LO phonon depopulation. Taken from [81].

The dominant LO phonon and BTC designs have also been modified extensively to obtain multi-colour emission from THz QCLs. An active region optimised to operate in dual frequency by changing polarity of the applied field was reported in [83]. This design operated at 2.3 THz in forward bias and 4 THz in reverse bias. Two-colour emission was also observed in a device reported in ref. [84], which involved growth of two disparate active regions in a single heterostructure growth. This premise of growing multiple active region designs in the same heterostructure growth was extended further to design a broadband THz QCL design, which was composed of three different active regions with optical transitions corresponding to 2.3, 2.7 and 3 THz [85]. A broadband emission from 2.2–3.2 THz was observed from the design. Variation of emitted frequency from a THz QCL was also obtained by varying growth parameters systematically to change the width of the QWs. In the first instance, emission at different frequency was observed in multiple wafers where the MBE growth rate was systematically varied [86]. This was improved in a subsequent demonstration of electrically tunable THz QCLs, by systematically varying the MBE growth rate during a single wafer growth [87].

It is worth pointing out that unlike mid-IR QCLs, the majority of THz QCLs reported in the literature use the GaAs/AlGaAs material system. A 15% Al content has been used extensively. However, THz QCLs in different material systems such as GaInAs/AlInAs on InP substrates have been demonstrated [88]. More recently, THz QCLs operating upto

142 K based on GaInAs/GaAsSb material have been shown [89]. Electroluminescence has also been observed from InAs/AlSb based THz QCLs [90].

1.3.2.4 THz QCL waveguides

The first THz QCL used a SP based waveguide and a semi-insulating (SI) GaAs substrate to achieve THz radiation waveguiding in the growth direction [Figure 1.14 (a)]. The SI–GaAs substrate lowered free–carrier loss in the waveguide compared to an n –type substrate. SP modes between the active material and the substrate were realised by using a highly doped ‘buried’ epilayer (with a negative dielectric constant), which was also used as an electrical contact to the device. The SP mode at the top of the ridge was realised by using another highly doped epilayer and metallised contacts. The optical mode in this waveguide extends from the SP mode at the top to the SP mode at the buried contact layer and into the substrate with an optical confinement of around 50% with the gain material. This waveguide geometry is referred to as a semi–insulating surface plasmon (SISP) or ‘single metal’ waveguide in the literature [66].

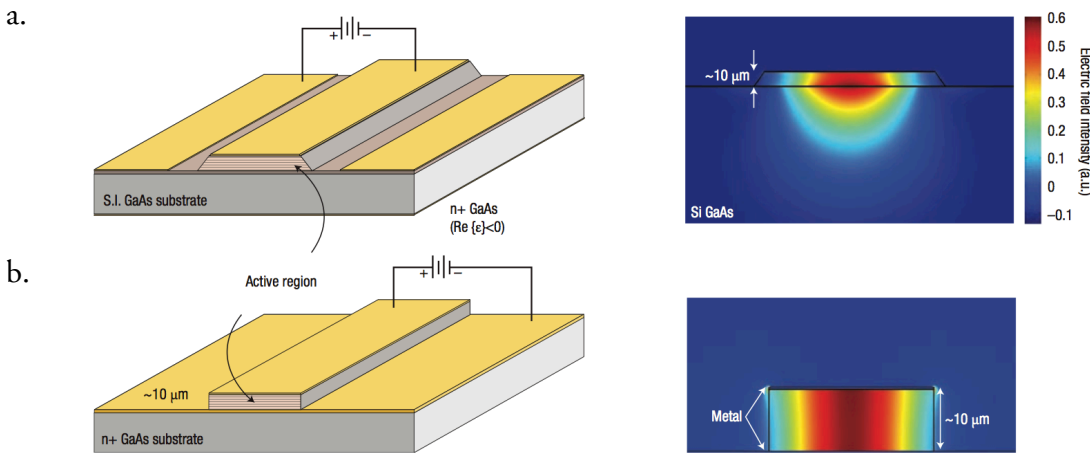


Figure 1.14: (Left) Schematic representations and (right) optical mode intensity profiles of THz QCLs with: (a) Single–metal and (b) double–metal waveguides. Taken from ref. [66].

While the single–metal waveguide was pivotal in extending QCL technology to the THz range, a variation of the SP scheme improved temperature performance of THz QCLs significantly. This is the so–called ‘double–metal’ waveguide [73], which features a metal cladding on either side of the active region [Figure 1.14 (b)]. Radiation is now confined in the active material between the metal cladding and an almost perfect optical confinement is

achieved. However fabrication of these waveguides is not straightforward and requires thermal compression bonding of metal-coated wafers. Another major difference between single and double metal waveguides is the doping of the substrate. Whereas single metal waveguide used an undoped GaAs substrate to reduce free-carrier losses, double-metal waveguides use a doped substrate for electrical connection to the device. Since, radiation is highly confined within the active material through the metal cladding, the doped substrate has little effect on waveguide loss. Although, a double metal cladding with Au was used for the first demonstration of double-metal waveguide, it was reported that the choice of metal for cladding has a major influence on temperature performance. A higher operating temperature was obtained using Cu, instead of Au, as the cladding material [91]. In a separate study, the effect of different cladding materials on temperature performance was investigated [92]. Maximum operating temperatures of 142 K [74], 155 K [93], 164 K [77], 172 K [75], 178 K [91], 186 K [94] and ~ 200 K [95] were sequentially reported from LO phonon devices with double-metal waveguides. In fact, the device reported in ref. [95] operating at ~ 200 K is the highest operating THz QCL to date.

It is worth noting, that due to the sub-wavelength confinement of radiation in double metal QCLs and the resulting impedance mismatch to free-space radiation, the far field emission from double-metal waveguides is highly non-uniform [66,96]. Far-field beam profiles from double-metal THz QCLs have been improved by using distributed feedback (DFB) gratings [97–99], integrated horn antennas [100], Si hemispherical lenses [101] and metamaterial based spoof SPs [102]. Double-metal waveguides have also been used to form microwave antenna based on lumped circuit components, as illustrated in Figure 1.15 [103–105].

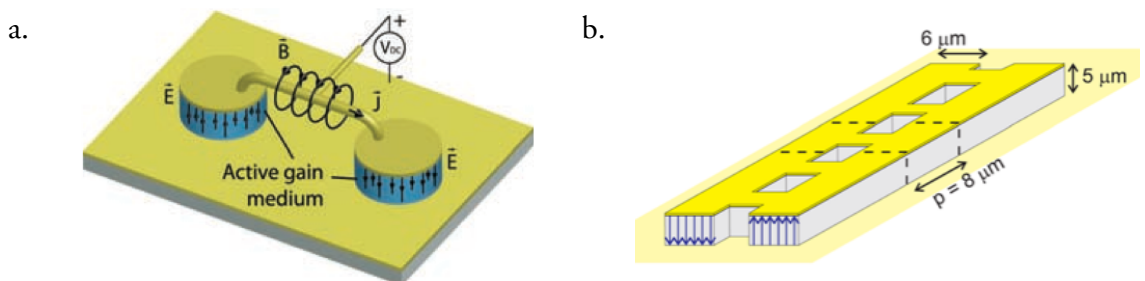


Figure 1.15: (a) Illustration of a microcavity LC resonator. Taken from [103]. (b) Illustration of a metamaterial based transmission line. Taken from ref. [104]. Both designs are based on a THz QCL with double-metal waveguide.

1.4 Single mode emission from THz QCLs

1.4.1 DFB/DBR lasers

THz QCL ridge waveguides are essentially Fabry–Pérot (FP) etalons, whose emission is characterised by multiple longitudinal modes spread across the gain bandwidth. Several applications require QCLs with spectral purity where emission is obtained in only a single mode (SM). SM emission has been observed in QCLs using a variety of waveguide designs including distributed feedback (DFB) gratings and photonic crystals (PhCs).

DFB gratings have a periodic perturbation introduced into the laser cavity that acts as scattering sites. These spatial perturbations can be a change in the refractive index or waveguide losses in the cavity, or a combination of both. An illustration of a THz QCL with DFB grating is shown in Figure 1.16 (a). In such DFB cavities, the feedback required for lasing is obtained from an effective reflectivity provided by the periodic gratings. Additionally, the periodicity of the DFB gratings, or the grating pitch, also plays an important part in the selection of the lasing mode in the cavity. The forward and backward propagating waves experience partial reflection at the periodic gratings. These partial reflections add in phase at a characteristic Bragg wavelength (λ_{BR}) that depends on the grating pitch (Λ) and the effective refractive index (n_{eff}) of the waveguide, and is given as [106]

$$\lambda_{BR} = \frac{2n_{eff}\Lambda}{m} \quad (1.14)$$

where m is the order of the grating.

The DFB gratings also act as a filter and introduce a stopband centred at the Bragg wavelength. As an illustration, the transmission spectrum of a THz QCL with DFB grating is shown in Figure 1.16 (b). A stop band is seen centred at a Bragg frequency of 2.50 THz. Emission from DFB cavities can be observed on either side of this stop band. Lasing is favoured at the edge of the stopband due to the relatively lower lasing threshold gain compared to other longitudinal modes.

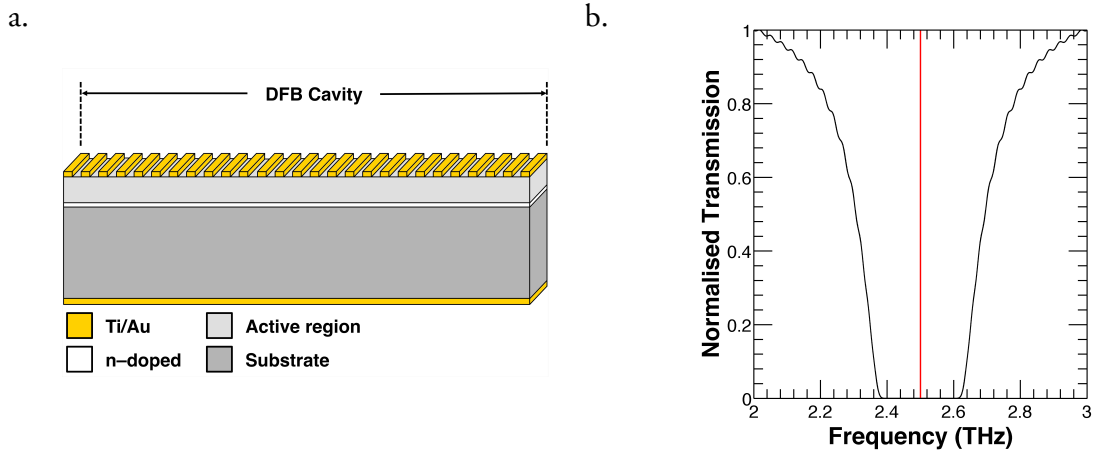


Figure 1.16: (a) Schematic diagram of a THz QCL cavity with DFB gratings. (b) Transmission spectrum (black) from a DFB grating with Bragg frequency at 2.50 THz (red). The DFB grating introduces a stop band centred at the Bragg frequency.

An important parameter of a DFB grating is the coupling constant (κ). The coupling constant measures the feedback in the DFB gratings, and is expressed in terms of spatial modulation of refractive index and loss. The coupling constant is expressed as [107,108]:

$$\kappa = \frac{\pi n_i}{\lambda_{BR}} + j \frac{\alpha_i}{2} \quad (1.15)$$

where n_i and α_i are the amplitude of modulation of the refractive index and losses respectively. The coupling strength of a DFB grating, which describes the coupling in the cavity, is calculated by multiplying the coupling constant with the cavity length. An optimum coupling and a uniform spatial distribution of the dominant lasing mode is observed when the coupling strength is between 1–2 [108].

Emission at the Bragg frequency is possible in DFBs that have an engineered defect, such as a $\lambda/4$ -shifted element in the grating [109]. The central $\lambda/4$ -shifted element modifies the phase in the cavity and results in constructive interference at the Bragg frequency. Gratings with a $\lambda/4$ -shifted element are discussed in Chapter 6.

DBR gratings, unlike DFBs, are etched only at the facet end and act as a passive effective reflector, as illustrated in Figure 1.17. DBRs have a separate active cavity that provides gain in the structure. To match the discontinuity between active and passive waveguide sections, additional phase matching sections are used in DBR designs. Such DBR designs are common in optical lasers and are used extensively to design frequency tunable lasers [106]. Frequency tunable lasers with sampled grating DBRs (SG-DBRs) are also used

in optical lasers. The SG–DBRs have a spatial square grating that is convoluted with the standard DBR design. This results in gratings with a periodic discontinuity. These lasers feature two SG–DBRs at either end of the laser ridge. Recently, such SG–DBRs have been demonstrated in mid–IR QCLs as well [110].

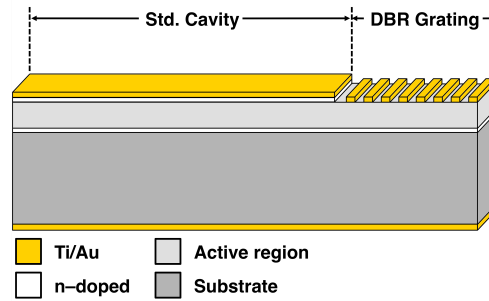


Figure 1.17: Schematic diagram of a THz QCL cavity with a DBR grating.

Fabrication of DFB/DBR gratings in optical or mid–IR lasers is quite challenging and involves etching of active heterostructure and regrowth of dielectric cladding. However, unlike optical or mid–IR lasers which require dielectric waveguides, the optical mode inside the THz QCL cavity is guided by surface plasmons formed at the interface of the waveguide core (active region) and metal cladding layers. DFB structures in THz QCLs are thus fabricated by simply etching away plasmonic cladding material.

The first few demonstrations of DFBs in THz QCLs featured single metal waveguides and were reported in Refs. [111–113]. All of these devices had a first–order DFB grating. Higher order gratings are of particular importance in THz QCLs with double metal waveguides. The sub–wavelength aperture in double metal THz QCLs results in diffraction and degrades far field beam profiles. Higher order DFB gratings facilitate radiation collection from the surface of the grating. The possibility of collection of radiation from the DFB grating surface has been developed extensively. THz QCLs with double metal waveguide featuring second and third order DFB gratings were reported in ref. [97,114,115] and [99] respectively. Double metal THz QCLs with laterally corrugated DFBs have also been demonstrated [116]. DFB structures in these devices were implemented as deep etched grooves on the waveguide ridges.

DFB gratings with a central $\lambda/4$ –shifted element have also been reported for double metal THz QCLs in [98]. The central $\lambda/4$ –shifted element not only resulted in emission at

the Bragg frequency, but also improved the far field beam profile from a dual lobed beam to a single lobed radiation. The SM emission and far field beam profile of double metal THz QCLs have also been investigated with two-dimensional PhCs [117–122]. PhCs form photonic bandgaps, analogous to energy bandgaps in semiconductors. Similar to DFBs, the far field emission from PhCs was improved by including a $\lambda/4$ -shifted element.

DFB grating geometries have been modified in many designs to improve device performance. Improved out coupling have been reported from DFBs with dual slits [123]. The possibility of achieving coarse and fine tuning of frequency by varying grating pitch and the mark-to-space-aspect or the grating duty cycle have been demonstrated in DFBs with a ‘*rib*’ geometry [124].

1.4.2 Photonic crystals

SM emission has also been observed from THz QCLs formed into PhCs [118–120,125]. The optical behaviour in PhCs is analogous to energy bands in semiconductors. In a semiconductor heterostructure, such as GaAs/AlGaAs system, the higher potential of one material (AlGaAs) forms an energy barrier and restricts movement of electrons across the barrier. PhCs, likewise, restrict the movement of photons in a material across ‘*photonic bandgaps*’. PhCs feature a periodic perturbation in the material to form regions of high and low dielectric constant (analogous to potential barriers in semiconductor heterostructures) [117,126–128]. The propagation of photons within such PhC structure is governed by the energy of the photons, and thus, certain frequencies (wavelengths) are allowed whereas others are forbidden.

THz QCLs with PhCs have been designed in a honeycomb lattice to form photonic band gaps [118,125]. The devices feature an array of air gaps, realised by patterning the cladding metal with holes, and subsequent etching of the top doped epilayer [Figure 1.18]. It is important to note that such devices differ from a QCL ridge geometry and radiation is collected from the top of the device, rather than end facets as in a standard QCL.

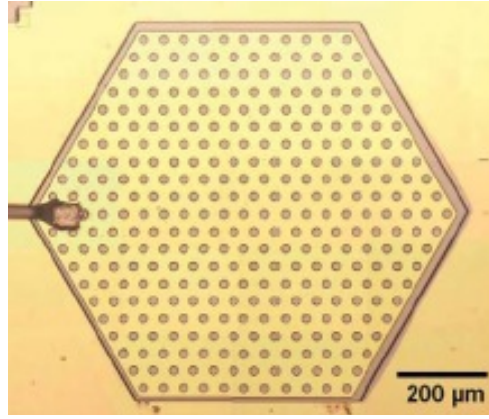


Figure 1.18: Optical image of a PhC from a double metal THz QCL with hexagonal geometry. Arrays of air gaps are evident on the device surface allowing perturbation of the dielectric constant of the top cladding and outcoupling of light. Taken from [118].

Single mode emission from PhCs has also been observed by incorporating side absorbers [119]. The side absorbers are regions at the edge of the PhC where the top doped layer is etched away. A schematic diagram of the side absorbers is shown in Figure 1.19 (a). The side absorber leads to mode mismatch at the edge of the cladding, and introduces high reflectivity, which forces lasing in a particular mode. Optimisation of the beam profile of a PhC has also been reported by incorporating a π -phase shifter in the air gaps structure [120] and improving the Q-factor, as shown in Figure 1.19 (b).

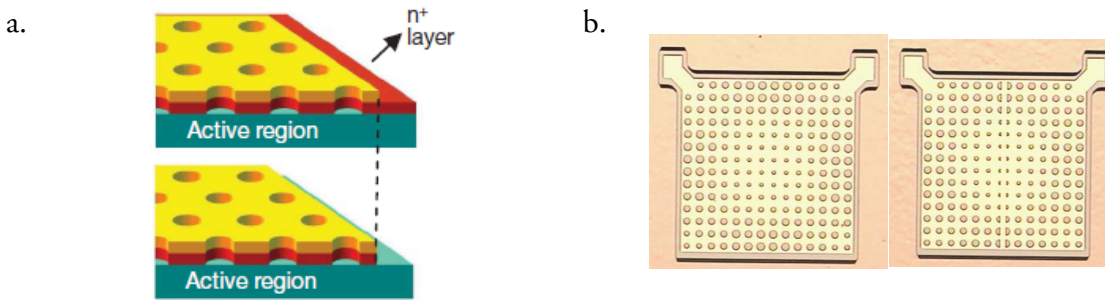


Figure 1.19: (a) Schematic diagram of a THz QCL with PhC (top) without side absorber, and (bottom) with side absorber. The top doped epilayer is removed along the device edge to form the side absorber. Taken from [118]. (b) Optical images of a PhC with optimised Q factor (left) without π -phase shifter, (right) with π -phase shifter. Taken from [120].

1.5 Thesis outline

The aim of the work described in this thesis is to obtain frequency tunable single mode emission from THz QCLs; THz QCLs with single-metal waveguide were used for all fabricated devices as this allows efficient coupling of radiation into imaging systems. Chapter 2 describes the general fabrication and characterisation techniques used.

Chapter 3 describes single mode emission from THz QCLs with one-dimensional photonic lattices (PLs). PLs were patterned using electron beam lithography (EBL) to deposit grating structures in the centres of single-metal QCL ridges. The effect of the PL stopband on the emission spectra was investigated from multiple devices fabricated with different grating pitches.

Chapter 4 investigates the possibility of obtaining a frequency tunable THz QCL from a three-segment THz QCL. The central section of the QCL ridge featured a finite PL, which was deposited after etching away the doped contact epilayer underneath the PL. The two outer segments at either side of the central PL featured a standard single-metal waveguide. Carrier depletion under the PL grating was investigated by applying a separate bias in the PL section.

Chapter 5 investigates discrete vernier tuning using a coupled-cavity geometry. Two FP cavities were coupled through an air gap separation. Frequency tuning was investigated by varying the refractive index of a '*tuning*' cavity through current induced Joule heating. A modified coupled-cavity design optimised for continuous tuning is described in Chapter 6. Continuous tuning from coupled cavities with an integrated PL is also investigated.

Chapter 7 summarises the results obtained from the previous chapters and discusses optimisation of the cavity design in a section outlining future work.

Chapter 2

Fabrication and characterisation of single–metal THz QCLs

2.1 Introduction

A number of high quality terahertz (THz) quantum cascade lasers (QCLs) with a single metal waveguide were fabricated for this project. This chapter describes a general fabrication and characterisation technique used for all THz QCL samples used for the project. Any specific variation in either the fabrication or the characterisation procedure used for a particular study would be mentioned in the respective chapters. The following section describes the detailed fabrication methodology.

2.2 Fabrication of THz QCL with single–metal waveguide

The processing methodology adopted for the fabrication of THz QCLs involved multiple iterations of optical photolithography. Electron beam lithography (EBL) was also used extensively to pattern periodic grating structures. Several devices were etched after device packaging using a focussed ion beam (FIB) milling system.

The THz QCL samples used in this project were grown using molecular beam epitaxy (MBE). All wafers were grown on a semi-insulating (SI) GaAs substrate. A typical wafer growth started with a 250-nm thick GaAs buffer layer and a 300 nm thick $\text{Al}_{50}\text{Ga}_{50}\text{As}$ etch stop layer. A 600–700-nm thick n -doped GaAs layer doped with a Si density between $1\text{--}2\times 10^{18}\text{ cm}^{-3}$ was grown next. Following the growth of this '*buried contact*' layer, the active-region heterostructures were grown next. The exact layers grown for the active region depends on the design. However, a typical THz QCL wafer would include 90–120 repetition of the active module. Growth was concluded with a 60–80-nm thick GaAs layer n -doped with Si at $5\times 10^{18}\text{ cm}^{-3}$. The MBE grown layer structure of a typical wafer with a bound-to-continuum design is tabulated in Table 2.1 as a reference. Samples with typical dimensions of $6\text{ mm} \times 8\text{ mm}$ were then cleaved from the wafer and were processed to fabricate a laser chip.

The typical fabrication steps of a THz QCL chip involved extensive micro and nano-fabrication techniques (as described, for e.g. in ref. [129,130]). The following are the major processing stages:

1. Sample cleaning and edge bead removal.
2. Mesa etching using wet chemicals to form laser ridge.
3. Deposition of ohmic side contacts.
4. Annealing of ohmic side contacts.
5. Deposition of ohmic top contacts.
6. Deposition of cladding metal.
7. Substrate etching and metallisation.
8. Sintering of top ohmic contact.
9. Cleaving, soldering and packaging of laser ridges.

All chrome masks used for the fabrication had three 6-mm long laser ridges in a chip. Each of the processing stages is described in the following sections.

Table 2.1: MBE layer growth structure of L1007.

Layer	Material		Thickness (nm)	Doping (cm ⁻³)	Comments
	III-V Material	Composition			
1	GaAs	-	250	-	Buffer layer
2	AlGaAs	Al ₅₀ Ga ₅₀ As	300	-	Etch stop layer
3	GaAs	-	600	1 x 10 ¹⁸	Buried contact
4	As	-	-	1.3 x 10 ¹⁶	Interrupt
Start of 110 period repeat					
5	AlGaAs	Al ₁₀ Ga ₉₀ As	5	-	
6	GaAs	-	12.6	-	
7	AlGaAs	Al ₁₀ Ga ₉₀ As	4.4	-	
8	GaAs	-	12.0	-	
9	AlGaAs	Al ₁₀ Ga ₉₀ As	3.2	-	
10	GaAs	-	12.4	1.3 x 10 ¹⁶	
11	AlGaAs	Al ₁₀ Ga ₉₀ As	3.0	-	
12	GaAs	-	13.2	1.3 x 10 ¹⁶	
13	AlGaAs	Al ₁₀ Ga ₉₀ As	2.4	-	
14	GaAs	-	14.4	-	
15	AlGaAs	Al ₁₀ Ga ₉₀ As	2.4	-	
16	GaAs	-	14.4	-	
17	AlGaAs	Al ₁₀ Ga ₉₀ As	1.0	-	
18	GaAs	-	11.8	-	
19	AlGaAs	Al ₁₀ Ga ₉₀ As	1.0	-	
20	GaAs	-	14.4	-	
End of 110 period repeat					
21	AlGaAs	Al ₁₀ Ga ₉₀ As	5.0	-	
22	GaAs	-	12.6	-	
23	AlGaAs	Al ₁₀ Ga ₉₀ As	4.4	-	
24	GaAs	-	12.0	-	
25	AlGaAs	Al ₁₀ Ga ₉₀ As	3.2	-	
26	GaAs	-	12.4	1.3 x 10 ¹⁶	
27	AlGaAs	Al ₁₀ Ga ₉₀ As	3.0	-	
28	GaAs	-	20.0	1.3 x 10 ¹⁶	
29	GaAs	-	70	5 x 10 ¹⁸	Top contact

2.2.1 Sample cleaning and edge bead removal

The first processing step involved cleaning of MBE grown samples. This was done to eliminate contaminants and organic residues. Samples were cleaned with acetone in an ultrasonic bath at 10 % power for one minute, and were rinsed with isopropyl alcohol (IPA). This sequence was repeated at least twice. Following the wet cleaning, samples were cleaned in

an Emitech K1050X Plasma Asher at 85 W for five minutes to remove stray organic residues. A similar cleaning procedure was followed before any optical or electron beam lithography steps.

After cleaning, the samples were spin coated with Shipley® Microposit® S1813 positive photoresist. A SUSS MicroTec resist spin-coater was used coat the samples at 5000 rpm for 30 seconds. A typical resist thickness of $\sim 1.2\ \mu\text{m}$ was obtained from the spin coating [131]. The resist coated samples were pre-baked in a digital hotplate at a temperature of 115°C for one minute to remove excess solvents from the resist. The sharp edges of the samples results in a thick build up of resist at the corner and along the edge of the sample. This resist build up was removed in the first stage of optical photolithography using an edge removal mask set. A Karl SUSS MJB3 optical mask aligner was used to expose samples with 310 nm UV radiation. Although a typical exposure dose of $10\ \text{mW}/\text{cm}^2$ for three seconds was used for the exposure of the $1.2\text{-}\mu\text{m}$ thick resist, the thick resist at the edge and corner of the samples required an increased exposure of approximate ten seconds. Following the UV exposure, the resist was developed in a Shipley® Microposit® MF-319 developer for two minutes. The developed samples were rinsed with de-ionised (DI) water and dried with nitrogen jet. The removal of the thick resist along the perimeter allowed better contact between the chrome mask and the sample, and results in better pattern exposure in subsequent lithography steps.

2.2.2 Mesa etching using wet chemicals to form laser ridge

Following the edge bead removal, the samples were processed to define laser ridges. This processing step aimed to etch ridges on the sample surface exposing the buried contact layer (layer 3 in Table 2.1). Thus, the depth of etching would depend on the active-region design. The depth of etching was critical to form an efficient electrical contact to the device. An over etching may risk a complete etching of the buried contact, which is essential to form a good electrical contact to the device. The etch depth of a typical THz QCL active-region was between $\sim 10\text{--}14\ \mu\text{m}$. The etch depth of the QCL active region for the MBE layer growth structure as tabulated in Table 2.1 was $\sim 14.1\ \mu\text{m}$.

A wet chemical etching using an aqueous solution of H_2SO_4 and H_2O_2 was used to define laser ridges, which results in anisotropic etch profile in GaAs [132–134]. The H_2O_2

in the etchant solution oxidises Ga and As. The oxides are subsequently attacked by H_2SO_4 and are removed from the surface [135]. The rate of this chemical etching is dependent on the crystallographic orientation and results in its characteristic anisotropic etch profile. This crystallographic preference of the wet-chemical etching process was exploited to form a sloping sidewall along the length of the etched ridge. An illustration of a sample after mesa etching to define laser ridge is shown in Figure 2.1.

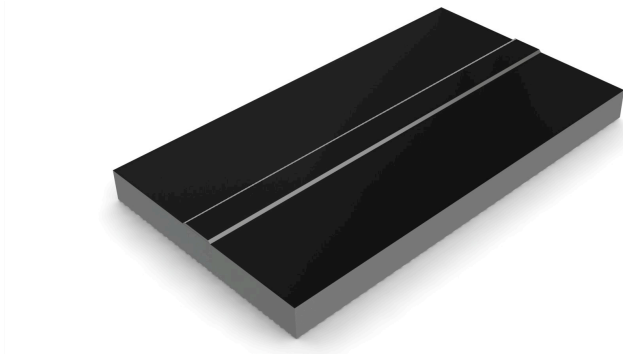


Figure 2.1: Illustration of a sample after laser ridge etching.

The resist-coated samples were exposed with UV for a second stage of photolithography at a dose of 10 mW/cm^2 for three seconds to define three $160\text{-}\mu\text{m}$ wide and 6-mm long rectangular features. After exposure, the samples were developed in MF-319 developer for 70 seconds. Development was seized by a rinse in DI-water. Samples were dried with nitrogen jet and were post-baked at 115°C for a further one minute. The post baking enhanced the adhesion of the resist with the sample surface and made the resist surface robust to withstand the wet chemical etching process that followed. The samples were loaded on a glass slide using S1813 resist with the patterned side facing up. This ensured an easier handling of the samples during the etching process. Optical microscopy of a sample after the photolithography for mesa laser ridge definition is shown in Figure 2.2.

An aqueous solution of wet chemical etchant of H_2SO_4 , H_2O_2 and H_2O , mixed in the ratio 1:8:40 by volume, was used for the mesa etching. The etch rate of the etchant is dependent on the temperature of the solution. The exothermic preparation process required the etchant solution to stand for ~ 15 minutes to attain a stable room temperature. The typical etch rate of the etchant solution varied between $800\text{--}900 \text{ nm/min}$ at room temperature.

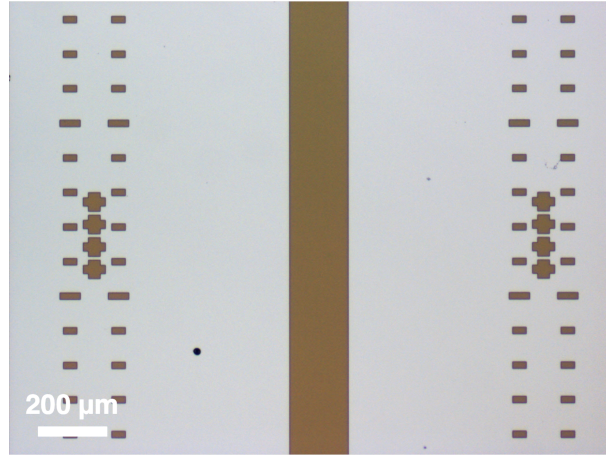


Figure 2.2: Optical microscopy of a sample after development of resist for mesa laser ridge definition. The cross marks along the sides served as alignment marks for subsequent lithography steps. The horizontal marks served as visual aid to measure device length during cleaving. The dark ‘dot’ in the sample is a oval defect, typical in MBE grown samples.

The etching process started with the measurement of resist thickness using a stylus based Alpha step surface profiler. Samples were subsequently etched at intervals of around four minutes. The etch depth was measured after each iteration to measure the depth of etching as well as to evaluate the etching rate. After the etching, the resist was removed with acetone. Samples were cleaned following an identical procedure as described in section 2.2.1. The etch depth of the samples were measured with the surface profiler after cleaning. Optical microscopy of a sample after etching is shown in Figure 2.3.

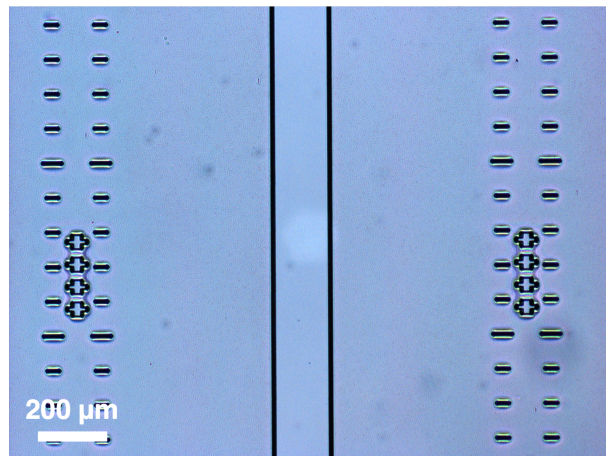


Figure 2.3: Optical microscopy of a sample after etching. Sloped sidewall along the length of the ridge is evident from the thick dark features.

2.2.3 Deposition of ohmic side contacts

Following the mesa etching, an ohmic contact metal was deposited on either side of the laser ridge. A eutectic alloy of Au/Ge/Ni was used to form a low resistance ohmic contact to the buried contact layer (layer 3 in Table 2.1). The eutectic alloy of Au/Ge/Ni is an established contact material for GaAs/AlGaAs heterostructures and *n*-GaAs [136,137]. An illustration of a sample after deposition of the ohmic side contact is shown in Figure 2.4.

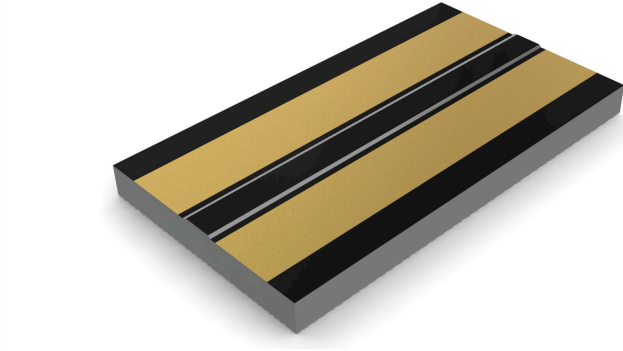


Figure 2.4: Illustration of a sample after deposition of ohmic side contact.

The side contact deposition process began by cleaning the samples after the mesa ridge etch. After cleaning, the samples were spin coated with the same S1813 photoresist at 5000 rpm for 30 seconds and were pre-baked at 90°C. The lower pre-bake temperature ensures optimal lift-off. Samples were aligned to the appropriate mask using the alignment cross-marks [Figure 2.2] in the mask aligner and were exposed to UV under the chrome mask for the third stage of photolithography with a typical dose of 10 mW/cm² for three seconds. After the UV exposure, the samples were soaked in chlorobenzene for two minutes. The chlorobenzene was dried with nitrogen jet and the samples were developed in MF-319 for 70 seconds. After development of the resist, the samples were rinsed with DI-water and dried with nitrogen jet. The chlorobenzene treatment renders the immersed surface more robust to development. Thus, the development rate at the resist surface is lower than that in the bulk of the resist. This difference in development rate results in an overhang of the developed feature, which helps in lift-off procedure [138]. An Optical microscopy of a sample after photolithography for side contact deposition is shown in Figure 2.5.

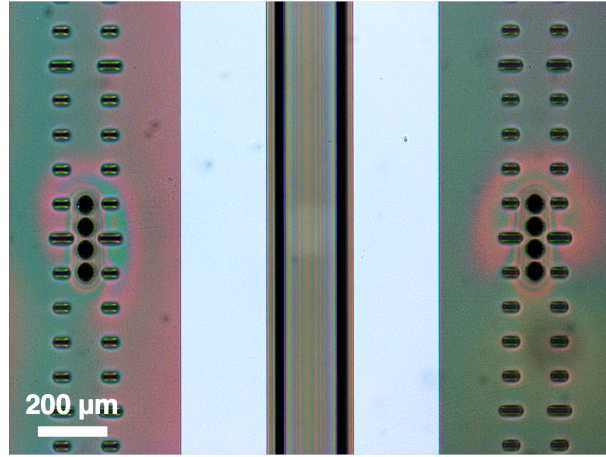


Figure 2.5: Optical microscopy of a sample after development of photoresist for side contact deposition.

After the development, the samples were cleaned with oxygen plasma at 25 W for 70 seconds to remove stray organic residues from the developed surface. Samples were loaded into a Leybold UNIVEX 300 thermal evaporator. Ingots of Au/Ge/Ni (premixed at 88% Au, 12% Ge, 5% Ni by weight) weighing approximately 0.60 gm were used for deposition onto the sample surface. The alloy was evaporated at a rate of 1–2 Å/sec and a chamber pressure below 2×10^{-6} mBar. Thin films of Au/Ge/Ni, approximately 250–300-nm thick, were obtained from the 0.60 gm ingots. Following the evaporation, samples were immersed in acetone for around ten minutes to lift-off metal from the residual surface and were cleaned following an identical procedure as described in section 2.2.1. An Optical microscopy of a sample after lift-off and cleaning is shown in Figure 2.6.

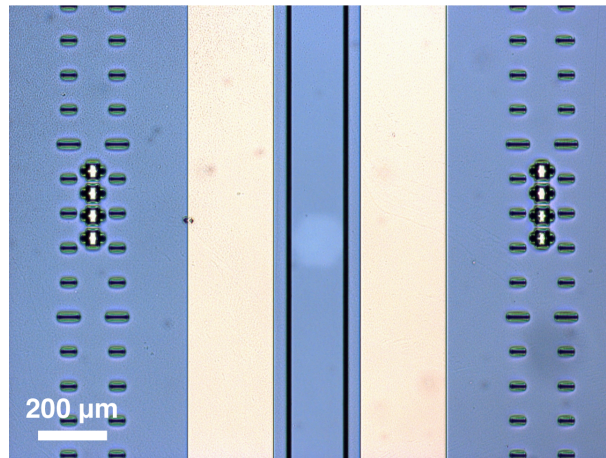


Figure 2.6: Optical microscopy of a sample after lift-off of side contact deposition.

2.2.4 Annealing of ohmic side contacts.

After cleaning, the ohmic side contacts were annealed at 430°C for one minute using a An-nalSys rapid thermal annealer.

On annealing at temperatures about 400-430°C, Ge atoms diffuse into the GaAs and substitute Ga atoms in the GaAs crystal, resulting in a high n^+ -doped region in the semiconductor [139]. The Ni atoms also diffuse into the GaAs crystal and enhance the diffusion of Ge atoms into the crystal [137]. The Ni atoms also reduce the surface tension of AuGe layer [140]. and serve as a barrier to the inter- diffusion between the AuGe layer and the Au top contact [137]. Au/Ge/Ni contacts to n -GaAs exhibits low contact resistivity of the order of $\sim 10^{-6} \Omega/\text{cm}^2$ [136,141].

After annealing, the morphology of the deposited Au/Ge/Ni contact metal changes due to the diffusion of Ge and Ni into the substrate and is evident on the physical appearance of the ohmic contact pads. An Optical microscopy of a sample after annealing of the ohmic side contacts is shown in Figure 2.7. It can be observed that the shiny reflecting surface of deposited ohmic metal is transformed after annealing. A common practice followed after annealing was to measure the contact resistance between the annealed contact pads using a probe station and a digital multi-meter. Typical resistances between 5–10 Ω were measured between the contacts. A high contact resistance is detrimental to device performance and may result in large heat dissipation at the contact regions.

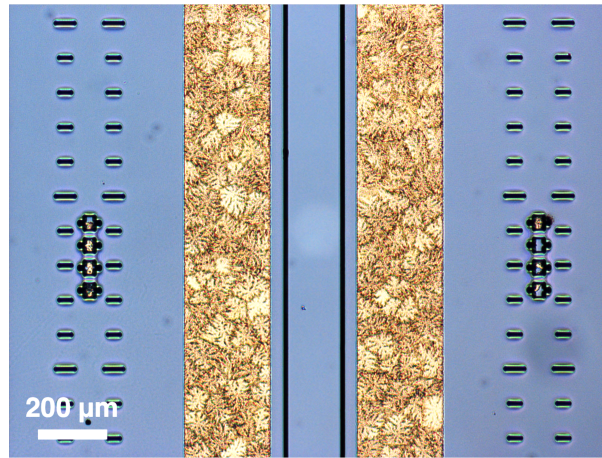


Figure 2.7: Optical microscopy of a sample after annealing of ohmic side contacts.

2.2.5 Deposition of ohmic top contacts

A similar ohmic contact metal was deposited on top of the QCL ridges to form a low resistance top contact. However, the ohmic metal was not deposited throughout the entire surface of the ridge, instead two 10- μm wide ohmic strips were deposited. This was done to reduce free carrier loss in the waveguide [62]. An illustration of a sample after deposition of ohmic contact at the top of the ridge is shown in Figure 2.8.

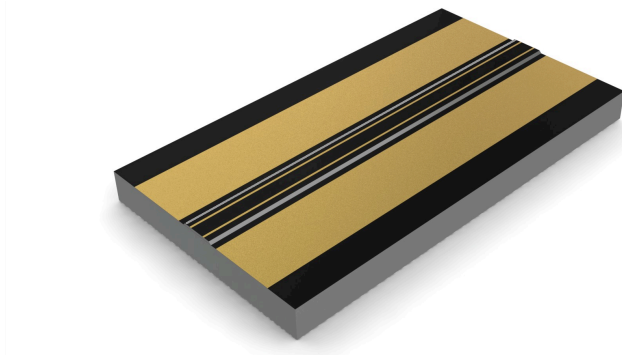


Figure 2.8: Illustration of a sample after deposition of ohmic side contact.

The fabrication procedure followed identical processing steps as described in section 2.2.3. The samples were spin coated with S1813 and were exposed under UV for the fourth stage of photolithography with an appropriate mask for the top ohmic contact. Samples were then soaked in chlorobenzene and were developed with MF-319. Optical microscopy of a sample after development is shown in Figure 2.9 (a). After development samples were cleaned with oxygen plasma asher at 25 W for 70 seconds. Au/Ge/Ni alloy was deposited using the same Leybold UNIVEX 300 thermal evaporator. Generally, 0.3 gm ingots of the alloy were used to obtain $\sim 100\text{--}130\text{-nm}$ thick metal films. After thermal evaporation, the samples were treated with acetone to lift-off metal and were cleaned with acetone/IPA and oxygen plasma at 85 W for five minutes. Optical microscopy of a sample after lift-off is shown in Figure 2.9 (b). The samples were not annealed after metal lift-off to prevent damage to the active material of the QCL due to diffusion of alloy material.

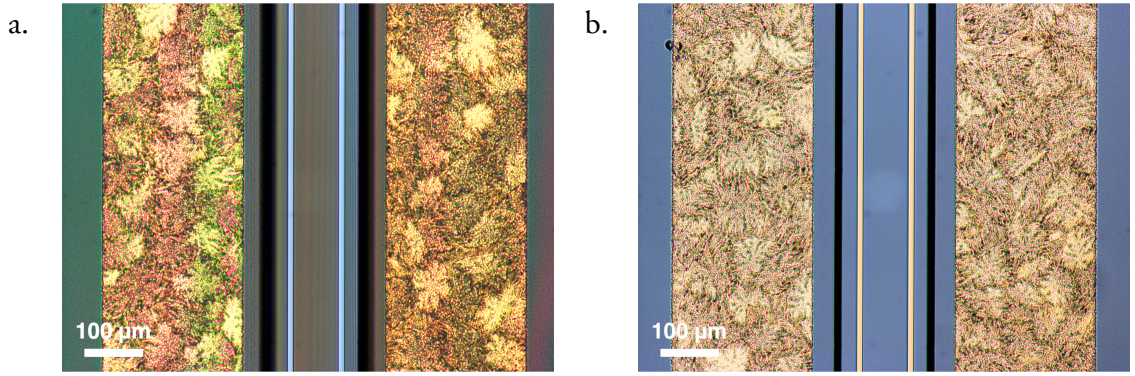


Figure 2.9: Optical microscopy of a sample during top ohmic contact deposition: (a) after development of photoresist, and (b) after metal lift-off.

2.2.6 Deposition of cladding metal

Since the top ohmic contact did not cover the entire surface of the laser ridge, a separate cladding metal of Ti/Au was used to confine radiation inside the laser cavity. A thin layer of Ti was deposited before Au to reduce surface tension and to promote adhesion of Au with the sample surface. The Ti/Au was also deposited at the side ohmic contacts. This enabled better wire bonding to the ohmic contact pads. An illustration of a sample after deposition of Ti/Au cladding metal is shown in Figure 2.10.

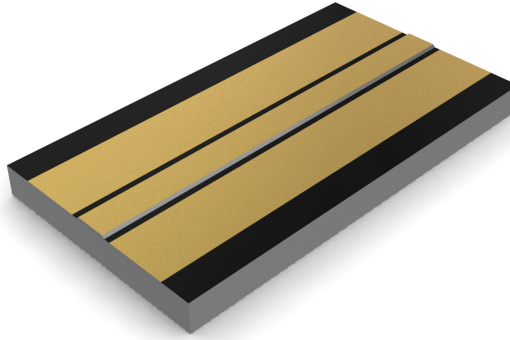


Figure 2.10: Illustration of a sample after deposition of cladding metal.

The cladding deposition process began by cleaning the samples after the top Ohmic contact deposition. After cleaning, the samples were spin coated with S1813 and were exposed under UV for the fifth and final stage of photolithography with a mask for the cladding metal deposition. Samples were then soaked in chlorobenzene and were developed with MF-319. Optical microscopy of sample after development is shown in Figure 2.11 (a). Following development of resist, the samples were cleaned with oxygen plasma asher at

25 W for 70 seconds. A Leybold UNIVEX 350 electron beam evaporator was used to deposit 20 nm of Ti followed by 200 nm of Au. After evaporation, the samples were again treated with acetone to lift-off metal. Samples were subsequently cleaned with acetone/IPA and oxygen plasma at 85 W for five minutes. An Optical microscopy of a sample after lift-off is shown in Figure 2.11 (b).

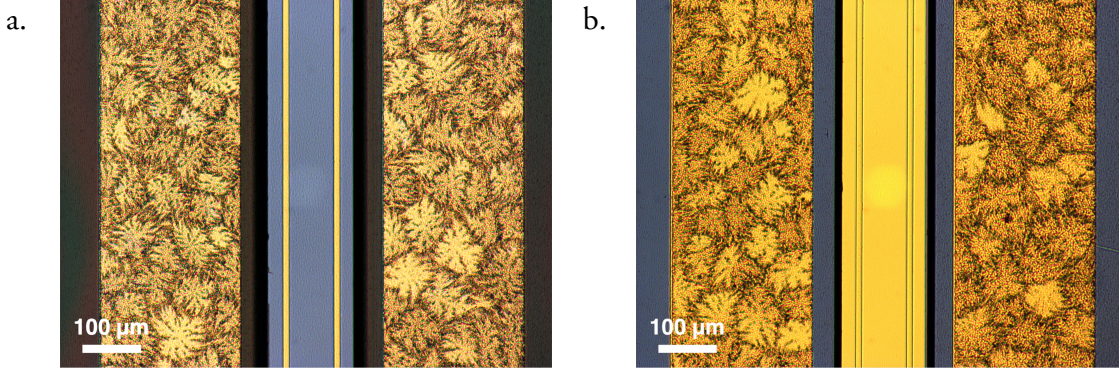


Figure 2.11: Optical microscopy of a sample during cladding metal deposition: (a) after development of photoresist, and (b) after metal lift-off.

2.2.7 Substrate etching and metallisation

To improve thermal dissipation from QCL ridges, the GaAs substrate was thinned to $\sim 200 \mu\text{m}$. Samples were mounted with wax to glass slides for better handling. Wax was melted in a hotplate at 70°C and samples were placed in the molten wax such that the fabricated ridges are buried under the wax. The glass slides were withdrawn from hotplate to cool the wax. Care was taken such that no wax spilled on to the substrate. The height of the wax-mounted sample was measured using a Tesatronic micrometer. The samples were subsequently etched with a wet chemical etchant of H_2SO_4 , H_2O_2 and H_2O mixed in a ratio of 1:8:1 by volume. The etchant was heated to a temperature of 50°C during the etching process to obtain a typical etch rate of $\sim 20 \mu\text{m}/\text{minute}$. After etching, the samples were rinsed with DI-water to stop the etching process. The etch depth was measured after every 5 minutes to evaluate the etch rate and to verify that the processed ridge are not affected by the etchant solution.

After substrate etching, the samples were separated from the glass mount. The wax was melted using a hotplate at 70°C and the samples were cleaned with trichloroethylene. The thinned substrate made handling of samples non-trivial and utmost care was taken during the sample handling. The samples were also cleaned with acetone and IPA in multi-

ple iterations. Both the substrate side and the ridge surface were cleaned with oxygen plasma at 85 W for five minutes. The substrate side of the samples were subsequently deposited with 20 nm of Ti and 150 nm of Au using the same UNIVEX 350 electron beam evaporator. The Au coating at the substrate surface helped in the soldering of samples during packaging.

2.2.8 Sintering of top ohmic contact

After substrate thinning, the top contact was sintered at a temperature of 270°C for four minutes using the same rapid thermal annealer. The separate annealing of the ohmic contacts at the side and at the top of the laser ridge follows an identical processing procedure, as was reported in ref. [61]. A lower sintering temperature was used to prevent the diffusion of alloy metals from the ohmic strips, at the top of the ridge, to the active material. The sintering process also enhanced the adhesion of the metal films to the sample surface. After sintering of top ohmic contact, the samples were ready for cleaving into Fabry–Pérot laser cavities and were package into a Cu mount.

2.2.9 Cleaving, soldering and packaging of laser ridges

All fabricated samples contained three laser ridges, as shown in Figure 2.12 (a). To obtain an operational laser device from the chip, the chip was diced to obtain individual laser ridges. This was done using a JFP S-100 automated scriber with a diamond cutter. The fabricated chips were scribed along the dotted lines as illustrated in Figure 2.12 (a).

The diced laser ridges were subsequently cleaved to obtain mirror-like facets to form Fabry-Perot cavities. The diced laser ridges were cleaved along the dotted lines shown in Figure 2.12 (b). The facets were carefully cleaved to obtain mirror like surface that would provide feedback for lasing with a minimum mirror loss. Any surface damage would increase mirror losses in the device and may increase the lasing threshold.

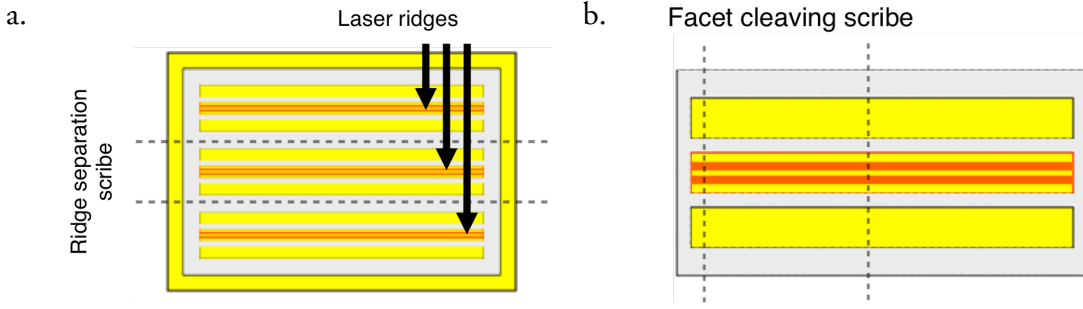


Figure 2.12: (a) Schematic of a fabricated THz QCL chip with three 6 mm long laser ridges. Samples were diced along the dotted lines to obtain three individual laser ridges, which were subsequently cleaved to obtain Fabry-Pérot cavities. (b) Schematic of cleaving of a diced laser ridge. The diced laser chips were cleaved along the dotted lines. During manual cleaving, a small crack was introduced at the edge of the diced laser, whereas during automated scribing process, a 500 μm long line was scribed from the edge into the sample.

The ridge separation and facet cleaving was performed using either a scalpel knife or a JFP S-100 automated scriber with a diamond point. Devices described in chapters 3 and 4 were cleaved manually with a surgical scalpel knife. The facet cleaving process involved introduction of a small controlled ‘*crack*’ at the edge of the diced laser ridge. Mirror facets were realised by breaking the laser ridge along the crystal plane of the GaAs/AlGaAs material. The measurement marks shown in Figure 2.2 were used as a guide to cleave devices of an approximate length. The cleaved facets were checked under a microscope to verify defects. However, a major disadvantage of this process is an uncontrolled shattering of laser ridge, which significantly decreased the fabrication yield. Another limitation of the manual scribing was the difficulty in cleaving lasers of precise length.

To improve the process yield the devices described in chapters 5 and 6 were cleaved using the automated scriber. The automated scriber operated on a similar principle as the manual scribing, however, it used a diamond tip to scribe 500 μm long scribe marks at the edge of the diced ridge. Facets were cleaved by applying a gentle force along the scribed marks. The automated scribing technique improved the processing yield and also cleaved laser ridges of precise lengths. Images of cleaved facets obtained from scanning electron microscopy (SEM) are shown in Figure 2.13.

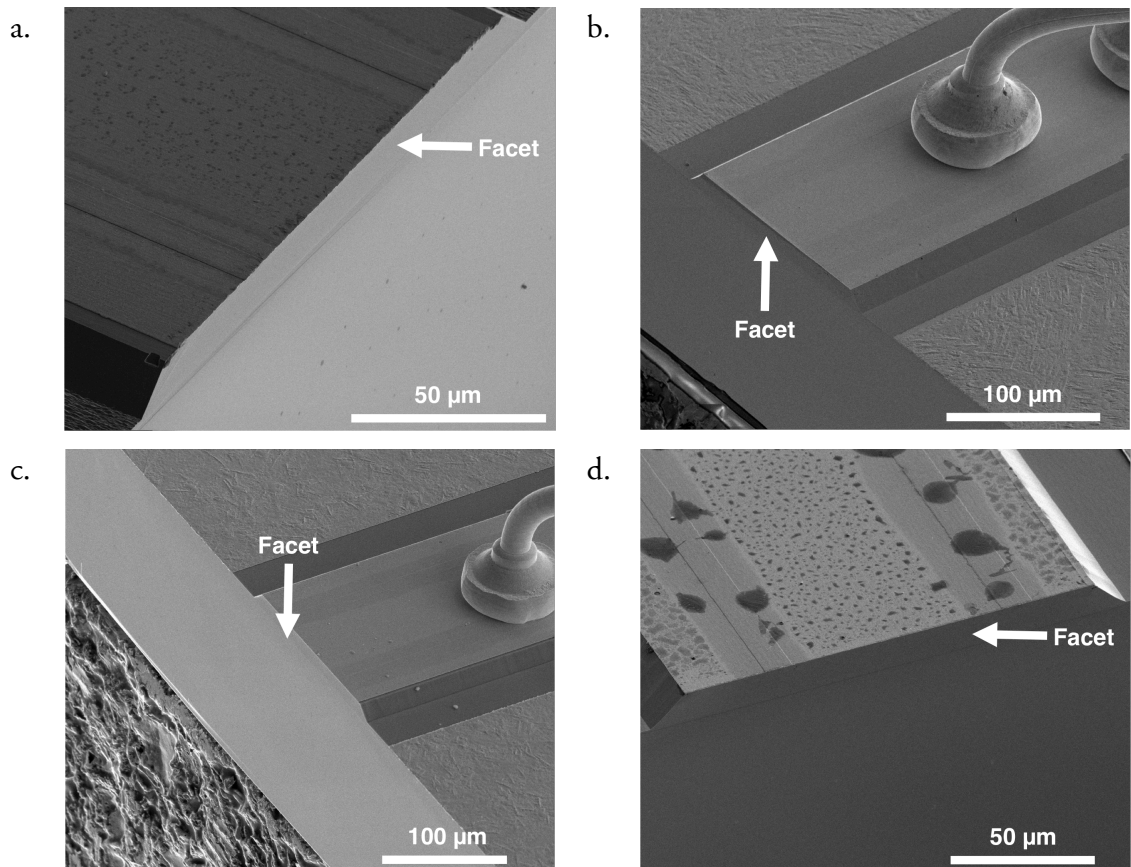


Figure 2.13: (a–d) SEM of cleaved facets using automated scriber.

The cleaved devices were mounted on a Cu block using In/Au soldering and were wire bonded. A typical Cu block houses two cleaved devices. A schematic diagram of the wire bonding is shown in Figure 2.14. The bottom ohmic contact of both of the devices was connected to the same small ceramic pad in the top-middle, whereas the top ohmic contacts were connected separately to two larger ceramic pads.

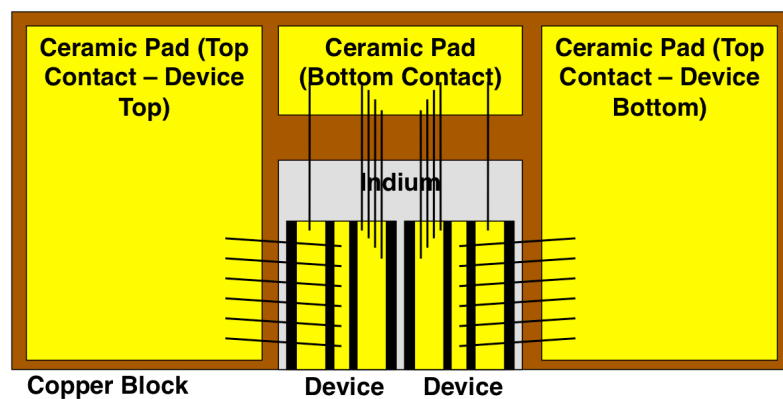


Figure 2.14: Schematic diagram of packaging of two THz QCL devices (labelled as device 'Top' and device 'Bottom') on a Cu block.

The Cu mounts used for the packaging were typically 19-mm long, 7-mm wide and 2-mm thick and were polished at one of the two faces. The Cu mounts were cleaned in an ultrasonic bath of acetone at 100% power for ten minutes. This was followed by another iteration of ultrasonic cleaning with IPA at 100% power for another ten minutes. After drying the Cu blocks with nitrogen jet, they were heated to a temperature of 170°C. The polished face of the Cu blocks was subsequently deposited with 20 nm of Ti and 150 nm of Au using the same Leybold UNIVEX 350 evaporator as described in section 2.2.6. The Au coating was used to solder the cleaved QCL device to the Cu mount.

Ceramic pads with a Au layer at top were used for bond wiring. The ceramic pads were glued to the Cu block using Oxford Instruments GE varnish C5-101. The cleaved devices were soldered onto the Cu mount with an In melt. The In film was placed on the Au coated Cu block and was melted using a hotplate at a temperature of 145°C. The molten In was spread even across the Au coated polished face of the Cu block and was cooled to a temperature of 130°C (below the melting temperature of In). Cleaved QCL devices were positioned at the Cu block, as illustrated in Figure 2.14, and were held firmly using two point probe needles. With this arrangement, the temperature of the hotplate was increased to 170°C when In would melt again and form a strong bond with the Au at the substrate side of the QCL devices (see section 2.2.7). With the probe needles still holding the QCL devices in place, the temperature of the hotplate was decreased to 100°C rapidly using heat sinks. Au wire connections to the device were subsequently established at a heated stage (80–100°C) using a Kulicke & Soffa 4524 Ball Bonder. An Optical microscopy of a bonded device is shown in Figure 2.15. After packaging, the devices were ready for characterisation.

Although THz QCLs with a ‘*standard*’ single-metal waveguide were fabricated following processing steps described above, devices with specialised waveguide structure required additional processing steps like electron beam lithography (EBL) (discussed in chapters 3 and 4) or focussed ion beam (FIB) milling (discussed in chapters 5 and 6). The following section describes the processing steps used for EBL and FIB milling.

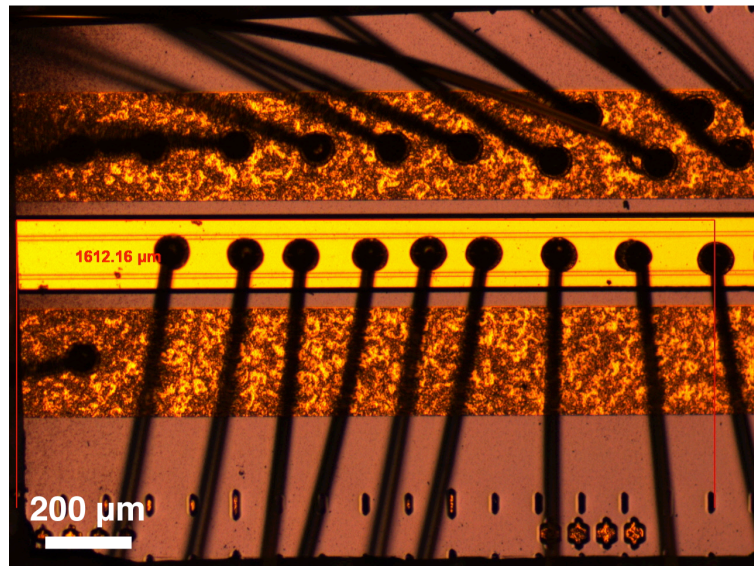


Figure 2.15: Optical microscopy of a QCL device after packaging and wire bonding.

2.2.10 Electron beam lithography

Optical photolithography was used for all stages of resist patterning discussed so far. This technique requires a chrome hard mask and is better suited for processing where pattern features do not need change. While this was perfectly suited for all lithographic stages discussed so far, it is not ideal for patterning grating features where feature dimensions vary with design. A significant proportion of devices fabricated for this project involved frequency selective grating structure, which were patterned with EBL. EBL provides flexibility in changing design parameters, and suited the rapid prototyping methodology adopted. EBL is used extensively in chapters 3 and 4.

A Raith 50 EBL workstation was used for all EBL patterning. A GDSII mask editor software accompanying the EBL system was used for the mask designs. In the initial trials a mono-layer resist process was used. Samples were spin coated with PMMA 950 A4 electron beam resist at 4000 rpm for 30 seconds and were baked in a convection oven at 170°C for an hour before the pattern exposure. An electron source at 30 kV was used for the exposure with a beam spot size of 250 and a dose of 200 $\mu\text{As}/\text{cm}^2$. Samples were developed in a solution of MIBK and IPA premixed at a volume ratio of 1:3 for one minute. An Optical microscopy of a sample with patterned grating features is shown in Figure 2.16 (a). Following the development the samples were cleaned in oxygen plasma at 25 W for 70 seconds to

remove any organic residue. Samples were subsequently deposited with 20 nm of Ti and 70 nm of Au. The samples were soaked in acetone overnight for metal lift-off and were cleaned with acetone and IPA. An Optical microscopy of a sample after lift-off is shown in Figure 2.16 (b). It was observed that the mono-layer resist processing did not yield good lift-off. Instead, a bi-layer PMMA processing was used, and would be discussed in Chapter 3.

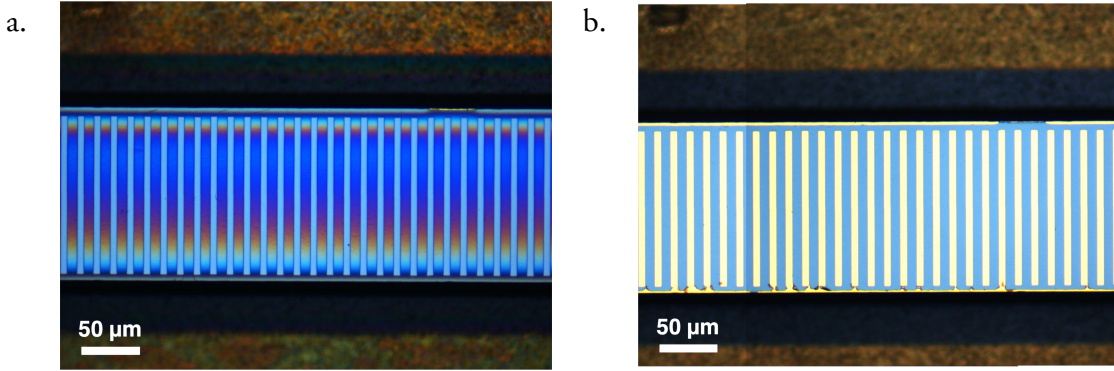


Figure 2.16: Optical microscopy of a sample patterned with EBL: (a) after resist development, (b) after lift-off. Unwanted metal was found shorting grating features due to poor lift-off.

2.2.11 Focussed ion beam milling

A majority of the fabrication steps discussed so far were followed sequentially with the final steps being device cleaving and packaging. However, certain devices required a post-packaging segmentation process. These devices, discussed in greater detail in chapters 5 and 6, required an initial device characterisation and were subsequently processed further to split them into multiple cavities. This post-packaging segmentation process was done with FIB milling.

FIB milling is a subtractive process that uses high-energy heavy ions (like gallium ions) to bombard sample surface and is used to pattern features. A typical FIB milling system consists of a SEM unit with an electron-beam column and an additional ion-beam column. The ion-beam is used as an imaging unit as well as a milling tool. Certain FIB stations also have facility to deposit materials like platinum. A FEI Nova 200 NanoLab FIB workstation with a high-resolution field emission gun scanning electron microscope and a precision focussed ion beam source was used for all post-packaging processing. A beam current of 7 nA accelerated with a 30 kV acceleration voltage was used for all patterning

used in this project. SEM of an alignment mark patterned with FIB milling is shown in Figure 2.17.

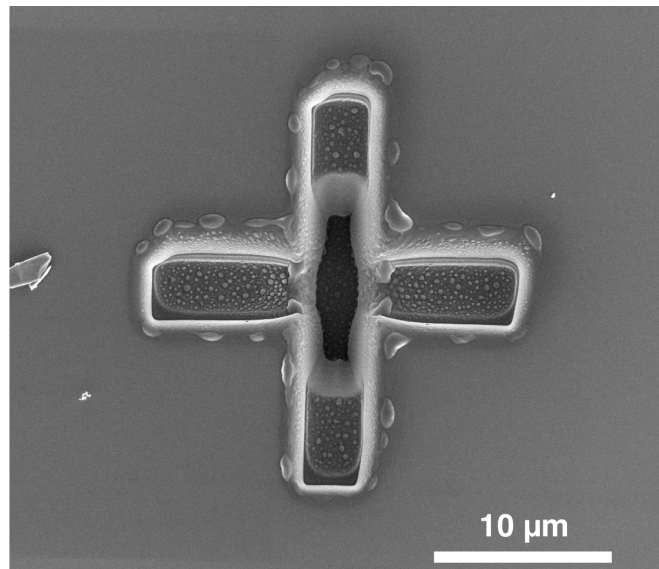


Figure 2.17: Scanning electron microscopy of an alignment mark patterned using FIB milling.

2.3 Characterisation of THz QCLs

After fabrication, the THz QCLs were characterised to study the light–current–voltage (LIV) as well as spectral characteristics. The LIV characteristics involve studying the emission power and voltage across the device as a function of drive current. Important device parameters like threshold current density, slope efficiency and peak power can be studied from LIV characteristics. Differential resistivity, which indicates band alignment process, can also be calculated from IV characteristics. LIV were also characterised at different heat sink temperatures to analyse the maximum thermal operation of devices. The spectra were also recorded at different drive currents and heat sink temperature to analyse emission behaviour.

2.3.1 Experimental setup

The optical setup required for the LIV and spectral characterisation differed slightly and is discussed next. However, the electrical connection to the device remained unchanged during both the characterisation technique and would be discussed in section 2.3.1.2.

2.3.1.1 Optical setup

Packaged devices were mounted on a cold finger of a Janis ST-100 continuous flow cryostat. Emission was collected from a polyethylene window in the cryostat. After loading samples, the cryostat was pumped with a turbo vacuum pump to reach 8×10^{-6} mBar and was then cooled with a continuous flow of He. The cryostat was attached to a Newport precision linear translation stage with x-y-z micrometer controller. The position controller allowed precise optical alignment of QCL with the detector. The cryostat heat sink temperature was controlled through a Lakeshore 331 temperature controller.

Emission was collected from cryostat using two off-axis parabolic mirrors (f/0.8 and f/1.0). The cryostat and the mirrors were housed in a nitrogen –purged chamber to minimise absorption of THz radiation by water vapour. The collimated radiation from the parabolic mirrors was detected using a cryogenically (He) cooled QMC QSIB/3 bolometer with a Ge thermistor. The electrical resistance across the thermistor varies as a function of temperature, which varied according to the intensity of the emitted THz radiation. The detected signal was recovered using an Amtek Signal Recovery 7225 DSP lock-in amplifier. The responsivity of the bolometric detector was 135 kV/W at a modulation frequency of 165 Hz [142]. Since radiation from the QCL was collimated and detected directly by the bolometer, this setup was used for analyse LIV behaviour and absolute power emission from QCL devices.

The absolute power emitted from the devices were characterised using a pressure transducer based detector system, Thomas Keating Absolute Terahertz Power Meter. The absolute power detection scheme required a different modulation frequency than the bolometric detection. A square wave of 30 Hz was used during the measurement of the absolute power. The 30-Hz modulation matched the optimum responsivity of the detector [143].

During the spectral characterisation, a slightly different optical arrangement was used. Emission from QCL device was collimated using three off-axis parabolic mirrors (f/1.0). Spectra were measured in a rapid scan mode using a Bruker Optics IFS66/V Fourier transform infra-red (FTIR) spectrometer with a resolution of 0.25 cm^{-1} (7.5 GHz). The spectral characterisation setup used the same bolometric detection and hence required a 165 Hz modulation signal.

2.3.1.2 Electrical setup

An ISO-TECH GFG-8216A function generator was used to generate square waves to match the responsivity of the detector and was used to synchronise the electrical circuit driving the QCL as well as the DSP lock-in amplifier. The function generator output was set as either 165 Hz or 30 Hz square waves for bolometric detection or absolute power reading respectively.

An Agilent 8114A 100 V/2 A pulse generator was used to drive the QCL device at a repetition rate of 10 kHz with 2% duty cycle (or a pulse width of 2 μ s). Since THz QCLs are driven in reverse bias, a negative current pulse train was used. The small duty cycle ensured efficient thermal extraction from the devices. The current pulses were gated with the square pulses from the function generator to match the detector responsivity. The pulse generator was operated in two modes – with a 50 Ω load delivering a maximum drive current of 2 A and a high impedance load capable of delivering a maximum drive current of 4 A.

The output from the pulse generator was connected to an AVTECH Electrosystems AVX-MRB5 transformer, which was used during the high current operation to reduce unwanted oscillations in the pulse generator signal. The high current mode was used during the characterisation of devices with frequency selective gratings and devices with long cavities. In both cases, a higher threshold current was required.

The output of the pulse generator (or the transformer, during high current measurements) was connected to the cryostat input through an inductive loop current probe. The current loop was terminated with a matched 50 Ω load and was connected to channel 1 of a four-channel Agilent InfiniVision 3000-X digital storage oscilloscope. Current to the device was measured as a proportional voltage in the current loop (i.e. 1 V = 1 A). The voltage across the QCL was measured through a 50 Ω ‘sense’ circuit and was connected to a different channel (channel 2) in the same oscilloscope. Two channels (channel 3 and 4) were redundant during operation of a standard QCL device, however, they were used extensively during multi-segment device characterisation, and would be discussed in chapters 4, 5 and 6.

The oscilloscope, the lock-in amplifier and the temperature controller were connected to a PC through a data acquisition system using GPIB connections. LIV were recorded using a National Instruments LabView instrument panel. The laser drive current from the pulse generators was varied incrementally at a particular heat sink temperature. The corresponding voltage across the device (from sense circuit) and power from the lock-in amplifier were tabulated and saved in a text file. Spectra were acquired using a dedicated software OPUS. Schematic diagram of the experimental setup used for the LIV and the spectral characterisation are shown in Figure 2.18 and Figure 2.19 respectively.

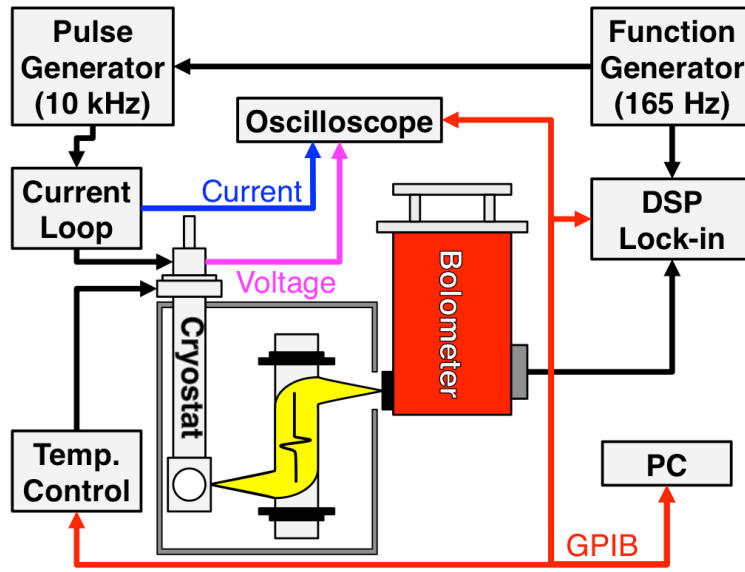


Figure 2.18: Schematic diagram of experimental setup for characterising LIV of a standard QCL device.

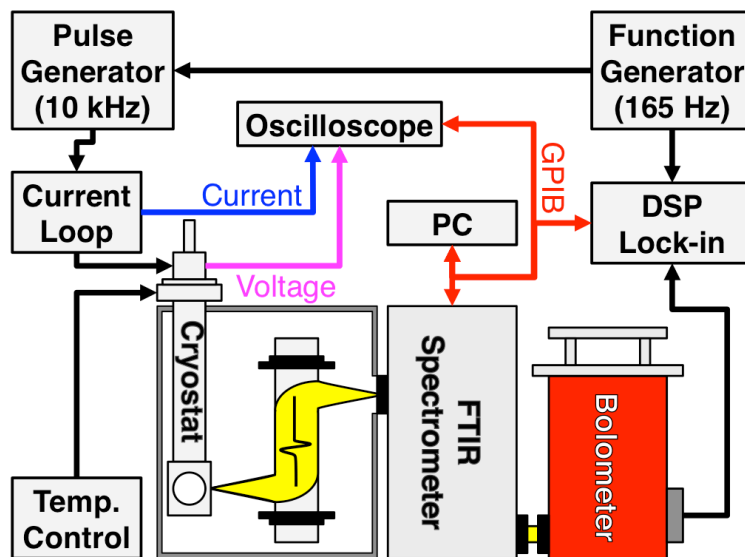


Figure 2.19: Schematic diagram of experimental setup for characterising spectra of a standard QCL device.

The characterisation techniques described were used extensively to characterise different THz QCL devices. Results from one such device are discussed in the following section.

2.4 Experimental results from a reference device from L1007

Experimental results obtained from a reference device from wafer L1007 is presented as an example. This wafer had the same MBE grown layers as mentioned in Table 2.1. As described in the previous chapter, LIV performance were characterised at different heat sink temperatures. LIV obtained from a device, labelled as L1007-S1-D1-T, at different heat sink temperatures is shown in Figure 2.20 (a). At a heat sink temperature of 4 K, lasing was observed at a threshold current density of $\sim 140 \text{ A/cm}^2$. A maximum power emission of $\sim 4.5 \text{ mW}$ was measured with the absolute power meter. With an increase in the heat sink temperature, the dynamic range of the device exhibited a characteristic narrowing. The device parameters, like threshold current density and peak power could be analysed further from the LIV characteristics obtained in Figure 2.20 (a).

The threshold current density was plotted as a function of heat sink temperature. An exponential increase in threshold current was observed [Figure 2.20 (b)], and followed the theoretical predictions. Similarly, peak emission power was plotted as a function of the heat sink temperature. The emitted optical power decreased with a rise in heat sink temperature. The power roll-off as a function of heat sink temperature were fitted with a Boltzmann's fit [Figure 2.20 (c)], as was obtained previously in ref. [144].

Spectra from this reference device were also characterised using the setup shown in Figure 2.19. Multiple mode emission, characteristic of Fabry-Pérot etalons, was observed [Figure 2.21]. Spectra were acquired at different drive currents with a heat sink temperature of 4 K [Figure 2.21 (a)]. Multi-mode emission centred at $\sim 2.23 \text{ THz}$ was obtained as the device was driven above the lasing threshold. With an increase in drive current, emission between $2.15\text{--}2.24 \text{ THz}$ was observed. Spectra were also recorded at different heat sink temperatures with a constant drive current of 1.14 A [Figure 2.21 (b)]. With an increase in heat sink temperature, the multi-mode emission spectrum gradually converged into a predominantly single mode emission at $\sim 2.20 \text{ THz}$.

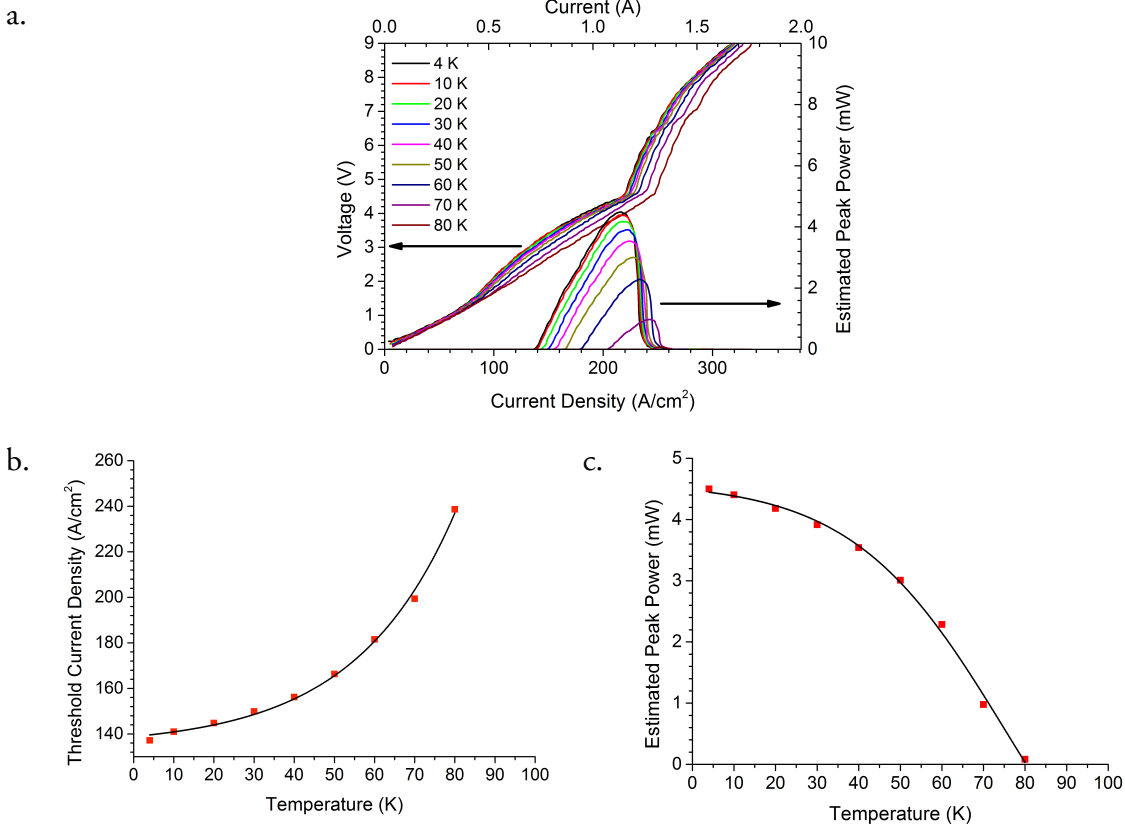


Figure 2.20: (a) LIV recorded from a reference device at different heat sink temperatures. (b) Threshold current density obtained from fig. (a) is plotted as a function of heat sink temperature. (c) Peak emission power plotted as a function of heat sink temperature. All data are obtained from the device L1007-S1-D1.

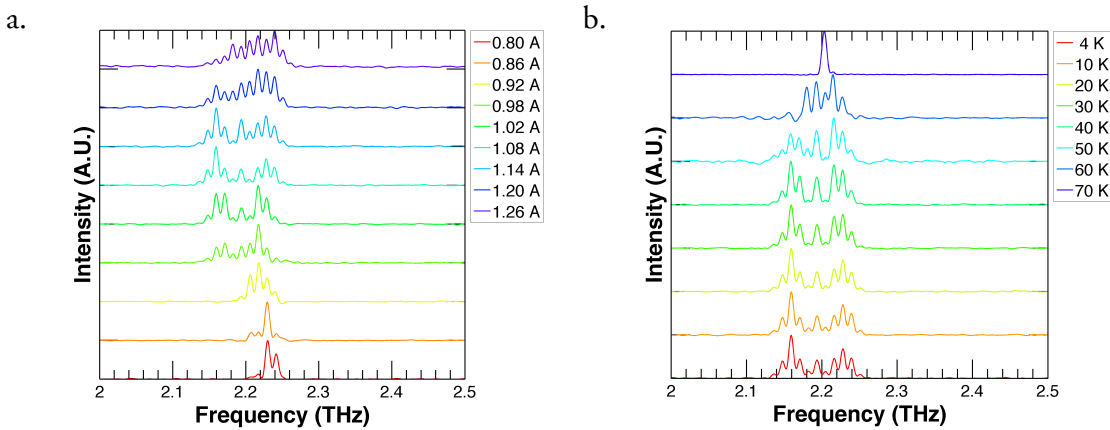


Figure 2.21: (a) Spectra obtained at various drive currents at a heat sink temperature of 4 K. (b) Spectra obtained at a drive current of 1.14 A at various heat sink temperatures. All data are obtained from the device L1007-S1-D1.

Several THz QCLs were fabricated during the course of the project. A multitude of such samples were used to ascertain the quality of growth of THz QCL wafers. Indeed,

some exemplar devices were used in various sensing applications, for e.g. the device reported in ref. [145] was fabricated and characterised during the course of this project, following identical procedures described in this chapter.

The characterisation techniques discussed here are generally followed throughout all devices reported in this thesis. In addition to these typical characterisation techniques, devices were further characterised to specifically study frequency tunability, details of which would be discussed in the relevant chapters.

2.5 Summary

This chapter described the detailed processing steps used to fabricate THz QCLs with single-metal waveguide. The fabrication includes several stages of optical photolithography and thin-film metal deposition. Advanced fabrication steps like EBL and FIB milling were also discussed. These fabrication steps were used extensively to fabricate multiple-section THz QCLs with frequency selective gratings. The detailed processing steps of EBL and FIB milling would be described in greater detail in the following chapters.

A detailed description of the experimental setup to characterise LIV and spectra from a standard THz QCL was also presented. The setup for the standard THz QCL would be modified further to characterise multi-cavity THz QCLs simultaneously, and would be discussed in subsequent chapters.

Experimentally obtained results from a reference device from wafer L1007 was also discussed to highlight the typical characterisation results from a THz QCL. A detailed discussion on specific characterisation techniques relevant to obtain frequency tunable THz QCLs would be discussed in the following chapters.

Chapter 3

THz QCLs with one-dimensional photonic lattice

3.1 Photonic lattice

Single mode (SM) emission from THz QCLs has been demonstrated using photonic lattices (PLs) [146]. A PL consists of periodic engineered defects in the laser cavity. Similar to THz QCLs with distributed feedback (DFB) gratings, PLs in THz QCLs have been realised by removing plasmonic cladding metal from the waveguide to pattern PL defect sites. The PLs sites have a high refractive index contrast between the ‘*metallised*’ and the ‘*un-metallised*’ sections and are usually formed by deep etched holes or gratings [147]. However, unlike DFB gratings, PL gratings may not be etched throughout the length of the cavity but can be localised and finite in number. Schematic diagram of a THz QCL cavity with a one-dimension PL is shown in Figure 3.1 (a). It is worth noting that unlike DFB lasers, optical feedback in PLs is provided by the end facet mirrors. Indeed, PLs can be classified as a one-dimensional photonic crystal. SM emission in PLs is achieved when a photonic bandgap forms in the dispersion characteristics and a Bragg resonance occurs where the wavelength is twice as the optical lattice constant (Λ) [128,148]. An enhanced density of photon states is observed around the Bragg wavelength due to this resonance and lasing

is favoured around the Bragg condition. The photonic bandgap in a PL can be calculated from its dispersion characteristics. The photonic bandgap (Δf_{BR}) formed in a PL with a deep etched grating is shown in Figure 3.1 (b), where a ‘detuning factor’ from the Bragg condition (f_{BR}) is plotted as a function of the propagation constant of the PL grating. The photonic bandgap in PLs would be discussed in greater detail in section 3.2.2.

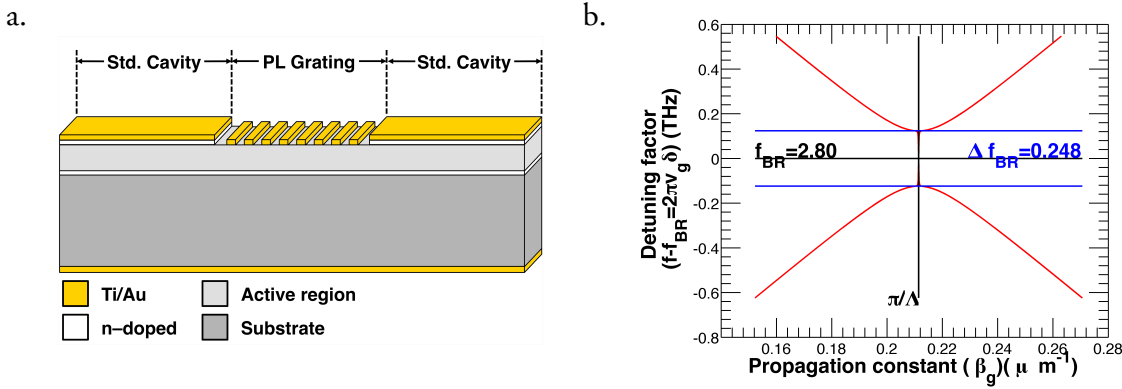


Figure 3.1: (a) Schematic diagram of THz QCLs cavities with PL grating. (b) Photonic bandgap in a one-dimensional PL with 2- μm deep etched unmetallised sections.

This study investigates SM emission from THz QCLs with an integrated PL in the waveguide. Unlike previous demonstrations of THz QCLs with PLs, reported in ref. [146], in this study PLs were fabricated using electron beam lithography (EBL) and vacuum thermal evaporation of cladding metals. This yielded shallow etched PL gratings with reduced refractive index contrast between PL metallised and unmetallised sections. To compensate for this reduced index contrast, the metal coverage of the PL was reduced to increase the loss modulation in the PL. A successful demonstration of this shallow etched grating can enable PL to be fabricated by standard lithography in addition to the FIB technique reported in ref. [146].

This chapter discusses the modelling, design, fabrication and measurement of THz QCLs with PLs. PL design parameters, like grating pitch, are calculated from analytical expressions. Photonic bandgap in PLs are calculated from the variation of detuning factor and propagation constant of the PL. THz QCLs with PLs of different grating pitches are fabricated and their spectra are compared with the simulated results.

3.2 Design and modelling of THz QCLs with PLs

3.2.1 PL design parameters

A PL is composed of periodic arrangement of two cavity sections with the cladding metal (forming the metallised section) and without the cladding metal (the unmetallised section), as illustrated in Figure 3.2. The characteristic Bragg wavelength (λ_{BR}) of a PL grating is determined from the pitch of the grating (Λ). The Bragg wavelength of a PL is given as [149]

$$\lambda_{BR} = \frac{2n_{eff}\Lambda}{l} \quad (3.1)$$

where n_{eff} is the effective refractive index of the grating and l is the order of the PL. For a first order PL, $l = 1$.

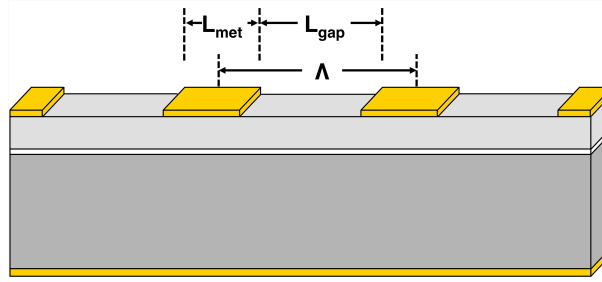


Figure 3.2: Schematic diagram of longitudinal cross section of grating pitch Λ , comprising metallised and unmetallised sections.

The effective refractive index of the PL (n_{eff}) depends on the refractive index at the metallised and the unmetallised sections, and is expressed as [149]

$$n_{eff}^2 \Lambda = n_{gap}^2 L_{gap} + n_{met}^2 L_{met} \quad (3.2)$$

where n_{met} and n_{gap} are the effective mode index at the metallised and the unmetallised sections of length L_{met} and L_{gap} respectively. The effective refractive index at the metallised and the unmetallised sections can be calculated using finite element modelling (FEM) and is discussed in section 3.2.1.1.

The duty cycle of a PL is the ratio of L_{met} and Λ and is expressed in percentage. The expression of duty cycle is given as

$$\gamma = \frac{L_{met}}{\Lambda} \quad (3.3)$$

It can be seen from eq. (3.1)–(3.2), that the effective refractive index of the PL, which is calculated from the effective refractive index of the metallised and the unmetallised sections of the PL is central to PL performance. The contrast in refractive index and the variation of waveguide losses in the metallised and unmetallised sections of the PL plays a crucial role in the photonic bandgap or the stopband in the PL. This would be discussed in greater detail in section 3.2.2. In this study, the effective refractive index and waveguide parameters in the metallised and the unmetallised sections of the PL were computed using a FEM technique and is described next.

3.2.1.1 Finite element modelling of device cross sections

This section describes two-dimensional FEM using a commercially available software COMSOL Multiphysics® – RF Module to compute effective refractive indices at the metallised and the unmetallised PL sections. This technique involved creation of a device cross-section that corresponded to the transverse waveguide structure. The model was subsequently optimised to form a densely packed meshed structure in the device cross-section. Finally, the mesh optimised device cross-section was simulated to compute propagation constants for selected eigenmodes at selected frequencies. Effective refractive index of a fundamental mode was then calculated from the computed spatial parameters.

A THz QCL with an active region described in ref. [67] was used for this study. Initially, an FEM model of a device cross-section at the metallised section of the PL was designed with a 150- μm wide and 11.7- μm thick bulk GaAs/AlGaAs active region with a uniform average doping of $7.5 \times 10^{15} \text{ cm}^{-3}$. The average doping of the active region was calculated from the sheet density of the QCL active region heterostructure. A 150 nm Au contact was modelled on top of the active region forming the cladding metal. A 450- μm wide and 700-nm-thick n^+ -GaAs layer doped at $5 \times 10^{18} \text{ cm}^{-3}$ formed the buried contact layer under the active region. A 200- μm thick SI-GaAs substrate was modelled under the buried contact. The device cross-section concluded with a 150-nm thick Au layer modelled under the substrate. The entire structure was surrounded by air and the perimeter of the device cross-section was made a conducting boundary to facilitate computation. Although, THz QCLs with single metal waveguides were simulated, the lateral ohmic contact strips were

not included in the FEM model to simplify the model. The perturbative coupling between the lateral contacts and the active region ridge was minimised as they were separated by a distance of 30 μm in real devices, as was reported in ref. [150]. The device cross-section of FEM model at the metallised section is shown in Figure 3.3.

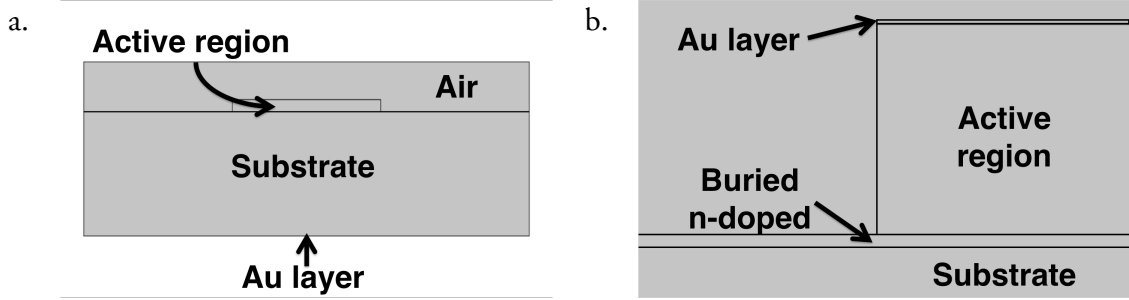


Figure 3.3: Device cross-section of the metallised section modelled in COMSOL Multiphysics®: (a) Complete view of the model, (b) magnified view of the active region.

A similar FEM model was used to simulate the unmetallised section of the PL. However, the 150-nm thick Au contact on top of the active region was removed from this model to account for the absence of cladding material at the unmetallised section. The complex refractive indices and the dielectric permittivity at the different constituent layers in the device cross-sections were calculated using a UNIX based Drude model solver, OWG-QCLSIM developed at the University of Leeds. The Drude model calculations for the active region, the doped contact layers and cladding metal were calculated at a temperature of 80 K, while those for the substrate and the Au soldering layer were calculated at heat sink temperature of 4 K. This temperature difference was included in the model, as the lattice temperature of a 150 μm -wide THz QCL ridge with 200 μm -thick substrate is ~ 80 K higher than the heat sink temperature [151,152].

Following the design of the device cross-section of the FEM, it was optimized with triangular mesh with maximum and minimum element size of 6 μm and 50 nm respectively. The final mesh optimized cross-section of the metallised section is shown in Figure 3.4.

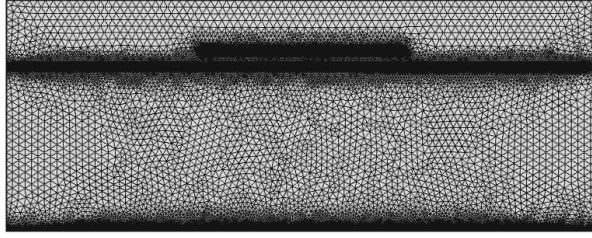


Figure 3.4: Device cross-section of the metallised section of the PL modelled in COMSOL Multiphysics®: after triangular mesh optimisation.

The model computed estimates of propagation constants for selected eigenmodes at the metallised and the unmetallised cross-sections at 2.77 THz. The complex effective refractive indices ($n_{eff} = n + jk$) of the optical mode in the metallised and the unmetallised sections were computed as $n_{met} = 3.62 - j0.0064$ and $n_{gap} = 3.48 - j0.0325$ respectively. The computed optical modes at both metallised and unmetallised sections are shown in Figure 3.5 (a, b). The optical mode in the metallised section exhibits a typical mode profile in THz QCLs with single metal waveguides [66]. The optical mode is pinned to the surface plasmon formed at the interface of the 150-nm thick Au layer and the active region at the top, and at the 700-nm thick buried n -doped layer. A significant portion of the mode decays into the substrate, typical in THz QCLs with single metal waveguide. The confinement of the optical mode in the gain region (Γ) was calculated from the ratio of power integral in the active region over the power integral in the entire cross-section. A confinement factor (Γ_{met}) of $\sim 30\%$ was observed at the metallised section.

The mode profile changed significantly in the unmetallised section [Figure 3.5 (b)]. Since the top cladding metal was etched away in this section, the optical mode is supported only at the buried n -doped layer. Hence, the mode penetration in the substrate is greater than in the metallised sections, with a confinement factor (Γ_{gap}) of $\sim 2\%$.

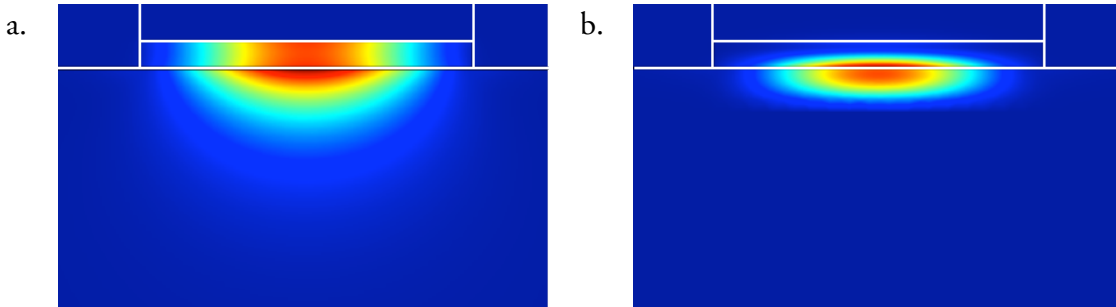


Figure 3.5: Computed optical mode at 2.77 THz using FEM. Contour of power distribution is plotted at: (a) metallised and (b) unmetallised sections.

The waveguide losses at the device cross-sections (α_{wg}) were calculated from the imaginary part of the computed effective refractive index (k) using the following expression:

$$\alpha_{wg} = \frac{4\pi k}{\lambda} \quad (3.4)$$

where λ is the free space wavelength used in the mode computation. The waveguide losses at the metallised and unmetallised sections were calculated as $\alpha_{wg,met} = 7.50 \text{ cm}^{-1}$ and $\alpha_{wg,gap} = 38.12 \text{ cm}^{-1}$ respectively. An index modulation $\Delta n = n_{met} - n_{gap} = 0.17$ and a loss modulation $\Delta\alpha_{wg} = \alpha_{wg,gap} - \alpha_{wg,met} = 30.62 \text{ cm}^{-1}$ was calculated from the simulated results.

The parameters derived from the FEM simulation were used to calculate the bandwidth of the stopband, and is described next.

3.2.2 Stopband in a PL

As previously noted, PLs, like DFBs, have periodic perturbations in the refractive index or waveguide losses, or a combinations of both. Waves propagating in such a waveguide experience Bragg scattering at the periodic sites and light is scattered between two counter propagating ‘*forward*’ and ‘*backward*’ waves in the cavity. This scattering or ‘*coupling*’ of light between the counter propagating waves is essential for SM emission and the formation of a photonic bandgap or a stopband in PLs. The stopband in a periodic structure like a PL is calculated from coupled mode theory, which describes the coupling between the forward and backward waves [106]. The stopband resulting from such periodic structures can be calculated from the phase of the propagating electric fields. The solutions to such coupled propagating electric fields typically yield multiple solutions for the forward and backward wave respectively. The phase factors of such coupled solutions are given as [106],

$$\beta_g = \beta_{BR} \pm \sqrt{\delta^2 - \kappa^2} \quad (3.5)$$

where β_{BR} is the ‘*propagation constant*’ at the Bragg condition, δ is the ‘*detuning parameter*’ and κ is the ‘*coupling coefficient*’ between the propagating modes.

The propagation constant at the Bragg condition defined by eq. (3.1) is expressed as [106]

$$\beta_{BR} = \frac{l\pi}{\Lambda} \quad (3.6)$$

where l is the order of the PL.

The detuning parameter measures the difference between the oscillating frequency and the Bragg frequency ($f_{BR} = c/\lambda_{BR}$) and is expressed as [106,108]:

$$\delta \equiv \bar{\beta} - \beta_0 = \frac{2\pi(f - f_{BR})}{v_g} \quad (3.7)$$

where $\bar{\beta}$ is complex propagation constant and v_g is the group velocity. The complex propagation constant is expressed as [106],

$$\bar{\beta} = \frac{2\pi n_{eff}}{\lambda} + j \left[\frac{g - \alpha_{wg}}{2} \right] \quad (3.8)$$

where λ is the wavelength, g is the transverse modal gain and α_{wg} is the waveguide loss in the grating, of pitch Λ . The group velocity is calculated from the group refractive index ($n_g = c/v_g$), which is measured from Fabry–Pérot mode spacing ($\Delta\nu$). In a waveguide of length L_C the group refractive index is given as [153]

$$n_g = \frac{c}{2L_C\Delta\nu} \quad (3.9)$$

The Bragg scattering and the coupling between the forward and backward waves is quantified by the coupling coefficient [108]. The coupling coefficient in a PL is calculated from the variation in the refractive index (Δn_{eff}) and waveguide loss ($\Delta\alpha_{wg}$) in the metallised and unmetallised sections of the PL and is given by the following expression [106]

$$\kappa = \frac{n_g}{n_{eff}} \frac{\pi}{\Lambda} \Gamma_{eff} \left[\Delta n_{eff} + j \cdot \frac{\Delta\alpha_{wg}}{2k_0} \right] \quad (3.10)$$

where Γ_{eff} is the optical confinement in the PL and k_0 is the free space propagation constant.

$$k_0 = \frac{2\pi}{\lambda} \quad (3.11)$$

When the detuning factor, δ , is plotted as a function of the propagation constant, β_g , the stopband of the PL (Δf_{BR}) is observed [Figure 3.6]. The coupled forward and backward waves result in a characteristic stopband centred at the Bragg frequency (f_{BR}) and

the propagation constant of the PL (β_0). The bandwidth of the stopband can be estimated from the gap in the dispersion curve shown in Figure 3.6. In a purely index coupled PL, the bandwidth of the stopband is given as [106,149]:

$$\Delta f_{BR} = \frac{\kappa v_g}{\pi} = \frac{\kappa c}{\pi n_g} \quad (3.12)$$

The spatial intensity distribution in a periodic structure like PL can be calculated from a dimensionless parameter called the ‘*coupling strength*’ [108], which can be calculated by multiplying coupling constant, κ , with the length of the grating ($N\Lambda$, where N is the number of grating repetitions). A uniform spatial distribution is achieved in a PL with coupling strength in the range of 1–2, which is referred to as a ‘*critical coupling*’ [108].

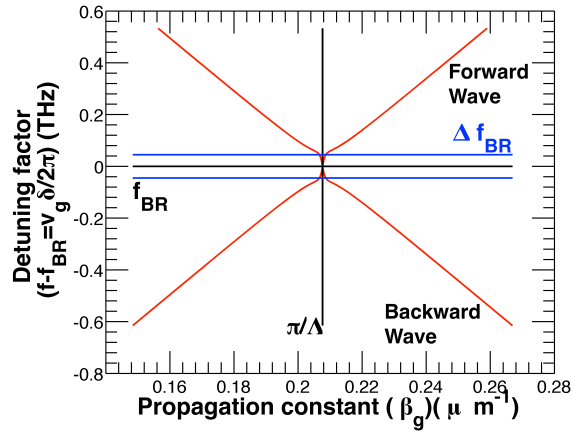


Figure 3.6: Dispersion curve in a PL. The detuning factor is plotted as a function of the propagation constant. A stopband is observed centred at Bragg frequency.

For this work, PLs were designed using the design parameters given in eq. (3.1)–(3.3) and the stopband behaviour modelled using the coupled mode theory. The detailed design steps are discussed next for a PL with Bragg frequency at 2.80 THz.

3.2.3 Designing a PL with Bragg frequency at 2.80 THz

In this section the steps followed to design a PL is discussed. All PLs discussed in this thesis followed the same general design procedure.

The first step to design a PL involves the selection of an appropriate Bragg frequency and the simulation of the effective refractive indices at the metallised and unmetallised sec-

tions of the PL. In this case, the PL was designed with a Bragg frequency f_{BR} at 2.80 THz (corresponding to a Bragg wavelength $\lambda_{BR} = 107.14 \mu\text{m}$). The effective refractive indices computed from FEM simulation in section 3.2.1.1 were considered for this design. A PL with a grating duty cycle of 40% was chosen for this study because a low metal coverage in a PL increases the waveguide loss.

The pitch of the PL was calculated by substituting the values of L_{met} , L_{gap} [expressed in terms of the duty cycle (γ)] and Λ to eq. (3.1) and (3.2) and is simplified in the following expression:

$$\Lambda = \frac{\lambda_{BR}/2}{\sqrt{(1 - \gamma) \cdot n_{gap}^2 + \gamma \cdot n_{met}^2}} \quad (3.13)$$

A grating pitch $\Lambda = 15.14 \mu\text{m}$ was calculated after substituting $n_{met} = 3.62$, $n_{gap} = 3.48$, $\gamma = 0.40$ and $\lambda_{BR} = 107.14 \mu\text{m}$ into eq. (3.13).

The effective refractive index, $n_{eff} = 3.53$ was calculated from eq. (3.2). The coupling constant of the PL was calculated from eq. (3.10) as $\kappa = 25.76 \text{ cm}^{-1}$. For a PL with 35 repetitions, the coupling strength was calculated as $\kappa(35 \times \Lambda) = 1.36$, within the critical range of 1–2 [108], suggesting a power distribution localised in the centre of the cavity where the PL is deposited.

The gain g in the active material was calculated as 27.5 cm^{-1} using a UNIX based software package QCLSIM developed at the University of Leeds, for the active region design of the QCL material reported in ref. [67]. The calculated value agrees well with an experimentally calculated gain for a similar active region, reported in ref. [154]. Waveguide losses were calculated from the imaginary part of effective refractive index [eq. (3.4)].

The stopband in the PL was simulated from the dispersion curve following the same procedure as described in section 3.2.2, and is shown in Figure 3.7. The bandwidth of the stopband was calculated as $\sim 90 \text{ GHz}$ from the dispersion curve.

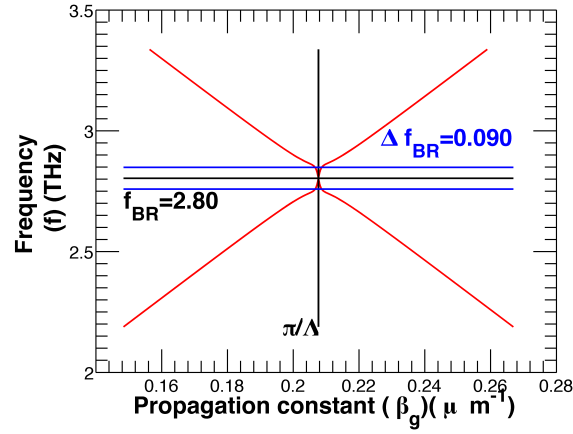


Figure 3.7: Simulated stopband in a PL with a Bragg frequency at 2.80 THz. The bandwidth of the stopband was calculated as ~ 90 GHz.

3.2.4 Final PL designs

Following similar design principles, a set of THz QCLs with PLs was designed with different f_{BR} . The stopband of the devices was calculated as ~ 90 GHz with emission predicted at either side of the stopband. A list of the PL designs used for this study is tabulated in Table 3.1. The QCL active region design used for this study had a gain bandwidth from 2.70–2.85 THz. Hence, the Bragg frequency of the PLs were deliberately selected such that the stopband edges were within the gain bandwidth of the active region. Emission was predicted by comparing the edge of the stopband and the gain bandwidth of the QCL active region. A grating duty cycle of 40% was used for all the devices.

Table 3.1: List of designed THz QCLs with PLs.

f_{BR} (THz)	λ_{BR} (μm)	Λ (μm)	L_{met} (μm)	L_{gap} (μm)	Predicted emission (THz)
2.77	108.30	15.31	6.12	9.19	2.815
2.80	107.14	15.14	6.06	9.08	2.760
2.81	106.76	15.09	6.04	9.05	2.765
2.82	106.38	15.04	6.02	9.02	2.775
2.84	105.63	14.93	5.97	8.96	2.795
2.88	104.16	14.72	5.89	8.83	2.835

As discussed earlier, a major objective of this study was to investigate the possibility of fabricating PLs using lithography and vacuum thermal evaporation of cladding metal, and is discussed next.

3.3 Fabrication

Single metal waveguides were used in this study for the fabrication of THz QCLs with PLs. All devices processed in this study were derived from wafer labelled ‘L701’, which had a bound-to-continuum active region similar to the one reported in ref. [67]. The wafer was grown on a semi-insulating (SI) GaAs wafer using molecular beam epitaxial (MBE) technique at the MBE Laboratory, University of Leeds, UK. Growth started with a 250-nm thick GaAs buffer layer, and a 300-nm thick $\text{Al}_{50}\text{Ga}_{50}\text{As}$ etch stop layer grown on top of the SI-GaAs substrate. A 700-nm thick n -doped GaAs layer doped with Si at $2 \times 10^{18} \text{ cm}^{-3}$ was grown next, which formed a buried contact layer. This was followed by 90 repetitions of the active-region layers. Growth was concluded with an 80-nm thick GaAs layer n -doped with Si at $5 \times 10^{18} \text{ cm}^{-3}$. The active region layer structure of the wafer is tabulated in Table 3.2.

Samples from wafer L701 were processed following identical fabrication steps used for THz QCLs with standard single metal waveguides, as described in section 2.2. Top ohmic contact and cladding metal were deposited following identical procedures, as described for standard THz QCLs, but with a different mask set. The mask used for the deposition of top ohmic contact and cladding metal used in this study had a break at the centre of the cavity. The ohmic contact at the top was not deposited on the central section deliberately to simplify the EBL processing steps. An illustration and optical microscopy of fabricated devices after deposition of segmented top ohmic contact and cladding material are shown in Figure 3.8. PL gratings were subsequently deposited at the central gap section after etching away the top n -doped layer, as illustrated in Figure 3.1 and Figure 3.2.

After the deposition of the cladding Ti/Au metal films, the n -doped top contact layer was etched away from the central section. An aqueous solution of wet chemical etchant of H_2SO_4 , H_2O_2 and H_2O mixed in the ratio 1:8:1280 by volume was used for the etching. Typical etch rate of the etchant solution was $\approx 31 \text{ nm/min}$. The sample was cleaned with oxygen plasma after the top contact layer etching and was patterned with EBL to form the PL gratings.

Table 3.2: MBE layer growth structure of L701.

Layer	Material		Thickness (nm)	Doping (cm ⁻³)	Comments
	III-V Material	Composition			
1	GaAs	-	250	-	Buffer layer
2	AlGaAs	Al ₅₀ Ga ₅₀ As	300	-	Etch stop layer
3	GaAs	-	700	2 x 10 ¹⁸	Bottom contact
4	AlGaAs	Al ₁₅ Ga ₈₅ As	3.8	-	
5	GaAs	-	11.6	-	
6	AlGaAs	Al ₁₅ Ga ₈₅ As	3.5	-	
7	GaAs	-	11.3	-	
8	AlGaAs	Al ₁₅ Ga ₈₅ As	2.7	-	
9	GaAs	-	11.4	3.2 x 10 ¹⁶	
10	AlGaAs	Al ₁₅ Ga ₈₅ As	2.0	-	
11	GaAs	-	12.0	3.2 x 10 ¹⁶	
12	AlGaAs	Al ₁₅ Ga ₈₅ As	2.0	-	
13	GaAs	-	12.2	-	
Start of 90 period repeat					
14S1	AlGaAs	Al ₁₅ Ga ₈₅ As	1.8	-	
15S1	GaAs	-	12.8	-	
16S1	AlGaAs	Al ₁₅ Ga ₈₅ As	1.5	-	
17S1	GaAs	-	15.8	-	
18S1	AlGaAs	Al ₁₅ Ga ₈₅ As	0.6	-	
19S1	GaAs	-	9.0	-	
20S1	AlGaAs	Al ₁₅ Ga ₈₅ As	0.6	-	
21S1	GaAs	-	14	-	
22S1	AlGaAs	Al ₁₅ Ga ₈₅ As	3.8	-	
23S1	GaAs	-	11.6	-	
24S1	AlGaAs	Al ₁₅ Ga ₈₅ As	3.5	-	
25S1	GaAs	-	11.3	-	
26S1	AlGaAs	Al ₁₅ Ga ₈₅ As	2.7	-	
27S1	GaAs	-	11.4	3.2 x 10 ¹⁶	
28S1	AlGaAs	Al ₁₅ Ga ₈₅ As	2.0	-	
29S1	GaAs	-	12.0	3.2 x 10 ¹⁶	
30S1	AlGaAs	Al ₁₅ Ga ₈₅ As	2.0	-	
31S1	GaAs	-	12.2	-	
End of 90 period repeat					
32	GaAs	-	80	5 x 10 ¹⁸	Top contact

Although, the PL gratings could be patterned using optical photolithography, EBL was used for processing flexibility. PLs with different grating pitch could be patterned with EBL by simply changing the feature sizes, without the need for a chrome mask. A bi-layer PMMA process was used for the EBL to facilitate metal lift-off. Initially, a layer of EBL re-

sist PMMA® 495 A8 was spun at 3000 rpm for 40 seconds. The resist was baked in a temperature-controlled hot plate for 2 minutes at a temperature of 170°C. A second layer of EBL resist PMMA® 950 A4 was spun subsequently at two stages – initially at 2000 rpm for 15 seconds, followed by 5000 rpm for 40 seconds. The bi-layer resist was baked in a temperature-controlled hot plate for further 2 minutes at a temperature of 170°C. The same Leo-Raith 50 EBL workstation described in section 2.2.10, was used to write the PL grating patterns. The PL gratings were designed using a CAD editor in a GDSII format and were patterned with a beam spot size of 250 and a dose of 200 $\mu\text{As cm}^{-2}$. The samples were developed in a solution of MIBK and IPA premixed at a volume ration of 1:3 for one minute. Optical microscopy of samples after EBL resist development is shown in Figure 3.9 (b, c).

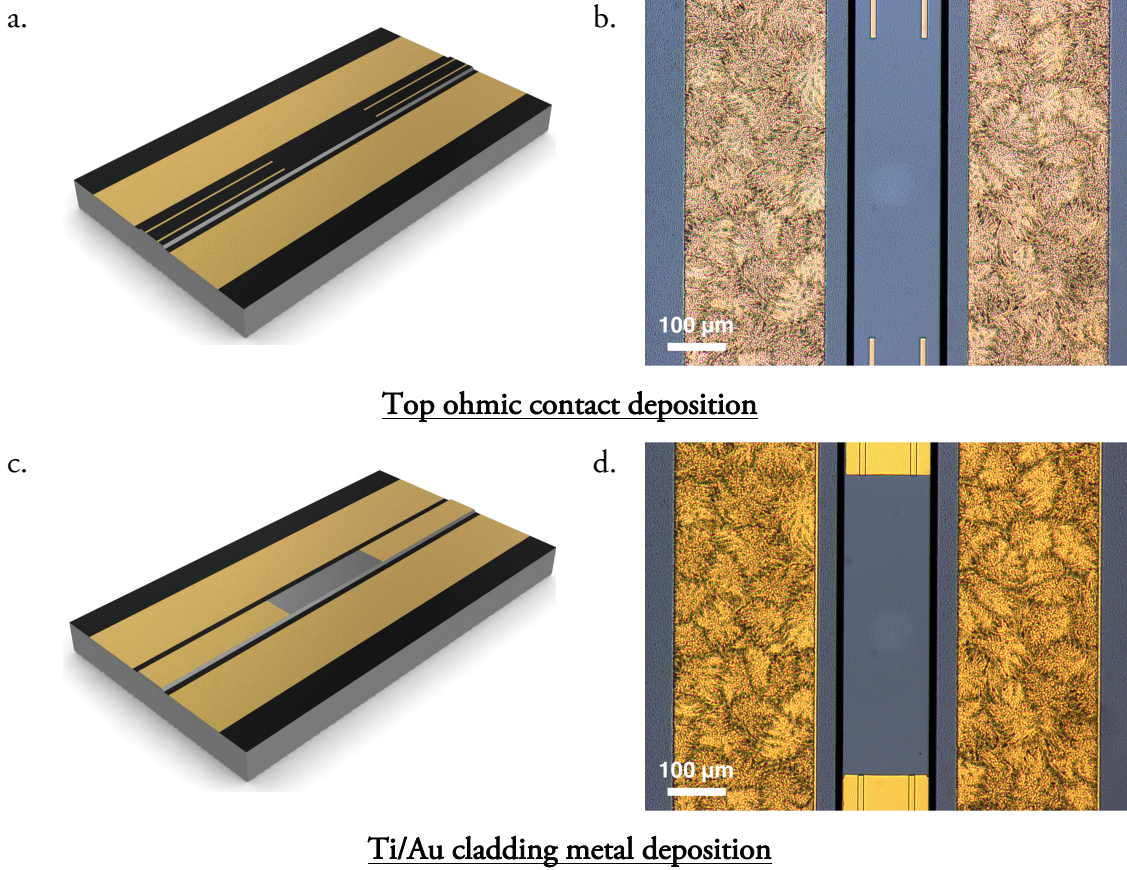


Figure 3.8: (a) Illustration and (b) optical microscopy from a fabricated device after top ohmic contact deposition with a central gap. (c) Illustration and (d) optical microscopy of a fabricated device after deposition of Ti/Au cladding metal with a central gap.

A 20-nm thick layer of Ti and a 100-nm thick layer of Au were deposited after EBL patterning with identical procedures followed during the deposition of the cladding metal.

After the vacuum thermal evaporation, the metal was lifted off using acetone. Optical microscopy of a sample after metal lift off is shown in Figure 3.10. It was observed that the grating features patterned in the devices deviated from the original PL design by a few tens of nanometres. This was later ascribed to minor aberrations in the beam focussing and write field alignment procedures. Fabrication then continued as described in section 2.2.

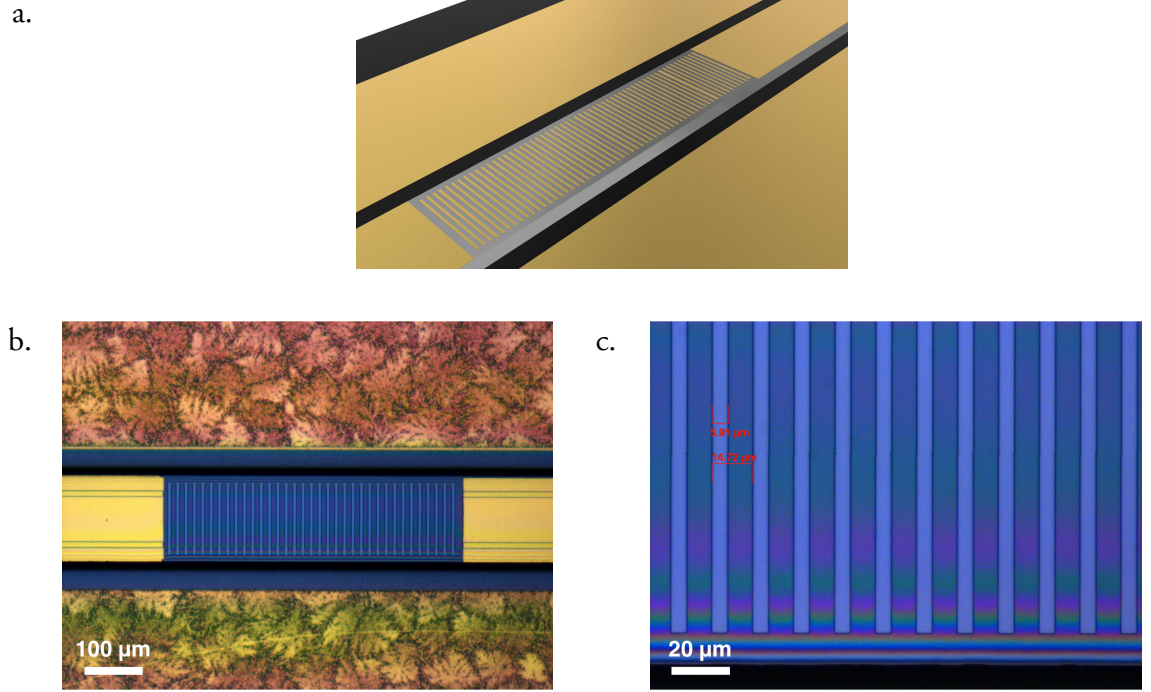


Figure 3.9: (a) Illustration of a PL grating deposited at the central gap. (b) Optical microscopy from a fabricated device after the development of resist following EBL patterning of PL grating. (c) Magnified view after the development of EBL resist.

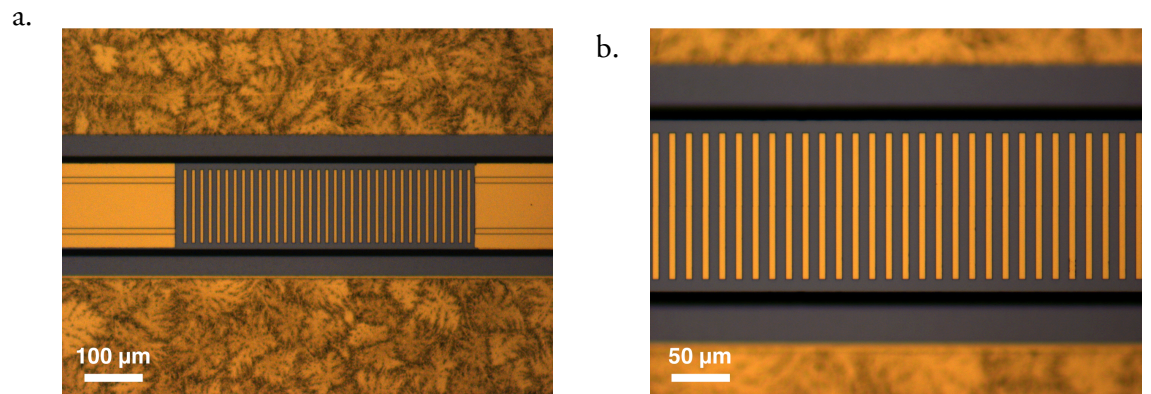


Figure 3.10: (a) Optical microscopy from a fabricated device after development of resist following EBL patterning of PL grating. (b) Magnified view.

A list of fabricated devices with PL grating parameters is listed in Table 3.3. Two sets of devices [Devices 3C and 3D] and [Devices 3G and 3H] were fabricated with the same PL dimensions with f_{BR} at 2.81 and 2.88 THz respectively.

After fabrication, devices were characterised to analyse the spectral and electrical behaviour, and is discussed in the next section.

Table 3.3: List of fabricated THz QCLs with PLs.

Device number	Unique Device ID	f_{BR} (THz)	λ_{BR} (μm)	Λ (μm)	L_{met} (μm)	L_{gap} (μm)
3A	L701-S10-D1-T	2.77	108.30	15.31	6.12	9.19
3B	L701-S4-D1-B	2.80	107.14	15.14	6.06	9.08
3C	L701-S5-D1-T	2.81	106.76	15.09	6.04	9.05
3D	L701-S10-D1-B	2.81	106.76	15.09	6.04	9.05
3E	L701-S11-D2-SM	2.82	106.38	15.04	6.02	9.02
3F	L701-S5-D2-T	2.84	105.63	14.93	5.97	8.96
3G	L701-S4-D2-B	2.88	104.16	14.72	5.89	8.83
3H	L701-S10-D2-T	2.88	104.16	14.72	5.89	8.83

3.4 Experimental results

The devices were operated in pulsed mode using the experimental setup described in section 2.3.1. Data from reference devices were also recorded, which facilitated a comparison of device performance and are discussed first.

3.4.1 Results from reference devices

Reference devices with a single metal waveguide and no PL from the same wafer, L701, were characterised to establish electrical [light-current-voltage (LIV)] and spectral behaviour of the wafer. Emission with multiple FP modes from 2.70–2.85 THz was observed in all reference devices. Spectra from a 3.1 mm long device are shown in Figure 3.11. It was observed that lasing was favoured at higher frequency regions (> 2.78 THz) at the start of the dynamic range [Figure 3.11 (a)]. A similar behaviour was also observed at higher heat sink temperatures [Figure 3.11 (b)].

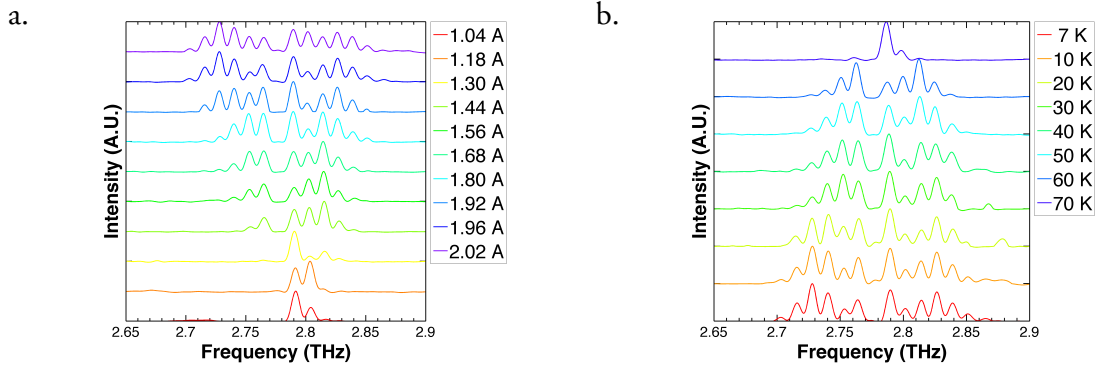


Figure 3.11: Spectra obtained from a reference device labelled L701-S2-B. (a) Spectra obtained at different drive currents with a heat sink temperature of 4 K. (b) Spectra obtained at different heat sink temperatures with a drive current of 1.96 A.

The LIV characteristics obtained from the same device at a heat sink temperature of 14 K are shown in Figure 3.12 (a). A peak power of ~ 11 mW and a threshold current density of ~ 200 A/cm² was observed at heat temperature of 14 K [Figure 3.12 (b)]. The threshold current density exhibited an exponential increase with heat sink temperature, typical in THz QCLs. The maximum operating temperature for this wafer was in the range of 80–85 K. All devices from L701 exhibited similar characteristics, as presented here.

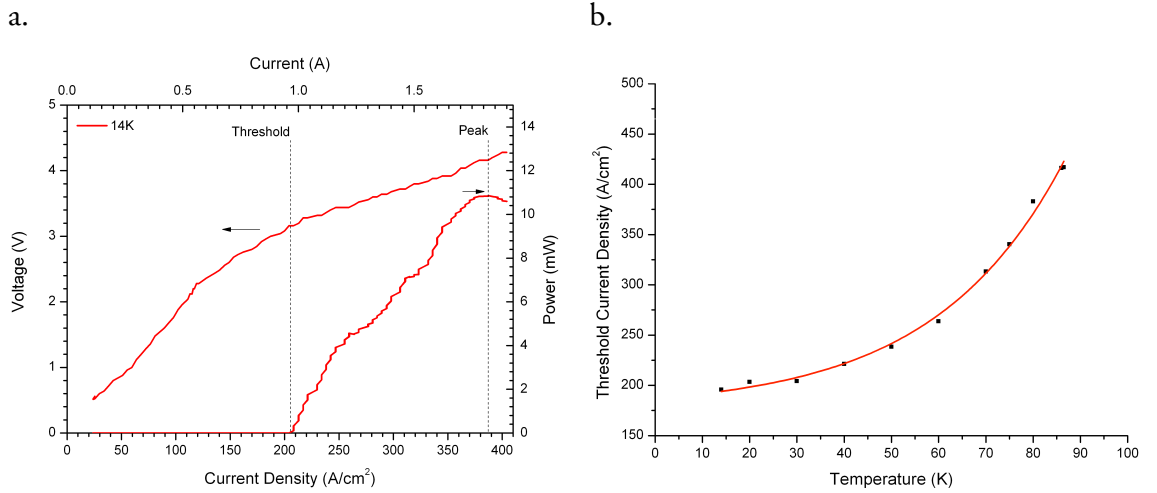


Figure 3.12: (a) LIV characteristics from a reference device labelled L701-S2-B at a heat sink temperature of 14 K. (b) Threshold current density is plotted as a function of heat sink temperature for the same reference device.

3.4.2 Results from THz QCLs with PLs

Emission from each of the fabricated devices was recorded at different drive currents with a heat sink temperature of 4 K. Observed emission was compared with the Bragg frequency and the estimated stopband calculated from the grating pitch measured in real devices. The following section describes the observed spectral characteristics.

3.4.2.1 Spectral characterisation

The emission spectrum recorded from one of the fabricated devices (device 3B) with $f_{BR} = 2.80$ THz is shown in Figure 3.13 (a). Emission was predicted at the edge of the stopband at ~ 2.76 THz [Table 3.1]. Although, the PL for this device was designed with $\Lambda = 15.14$ μm and $L_{met} = 6.06$ μm , the PL patterned on the real device was observed to have a grating pitch $\Lambda = 15.13$ μm and $L_{met} = 6.05$ μm . The PL pitch on the sample differed from the design by ~ 10 nm. The Bragg frequency of the PL patterned on the device was calculated as $f_{BR} = 2.804$ THz. A SM emission at ~ 2.76 THz was observed at all drive currents. It is observed that the emission is at the edge of predicted stopband [Figure 3.13 (b)]. The stopband was calculated as ~ 86 GHz from the difference between the Bragg frequency and emission frequency, and agrees closely with the simulated stopband of ~ 90 GHz.

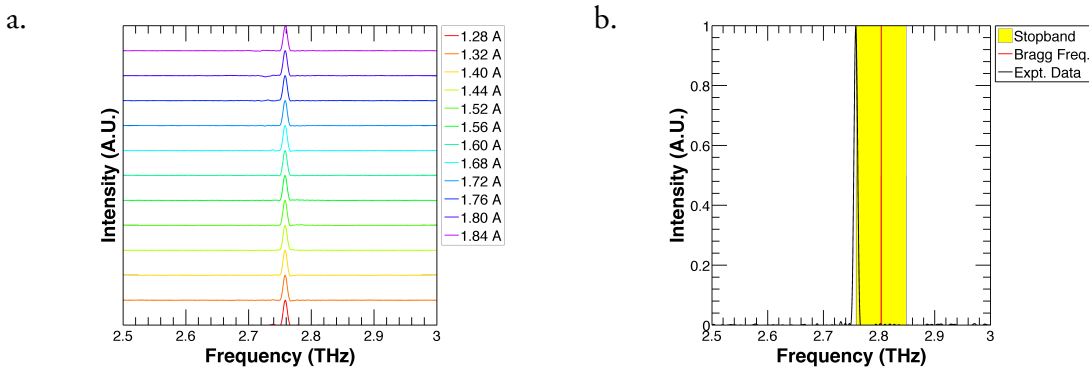


Figure 3.13: (a) Spectra obtained from device 3B with $f_{BR} = 2.80$ THz.
(b) The emission was observed at the edge of the stopband.

Spectra were similarly acquired from two other devices (devices 3G and 3H), both with a similar grating pitch ($\Lambda = 14.72$ μm , $L_{met} = 5.89$ μm) designed at $f_{BR} = 2.88$ THz [Figure 3.14 (a, c)]. Emission from both the devices was predicted at the edge of the stopband at ~ 2.835 THz [Table 3.1]. In both the devices the actual grating pitch that

was patterned on the sample was measured to be $\Lambda = 14.72 \mu\text{m}$ with $L_{met} = 5.91 \mu\text{m}$. Emission at $\sim 2.79 \text{ THz}$ was observed from each of the two devices. While the emission was predominantly single mode, at higher drive currents a second mode was observed at $\sim 2.82 \text{ THz}$. Emission frequency was compared with the predicted stopband [Figure 3.14 (b, d)]. It was observed that the primary mode (2.79 THz) was beyond the band edge of the stopband and the secondary mode was at the band edge of the stopband. This effectively demonstrates that emission is possible beyond the stopband edge if there is sufficient gain bandwidth. This behaviour was exploited in a PL design and would be discussed in section 6.3.1.2.

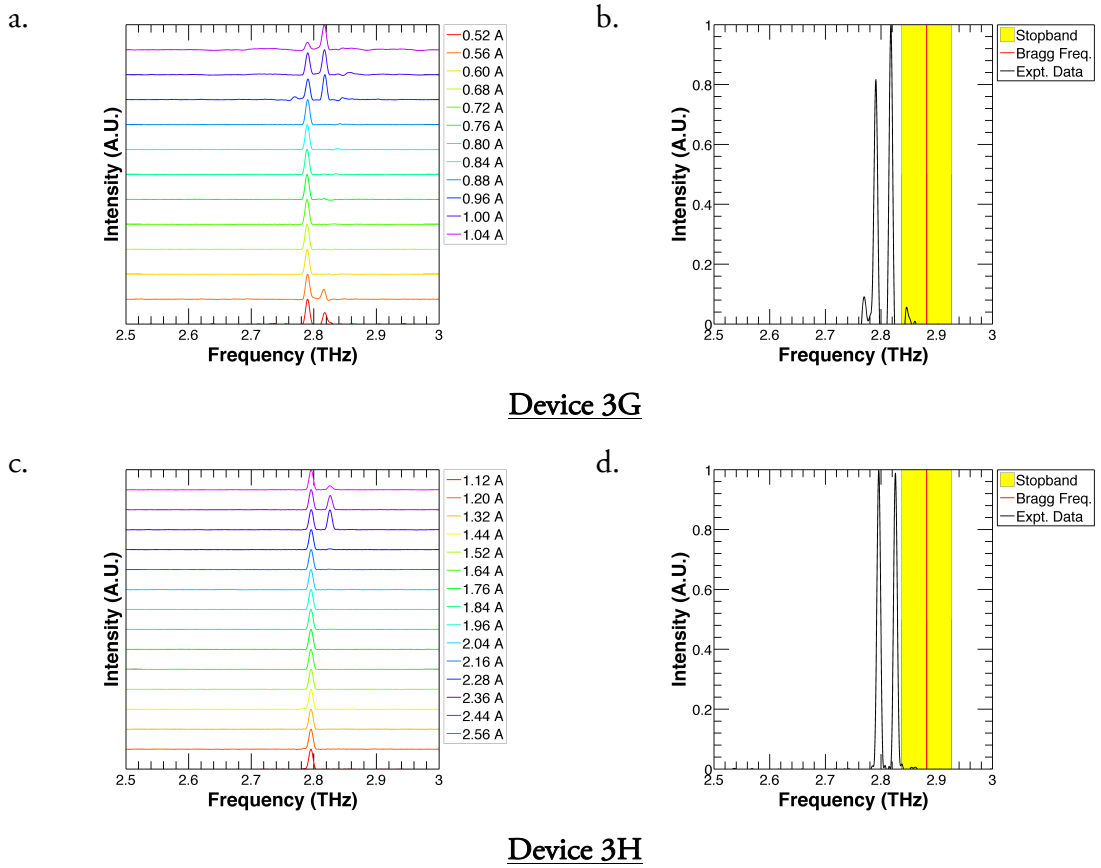


Figure 3.14: Spectra obtained from devices: (a) 3G and (c) 3H, both with $f_{BR} = 2.88 \text{ THz}$. (b, d) The emission was observed at the edge of the stopband.

Repeatability of device performance was also tested from two devices (devices 3C and 3D) both with a similar grating pitch ($\Lambda = 15.09 \mu\text{m}$, $L_{met} = 6.04 \mu\text{m}$) designed at $f_{BR} = 2.81 \text{ THz}$ [Figure 3.15 (a, c)]. Emission was predicted at the edge of the stopband at $\sim 2.765 \text{ THz}$ [Table 3.1]. In both the devices the actual grating pitch was measured to be $\Lambda = 15.08 \mu\text{m}$ with $L_{met} = 6.05 \mu\text{m}$. The emission from both the devices was observed at

~ 2.765 THz. In both the devices, emission frequency was observed at the edge of the predicted stopband, as in Figure 3.13 and Figure 3.14. Thus, an identical behaviour could be replicated from two devices with a similar grating pitch.

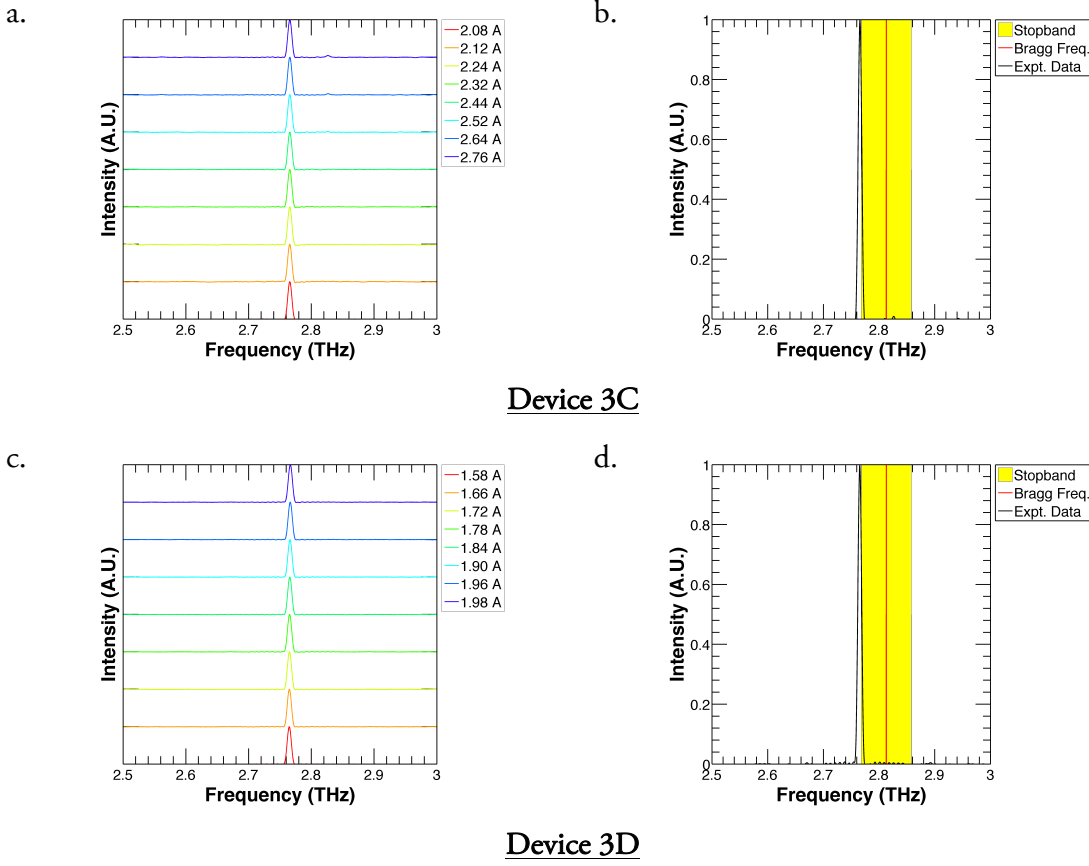


Figure 3.15: Spectra obtained from devices: (a) 3C and (c) 3D both with $f_{BR} = 2.81$ THz. (b, d) The emission was observed at the edge of the stopband.

A similar spectral measurement was carried out on three more devices (devices 3F, 3A and 3E) with designed grating pitches of $\Lambda = 14.93, 15.31, 14.93 \mu\text{m}$ and $L_{met} = 5.97, 6.12, 6.02 \mu\text{m}$, corresponding to a Bragg frequency $f_{BR} = 2.84, 2.77, 2.82$ THz respectively. Emission was predicted at the edge of the stopband at $\sim 2.795, 2.815$ and 2.775 THz for devices 3F, 3A and 3E respectively [Table 3.1]. A SM emission was observed at $2.79, 2.82$ and 2.76 THz from the three devices respectively [Figure 3.16].

The grating pitches at the devices 3F, 3A and 3E were measured as $\Lambda = 14.92, 15.30, 15.08 \mu\text{m}$ and $L_{met} = 5.97, 6.12, 6.03 \mu\text{m}$ respectively. The device 3E, unintentionally, had a similar grating pitch as the devices 3C and 3D shown in Figure 3.15. However, the width of the metallised section in this device was greater than

the devices 3C and 3D by ~ 20 nm. This resulted in a different emission frequency at 2.759 THz, as compared to the emission from the other two devices [Figure 3.15], which lased at 2.765 THz respectively. This is in agreement with the theory that fine changes in emission frequency can be observed by simply changing the duty cycle of the grating with an identical pitch. Such an observation was also reported for THz QCLs with DFBs in ref. [124].

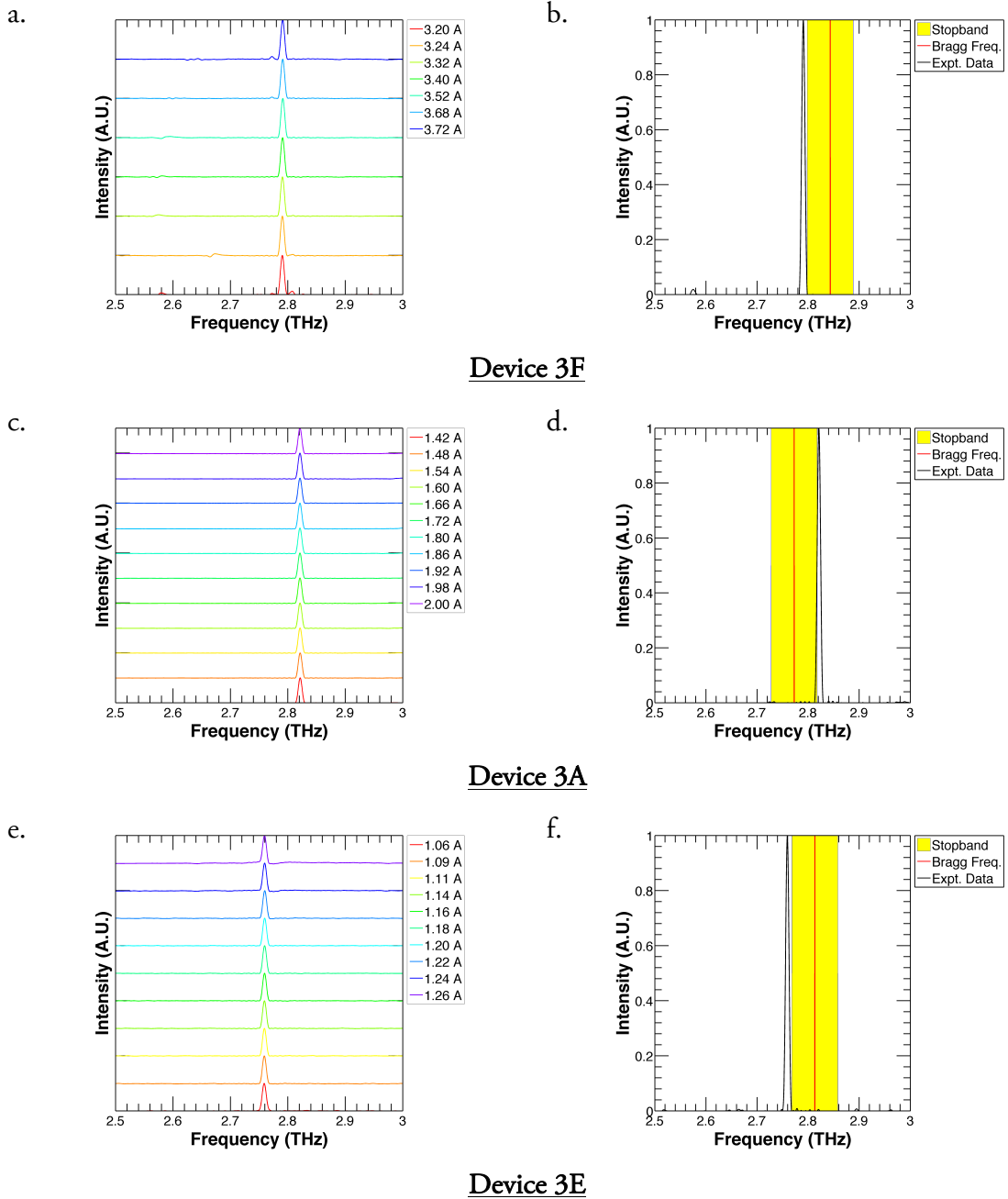


Figure 3.16: Spectra obtained from devices: (a) 3F [$f_{BR} = 2.84$ THz] (c) 3A [$f_{BR} = 2.77$ THz] (e) 3E [$f_{BR} = 2.82$ THz]. (b, d, f) Emission was observed at the edge of the stopband.

Another interesting result was observed in the device 3A. The emission in this device was observed at the stopband edge at the higher frequency, while those at all other devices were observed at the stopband edge at the lower frequency. The stopband in this device was at the centre of the gain bandwidth (2.77 THz). Hence, lasing could be favoured at either edge of the stopband.

A summary of the device performance from all devices is presented in Figure 3.17. The Bragg frequency calculated from the grating pitch measured in real devices and the corresponding stopband edges are also plotted. Emission is always observed beyond the stopband edge in all devices. The stopband width estimated from the difference between emission frequency and Bragg frequency in all devices is ~86–89 GHz, and agrees well with the simulated stopband width of ~90 GHz calculated from dispersion curve [Figure 3.7].

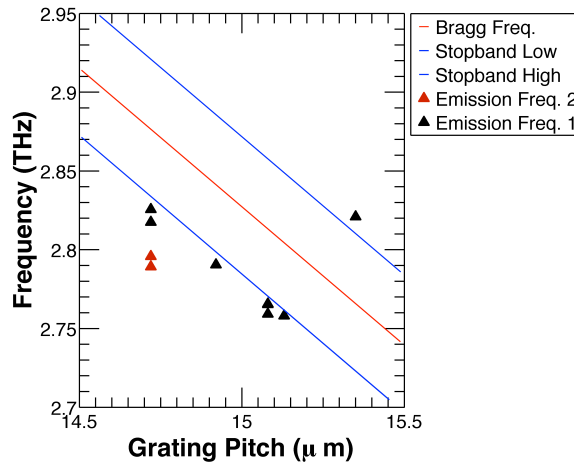


Figure 3.17: Summary of emission frequency for all devices as a function of grating pitch measured in real samples. The Bragg frequency and the stopband edges calculated from the grating pitch are also shown. Multiple mode emission is shown as black and red triangles. Emission is always observed beyond the stopband edge. Multiple devices were tested with grating pitch at $\Lambda = 14.72$ & 15.08 μm .

The side mode suppression ratio (SMSR) of the emission spectrum in all devices was observed at more than 20 dB. The SMSR from the device 3A is shown in Figure 3.18 (a) for all drive currents. The emission peaks also exhibited a temperature tuning of ~2 GHz with an increase in the heat sink temperature. The temperature tuning of the lasing mode from one of the devices, device 3H, is shown in Figure 3.18 (b).

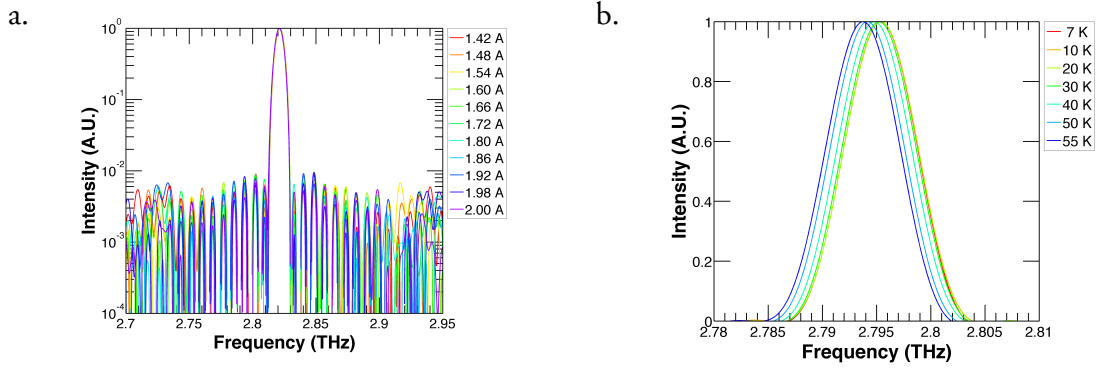


Figure 3.18: (a) Spectra from device 3A. A SM emission with an SMSR of more than 20 dB was observed. (b) Spectra from device 3H: with a drive current of 3.24 A at different heat sink temperatures.

3.4.2.2 Electrical characteristics

LIV characteristics were obtained from devices with PLs at different heat sink temperatures. LIV characteristics from an exemplar device; device 3H is shown in Figure 3.19 (a). A lower optical power was observed from all devices with PLs. A peak emission power in the range of 0.8-2 mW was observed from devices with PL, compared to ~ 11 mW of peak emission power observed from reference devices. This was expected due to the lower duty cycle of the PLs and the higher waveguide losses used in the design. Increasing the grating duty cycle could increase the emission power but would reduce the coupling in the PL. The devices with PLs also exhibited a lower maximum operating temperature for similar reasons. The maximum operating temperature in the devices with PLs were in the range of 45–65 K, lower than the ~ 85 K operation from reference devices.

The threshold current density also exhibited an increase due to the increased waveguide losses. The LIV shown in Figure 3.19 (a) was acquired using the high current mode of the pulse generator, which resulted in oscillations in current pulses. These oscillations can reach the lasing threshold for a fraction of the pulse duration even though the steady state current is below the lasing threshold. This manifests as a low power emission in the LIV characteristics, as is observed in between ~ 170 – 340 A/cm² (emission power < 0.2 mW) in Figure 3.19 (a). Hence, the real threshold current density may be an underestimation by studying Figure 3.19 (a). Instead, threshold current observed from a different device (device 3A) is presented in Figure 3.19 (b), where the pulse generator was driven in low current mode. A comparison with the threshold current observed in reference devices

[Figure 3.12 (b)], would reveal the increase in threshold current in devices with PLs. This corresponds well with the reduction in emission power and operating temperature.

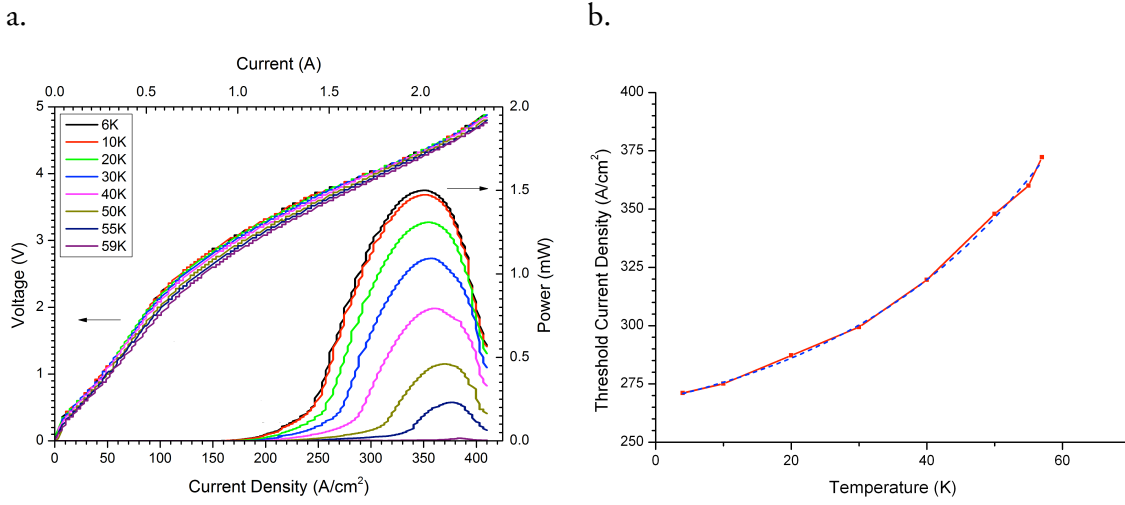


Figure 3.19: (a) LIV characteristics from the device 3H obtained at different heat sink temperatures. (b) Threshold current density from device 3A plotted as a function of heat sink temperature.

3.5 Summary

Single mode emission from THz QCLs with lithographically fabricated PLs was investigated in this study. This technique allowed easier fabrication compared to post-packaging etching of PL gratings. The effective refractive mode index at the metallised and the unmetallised PL sections were computed using finite element modelling. The stopband behaviour of PLs were modelled using the coupled mode theory. A series of PL gratings were designed using established analytical techniques. The bandwidth of the stopband in the designed PLs were calculated to be ~ 90 GHz with emission favoured at the edge of the stopband.

THz QCLs were fabricated with single metal waveguides. EBL was used to deposit PL gratings on to a central section of the ridge waveguide. The top n -doped contact layer in the central section was etched away using wet chemical etchants. The grating features were offset by about ~ 10 – 20 nm from the designed dimensions due to minor aberration in beam focussing.

Single mode emission was observed in all devices, with emission at the edge of the predicted stopband. Emission was also observed away from stopband edge by careful selection of Bragg frequency with respect to gain bandwidth of active region design. Stopband

was experimentally determined to be around ~86–89 GHz and agreed well to the simulated value.

The fabricated PLs with a low grating duty cycle increased the waveguide losses due to a lower confinement of radiation in the gain medium. This degraded device parameters such as the threshold current density, the emitted power and the operating temperature. The degradation in device performance can be improved by using PLs with higher duty cycles.

An understanding of the operation of THz QCLs with PLs led to a series of experiments investigating frequency tunability from such devices by controlling depletion of carriers in the cavity, and is discussed in greater detail in the following chapter.

Chapter 4

Three–section THz QCLs with electrically-controlled photonic lattices

4.1 Introduction

Single mode (SM) emission from terahertz (THz) quantum cascade lasers (QCLs) using a one-dimensional photonic lattice (PL) has been described in the previous chapter. SM emission from THz QCLs is desired for a plethora of applications like atmospheric observation and self-mixing sensing, as discussed in the previous chapter. However, *frequency tunable* THz QCLs with stable SM emission are similarly highly desirable for a range of applications, including gas spectroscopy [4] and spectroscopic imaging [155,156]. Such tunable QCLs would also find application in sensing techniques like self-mixing interferometry [157,158].

Continuous frequency tunable optical lasers have been demonstrated with distributed feedback reflectors (DBRs) [159–162]. These lasers feature multiple cavity sections with a DBR at the rear of the cavity and a gain section at the front. A phase matching section is incorporated between the DBR and gain sections, which enables phase matching between the two sections [106]. Frequency tuning in these lasers is obtained by varying the refractive index at the phase matching and DBR sections, which is usually achieved by varying

the current at these sections. The optical DBR lasers have been further modified to incorporate sampled grating DBRs (SG-DBRs) at both ends of the laser cavity [163–166]. The SG-DBRs have a spatial square grating which is convoluted with the standard DBR design. The SG-DBR gratings at both ends are engineered such that the reflectivity of the DBR sections are closely spaced and are aligned at a particular frequency. Frequency tuning is achieved by varying the current at the SG-DBR and phase matching sections. Frequency tunable mid-IR QCLs with SG-DBRs have been recently demonstrated [110,167].

These multiple-cavity lasers can also feature additional cavity sections like semiconductor optical amplifier, or electro-absorption (EA) or Mach-Zehnder modulators. A schematic diagram of such a multiple cavity laser is shown in Figure 4.1. The tuning mechanism in these lasers follows discrete Vernier selection. Yet another technique of achieving frequency tuning in optical lasers has been demonstrated by using quantum confined stark effect [168]. In this technique, a reverse bias is applied to change the refractive index by shifting excitonic absorption peaks.

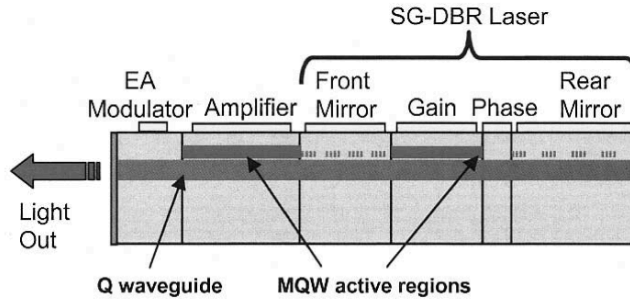


Figure 4.1: Schematic diagram of a single-chip optical laser with SG-DBRs on either side of gain section. Phase between the SG-DBRs and the gain section is controlled through a phase matching section. A semiconductor optical amplifier and an EA modulator are integrated in the chip for amplification and modulation of the emitted radiation. Light is collected from the direction marked with an arrow. Figure taken from ref. [165].

Frequency tunable semiconductor optical lasers or mid-IR QCLs operate by varying temperature dependent material refractive index. However, the material refractive index also depends on the frequency and at THz frequencies the change in material refractive index with temperature is two orders of magnitude order lower than in near-IR frequencies [169]. Moreover, the cryogenic operation of THz QCLs further limits the change in refractive index with temperature. Due to the inherent limitations of THz QCLs, wide

band frequency tunable THz QCLs with temperature dependent tuning have not yet been demonstrated.

The following section describes the various techniques that have been adopted to obtain frequency tunable THz QCLs.

4.1.1 Frequency tunable THz QCLs

Frequency tunability in THz QCLs has been demonstrated using different techniques including external coupled cavities [170–172], by changing growth parameters of active region designs [84,86,87], deposition of exotic dielectric layers [173] and aperiodic photonic lattices [174,175]. Temperature tuning of a few gigahertz has been observed from THz QCLs with DFB grating [169].

In THz QCLs with external cavity mirrors, tunability is controlled through variation of the distance between the facet of the device and an external mirror. Thus, frequency control is achieved through a mechanical process of controlling the optical path length. This arrangement requires suppression of laser feedback from the end facet, and hence requires an anti-reflection coating at the facet facing the external mirror. An anti-reflection coating of SiO_2 was used in ref. [170]. The long wavelength (of the order of $\sim 100 \mu\text{m}$) of electromagnetic radiation in the THz range dictates a thick layer of anti-reflection coating to effectively suppress laser oscillations. Fabrication of thick anti-reflection coating has been a challenge, and is a major limitation of this technique.

Another method to obtain frequency tunability through an external cavity involves using an external grating to select longitudinal modes of the QCL [171]. In this method, frequency tuning is controlled through variation of the angle of the grating. Additionally, instead of depositing thick anti-reflection coating, a hemispherical Si lens was used to facilitate collimation of the beam and to act as an anti-reflection layer. In yet another demonstration of a frequency tunable THz QCL, a QCL with a second order DFB grating was coupled to a micro-cavity [172]. In this arrangement, vertical emission from second-order DFB gratings was used to couple a microcavity placed on top the DFB grating. Frequency tunability was realised by varying the path between the DFB laser and the external mirror, and the resulting detuning of the external cavity with respect to the DFB resonator. A major constraint in external-mirror-based tuning schemes is the mechanical process to control

the path between laser aperture and the external mirror, which requires external optics and a precision motion controller. An electrically-controlled frequency tuning mechanism would make the system compact and easy to operate.

A variation of emission frequency in THz QCL has been studied systematically by varying the molecular beam epitaxial (MBE) growth parameters. In these devices, frequency emission is not controlled by the variation of refractive index of the waveguide, but by variation of the semiconductor heterostructure itself, which formed the active region. In one such demonstration (ref. [86]), the thickness of the GaAs/AlGaAs heterostructure layers in the active region was systematically varied in different wafer samples to achieve frequency tuning of 100–35 GHz. However, it is important to note that frequency tunability is not evident from a single device, rather a predictable shift was observed in different wafers grown with different active region variations. Devices from different samples with different growth parameters can be arranged into an array with an electrical control circuit to drive only one laser ridge at a time, as has been demonstrated in mid-IR DFB QCLs in ref. [176].

The MBE growth was further improved in another design, where two different active region heterostructures were grown on the same wafer [84]. Such an integration of different active region designs into the same heterostructure growth has been demonstrated previously in mid-IR QCLs [177]. The two active regions in ref. [84] were separated by a spacer layer, which addressed the issue of electric-field domain formations in the active material [178]. A two-colour emission was observed from this laser, with emission frequency controlled by drive current. The precise control of lasing in only one the stacks permitted a controlled two-colour emission from this device. This paradigm was developed further, and in the design reported in ref. [87] the deposition rate of Ga was reduced monotonically during the MBE growth of the wafer. This resulted in a heterostructure with 23 different lasing sections. Successive emission over a range of over 300 GHz was observed as the drive current to the device was varied. It is worth noting here, that only a few of all the stacked active region designs allow optical transition of electrons in the cascade depending on the applied bias field. Thus frequency tunability observed in these devices is not governed by variation of refractive index in the cavity.

In tunable THz QCLs discussed so far, emission was controlled either through variation of mechanical mirrors, or by selective lasing of active region heterostructures. None of these designs aimed to vary the refractive index of the waveguide. However, a recent demonstration of a tunable THz QCL has achieved variation of the refractive index of the waveguide by gas condensation and successive deposition of dielectric layers [173]. In this device, a THz QCL wire laser with a laterally etched third-order DFB grating was used. The QCL ridge was deposited with dielectric layers iteratively to vary the refractive index. In another scheme, nitrogen gas was condensed on the DFB cavity. These approaches introduced variations to the refractive index of the cavity that shifted the Bragg condition. A continuous tuning of 25 GHz was observed in the reported device. However, a major limitation of this technique is the slow condensation/evaporation cycle and the irreversible nature of the dielectric deposition.

A truly electrically-controlled frequency tunable THz QCL has been demonstrated using an aperiodic photonic lattice (APL) [174,175]. In this design an APL was used to provide optical feedback as well as act as a filter, analogous to DBR gratings in optical lasers. The combined effect of feedback from this photonic lattice (PL), along with a phase matching mechanism achieved through variation of the drive current, resulted in discrete mode hopping over 160 GHz. The operation of this device follows the tuning mechanism of SG-DBR optical lasers, but rather than using multiple-cavity sections of optical lasers, this device achieves similar results through an optimised asymmetrically-spaced PL. Indeed, the shorter wavelength of electromagnetic radiation in the optical and mid-IR range results in cavity lengths that are a few hundreds of microns long. However, the long wavelength of the THz range requires the overall cavity length of a standard SG-DBR laser to be a few centimetres. The longer cavity sections and the resultant thermal inefficiency could be one of the reasons for the failure to adopt multiple-section SG-DBRs in THz QCLs as yet.

This study explores the possibility of obtaining electrically-controlled frequency tunability in THz QCLs using multi-section cavities with an integrated PL. Perturbation of the refractive index of the PL is attempted by applying a reverse bias and depleting carriers under the metallised section of the PL. Since THz QCLs are driven in reverse bias, the polarity of the electrical connection to the PL is identical to a standard QCL connection.

The following section briefly describes the device design and the operating principle.

4.2 Device design and operating principle

A three-section THz QCL with a central ‘PL section’ and two ‘outer’ sections at either end of the PL was designed. The three sections were electrically isolated by etching away the doped contact epilayer at the central section. The PL sections were fabricated with additional bond pads and side rails to facilitate electrical connection to metallised sections of the PL. A schematic illustration of the proposed device is presented in Figure 4.2 (a, b).

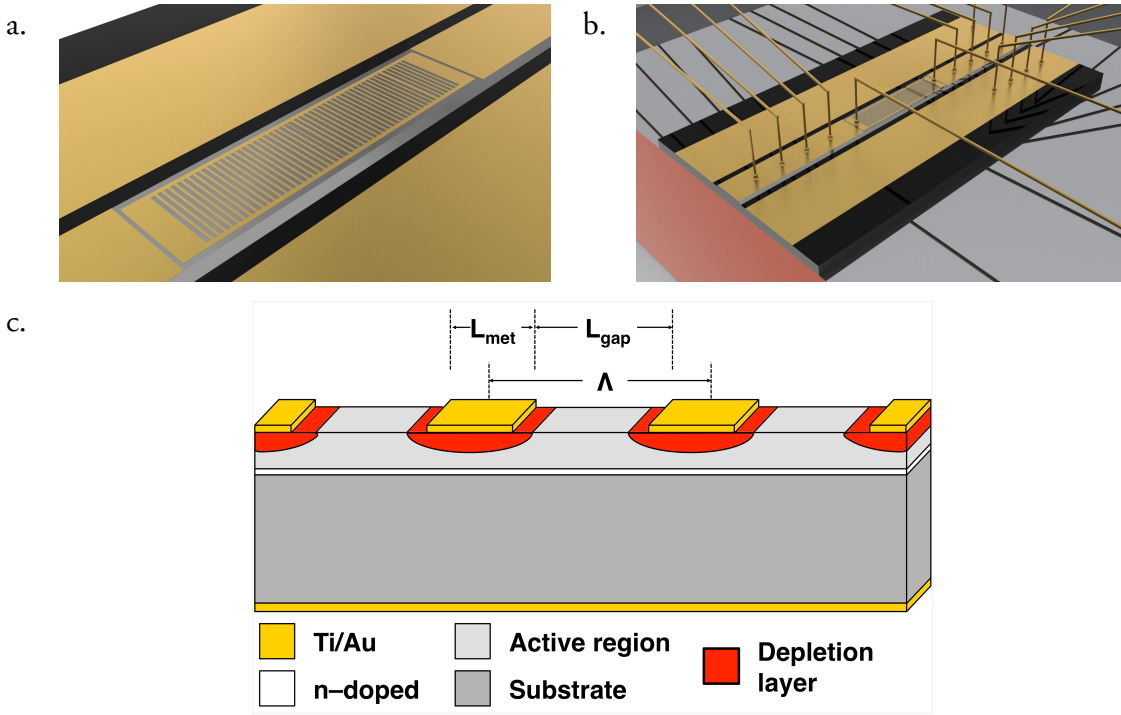


Figure 4.2: (a) Illustration of a THz QCL with PL with bond pads and side rail. All grating sites are connected to two bond pads through the side rails. (b) Wire bonding of the device. The PLs are connected with bond wires that enable application of independent bias to the PL. (c) Schematic diagram of depletion layer formed under the metallised section of the grating.

In this study, the effect of variation of carrier concentration under PL gratings on spectral behaviour was investigated. The outer two segments served as normal single plasmon QCL waveguides and the central section had PL deposited directly on to the active material after removal of the top n -doped semiconductor used for electrical contact. The Au cladding metal forms a Schottky junction at the metal–active region interface and results in a depletion layer devoid of free carriers [135]. The width of this depletion layer was controlled by applying a reverse bias to the PL section. A schematic diagram of the depletion layer under the PL metallised section is shown in Figure 4.2 (c). The resultant change

in the carrier concentration under the metallised section and the corresponding shift in refractive index were modelled using a bulk semiconductor Drude model.

Devices were fabricated with the three-section design but with different PL grating pitch. Initially, the devices were characterised to study their electrical behaviour. A circuit model describing the electrical behaviour observed from fabricated devices was also developed. The devices were subsequently characterised to analyse spectral variation.

The following section describes the variation of refractive index in the PL section with carrier concentration. The depletion region formed at the metal–semiconductor interface is also discussed in section 4.3.2.

4.3 Tuning refractive index by changing carrier concentration

SM emission from THz QCLs using a one-dimensional PL was described in Chapter 3. It was observed that the PL introduced a stopband centred at a characteristic Bragg frequency and emission was observed at the edge of the stopband. The Bragg frequency depended on the effective refractive index and grating pitch of the PL. A frequency shift can, therefore, be achieved by variation of the refractive index of the active material. In this study the refractive index of the PL was varied through a variation of the carrier concentration under the PL metallised section.

4.3.1 Variation of refractive index with doping

A Drude model from the program OWG was used to estimate the variation of the refractive index of the QCL active material as a function of carrier concentration [Figure 4.3 (a)]. OWG is included in the package QCLSIM, a software developed at the University of Leeds to model THz QCL active regions and waveguides. For simplicity the active material was modelled as bulk GaAs. THz QCL active regions include *n*-doped heterostructure layers. To estimate the doping level for the bulk GaAs used in the model, the average doping of the active region [Table 3.2] was calculated. The average doping of the active region design used for this study was calculated to be $7.5 \times 10^{15} \text{ cm}^{-3}$, and is indicated by an arrow in Figure 4.3 (a). It is observed that the refractive index decreases non-linearly as the carrier

concentration is varied between 10^{16} – 10^{17} cm^{-3} and increases monotonically as it is increased above 10^{17} cm^{-3} . The Bragg frequency of a PL with $\Lambda = 15.25$ μm is also calculated as a function of carrier concentration [using the expression eq. (3.1), described in Chapter 3] and plotted in Figure 4.3 (b).

Therefore, the refractive index can be significantly modified if a QCL active region is designed with higher carrier concentration. However, the free carrier losses in the waveguide also increase with higher doping. Therefore, the variation in refractive index in the non-linear region between 10^{15} – 2×10^{16} cm^{-3} deemed as an ideal trade off [Figure 4.3 (b)]. A similar change in the carrier concentration can be introduced by applying a reverse bias voltage to the Schottky junction formed at the metal-semiconductor interface of the PL section. A strong shift in refractive index can be achieved if the carrier concentration lies in this non-linear region range 10^{15} – 2×10^{16} cm^{-3} [Figure 4.3 (b)].

The following section describes the modelling of the PL section as a metal-semiconductor junction interface.

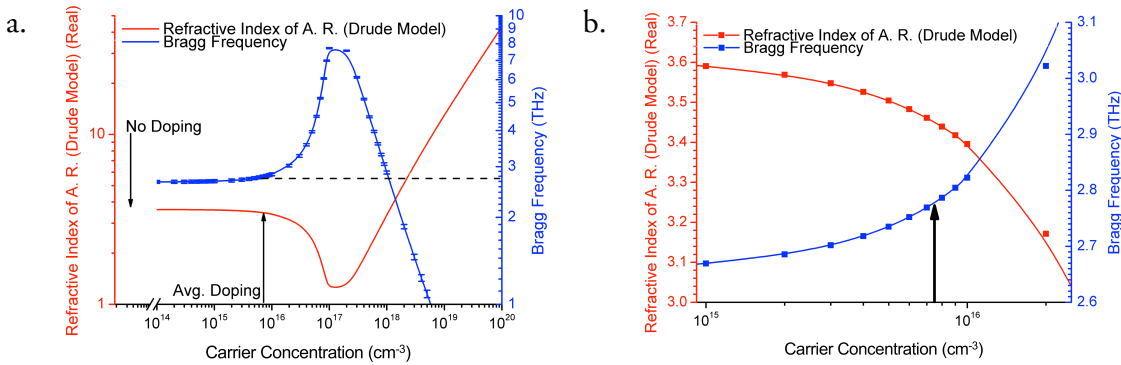


Figure 4.3: Refractive index (red) and the corresponding Bragg frequency (blue) for $\Lambda = 15.25$ μm as a function of carrier concentration of active material calculated using Drude model. QCL active material simulated as bulk $\text{Al}_{0.15}\text{Ga}_{0.85}\text{As}$. Average doping of QCL material is indicated with an arrow. Doping varied between (a) 10^{14} – 10^{20} cm^{-3} (b) 9.5×10^{15} – 2.5×10^{16} cm^{-3} .

4.3.2 Depletion of carrier at PL grating

Since the PL is deposited directly on top of the active region, it is modelled as a metal-semiconductor junction. A depletion layer devoid of carriers is formed at the metal-semiconductor interface whose width can be increased on application of a reverse bias. The

width of the depletion layer is calculated from the energy band diagram of a metal–semiconductor interface. Since some of the active region layers are doped with n -type dopants, the QCL active region was modelled as a n -doped semiconductor.

A metal–semiconductor interface acts like a Schottky junction when the work function of the semiconductor (ϕ_s) is smaller than the work function of the metal (ϕ_m) [179]. The energy band diagram of a metal–semiconductor interface is shown in Figure 4.4. The energy bands in an isolated metal and semiconductor are shown in Figure 4.4 (a), in which (χ_s) is the electron affinity of the semiconductor. The energy level of the conduction band, valence band and the Fermi level are indicated by E_C , E_V and E_F respectively. The vacuum energy level is used as a reference.

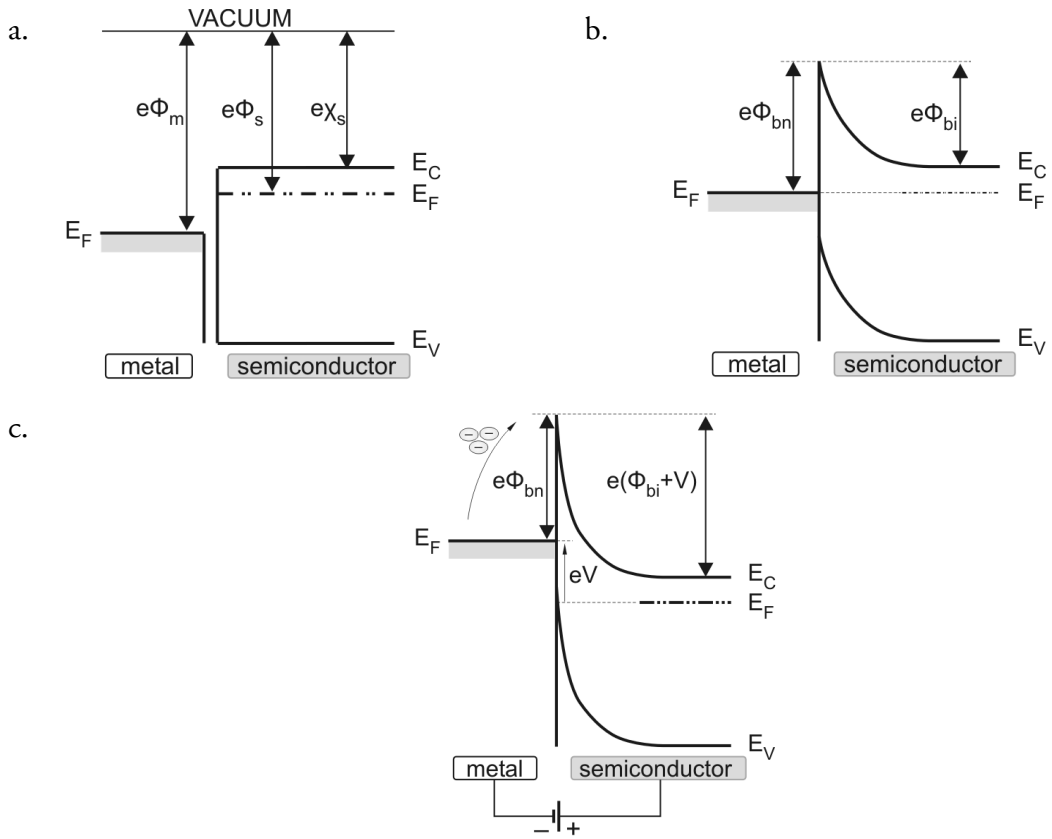


Figure 4.4: Energy band diagram of: (a) metal and semiconductor. Metal–semiconductor interface at different conditions: (b) equilibrium and (c) with a reverse bias. Image adapted from [180].

In a metal–semiconductor junction interface at thermal equilibrium [Figure 4.4 (b)], the Fermi levels in the metal and semiconductor are at the same energy. Electrons from the semiconductor flow into the lower energy levels in the metal resulting in a positively charged donor atoms at the interface, forming a space charge layer. An electron moving

from the semiconductor to the metal has to cross this potential barrier, which is defined as [179]

$$\phi_{bn} = \phi_m - \chi \quad (4.1)$$

The work function of Au is 5.1 eV and the electron affinity of n -GaAs is 4.07 eV. Thus, the barrier height is calculated as $\phi_{bn} = 1.03$ eV. However, experimentally the value of ϕ_{bn} has been determined to be 0.92 eV for a Schottky junction formed at the interface of Au and GaAs, and this value was used for the model [135].

The width of the depletion layer is calculated from the built-in potential (ϕ_{bi}) across the Schottky junction, which is given by [179]

$$\phi_{bi} = \phi_{bn} - V_t \ln\left(\frac{N_c}{N_d}\right) \quad (4.2)$$

where N_c , N_d are the effective density of states in conduction band and donor doping density respectively; and V_t is the thermal voltage given as:

$$V_t = \frac{kT}{e} \quad (4.3)$$

where k , T and e are Boltzmann's constant, temperature and electronic charge respectively.

The effective density of states for electrons in the conduction band (N_c) is given by the following expression:

$$N_c = 2 \left[\frac{2\pi m_e^* kT}{h^2} \right]^{3/2} \quad (4.4)$$

where m_e^* is the effective mass of electron and h is Plank's constant.

The width of depletion layer (w_d) formed at the metal–semiconductor junction interface on application of a reverse bias [Figure 4.4 (c)] is given as [179]:

$$w_d = \sqrt{\frac{2\varepsilon_s(\phi_{bi} + V)}{qN_d}} \quad (4.5)$$

where V is the applied reverse bias and ε_s is the permittivity of the semiconductor.

Therefore, from eq. (4.5) it can be inferred that increasing the reverse bias would increase the width of the depletion layer. Similarly, in a three-section QCL device, applica-

tion of a reverse bias to the PL section would, thus, increase the width of this depletion layer. This would result in a change in the distribution of free-carriers under the PL section.

The depletion layer formed at the metal–semiconductor junction can also be modelled as a capacitor, whose capacitance is given as [179]:

$$C_d = \frac{\epsilon_s A}{w_d} \quad (4.6)$$

where A is the area of the Schottky junction. The effect of the capacitance in the Schottky junction under an applied reverse bias was also considered during the calculation of carrier density under the PL metallised section.

In the designed three-section THz QCL, although the PL section is deposited on an electrically isolated central section, the PL section is still connected to the outer sections through a high impedance path. This is because all three sections still share the same active region heterostructure, and this might result in a ‘*cross-talk*’ voltage between the sections. Under such circumstances, the reverse voltage at the PL section would depend not only on the reverse bias voltage applied to the PL section, but also on the bias applied to the outer sections. The depletion region formed in a real QCL device is discussed in greater detail in section 4.6.1.2 where an electrical model is established that describes the electrical behaviour of the three-section QCLs with electrically-controlled PLs.

The following section describes the fabrication of THz QCLs with this modified PL design.

4.4 Fabrication

THz QCLs were fabricated from the same wafer ‘L701’ (with a bound-to-continuum active region reported in ref. [67]) used for the study of PLs, following identical processing steps as described in section 3.3.

The PL design, described in the Chapter 3 was modified to add two contact pads at either end of the PL to enable wire bonding. All PL gratings were connected to both of the contact pads through two side rails running at the edge of ridge to enable electrical connection throughout the PL region [Figure 4.5 (a)]. The PL was deposited on an electrically isolated central section, with two identical single plasmon waveguide sections (outer sections)

on either side of the PL. The outer sections were electrically isolated from the central PL section and experimental devices had high resistance of 20–23 M Ω between the outer sections and the PL section. An Optical microscopy of a fabricated device is shown in Figure 4.5 (b).

Following the deposition of the PL, substrate was thinned and devices were cleaved to form mirror facets from the III–V material crystal, as described in section 2.2.9. Due to the manual cleaving process used in this study, the cavity lengths of the two outer sections were not identical. Cleaved samples were In soldered onto Cu blocks and were wire bonded. The electrically isolated PL was wire bonded separately to enable independent bias to the PL section. Scanning electron microscopy (SEM) of a device after wire bonding is shown in Figure 4.5 (c). A list of fabricated devices is tabulated in Table 4.1.

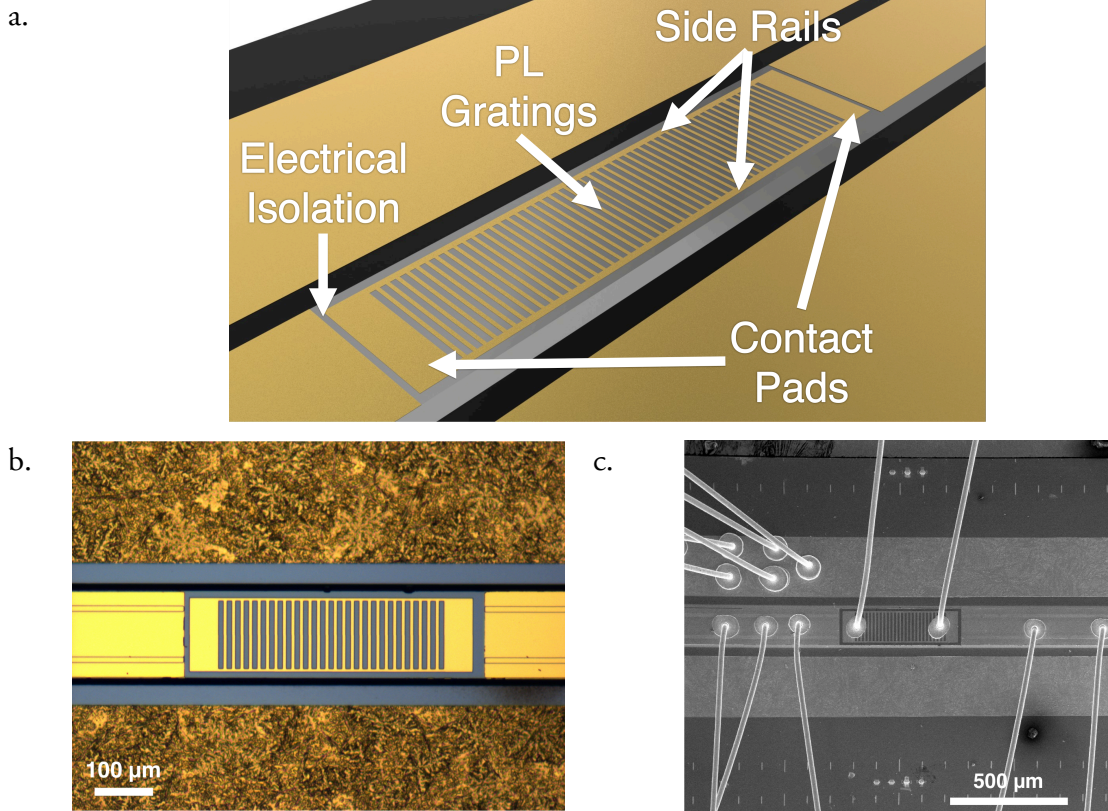


Figure 4.5: (a) Illustration of a PL with contact pads and side rail. (b) Optical microscopy of a fabricated device. PL and outer cavity sections are illustrated in the image. (b) SEM image of a device after wire bonding. Separate wire bonds were applied to the PL section.

Table 4.1: List of fabricated THz QCLs electrically-controlled PLs.

Device Number	Unique Device ID	f_{BR} (THz)	Λ (μm)	L_{met} (μm)	L_{gap} (μm)
4A	L701-S14-D1	2.760	15.38	6.14	9.24
4B	L701-S16-D3	2.705	15.68	6.26	9.42
4C	L701-S14-D2	2.840	14.95	5.98	8.97
4D	L701-S16-D1	2.720	15.61	6.23	9.38
4E	L701-S16-D2	2.685	15.80	6.32	9.48

4.5 Experimental setup

The experimental setup used for the characterisation of THz QCLs with electrically-controlled PL differed slightly from the setup used for standard QCLs (section 2.3.1). Two pulse generators were used in this study to drive the outer sections and the central PL section independently. Current pulse trains with a negative polarity were applied to the outer sections enabling lasing, while the central PL section was biased with voltage pulses with a similar negative polarity, time synchronised with the current pulses. The aim of this setup was to cause lasing only at the outer waveguide sections whilst keeping the central section as an absorber, and to vary the depletion layer formed under the PL because of the reverse bias. Devices were characterised on a closed cycle cryostat and cooled with liquid He, as described in section 2.3.1. The outer sections were biased with 10 kHz current pulses gated with a 165 Hz pulse matched to the responsivity of the detector. The PL was biased with a similar 10 kHz gated pulse train synchronised to the current pulses.

In the first instance, the devices were measured to obtain light-current-voltage (LIV) characteristics without any bias applied to the PL section, [the ‘*floating gate*’ configuration as shown in Figure 4.6 (a)], and then with varying bias voltages, as shown in Figure 4.6 (b). Although the PL was electrically isolated from the outer sections, the three separate sections were deposited on moderately doped GaAs/AlGaAs heterostructure active material. Hence, any bias applied to the outer sections would result in a field forming across the central PL section (cross-talk). The data acquisition setup used to obtain the LIV characteristics was modified to read the voltage and current at the PL as the drive current supplied to the outer sections were varied. Spectra were acquired using the same Bruker Optics Fourier transform infra-Red (FTIR) spectrometer, as described in section 2.3.1. Spectra were acquired

for different drive currents supplied to the outer sections, with a floating gate and different reverse bias voltages applied to the PL.

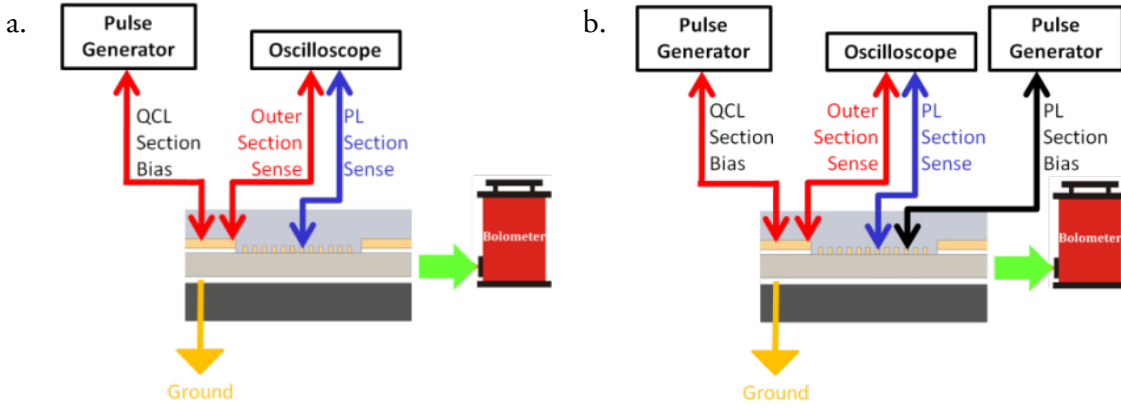


Figure 4.6: Schematic diagram of the experimental setup to obtain LIV data with: (a) a floating PL section (no applied bias on the PL section), (b) a reverse bias applied to the PL section. Both pulse generators are gated to a square wave function generator (not shown).

4.6 Experimental results

Initially, the devices were measured to obtain their LIV characteristics, and to study the electrical behaviour of the three-section device. An electrical model was developed to understand the electrical properties of the device. Spectra were acquired after the electrical characterisation.

Data obtained from device 4A is used to analyse the electrical behaviour of such devices and is discussed next. A similar electrical behaviour was observed in all other fabricated devices.

4.6.1 Electrical characterisation

In the first instance, devices were characterised to observe their electrical behaviour with a floating PL section, and were subsequently characterised with a bias applied to the PL section. The cross-talk between the PL and outer sections was investigated in the floating PL configuration. The extent of carrier depletion under the PL gratings was estimated with an applied bias to the PL section.

4.6.1.1 Floating PL section

The LIV obtained without any bias applied to the PL section is shown in Figure 4.7. The cross-talk voltage measured across the central PL section is also plotted (in blue) for different current applied to the outer sections. The voltage measured at the PL section exhibited a characteristic offset, observed in all devices, and only manifested after 0.8–1 V was applied to the outer sections. The maximum-recorded cross-talk voltage in the PL was around 2 V for the maximum drive current in the outer sections.

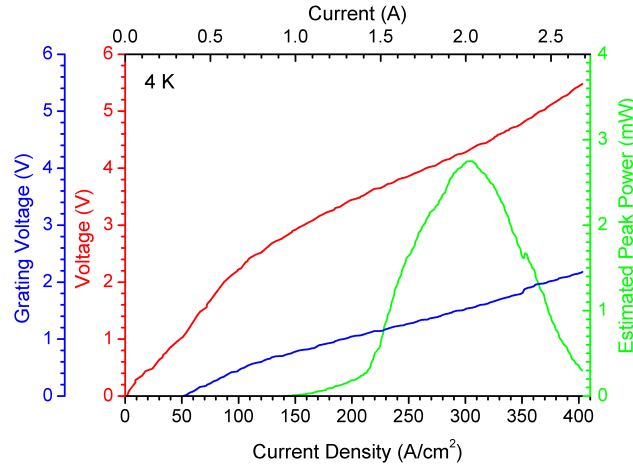


Figure 4.7: LIV obtained from device 4A, without any bias applied to the PL section. Voltage across the outer sections (red) and the PL section (blue), and the THz output power (green) are plotted as a function of current across the outer sections.

To explain this electrical behaviour, a circuit representation of the device cross-section was designed [Figure 4.8 (a)]. The major components of the circuit are described as following:

- Negative differential resistance at the outer sections

A low-resistance ($2\text{--}4\ \Omega$) negative-differential resistor was used to simulate the negative differential resistance across the QCL active region in the outer sections. The value of this resistor was varied as a function of the current in the outer sections. Experimental IV characteristics obtained from the device 4A were used to obtain this differential resistance as a function of the bias voltage.

- High resistance at the PL contacts

A large resistance ($23\ \text{M}\Omega$) was used to simulate the PL contact impedance. This resistance value was obtained from DC measurements and is due to the removal of

the n -doped contact layer under the PL section. A constant value of 23 M Ω for the high impedance was used in the circuit as a small signal approximation, although its value changed according to the applied bias on the outer sections. However, this resulted in only a minor disagreement with experimentally observed characteristics and was ignored.

- PL Schottky junction

The Schottky junction formed at Ti/Au and active region interface of the PL section was modelled with a Schottky diode.

- Channel potential barrier

The absence of doped semiconductor at the PL section formed a potential barrier at the junction between the PL section and the outer sections (referred to as the '*channel*'). The characteristic offset observed at the voltage in the PL section [Figure 4.7] was due to this barrier and was represented by a diode in the circuit.

- Channel high resistance

A second large resistance of 23 M Ω was used to represent the impedance of the channel regions. This high resistance was due to the absence of n -doped contact layer in the PL section.

- Device capacitance

Capacitance of the device was calculated as 8 pF from the device geometry using a simple parallel-plate capacitor model. The capacitance was also included in the model to provide an accurate transient response.

- Circuit sense resistance at the PL and the outer sections

The experimental setup included a 50 Ω '*matching*' resistor in the sense circuit used to read voltage at device terminals. Two 50 Ω resistors used in the sense circuits to read the voltage at the PL section and the outer sections were also included in the circuit model.

The circuit was simulated using a SPICE based circuit simulator Volta® on Apple Macintosh OS X. Initially, the outer sections were driven with current pulses and the PL section was left floating, in accordance with the experimental setup. The outer sections in the simulated circuit were driven with current pulses at 10 kHz with a 2% duty cycle. The current pulses were modulated with a 165 Hz square wave. This arrangement corresponded with the current pulses in the experimental setup. The cross-talk voltage at the PL section

was measured for various biases applied to the outer sections. The results from the simulations, plotted in Figure 4.8 (b), agree well with the experimentally observed IV.

The RC node in the circuit resulted in a characteristic decay observed at the PL section when the gate signal was switched off. The experimentally observed RC decay is shown in Figure 4.8 (c). A similar RC decay was observed in the simulated circuit [Figure 4.8 (d)], validating the circuit description of the device cross-section. The value of the capacitance was calculated from the RC time constant of the experimentally observed decay (0.36 ms) and was calculated to be ~ 8 pF. This experimentally measured capacitance agrees perfectly with the parallel plate capacitance calculated from the device dimensions.

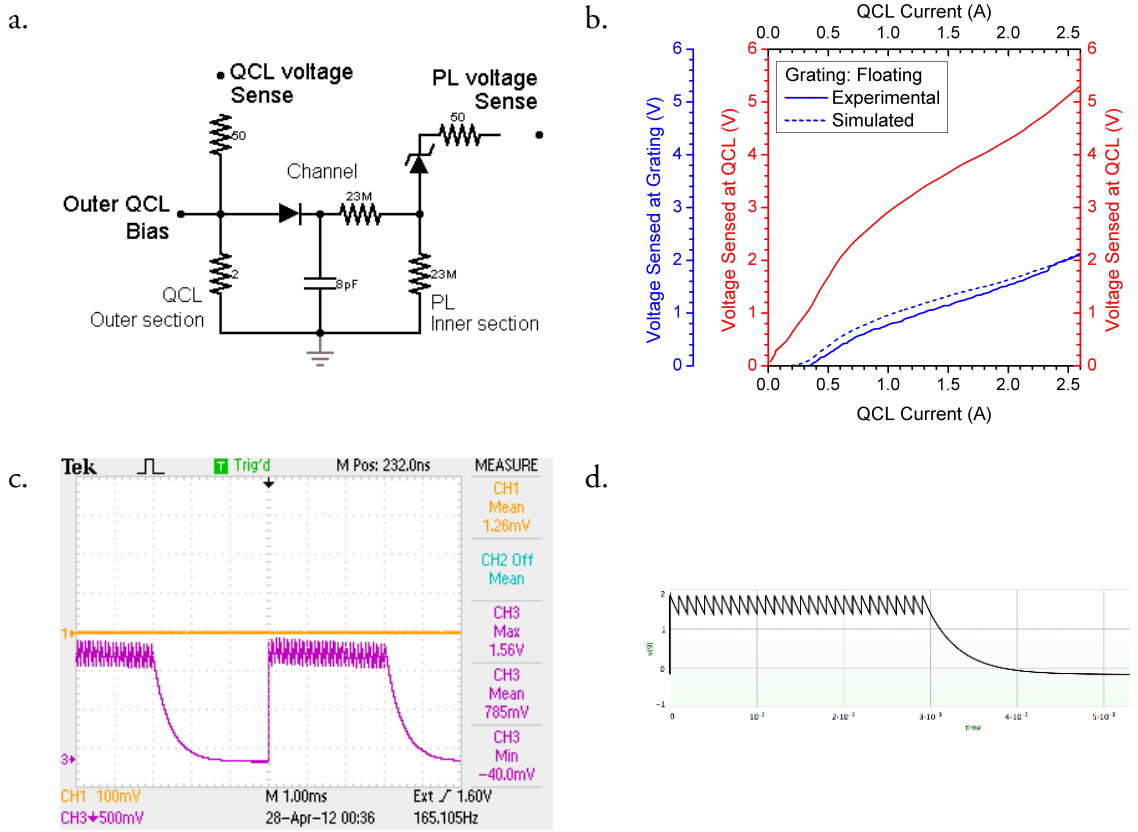


Figure 4.8: (a) Equivalent circuit model describing the observed electrical characteristics of three-section QCL with PL. (b) Cross-talk voltage in PL (blue) as the current through the outer sections is varied. Both experimental (solid) and simulated (dashed) cross-talk voltage are plotted. (c) Experimental and (d) simulated capacitive decay observed at the PL section when the bias at the outer sections is switched off. All experimental data are obtained from device 4A.

The simulated results obtained from the circuit model agree excellently with the observed electrical characteristics. Following the characterisation with a floating PL section,

the devices were experimentally characterised with a bias applied to the PL section. The following section describes the observed electrical behaviour and compares them with the simulated electrical characteristics obtained from the circuit model.

4.6.1.2 PL section with a bias

Following the characterisation with a floating PL section, LIV was acquired with a bias applied to the PL section. Device parameters like threshold current density and output optical power output were unaffected by the bias applied to the PL section, as can be observed from Figure 4.9.

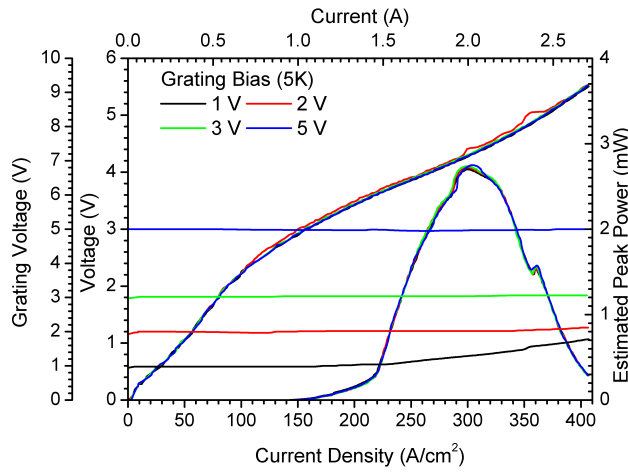


Figure 4.9: LIV obtained from device 4A, with a bias applied to the PL section. Device parameters, like threshold current density and output power remain unaffected by the applied bias on the PL section. Voltage measured at the PL section is also plotted.

The voltage at the PL section is also plotted as a function of the current at the outer sections, as shown in Figure 4.9. It was observed that the cross-talk voltage from the outer sections affected the voltage at the PL section [Figure 4.9]. This was especially evident when the applied bias at the PL section was lower than the cross-talk field [Figure 4.9, when the current at the outer sections is greater than 1.5 A]. The net voltage measured at the PL grating was a superposition of the bias applied to the PL section and the cross-talk voltage. For example, the voltage sensed at the PL section (with a bias of 1 V) increased with the cross-talk. A similar behaviour is also predicted using the simulated circuit [Figure 4.10].

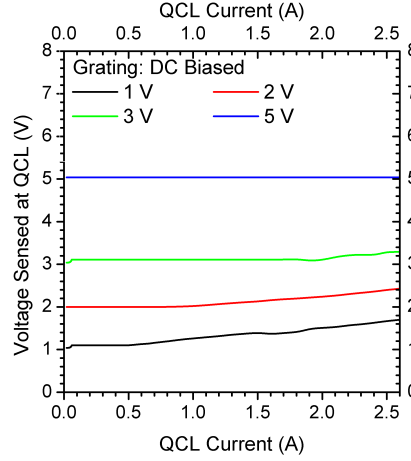


Figure 4.10: Simulated voltage at the PL section as a function of current at the outer sections, with different bias applied to the PL section. The cross-talk from the outer sections increases the voltage at the PL section.

The effect of the cross-talk is particularly significant to calculate the depletion layer formed under the PL metallised sections. The effective bias at the PL-active material interface was calculated from both the applied bias to the PL section as well as the cross-talk from the outer sections. The width of the depletion layer was calculated from eq. (4.5) using this effective bias, and is shown in Figure 4.11 (a). A variation of the depletion region changes the carrier concentration as the carriers are effectively pushed into a smaller volume of the active material. The carrier concentration under the PL metallised section was modelled as two regions – a thin layer depleted of carriers and the remaining active region whose carrier concentration is higher than the intrinsic doped density. The width of the former equalled the width of the depletion layer. The carrier concentration in the latter was calculated from the intrinsic doping of the active region and the reduced volume of the active material due to the depletion layer. The change in the carrier concentration under the PL metallised section is shown in Figure 4.11 (b). The resulting change in refractive index of the active material under the PL metallised section was computed from the Drude model solver, and is shown in Figure 4.11 (c). Based on the intrinsic carrier concentration and the variation of the width of the depletion region, a maximum change in Bragg frequency of around 15–20 GHz was predicted. The effect of the carrier profile on the optical mode was further verified using the finite element modelling (FEM) described in section 3.2.1.1. The stopband in the PL a depletion layer was also simulated and would be briefly described in section 4.6.1.2.1.

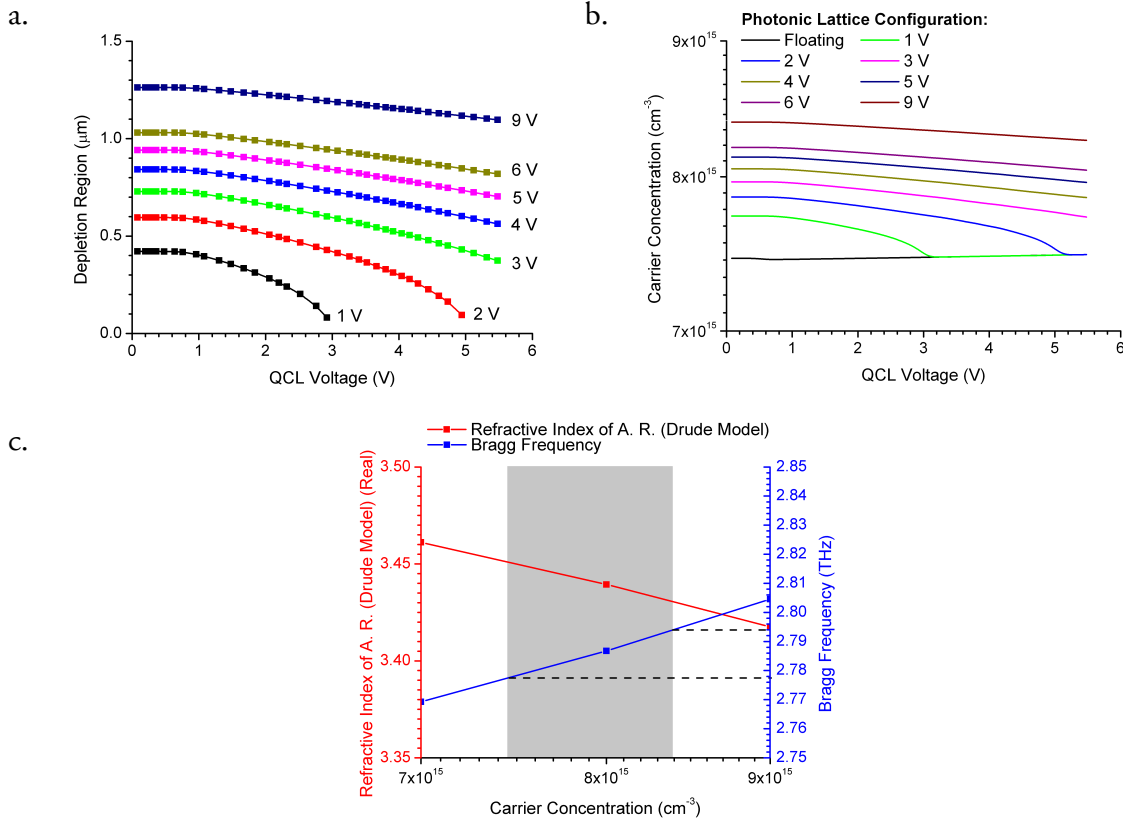


Figure 4.11: (a) Depletion layer formed under the PL metallised section (with different bias at the PL section) as a function of the bias at the outer sections. (b) Change in the carrier concentration is plotted as a function of the bias to the outer sections, for different bias applied to the PL section. (c) Variation of refractive index corresponding to the change in carrier concentration in (b).

The devices were further characterised to analyse the LIV at various heat sink temperatures, as shown in Figure 4.12 (a). In further measurements, device parameters including voltage and current at the outer sections, emission power and current at the PL section, were recorded as a function of bias voltage applied to the PL section [Figure 4.12 (b–d)]. It was observed that negligible current flows through the PL section ($\sim 10 \mu\text{A}$) throughout the operating regime used in this work. As such, there was no optical emission from the PL section and negligible Joule heating in this region. Furthermore, the bias at the PL section had no influence on the emission power from the outer sections.

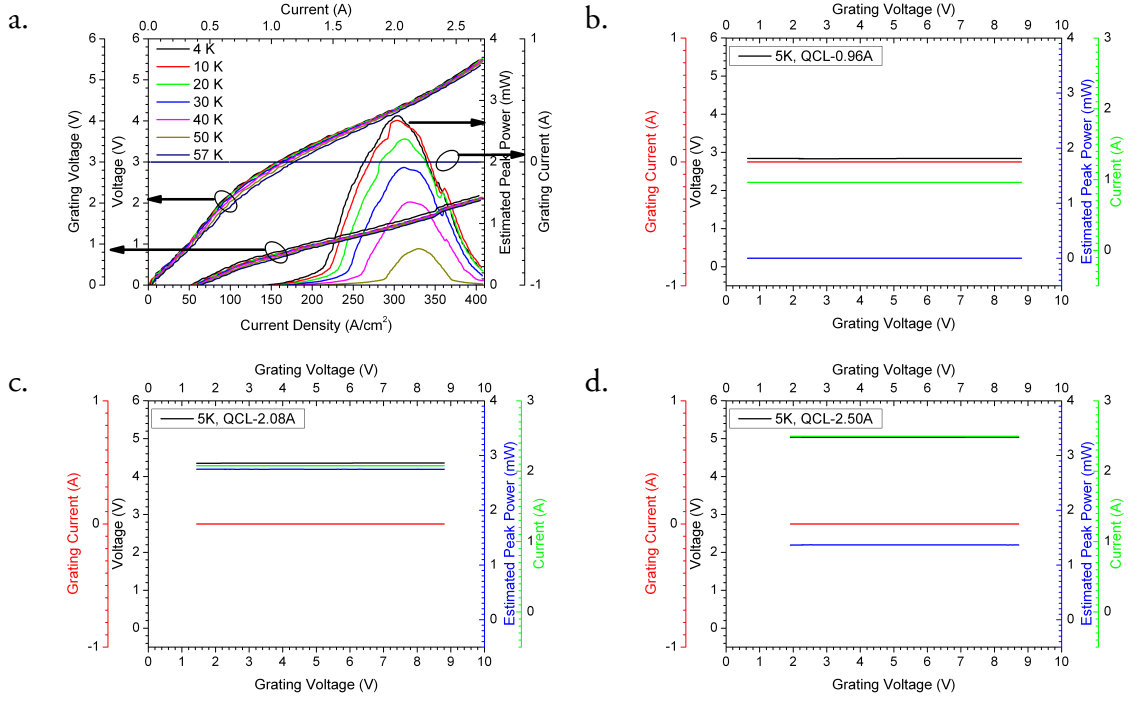


Figure 4.12: (a) LIV with a floating gate (no applied bias on the PL section) recorded at various heat sink temperatures. (b–d) Variation of device parameters – voltage (black), power (blue) and current (green) at the outer sections, and current at the PL section (red) as a function of bias applied to the PL section. Outer sections are biased at (b) threshold, (c) peak power and (d) maximum applied bias. Device parameters are unaffected by the bias applied to the PL section.

4.6.1.2.1 Stopband in the PL with a depletion layer

The FEM technique described in the Chapter 3 was used to compute optical mode in the metallised section of the PL with a depletion layer. The device cross-section was modified to include a depletion layer in the active region and a top cladding interface. The computed optical mode is shown in Figure 4.13. The effective refractive index at the metallised section was computed as $n_{met} = 3.58 - j0.0087$, lower than that without any depletion layer ($n_{met} = 3.62 - j0.0064$), described in section 3.2.1.1. Thus, it can be substantiated from the FEM simulations that a small change in the refractive index at the metallised section is obtained by applying a bias on the PL section.

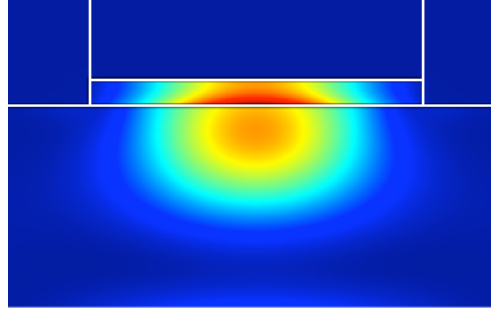


Figure 4.13: Computed optical mode of a PL metallised section with a depletion layer (2.77 THz) using FEM.

The variation in the refractive index with a bias applied to the PL section would also influence the stopband in the PL. The coupled mode theory model, described in section 3.2.2, was used to calculate the stopband for device 4A. It was observed that with PL in a floating gate configuration, a stopband of ~ 90 GHz was observed at $f_{BR} = 2.76$ THz [Figure 4.14 (a)]. However, when the depletion layer was included in the metallised section of the PL, the Bragg frequency shifts by ~ 12 GHz to $f_{BR} = 2.772$ THz [Figure 4.14 (b)]. The bandwidth of the stopband also reduces from $\Delta f_{BR} \approx 90$ GHz to ~ 77 GHz. Therefore, the upper edge of the stopband (i.e. $f_{BR} + \Delta f_{BR}/2$) with a floating PL and with an applied bias on the PL was calculated to be 2.805 THz and 2.8105 THz, respectively. This greatly revises the initial tuning range of ~ 15 – 20 GHz calculated from the Drude model for variation in Bragg frequency only. Instead, a maximum continuous tuning in the range ~ 5 – 6 GHz is predicted when the effect of a reduced bandwidth of the stopband is included in the model.

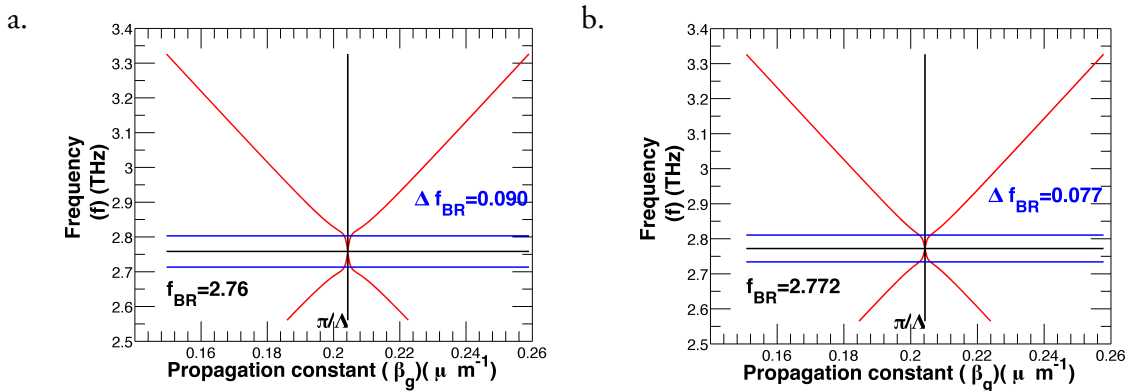


Figure 4.14: Dispersion curve in the PL section. A stopband with bandwidth (Δf_{BR}) is observed centred at the Bragg frequency (f_{BR}). (a) PL with a no applied bias (floating gate), (b) PL with a depletion region formed in the metallised section.

4.6.2 Spectral characterisation

In an exemplar device 4A, SM emission at ~ 2.76 THz was observed with a floating PL section [Figure 4.15 (a)]. Emission was experimentally observed to be at the stopband centre corresponding to the Bragg frequency [Figure 4.15 (b)]. Although none of the devices with PL, described in Chapter 3, lased at the Bragg frequency, such behaviour can be explained with the coupled mode theory. According to this theory, the threshold gain is lower at the Bragg frequency in a periodic structure that has a greater loss (or conversely gain) perturbation [108]. Thus, emission is possible at the centre of stopband in such devices. Following a similar analogy, it was inferred that the PL in device 4A had a higher loss perturbation, which resulted in the emission at the Bragg frequency. However, the possible reason for such behaviour is yet unknown. Following the initial characterisation with a floating PL section, the device was characterised with an applied bias from 2–16 V.

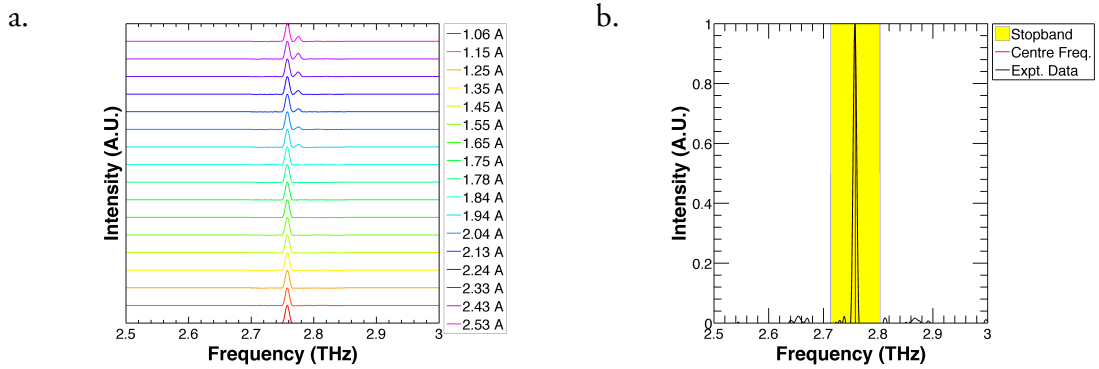


Figure 4.15: (a) Emission spectra from the device 4A obtained with a floating PL section and at a heat sink temperature of 4 K. Spectra are vertically offset and are shown in colour coded for a range of current applied to the outer sections. (b) Emission was observed at the centre of stopband at the Bragg frequency calculated in Figure 4.14 (a).

On application of a bias of 2 V to PL section, an additional higher-frequency mode spaced at ~ 15 GHz was observed in the emission spectrum, with emission observed predominantly at ~ 2.777 THz under high current at the outer sections [Figure 4.16 (a)]. It is worth noting that this higher-frequency mode was observed in the spectra recorded during the floating PL characterisation [Figure 4.15 (a)], albeit with a small amplitude. Therefore we can conclude that a small change in spectral power density (SPD) amongst these modes was observed on applying a 2V PL bias. Increasing the bias further resulted in a small change in the spectral power distribution amongst the modes, as can be observed for the

outer section current of 1.84 A [Figure 4.16 (b)]. The observed change in SPD between the modes agrees well with the 12 GHz shift in Bragg frequency predicted in Figure 4.11 (b) and Figure 4.14 (b). The emission observed at outer section currents > 1.84 A is shown in Figure 4.16 (c).

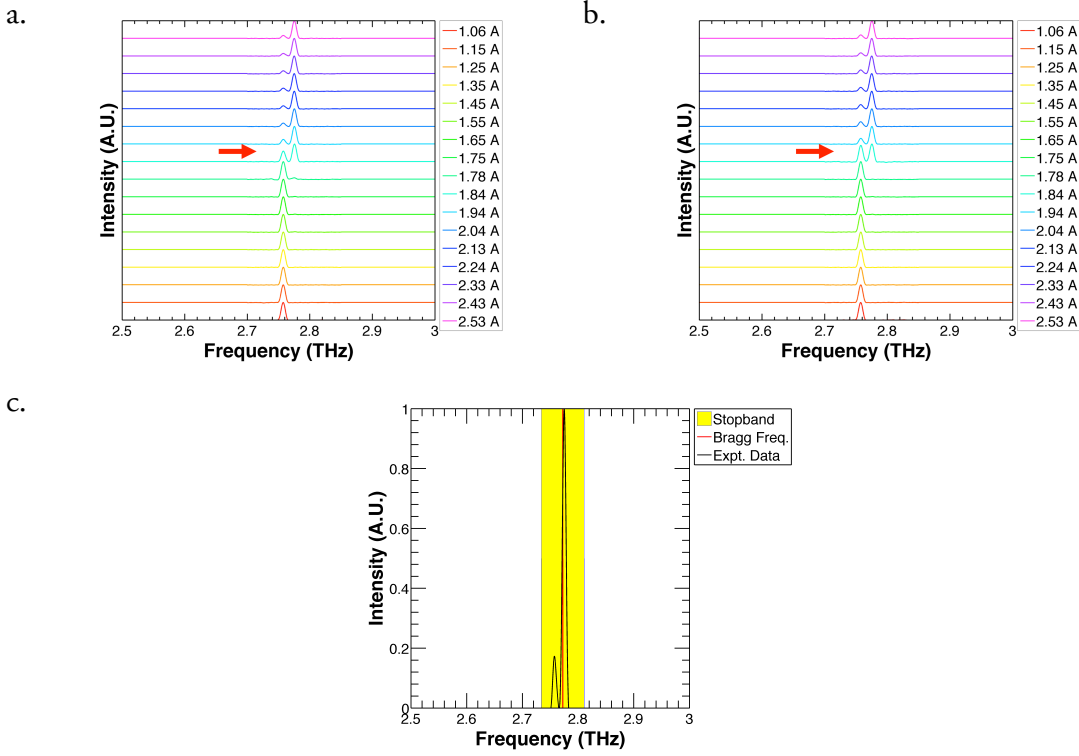


Figure 4.16: Emission spectra from device 4A at a heat sink temperature of 4 K, with a bias of (a) 2 V and (b) 6 V applied to the PL. Spectra are vertically offset and are shown in colour coded for a range of current applied to the outer section. (c) Simulated Bragg frequency (red) and stopband (yellow) in the PL with depleted carriers under grating calculated in Figure 4.14 (a). Emission (black) was observed at the shifted Bragg frequency.

While device 4A lased at the Bragg frequency all other devices fabricated for this study lased beyond the stopband, as was observed in Chapter 3. In one such device (4B), emission was observed at the edge of the stopband at all drive currents with a floating PL section [Figure 4.17 (a, b)]. Unlike the results obtained in Figure 4.16, a change in the SPD amongst modes resulting in a complete mode hopping was not observed from this device after applying a bias at the PL section. Instead, a small change in the SPD amongst modes was observed when the current at the outer section was > 2.10 A, and a bias was applied to the PL section [Figure 4.17 (c)]. The SPD at 2.815 THz increased monotonically with an increase in the bias applied to the PL section [Figure 4.17 (d)]. Furthermore, it is

also noted that this mode was observed when the spectra was recorded during the floating PL characterisation, as a secondary mode. A similar behaviour was also noted in device 4A.

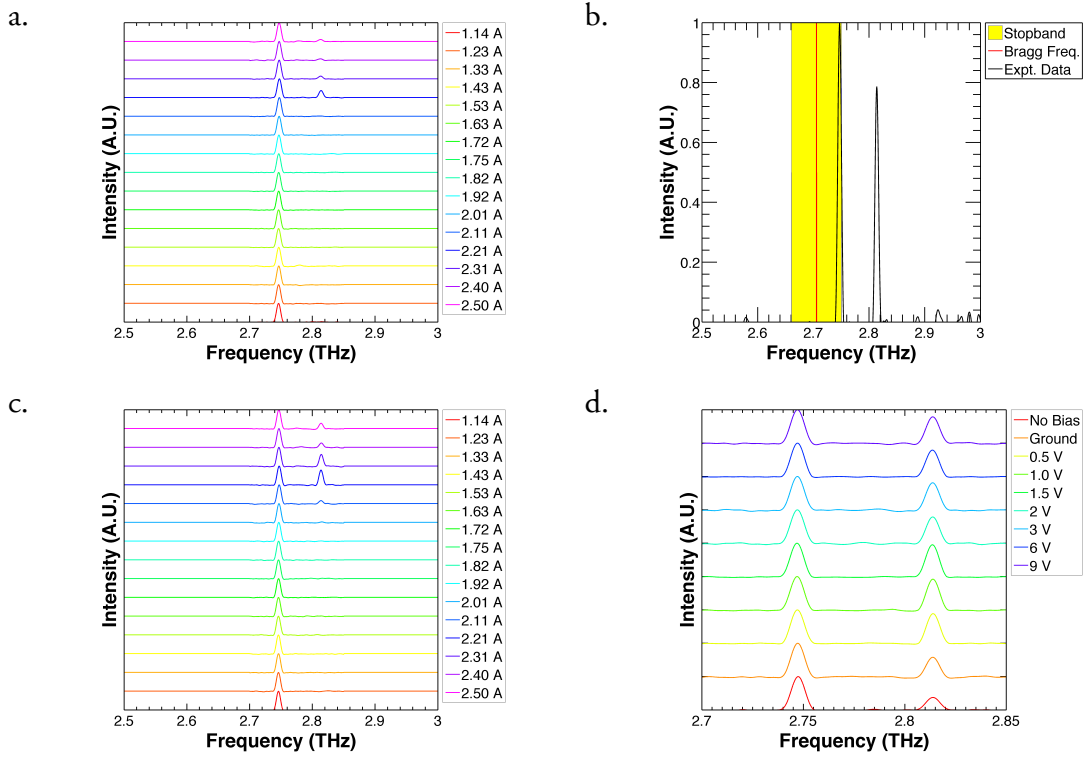


Figure 4.17: Emission spectra from device 4B at different drive current at outer section with (a) floating PL (4 K), (c) bias of 9 V applied to the PL section. (b) Emission was observed beyond the edge of the stopband. (d) Spectra under different PL bias with an outer section current of 2.21 A. Spectra are vertically offset and are colour coded for a range of applied to the outer section.

It can be inferred that the change in stopband conditions due to the applied bias on the PL section manifests as a variation in SPD amongst multiple modes. This premise was further investigated in three other devices (4C, 4D, 4E). These devices featured longer outer sections. The close mode spacing in such devices allowed additional modes outside the stopband. Emission in these devices (4C, 4D and 4E) was beyond the edge of the stopband. Spectra acquired from the devices with a floating PL section and with a bias of 9 V applied on the PL is shown in Figure 4.18. In all three devices, a small change in SPD was observed (Figure 4.18, marked with arrows) as observed in device 4B.

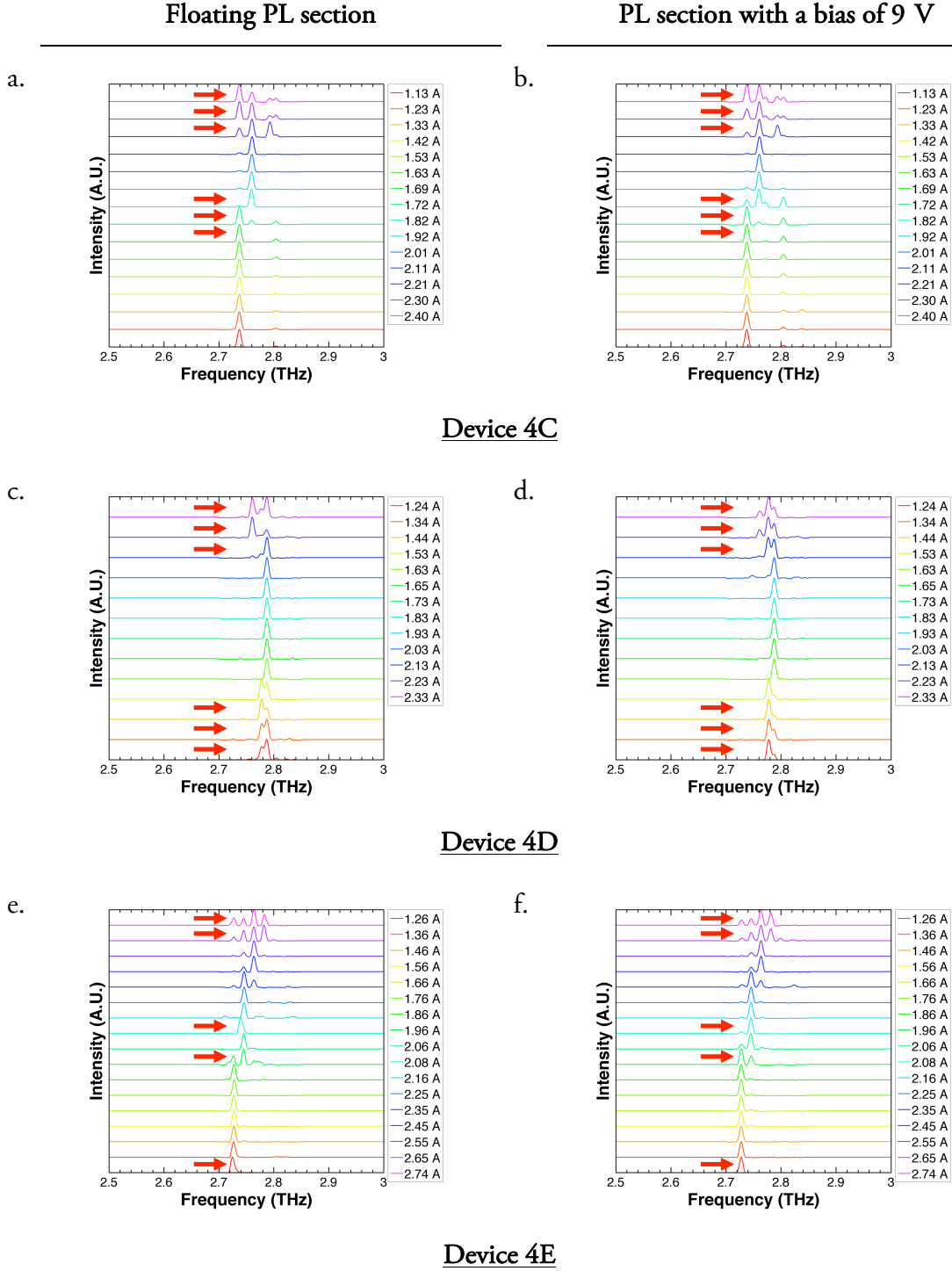


Figure 4.18: Emission spectra at different drive currents at the outer section from devices (a, b) 4C, (c, d) 4D and (e, f) 4E, at a heat sink temperature of 4 K: (a, c, e) with a floating PL section, and (b, d, f) with a bias of 9 V applied on the PL section.

It is worth noting that the variation of the band edge of the stopband with PL bias ($\sim 5\text{--}6$ GHz) is below the resolution of the FTIR spectrometer (~ 7.5 GHz). Hence, a mode shift or continuous tuning might be resolution limited in devices where emission was observed at the edge of the stopband. Frequency tunability with PLs could be better evaluated

in a PL with central shifted element, which has a lower lasing threshold at the Bragg frequency [109]. Continuous tunability in such designs is described in greater detail in section 6.3.

4.7 Summary

Frequency tunability in THz QCLs with PLs was investigated by varying refractive index through carrier depletion. The refractive index of the active region was studied by varying the carrier concentration in the active region. A Drude model was used to calculate refractive index in a THz QCL active region, modelled as a bulk GaAs semiconductor. The refractive index exhibited a sharp decrease as the carrier concentration varied between 10^{15} – $2 \times 10^{16} \text{ cm}^{-3}$. A frequency-tuning scheme was developed exploiting this non-linearity.

A variation in the refractive index was investigated by depleting carriers under the PL metallised section. This was achieved by depositing a Ti/Au based PL on top of the active material, forming a Schottky contact. The carriers under the PL metallised section were depleted by applying a reverse bias to this Schottky junction formed at the PL.

A series of THz QCLs were fabricated with a three-section cavity comprising of a central PL section placed between two outer sections. The central PL section was electrically isolated from the outer sections and PL gratings were patterned after etching away the top n -doped layer in the central section. The PL grating structure was modified to include bond pads for electrical connection and side rails to connect all metallised sections.

Initially, the devices were characterised with a drive current applied to the outer sections above lasing threshold and with no bias applied to the PL section (in a floating configuration). The electrical behaviour obtained in this floating configuration was simulated with the help of an electrical circuit model of the device. Electrical behaviour simulated from the circuit model was found to agree well with experimental observations. Devices were subsequently characterised with a bias applied to the PL section. The resulting variation of the depletion layer under the PL metallised section was estimated from the electrical characterisation results and the simulated circuit model. A frequency tuning of ~ 15 – 20 GHz was predicted from the Drude model. The stopband in the PL was also calculated and the bandwidth of the stopband was found to reduce from $\sim 90 \text{ GHz}$ to $\sim 77 \text{ GHz}$. An

overall shift in emission at the edge of the stopband by $\sim 5\text{--}6$ GHz was predicted from both the bulk Drude model and the dispersion relation.

Spectra from devices were acquired experimentally in both floating PL configuration as well as with an applied bias on the PL section. In an exemplar device, emission was observed at the Bragg frequency with a floating PL section. A mode hopping by 15 GHz was observed on application of a bias to the PL section, in agreement with the bulk Drude model. In all other devices, emission was observed at the edge of the stopband. A change in SPD was observed as the bias to the PL was varied. However, no continuous tuning was evident, presumably, due to the resolution limit of the FTIR spectrometer.

It is worth noting that a similar tuning mechanism based on a variation of electron density in a buried high electron mobility transistor was recently demonstrated in ref. [181]. A tuning of 2 GHz was observed in the reported device. Therefore, based on behaviour observed in this study and that reported in literature, it can be concluded that variation of refractive index through a change in carriers manifests as a small observable change in refractive index. It can be inferred that this small variation in the refractive index makes it inherently difficult to achieve a wide band frequency tuning in THz QCLs. A different tuning technique based on a two-section coupled-cavity QCL based on Vernier selection promises to expand the tuning range within the confines of the small index perturbation, and is discussed next.

Chapter 5

Discrete Vernier tuning using coupled cavity QCLs

5.1 Introduction

A means to achieve frequency tunable terahertz (THz) quantum cascade lasers (QCLs) through carrier depletion in a three-section device was described in the previous chapter. However, it was realised that the perturbation of the refractive index in the waveguide manifests as a small observable change in frequency. This tuning scheme was modified and a perturbation of the refractive index through current induced Joule heating and a tuning mechanism based on discrete Vernier frequency tuning using coupled cavity THz QCLs is described in this chapter. In this technique, two cavities are coupled through a central section with a high refractive index contrast, for e.g. an air gap. The emission in such coupled cavity devices is supported where the longitudinal modes in both the cavities coincide. Frequency tuning is achieved by shifting the longitudinal mode spacing in either of the two cavities and is analogous to a Vernier selection mechanism [106]. A major advantage of this Vernier tuning is the possibility of wide band tuning range with engineered cavities and small perturbations of refractive index.

Electrically-controlled discrete Vernier tuning of frequency using coupled cavities has been demonstrated in both optical lasers [182–184] as well as mid-infrared QCLs [185,186]. Discrete frequency tuning has also been demonstrated in THz QCLs recently, using aperiodic photonic lattices (APLs) [174,175] where mode hopping over 100 GHz was reported. However, a major disadvantage of this technique is the complex design methodology and multiple iterations of focussed ion beam (FIB) milling of the APL grating sites. A simpler approach towards the same goal was achieved in this study by using coupled cavity QCLs.

In this study, coupled cavities were realised using a segmented THz QCL ridge. Each device consisted of two individual laser ridges on the same substrate, which were separated by an air gap and were coupled via the adjacent laser facets. The high refractive index contrast between the laser ridges and the air gap increases the Fresnel reflectivity, which subsequently increases the effective reflectivity in the coupled cavity. In the two-section coupled cavity used for this study, one of the ridges formed the ‘*laser*’ section, and was electrically driven at a constant bias above the lasing threshold, so as to emit THz radiation. The other ‘*tuning*’ section was electrically driven below the lasing threshold, using a variable current source. This allowed the refractive index of the tuning section to be adjusted through localised Joule heating, resulting in tuning of the frequency supported by the coupled cavity device. The work presented in this chapter was published in ref. [187].

The coupled-cavity devices described in this work were adapted from standard THz QCL structures processed with non-segmented single-plasmon ridge waveguides. 4.5–4.8-mm long devices were fabricated and characterised following identical processing steps described in Chapter 2. After the initial processing and characterization of the standard waveguide structures, a transmission-matrix model was used to design the coupled-cavity devices. The standard devices were subsequently etched using FIB milling to form lasing and tuning sections with the precise desired lengths. The electrical and spectral characteristics obtained from the unsegmented devices were identical to the reference devices, discussed in section 2.3.1.

The following section briefly describes the theory behind the operation of coupled cavity lasers. A transfer matrix model to simulate coupled cavity QCLs is also discussed. Various design aspects such as the frequency spacing, tuning range and thermal control of

the frequency tuning are also considered. Finally, the results of the study are presented, in which it is shown that both red- and blue-shifts in the emission frequency of the laser are obtainable over a wide tuning range.

5.2 Theory of coupled cavity QCLs

THz QCL ridges with a single plasmon waveguide are essentially Fabry–Pérot (FP) etalons [106]. The longitudinal mode spacing in such FP cavities depends on the refractive index of the waveguide (n) and the length of the cavity (L), and is given by [188]

$$\Delta\nu = \frac{c}{2nL} \quad (5.1)$$

where c is the velocity of light in vacuum. Thus, the longitudinal mode spacing in a laser can be engineered by either choosing an appropriate cavity length or by modifying the refractive index. An electrical control of n requires no mechanical variation of geometry. Therefore, it's potentially faster and allows more compact systems. However, typically it is accompanied by a change in gain and therefore leads to power variations. In this study, this was circumvented by separating the tuning section from the lasing section of the cavity and the longitudinal mode spacing was modified in the tuning cavity only, by varying the refractive index. This eliminated the variation of emitted power that is usually associated with electrical control of refractive index.

A coupled cavity is formed by coupling two FP etalons through their facets [106,185], as shown in Figure 5.1. The laser section in this coupled cavity forms the ‘*active*’ component. This section is biased above the lasing threshold and provides gain in the coupled cavity. The tuning section forms the ‘*passive*’ cavity. The tuning section is biased below the lasing threshold and does not contribute to the gain in the coupled cavity. The two cavity sections are separated by an air gap.

The coupled cavity, shown in Figure 5.1, is modelled as a four-mirror laser system [106]. In such a four-mirror system, the passive tuning cavity and the air gap section are approximated as an ‘*external*’ cavity [Figure 5.2]. The reflectivity of the rear facet of the active laser cavity is approximated as the ‘*effective reflectivity*’ of the external cavity. The length of the tuning section and the air gap are optimised such that the maximum effective reflectivity of the external cavity and the minimum mirror loss in the entire coupled cavity

coincide with the longitudinal axial modes of the passive tuning cavity [106]. In such a coupled cavity, a lower lasing threshold is observed where longitudinal modes from the laser section coincide with those from the tuning section [106].

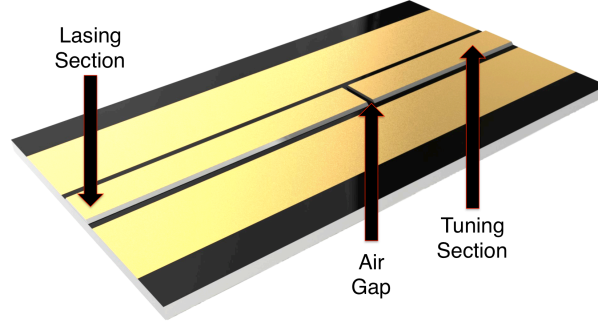


Figure 5.1: Schematic illustration of a coupled cavity THz QCL with a single-plasmon waveguide containing separate lasing and tuning section, which are separated by an air gap.

The alignment of the longitudinal modes in the two sections is varied by perturbing the refractive index in the tuning section while keeping the bias on the lasing section constant. In an optimised design, the different longitudinal modes in the laser section can be progressively selected by a careful variation of the refractive index in the tuning section, and the resulting variation in the alignment with the longitudinal modes at the tuning section. This control of alignment through the tuning section is analogous to Vernier selection. In this study, coupled cavity THz QCLs were designed following these underlying principles and were modelled using transfer functions based on scattering (S) and transmission (T) matrices.

The following section briefly describes the S and T matrices that are used to model multi-port networks and their application in modelling laser cavities is discussed in section 5.2.1.1. The modelling of a controlled perturbation of the refractive index with temperature as well as current induced Joule heating are discussed in sections 5.2.1.2 and 5.2.1.3. The simulation and modelling techniques used in this study were optimised for the frequency range 2.70–2.85 THz, which corresponded to the gain-bandwidth of the wafer (L701) used in this study.

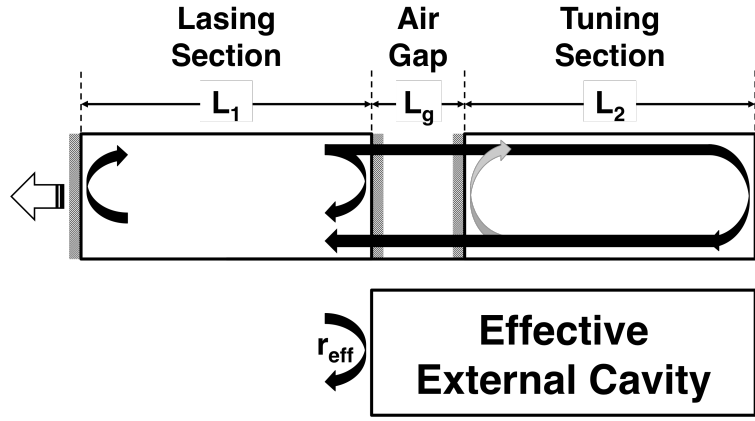


Figure 5.2: Schematic diagram of a coupled-cavity laser modelled as a four-mirror system. The tuning section and the air gap section together form an external cavity. Emitted radiation is collected from the front facet of the lasing section as indicated by the arrow. The reflectivity of the rear facet of the lasing section is approximated as the effective reflectivity from the external cavity.

5.2.1 Modelling using scattering and transmission matrices

Transfer functions from S and T matrices are simple and efficient tools to model transmission and reflectivity at laser cavities [106]. The S matrix describes the linear relation between output b at any port j and input a at all other ports [Figure 5.3], and is given as [106]

$$b_i = \sum_j S_{ij} a_j \quad (5.2)$$

where S_{ij} are scattering coefficients and describe the ratio of the output at a port i and the input at port j , with all other ports terminated by their matched impedance. Therefore, S_{ij} can be expressed mathematically as [106]

$$S_{ij} = \left. \frac{b_i}{a_j} \right|_{a_k=0, k \neq j} \quad (5.3)$$

In a two-port network, the relation between the output b and the input a can be expressed as the following matrix [106]

$$\begin{bmatrix} b_1 \\ b_2 \end{bmatrix} = \begin{bmatrix} S_{11} & S_{12} \\ S_{21} & S_{22} \end{bmatrix} \begin{bmatrix} a_1 \\ a_2 \end{bmatrix} \quad (5.4)$$

The diagonal elements in the S matrix shown in eq. (5.4) are complex amplitude reflection coefficients. The off-diagonal elements describe the output at a port due to the input at another port and are essentially transfer functions.

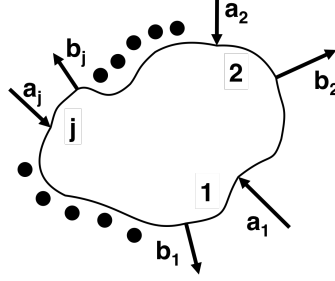


Figure 5.3: Schematic diagram of a multi-port network used to describe S matrices. Adapted from [106].

The T matrices, on the other hand, describe the input and the output at a given port in terms of those at other ports. In a two-port network [Figure 5.4 (a)], the input A and the output B at port 1 can be expressed in terms of those at port 2 in matrix formulation as [106],

$$\begin{bmatrix} A_1 \\ B_1 \end{bmatrix} = \begin{bmatrix} T_{11} & T_{12} \\ T_{21} & T_{22} \end{bmatrix} \begin{bmatrix} A_2 \\ B_2 \end{bmatrix} \quad (5.5)$$

T matrices offer greater flexibility over S matrices in designing networks with multiple cascaded components. An extended network can be modelled easily using T matrices by simply multiplying the T matrices of the individual components [Figure 5.4 (b)].

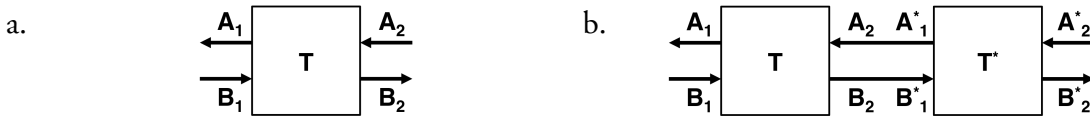


Figure 5.4: (a) Schematic diagram of a two-port network used to describe the T matrices. (b) Schematic diagram of a cascading of two-port networks. Adapted from [106].

The S matrices, which describe the transmission and reflectance in a network, can be calculated from the T matrices using the conversion formula given as [106],

$$S = \frac{1}{T_{11}} \begin{bmatrix} T_{21} & \det(T) \\ 1 & -T_{12} \end{bmatrix} \quad (5.6)$$

where T_{mn} is the T matrix element at row m and column n .

To describe a laser cavity, the input and the output are replaced by forward and backward wave, and the T matrices are formed by cascading dielectric interface and transmission along the propagation path [Figure 5.5]. The dielectric interface simulates the mirror facets and the propagation path simulates the gain region of the laser. The T matrix of a dielectric interface is given as [106],

$$T = \frac{1}{t} \begin{bmatrix} 1 & -\bar{r} \\ -\bar{r} & 1 \end{bmatrix} \quad (5.7)$$

where \bar{r} and t are the reflectivity and the transmission at the dielectric interface and are given as [106],

$$\bar{r} \cong \frac{n_2 - n_1}{n_2 + n_1} \quad (5.8)$$

where n_1 and n_2 are the effective group refractive indices at the two dielectric materials. Assuming a lossless interface, the transmission t is given as [106],

$$t = \sqrt{1 - \bar{r}^2} \quad (5.9)$$

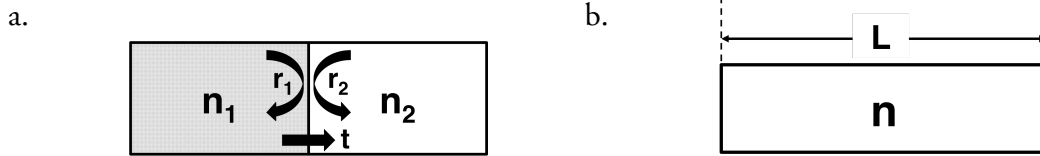


Figure 5.5: (a) Schematic diagram of a dielectric interface between two materials with effective refractive indices n_1 and n_2 . Owing to the difference in refractive index, a part of the wave is reflected back (r_1 and r_2), as illustrated with curved arrows, and part is transmitted (t). (b) Schematic diagram of a transmission line of length L with no discontinuity in the material with an effective refractive index n .

The T matrix of a transmission line with no discontinuity, with length L , is given as [106],

$$T = \begin{bmatrix} \exp(j\bar{\beta}L) & 0 \\ 0 & \exp(-j\bar{\beta}L) \end{bmatrix} \quad (5.10)$$

where $\bar{\beta}$ is the complex propagation constant and is given as [106],

$$\bar{\beta} = \frac{2\pi n}{\lambda} + j \left[\frac{1}{2} (g - \alpha_{wg}) \right] \quad (5.11)$$

where n is the effective refractive index, λ is the wavelength, g is the transverse modal gain and α_{wg} is the waveguide loss.

An FP etalon is modelled by cascading a dielectric interface followed by a transmission path equalling the length of the cavity and is terminated with another dielectric interface. The transmission matrix for this structure is easily obtained by multiplying the corresponding matrices of the constituent elements and is given as [106]

$$T = \frac{1}{t^2} \begin{bmatrix} 1 & -r \\ -r & 1 \end{bmatrix} \begin{bmatrix} \exp(j\bar{\beta}L) & 0 \\ 0 & \exp(-j\bar{\beta}L) \end{bmatrix} \begin{bmatrix} 1 & -r \\ -r & 1 \end{bmatrix} \quad (5.12)$$

Solving the above equation and using eq. (5.6), the scattering matrix elements for a FP etalon is calculated as [106],

$$S_{11} = S_{22} = -r + \frac{t^2 r \exp(-2j\bar{\beta}L)}{1 - r^2 \exp(-2j\bar{\beta}L)} \quad (5.13)$$

$$S_{12} = S_{21} = \frac{t^2 \exp(-2j\bar{\beta}L)}{1 - r^2 \exp(-2j\bar{\beta}L)}$$

The magnitude and phase of the transmission and the reflectivity in the laser cavity can be computed from S_{12} and S_{11} respectively. As an example, the magnitude and the phase of reflection in a 4-mm-long laser cavity is shown in Figure 5.6. It is observed that a maxima of reflectivity corresponds to a phase of π with respect to frequency. The transmission in a laser cavity can be computed similarly. The transmission spectrum in a laser cavity exhibits longitudinal modes that correspond to minima in the reflection spectrum.

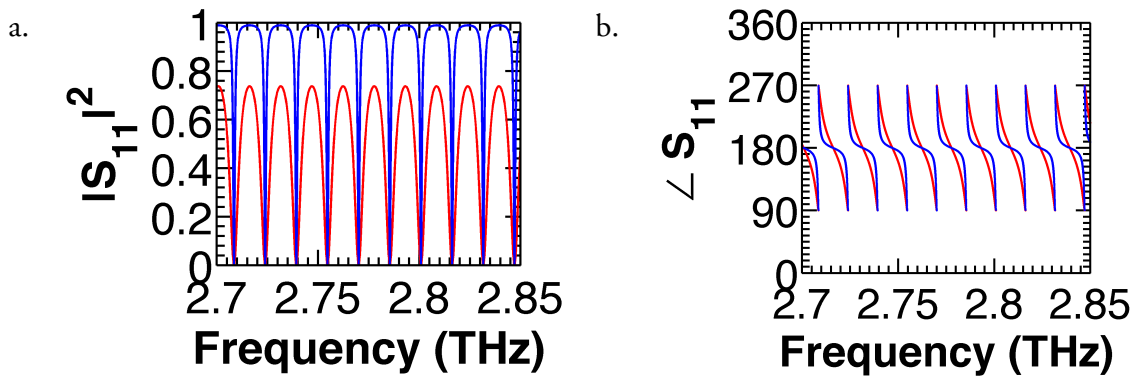


Figure 5.6: (a) Magnitude and (b) phase of the reflectivity calculated for a 4-mm long loss-less laser cavity with mirror reflectivity of 0.56 (red) and 0.9 (blue).

The description of a FP etalon with scattering and transmission matrices is treated as a framework to model complex cascaded structures, such as coupled cavities and is discussed next.

5.2.1.1 Modelling coupled cavity QCLs

Coupled-cavity QCLs were modelled using T matrices by cascading two FP cavities of length L_1 and L_2 with an air gap separation of L_g between them. A schematic diagram of a coupled cavity is shown in Figure 5.7. Both the lasing and the tuning sections were composed of the same active material and had identical effective refractive indices (when both sections are at the same temperature). However, since the refractive index of the tuning section was varied, the indices of the two sections are labelled differently as n_1 and n_2 .

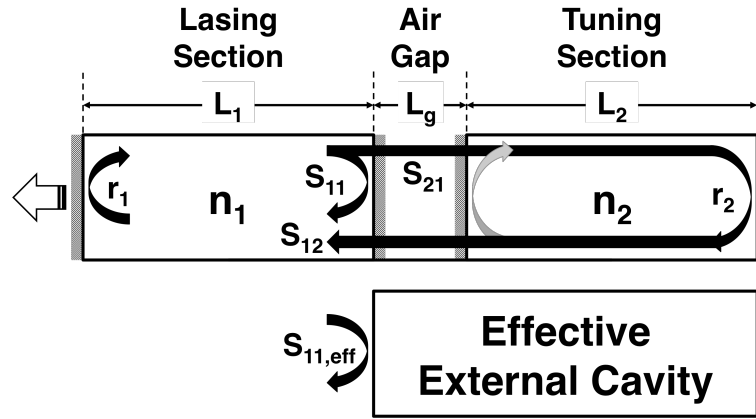


Figure 5.7: Schematic diagram of a coupled cavity QCL. Two FP cavities of length L_1 and L_2 formed the lasing and the tuning sections respectively, and were separated by an air gap of length L_g . The effective refractive index of the lasing and the tuning sections are n_1 and n_2 respectively. The reflectivity and the transmission at the laser facets are indicated as r_n and t_n respectively. Radiation is collected from the front facet of the lasing section as indicated by the arrow.

The group refractive index of the active material was calculated as 3.61, by substituting the longitudinal mode spacing obtained from a 3.1-mm-long reference device [Figure 5.8 (a)] into eq. (3.1). The effective group refractive index was also calculated using the finite element modelling (FEM) technique, described in section 3.2.1.1. A refractive index of 3.62 was computed by simulating a device cross-section at 2.75 THz, which agrees well with the experimental value. The cross-sectional profile of the optical mode (in-plane with the facet), simulated using COMSOL Multiphysics® is shown in Figure 5.8 (b).

This enabled calculation of the Fresnel reflection coefficients (r) used in the model, as well as the optical path lengths of each section.

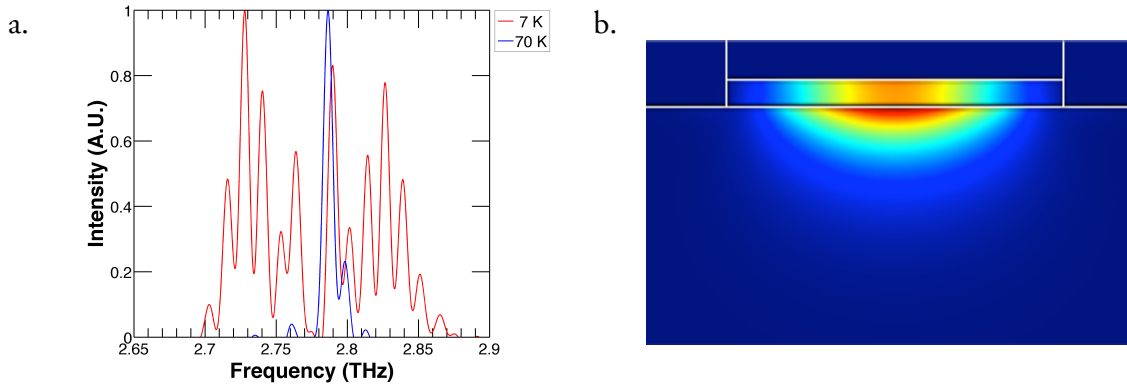


Figure 5.8: (a) Spectra obtained from a reference device from wafer L701 at 7 K. Multiple FP modes were observed between 2.70 and 2.85 THz. (b) Computed optical mode at 2.75 THz using finite element modelling of the device cross section with an effective refractive index of 3.62. The intensity distribution of the optical field is represented as a colour map with red being most intense and dark blue being least intense.

An important criterion for designing coupled cavity QCLs is the selection of appropriate cavity lengths of the tuning section and the air gap. The length of the tuning section was selected such that it exhibited maximum reflectivity at a ‘*resonant*’ frequency corresponding to a longitudinal FP mode of the lasing section. The section lengths were further constrained to multiples of half of the corresponding wavelength, λ_{res} in order to optimise the phase matching between the lasing and the tuning sections. Thus, lasing is favoured at the longitudinal mode (λ_{res}) where the normalised transmission of the lasing section is aligned with that of the tuning section [106]. Although an air gap of $\lambda_{res}/2$ is optimal for phase matching, a gap width of $\lambda_{res}/8$ was used owing to limitations imposed by the focused ion beam (FIB) milling. This smaller air-gap section is expected to reduce the continuous frequency tunability of the coupled cavity devices and affect spurious mode suppression [106].

The longitudinal modes simulated for a 2.45-mm long lasing section and a 2.30-mm long tuning section in a coupled cavity with a 13- μm wide air gap are shown in Figure 5.9. An emission from such a coupled cavity is predicted to be at 2.745 THz due to the alignment of the longitudinal modes in the lasing and tuning sections and the corresponding reduction of lasing threshold. It can also be observed that a small perturbation to the fre-

quency of the modes in either section of the device will detune the resonance, causing the dominant mode of the coupled-cavity to ‘hop’ to a different frequency, in a manner analogous to the Vernier effect. Perturbation of tuning modes was investigated by varying temperature and localised current induced Joule heating and is discussed next.

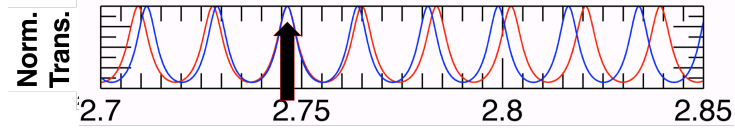


Figure 5.9: Simulated normalised transmission in a 2.45-mm-long lasing section (blue), and in a 2.30-mm-long tuning section with a 13- μm wide air gap section (red). The length of each section is selected such that the longitudinal modes coincide at a resonant frequency of 2.745 THz (bottom panel).

5.2.1.2 Modelling tuning of refractive index with temperature

The effect of Joule heating on the refractive index of the tuning section was incorporated in the model to understand the tuning behaviour in coupled cavity devices. To study the effect of heating on the mode profile, spectra from a reference device were recorded at heat sink temperatures between 7 and 70 K [Figure 5.10 (a)]. The temperature tuning of individual lasing modes df/dT ($d\lambda/dT$) was found to be linear with respect to temperature. The tuning coefficient was calculated to be 63 MHz/K (2.74 nm/K), corresponding to a 4-GHz red shift as the heat-sink temperature was varied from 7 K to 70 K [Figure 5.10 (b)].

The temperature tuning of refractive index was calculated from the mode order relation, given as [188]

$$L = m \frac{\lambda}{2n} \quad (5.14)$$

where L is the length of the laser cavity, m is the mode order, λ is the wavelength and n is the group refractive index of the cavity. Rearranging eq. (5.14) and differentiating it with respect to temperature gives the temperature tuning of refractive index (dn/dT) in terms of $d\lambda/dT$, as

$$\frac{1}{n} \frac{dn}{dT} = \frac{1}{\lambda} \frac{d\lambda}{dT} \quad (5.15)$$

The change in refractive index with temperature corresponding to $d\lambda/dT$ was calculated to be $9.5 \times 10^{-5} \text{ K}^{-1}$. The observed tuning coefficient is close to a value of $2 \times 10^{-5} \text{ K}^{-1}$ reported in ref. [112] for a different active region design [189]. The temperature tuning coefficients were used in the coupled cavity model to simulate the tuning of refractive index in the tuning section.

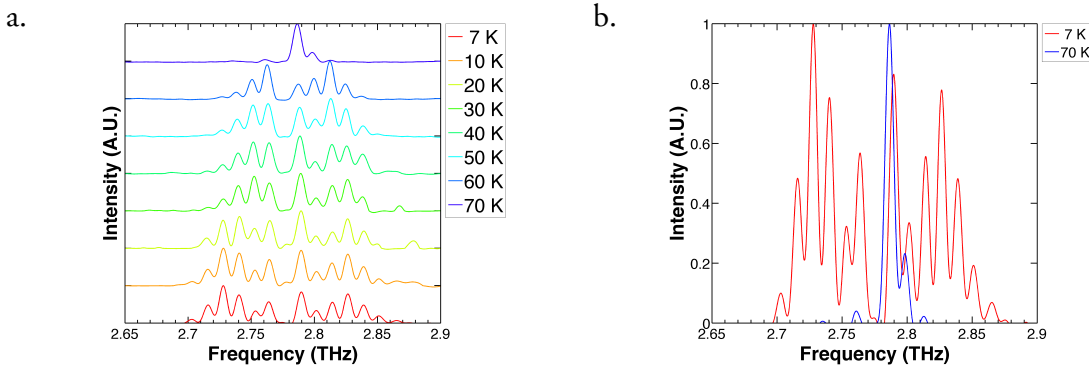


Figure 5.10: (a) Spectra obtained from a reference device from wafer L701 at different heat-sink temperatures. (b) Modes exhibit a red shift of 4 GHz as the heat sink temperature was increased from 7 K to 70 K.

Although, a change in the refractive index is achieved by varying the heat-sink temperature, it was not used as a means of control in the chosen design. This is because the coupled cavity structure was fabricated on a monolithic laser cavity, and therefore, changing the heat-sink temperature would change the refractive indices in both the lasing and the tuning sections. Thus, changing the heat-sink temperature impedes selective variation of refractive index at the tuning section. Additionally, the emitted power from THz QCLs degrades significantly as the heat-sink temperature in the lasing section is increased [66]. Instead, wide current pulses were used to induce localised Joule heating, and to change refractive index selectively in the tuning section only. The following section describes a bulk thermal model used to predict electrical heating effects in QCL sections.

5.2.1.3 Current induced Joule heating of tuning section

Current pulses wider than the thermal equilibration time of the QCL were used to heat the tuning section of the coupled cavity devices to attain a steady state temperature. The steady state temperature change ΔT is calculated from the thermal resistance of the QCL (R_{Th}) and is given as [190]

$$\Delta T = R_{Th} V_t I_t \quad (5.16)$$

where V_t and I_t are the voltage and current in the tuning section. The thermal resistance depends on the dimensions of the laser ridge. As such, the normalized thermal resistance, which is calculated from the area (A) and the thickness (d) of the QCL ridge, is better suited to evaluate the thermal behaviour of a QCL wafer. The normalised thermal resistance is expressed as [191]

$$R_{Th}^* = \frac{R_{Th} A}{d} \quad (5.17)$$

The thermal behaviour of QCL ridges was studied by measuring the output power as a function of heat-sink temperature and duty cycle [Figure 5.11 (a)]. First, the optical power emitted from the device was recorded at a range of duty cycles of the current pulses with a constant heat-sink temperature of 10 K being maintained throughout. Similar measurements were then recorded at range of heat-sink temperatures with a constant duty cycle of 2%. By comparing the output powers under these different driving conditions, it was possible to infer the internal temperature of the QCL as a function of the electrical duty cycle, as shown in Figure 5.11 (b). The thermal resistance R_{Th} , was calculated from the slope of Figure 5.11 (b), as described in ref. [151] as 9.92 K/W, for a maximum input power of 6 W. This agrees well with the value reported in [151,192]. The normalised thermal resistance was calculated from the QCL ridge dimensions as 31.7 Kcm/W. A similar normalised thermal resistance for a QCL with an identical active region design and with a single metal waveguide was reported in ref. [193].

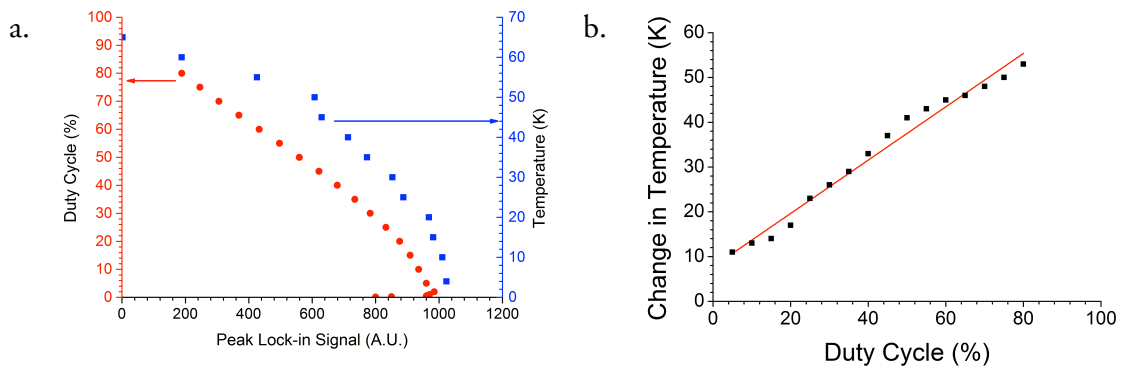


Figure 5.11: (a) Peak output measured in the lockin amplifier as a function of heat sink temperature and duty cycle. (b) Change in temperature as a function of duty cycle and input tuning power.

The maximum change in temperature (ΔT_{max}) in the tuning section was calculated using eq. (5.16) and (5.17), with a maximum input electrical power ($V_t I_t$) of 5–6 W for the designed tuning section. The corresponding change in refractive index in the tuning section was calculated by multiplying the temperature-tuning coefficient (dn/dT) by ΔT_{max} . This tuning behaviour was then incorporated into the model of the coupled cavity device, enabling the longitudinal modes in the tuning section to be calculated as a function of the input tuning power.

The alignment of longitudinal modes in the lasing and tuning sections was calculated for a range of tuning currents (or equivalently, input powers in the tuning section). For the device shown in Figure 5.9, the change in alignment of the longitudinal modes is shown in Figure 5.12. With an increase in tuning current, the alignment shifted and lasing is favoured at the frequencies indicated by arrows.

The model was used to simulate various coupled cavity device geometries to optimise the tuning range and the frequency spacing, and is discussed next.

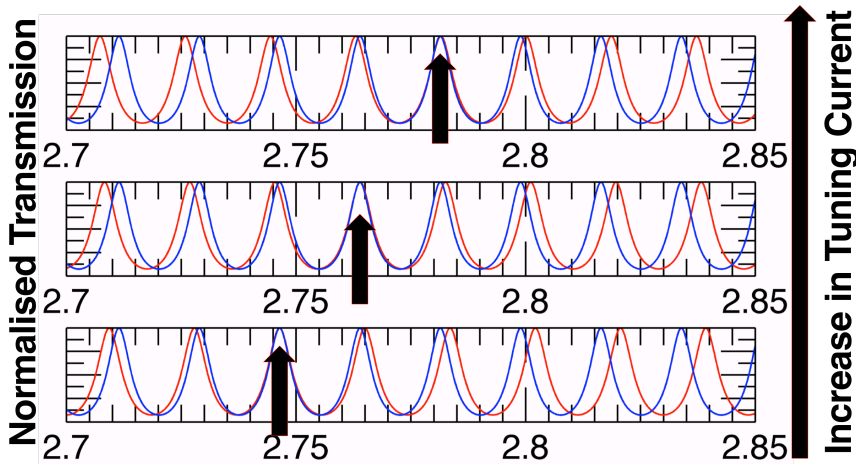


Figure 5.12: Simulated normalized transmission in the lasing section (blue) and in the tuning sections (red) of the device. The length of each section is selected such that the longitudinal modes coincide at a resonant frequency of 2.745 THz (bottom panel). Illustration of the shift in the resonant frequency as the refractive index of the tuning section is perturbed (middle and top panel). The dominant mode of the coupled cavity, indicated by a black arrow in each case, shifts to a higher frequency.

5.3 Designing coupled cavity QCLs

The transfer-matrix-based coupled-cavity model and the bulk thermal model of refractive index perturbation were used to design coupled cavity QCLs. The gain bandwidth of the wafer, obtained experimentally from unsegmented devices before FIB milling, was also included in the coupled cavity model for a better estimation of frequency hopping. To illustrate the frequency tuning, the normalised product of the longitudinal modes at the lasing and the tuning sections was plotted as a function of the applied input electrical power at the tuning section. The maxima of this product illustrate a complete modal alignment and consequently the emission frequency with the lowest lasing threshold. This simple design paradigm enables flexibility in designing the range and direction of the frequency tuning. Two variations of the coupled geometry were designed.

1. Frequency mode hopping between adjacent modes in the lasing section.
2. Frequency mode hopping between alternate modes in the lasing section.

5.3.1 Design 1: Mode hopping between adjacent modes

The first design investigated the possibility of frequency hopping between adjacent modes in the lasing section. The primary requirement for this design was choosing lasing and tuning sections of comparable lengths, with a difference of a few half wavelengths ($\lambda_{\text{res}}/2$). This results in longitudinal FP modes in the lasing and tuning sections with similar mode spacing. Thus, with careful perturbation of the refractive index in the tuning section, the emission frequency of the coupled cavity device is predicted to hop progressively between adjacent modes of the lasing section [Figure 5.13]. In this design, the discrete-tuning resolution is equal to the FP mode spacing of the lasing section.

A coupled cavity device with a 2.45-mm-long lasing section and a 2.30-mm-long tuning section separated by a 13- μm wide air gap was used in this design, identical to the design presented in Figure 5.9 and Figure 5.12. However, the gain bandwidth of the wafer was also included in the model for a more accurate prediction of the frequency tuning range.

The thermal resistance of the tuning section was calculated from the normalised thermal resistance to be $R_{Th} \approx 9.92 \text{ K/W}$. A tuning power of $\sim 5 \text{ W}$ (corresponding to a

sub-threshold tuning current of ~ 1 A) was used to model the perturbation of the refractive index in the tuning section, which corresponded to a temperature change $\Delta T \sim 50$ K. Simulations predict a blue shift in frequency from ~ 2.74 to ~ 2.81 THz with a mode spacing of ~ 15 GHz, as the shorter section is heated by ~ 5.5 W input power [Figure 5.13 (a)].

The coupled cavity design discussed so far assumed the tuning section to be the shorter cavity. Since the dimensions of the coupled cavities were nearly identical, this design allowed swapping the functions of the lasing and the tuning sections. Thus, the longer cavity formed the tuning section and the shorter cavity formed the lasing cavity in this ‘*alternate*’ arrangement. Since, the length of both lasing and tuning direction were comparable, laser performance parameters like power, gain, waveguide losses etc. were identical in both sections. Thus, it was estimated that alternating between the lasing and tuning sections would not affect overall performance (i.e. threshold current and power) of the device.

By swapping the function of the lasing and tuning sections, the direction of the simulated mode-hopping was reversed. A red shift in frequency from ~ 2.75 to ~ 2.70 THz was predicted when the shorter section serves as the lasing section [Figure 5.13 (b)], with the same mode spacing as in the original configuration.

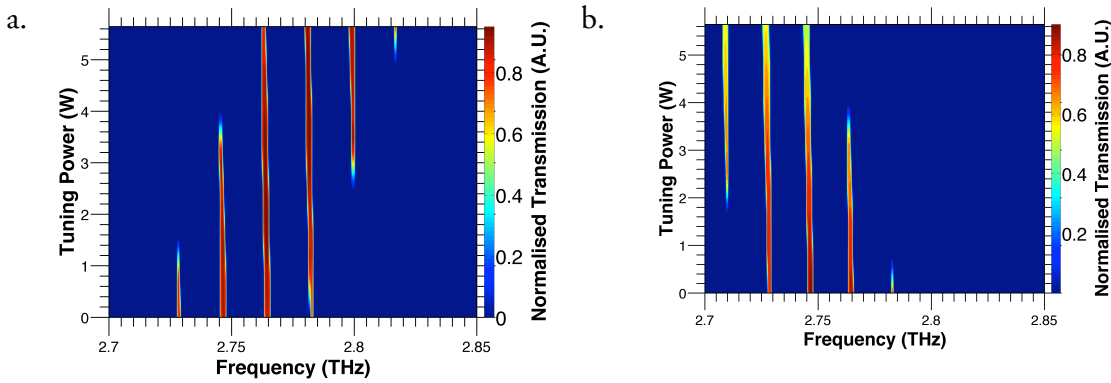


Figure 5.13: Simulated transmission spectra of design 1 as a function of heat-induced shift of longitudinal modes in the tuning section only.
(a) blue shift of frequency induced by heating the shorter cavity,
(b) red shift of frequency induced by heating the longer cavity.

5.3.2 Design 2: Mode hopping between alternate modes

The second design investigated the possibility of hopping between alternate modes of the lasing section. The underlying principle for this design was to select cavity lengths such that

the separation between transmission modes in the tuning section was almost twice than that in the lasing section. Hence, the modes of the tuning section are designed to coincide with alternate modes of the lasing section, and the emission frequency of the coupled-cavity device was predicted to hop accordingly as the electrical power delivered to the tuning section is varied. A greater tuning range is predicted for this design, but with increased frequency spacing between the lasing modes.

In this second design, the length of the lasing section (3.4 mm) was chosen to be almost twice that of the tuning section (1.5 mm). As shown in Figure 5.14 (a), the simulated emission frequency hops from ~ 2.75 – 2.83 THz in ~ 25 -GHz steps as the shorter section is heated. As in design 1, the measured normalized thermal resistance $R_{Th}^* \approx 31.7$ Kcm/W was used in these simulations.

The possibility of changing the tuning direction by swapping the functions of the lasing and the tuning sections was also investigated for this design. A red shift from 2.77 to 2.70 THz is predicted when the longer section serves as the tuning section [Figure 5.14 (b)]. However, since the cavity lengths were different in this design, device parameters like gain and emitted power depend on the dimensions of the lasing section. In fact, it was observed in reference devices from L701 that the gain bandwidth was reduced and shifted to higher frequencies as the cavity length was reduced below 1.5 mm. Thus, the predicted shift with the shorter section as the lasing section might be misrepresentative.

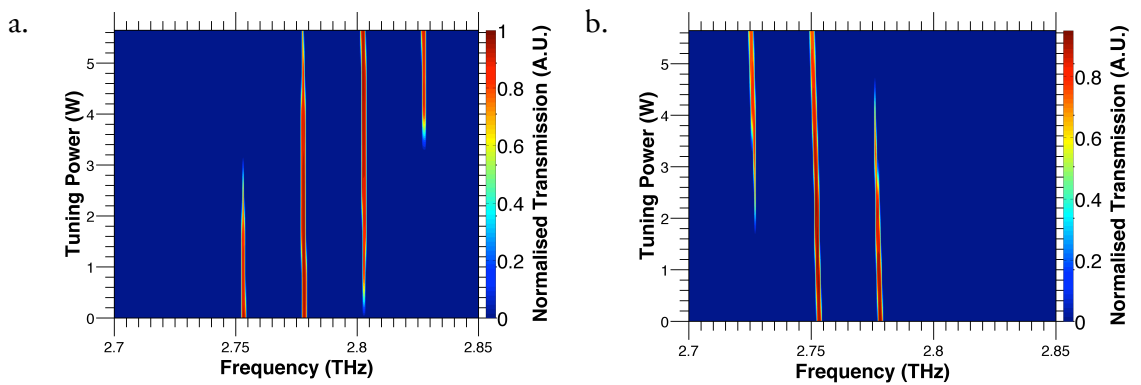


Figure 5.14: Simulated transmission spectra of design 2 as a function of the heat-induced shift of longitudinal modes in the tuning section only. (a) blue shift of frequency induced by heating the shorter cavity, (b) red shift of frequency induced by heating the longer cavity.

5.4 Fabrication

THz QCLs with a single-plasmon waveguide were fabricated following identical procedures as those described in section 2.2. Devices of precise lengths calculated using the scattering matrix model were cleaved using an automated scribe. The cleaved devices had no air gap sections and were essentially long standard devices. The packaging of these devices was different from standard QCLs. While a standard QCL package housed two devices in a single Cu mount, only a single coupled-cavity device was soldered onto each mount. This was done to independently connect the lasing and the tuning sections using the available packaging design. Wires from the same ridge were bonded into two thermally isolated ceramic pads to enable independent electrical control after milling the air gap using FIB. A schematic of the device packaging and electrical connections is shown in Figure 5.15.

The device fabricated with design 1 specification was packaged following the scheme shown in Figure 5.15. However, the ceramic pad for the ground connection was not used in the packaging for the device with design 2 specification. Instead, ground connections were made directly on the Cu block. This allowed THz power to be collected from the outward facets of both cavities. This packaging facilitated better evaluation of device characteristics when the lasing and tuning cavities were swapped.

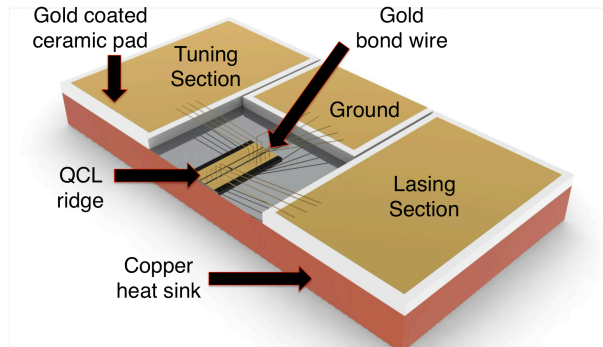


Figure 5.15: Schematic illustration of the packaging and physical connection scheme of a coupled cavity THz QCL.

A FIB milling process was used to sculpt air gaps of precise dimensions. An etch depth of 12 μm was used for all devices to ensure complete electrical isolation of the lasing and the tuning sections. SEM of a device before and after FIB milling are shown in Figure 5.16. A high ion-beam current was required to etch the 12- μm -deep air cavities.

However, since the coupled-cavity devices required high quality facets to minimise mirror losses, the milling current was optimised to minimise damage to etched facets. An ion beam current of 7 nA was selected for the milling process as a trade-off between high quality facets and long etching times (extending over 3 hours). Micrographs of the facets obtained by FIB milling are shown in Figure 5.17, and are compared with those obtained from scribing. The milled facets did not exhibit significant visible damage and visually compared well with the scribed facets. However, surface irregularities were observed due to re-deposition of the etched material and vertical impressions resulting from the etching process [Figure 5.17 (c)].

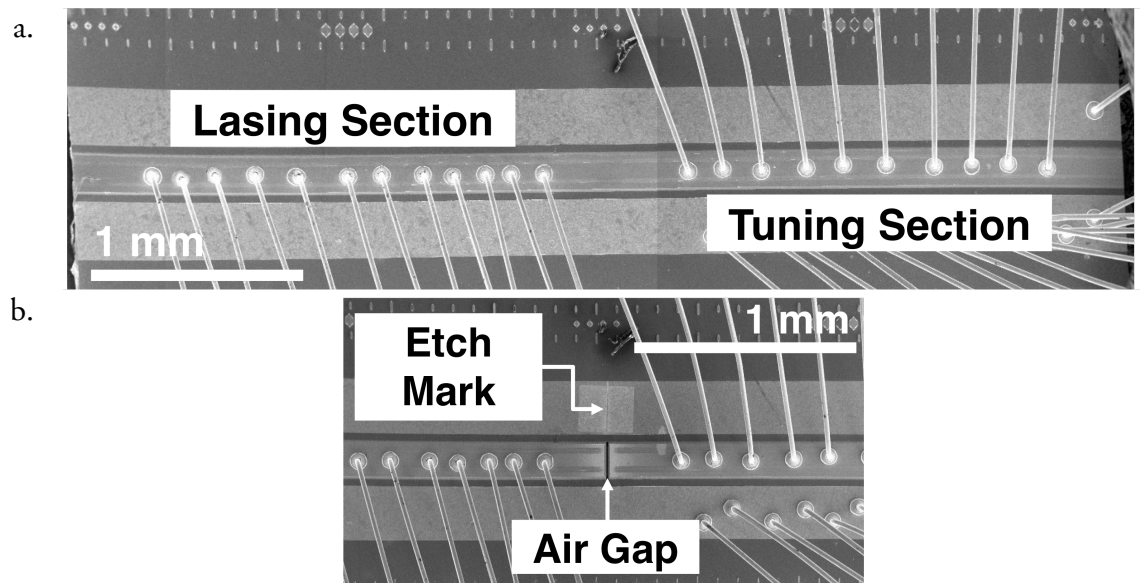


Figure 5.16: Scanning electron microscopy of a THz QCL ridge (a) before and (b) after FIB milling. Etch marks to determine precise cavity lengths are visible above the etched air gap.

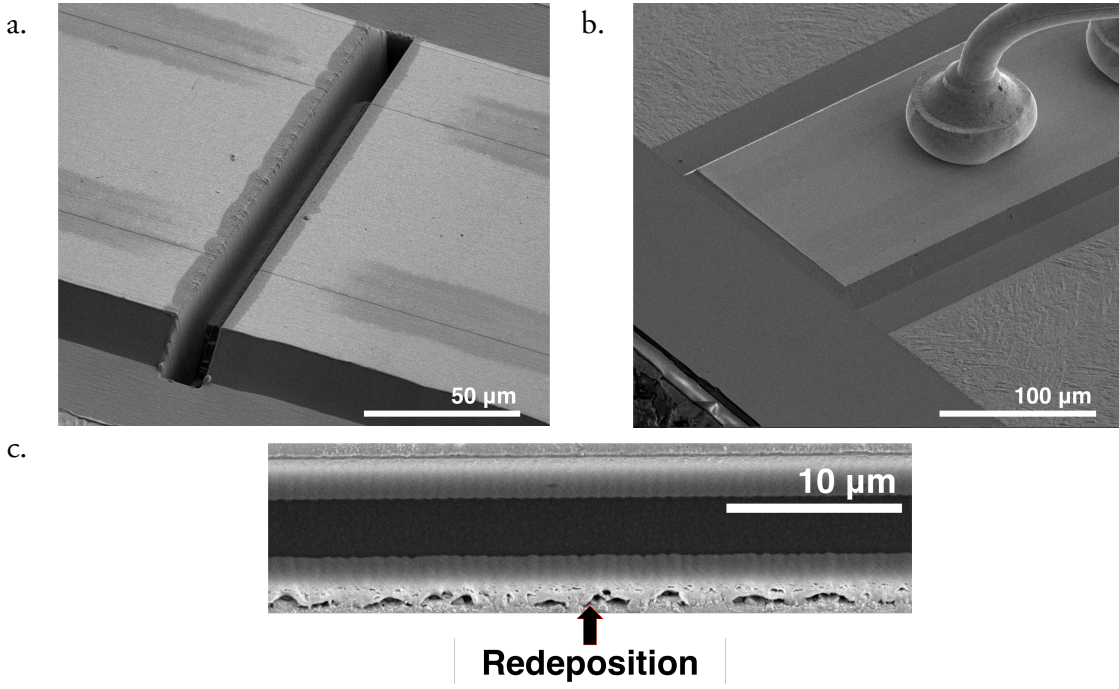


Figure 5.17: Scanning electron microscopy of (a) FIB milled facet, (b) scribed facet and (c) FIB milled facet at higher magnification. Redeposition of the etched material along the milled surface is evident at higher magnification. The milling process also resulted in vertical impressions along the surface of the milled facet.

A list of fabricated devices is tabulated in Table 5.1.

Table 5.1: List of processed coupled cavity THz QCLs.

Device Number	Device Unique ID	Lasing Cavity (mm)	Tuning Cavity (mm)	Air Gap (μm)	Mode spacing
5A	L701-S21-D1	2.446	2.305	13.39	Adjacent
5B	L701-S21-D3	3.380	1.570	16.67	Alternate

5.5 Experimental setup

The coupled-cavity devices obtained after FIB milling were characterised using a continuous train of current pulses as the electrical input. While the experimental setup described in section 2.3.1 was optimised for efficient thermal extraction from QCLs, the setup used for this study was modified to heat the tuning section deliberately. As such, the frequency of the current pulses supplied to the lasing and tuning sections were modified. Instead of a 165 Hz gating pulse, a reference frequency of 600 Hz was used to trigger the lasing and tuning pulses. The tuning section of the laser was heated using a train of 10-μs-long current pulses at a repetition rate of 8.21 kHz. This frequency was optimised to the Bolometer

detector responsivity. A second pulse generator was used to drive the lasing section above threshold using single 500-ns-long pulses, which were triggered using the same 600-Hz reference. Under these driving conditions, the laser driving pulse was much shorter than both the duration of the tuning pulse and the intra-pulse thermal time-constant of the QCL (1–2 μ s) [192]. As such, the temperature of the tuning section was kept approximately constant over the duration of the lasing pulse. This allowed the spectrum of the laser to be measured while the temperature of tuning section was controlled.

Spectral measurements were performed using the same FTIR spectrometer and Ge:Ga bolometric detector, described in section 2.3. The lock-in amplifier used to recover the signal from the detector was synchronised with the lasing pulses. The tuning pulses and all associated electronic systems were synchronised with the 600-Hz reference frequency. The experimental setup used for the spectral characterisation of coupled cavity QCLs is shown in Figure 5.18.

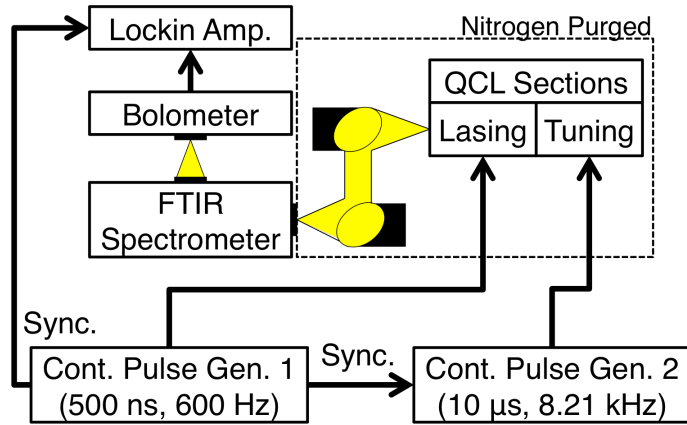


Figure 5.18: Schematic diagram of the experimental setup for measuring spectra from a coupled cavity QCL.

Two approaches to controlling the electrical heating of the tuning section and its effect on the emission spectrum of the device were explored. In the first instance, the delay between the start of the tuning section pulse and the shorter lasing pulse was varied, with the amplitude of the tuning pulse being kept constant. In pulsed operation, the temperature of the active region evolves with time and increases progressively before reaching a thermal equilibrium [194]. A steady-state temperature of the tuning section is expected to be reached with a 1–2- μ s intra-pulse thermal time-constant [192]. Thus, the 10- μ s-wide tuning pulses ensured thermal equilibration. A similar gradual decline in temperature is also

observed after the pulse off state. Hence, the first measurement technique allows the instantaneous spectrum to be sampled (in the time domain) as the temperature of the tuning section varied [Figure 5.19].

In the second approach, the amplitude of the tuning-section pulse was varied (while maintaining currents below the lasing threshold). The delay between the lasing and tuning pulses was kept constant at 8 μs , so as to reach a thermal equilibrium in the tuning section before the laser was switched on. This allowed greater control over the heating of the tuning section. Through these two approaches, both the dynamic and steady state thermal response of the device could be investigated.

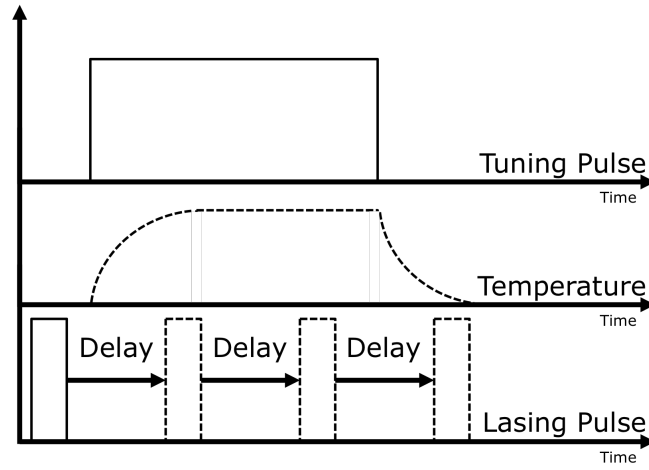


Figure 5.19: Schematic diagram of a wide tuning pulse and the resulting temperature profile at the tuning section. Time-resolved sampling of the laser performance is achieved by systematically varying the delay between the wide tuning pulse and the narrow laser pulse over the duration of the thermal transients.

5.6 Experimental results

5.6.1 Electrical characterisation

LIV characteristics were obtained independently from each section [Figure 5.20 (a, b)] of coupled-cavity device 5A, while keeping the other section unbiased. The LIV characteristics obtained before FIB milling are also shown in Figure 5.20 (c). The THz power emitted from each section of device 5A was lower than that obtained before milling, owing to the reduced cavity length. The individual sections exhibited identical threshold current densi-

ties, which were comparable with that observed before FIB milling. Similar behaviour was observed for device 5B. The THz power emitted from both sections was comparable in the device designed for adjacent mode-hopping (device 5A). However, in the device designed for alternate mode hopping (device 5B), the power emitted from the shorter section was lower than that in the longer section.

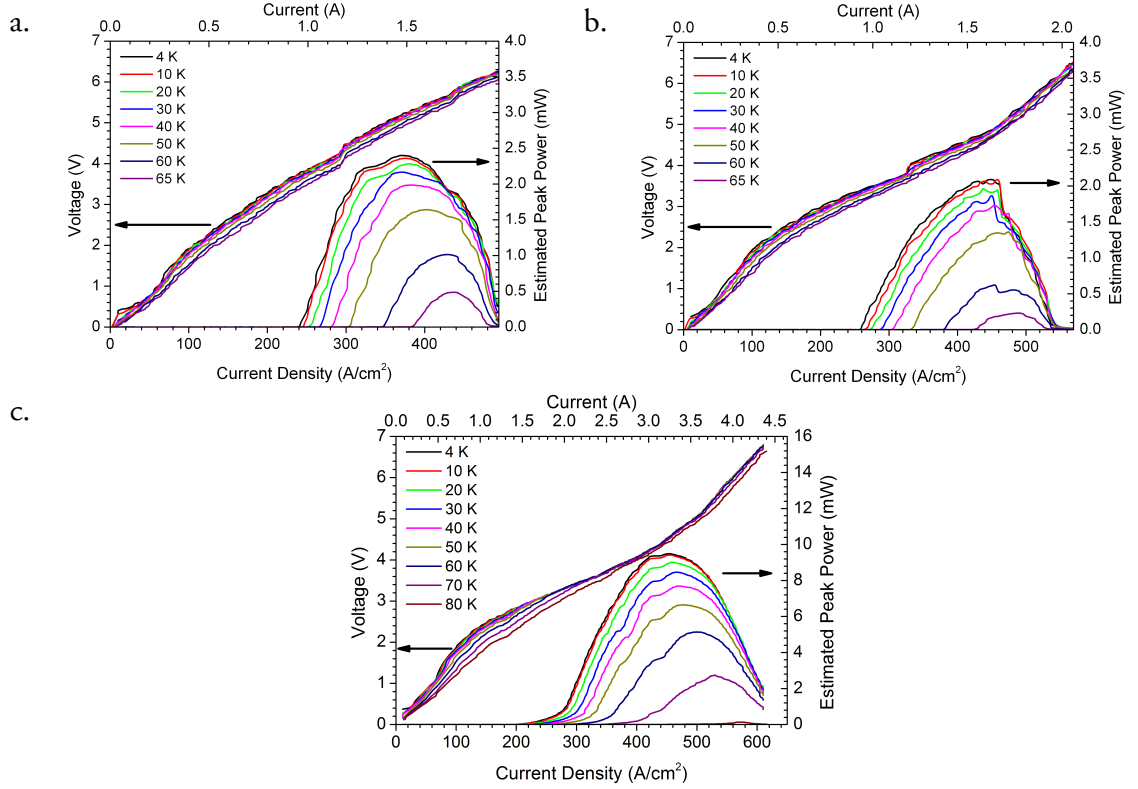


Figure 5.20: LIV characteristics obtained at different heat-sink temperatures after FIB milling (device 5A): (a) longer and (b) shorter sections of comparable lengths. (c) LIV characteristics obtained before FIB milling.

5.6.1.1 THz power stability

An important aspect of our coupled-cavity approach is that the emitted power remains constant as the tuning power is varied, as shown in Figure 5.21. In conventional devices, the change in lasing frequency is accomplished through control of the laser driving current, which also leads to significant changes in the emitted power. Conversely, in our coupled-cavity devices, the tuning is accomplished through adjusting the bias on the tuning-section while the lasing section bias is kept constant. As such, the effect on the gain of the device is very weak.

Power emitted from the lasing section was characterised using a range of tuning section currents. The emitted power varied within a few tens of microwatts with respect to tuning current while the lasing section current was kept constant. This variation is within the tolerance limits of the bolometric detection system and could be caused by external influences independent of device configuration. The variation of the emitted power as a function of tuning section current from device 5A is shown in Figure 5.21. A similar behaviour was also observed in device 5B.

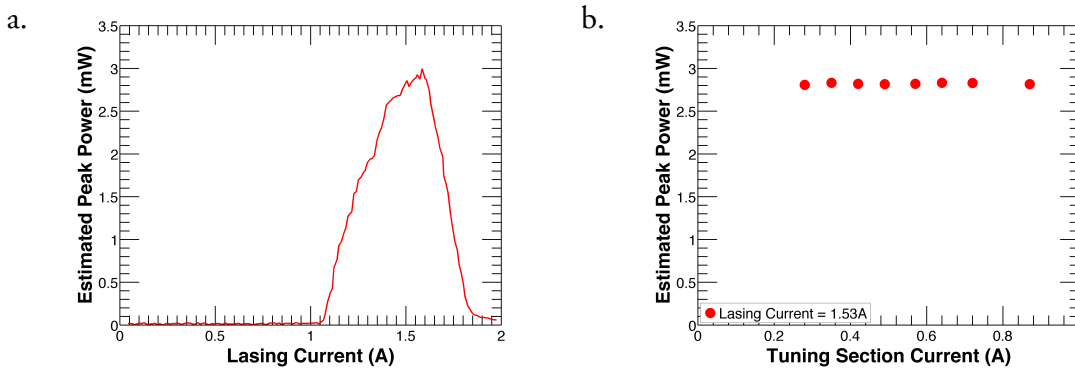


Figure 5.21: (a) Light-current (LI) characteristics of the lasing section. (b) Variation of the emitted power from the lasing section as a function of current in the tuning section. Data from device 5A.

5.6.2 Spectral characterisation

5.6.2.1 Device 5A: Design 1

The device was initially characterised with the shorter cavity as tuning section and the longer section as the lasing section. The device was subsequently characterised by swapping the functions of the lasing and the tuning sections with the shorter cavity as the lasing section, so as to reverse the direction of the frequency shifting.

5.6.2.1.1 Shorter cavity as the tuning section

A reduced emission bandwidth in the range of 2.75–2.80 THz was observed after FIB milling (compared with 2.70–2.85 THz in the single-ridge device). This reduction is likely to be caused by an increase in mirror losses arising from the roughened facets of the milled gap [195].

The amplitudes of the tuning and lasing pulses were initially set as 800 mA (corresponding to a tuning power of 3.85 W) and 1.53 A, respectively. As the lasing pulse was delayed relative to the rising edge of the tuning pulse, the emission was observed to hop from 2.755 THz to 2.770 THz, before reaching a steady-state value of 2.785 THz for delays greater than ~ 100 ns [Figure 5.22 (a)]. When the lasing pulse was delayed beyond the trailing edge of the tuning pulse, the emission hopped back to 2.755 THz. The weighted average of the emission frequency, revealing the mean power distribution amongst the lasing modes, plotted as a function of the delay, maps these spectral transitions, as shown in Figure 5.22 (b). The observed behaviour is due to the dynamic heating and cooling of the tuning section in response to the wide heating pulse, which results in a temporal variation of the refractive index. As can be seen, a short thermal equilibration time (< 1 μ s) is observed, which is consistent with the 1–2- μ s intra-pulse thermal time-constants previously reported for THz QCLs [192].

In the second measurement approach, the amplitude of the tuning pulse was varied, while the time-delay was fixed at 8 μ s to ensure thermal equilibration of the tuning section. Single-mode emission was observed at 2.755 THz by applying a current of 1.53 A to the lasing section only [Figure 5.22 (c)]. As the tuning power was increased above ~ 600 mW, a second mode was observed at ~ 2.770 THz, with the power distribution shifting progressively to the higher frequency mode as the tuning power is increased. At higher tuning power, further modes at 2.785 THz and 2.800 THz were observed. This observed hopping between modes spaced by 15 GHz, over a ~ 50 -GHz bandwidth, matches closely the simulated behaviour [Figure 5.13 (a)].

The weighted average of the measured emission frequency increased monotonically with respect to the tuning power [Figure 5.22 (d)]. A value of $df/dP = 8.3$ GHz/W was obtained from the linear fit to the data. Based on the normalized thermal resistance ($R_{Th}^* \approx 31.7$ Kcm/W), a frequency tuning of the coupled cavity was calculated as $df/dT = 840$ MHz/K, which was much higher than the frequency tuning of a standard device $df/dT = 63$ MHz/K. The corresponding variation of the weighted emission frequency with tuning power obtained from the simulation is also shown in Figure 5.22 (d). Despite the simulation accounting for neither Joule heating within the lasing section, nor heat conduction between the two sections of the device, an excellent agreement between the simulated and the experimental behaviour is observed.

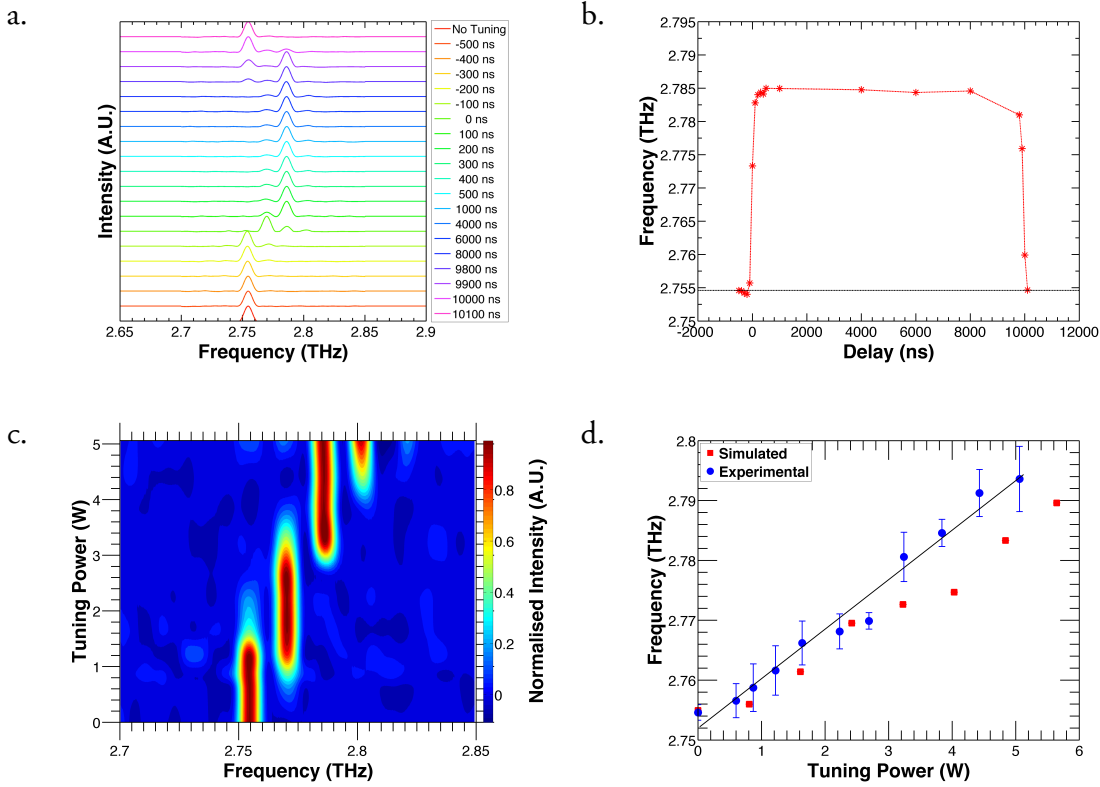


Figure 5.22: Experimental data obtained from device 5A, with tuning power applied to the short tuning section. (a) Spectral evolution and (b) weighted mean of spectral power density (SPD), as a function of the delay between the lasing and tuning pulses, as the former is scanned through the wider tuning pulse. The horizontal line in (b) shows the mean SPD when no current is applied to the tuning section, and serves as a reference. (c) Spectral evolution as tuning power amplitude varies. (d) Weighted mean of the SPD from experimental and simulated data shown in Figure 5.13 (a), as a function of tuning power. Error bars in the experimental data correspond to weighted standard deviation.

5.6.2.1.2 Longer cavity as the tuning section

The device was characterised following identical procedures but with the longer cavity as the tuning section. However, owing to limitations of the device packaging, emission was collected from the facet of the longer cavity. A red shift of frequency was observed in this alternate configuration, as predicted by the simulated model.

Emission with a dominant frequency of 2.78 THz and additional peaks at 2.795 and 2.765 THz was observed when no tuning current was applied. This multi-mode emission can result from an additional optical path introduced by longer tuning section from where

radiation was collected and the shorter air gap, which affects the spurious mode suppression.

The amplitudes of the tuning and lasing pulses were initially set as 720 mA and 1.35 A, respectively. As the lasing pulse was delayed relative to the rising edge of the tuning pulse, a single mode emission was observed at 2.765 THz for delays greater than ~ 100 ns [Figure 5.23 (a)]. When the lasing pulse was delayed beyond the trailing edge of the tuning pulse, the emission reverted back to the multiple mode emission with a dominant peak at 2.78 THz. The gradual red shift of frequency was observed from the weighted average of emission [Figure 5.23 (b)].

Similarly, as the power in the tuning section is increased, the spectral power distribution red-shifts towards the 2.765-THz mode, and single mode emission at this frequency is attained at a tuning power of ~ 2.3 W [Figure 5.23 (c)]. The weighted average of the emission frequency is shown in Figure 5.23 (d), revealing a red shift in frequency as the tuning power increases. A tuning coefficient $df/dT \approx -817$ MHz/K is obtained from this data. Note that this is similar (but with the opposite sign) to the result with the opposite configuration.

Although the tuning bandwidth obtained is narrow in this alternate configuration with the longer cavity as tuning section, this still acts as a proof-of-concept that the tuning direction can be changed by switching cavities. Such a design can be optimised further to extend the tuning range.

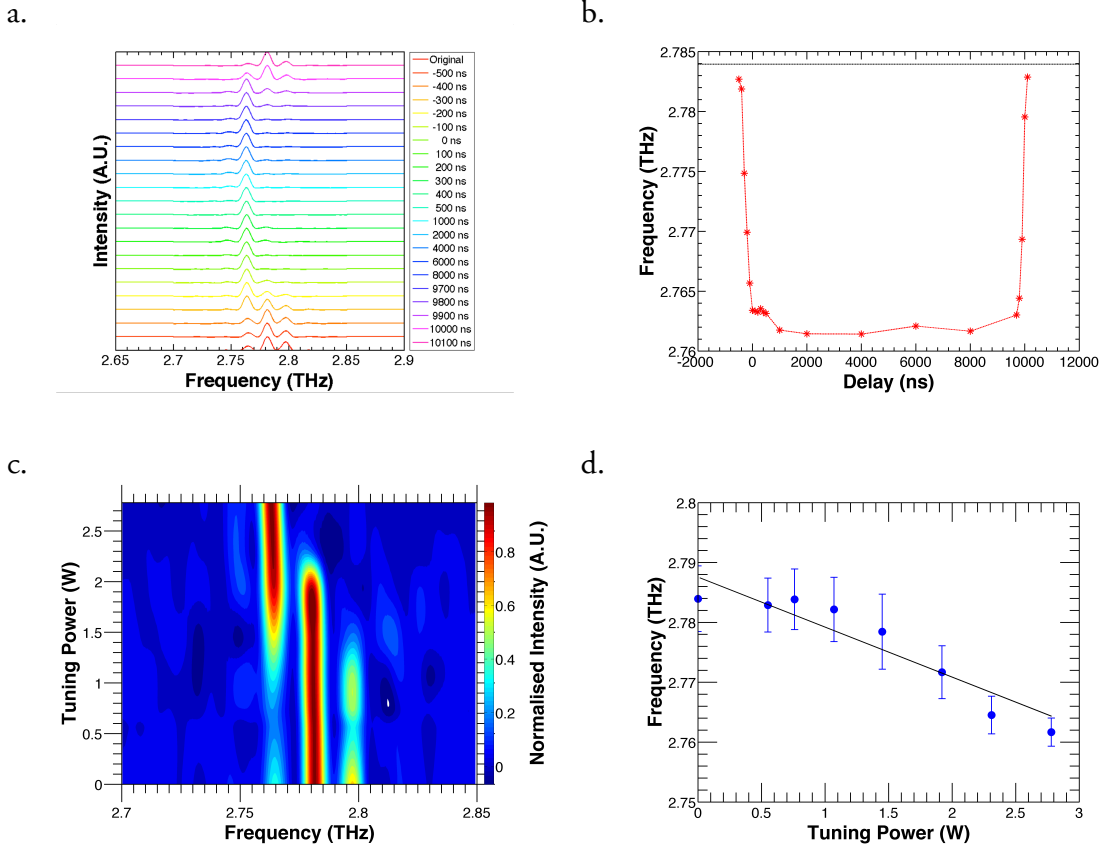


Figure 5.23: Experimental data obtained from device 5A, with tuning power applied to the longer section. (a) Spectral evolution and (b) weighted mean of SPD, as a function of the delay between the lasing and tuning pulses, as the former is scanned through the wider tuning pulse. The horizontal line in (b) shows the mean SPD when no current is applied to the tuning section, and serves as a reference. (c) Spectral evolution with applied tuning power at the longer tuning section. (d) Weighted mean of the SPD as a function of the tuning power. Error bars in the experimental data correspond to weighted standard deviation.

5.6.2.2 Device 5B: Design 2

The second device (device 5B) was characterised following identical procedures, with the longer cavity as the lasing section. In this device, the spectral evolution with tuning power was studied by varying the amplitude of the tuning power only.

5.6.2.2.1 Shorter cavity as the tuning section

Initially, the long section was used as the lasing section and the short section as the tuning section. The frequency spacing between the longitudinal modes of the tuning section in this configuration (~ 30 GHz) was almost twice that of device 5A (15 GHz), and more than

twice the mode spacing (12 GHz) expected for the 3.4-mm-long lasing section alone. As shown in Figure 5.24 (a), mode hopping from 2.740 THz (with no applied tuning power) to 2.825 THz was observed as the tuning power was increased, with intermediate mode hopping to 2.770 and 2.800 THz. This hopping observed between modes spaced by ~ 30 GHz over a range of ~ 85 GHz agrees well with simulations, which reveal hopping between alternate longitudinal modes of the lasing section as the tuning power is increased [Figure 5.14 (a)]. This increase in frequency spacing arises from the >2 ratio of the section lengths in this design. A value of $df/dP = 12.5$ GHz/W was calculated from the linear fit to weighted mean SPD [Figure 5.24 (b)].

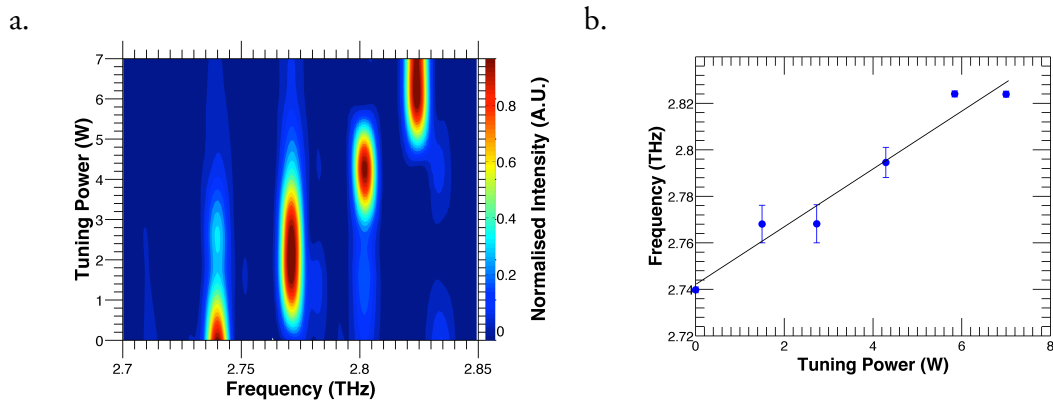


Figure 5.24: Experimental data obtained from device 5B with the shorter cavity as the tuning section. (a) Blue-shift of spectrum and (b) the mean SPD with a constant lasing section current of 2.03 A, when the tuning power is varied in the shorter section. Error bars indicate weighted standard deviation of the spectral distribution.

5.6.2.2.2 Longer cavity as the tuning section

Spectra were acquired by alternating the lasing and tuning sections to use the shorter cavity as the lasing section. Single-mode emission at 2.825 THz was observed in the absence of tuning current. By alternating the lasing and tuning sections, a red shift of 30 GHz from 2.825 THz to 2.795 THz was observed as the tuning power was increased [Figure 5.25]. It has been observed experimentally that devices with lengths shorter than ~ 1.5 mm lased predominantly at higher frequencies (~ 2.78 – 2.85 THz) for this wafer. Thus, the red-shift tuning range predicted by the simulations (2.77–2.70 THz) may be misrepresentative, with the actual red-shift being observed only within the lasing range of the shorter section (i.e. ~ 2.78 – 2.85 THz). Reversal of the tuning direction could be better evaluated in a wafer with a broader emission range.

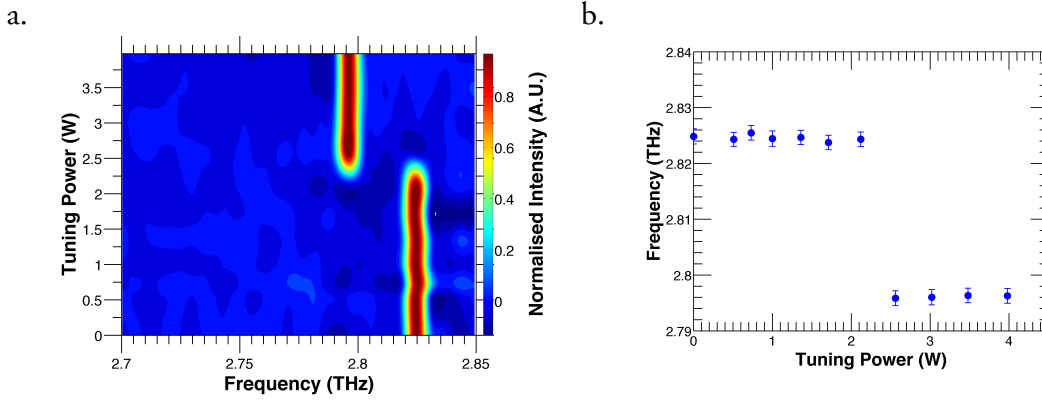


Figure 5.25: Experimental data obtained from device 5B with the longer cavity as the tuning section. (a) Red shift of spectrum and (b) the mean SPD with a constant lasing-section current of 0.95 A, when the tuning power is varied in the shorter section. Error bars indicate weighted standard deviation of the spectral distribution.

5.7 Summary

Discrete Vernier tuning of frequency using coupled cavity THz QCLs was investigated in this study. A simple two-cavity device separated by an air gap was used. One of the two cavities formed the lasing section and was driven above the lasing threshold. The second cavity, the tuning section, was used as an electrical control and was driven below the lasing threshold. Frequency tuning was investigated by perturbing the refractive index in the tuning section through localised current induced Joule heating.

Emission from the coupled cavity device was simulated using a transfer matrix based model. Normalised transmission through the lasing and the tuning section were calculated using this coupled model. Emission was predicted where a complete alignment of the longitudinal modes in the lasing and the tuning sections was obtained due to the lowering of lasing threshold. Two coupled cavity designs were implemented in which the laser cavity was split into two sections with approximate length ratios of either 1:1 or 2:1. Mode-spacings in these designs were predicted to correspond to adjacent or alternate FP modes in the lasing section, respectively. A reversal in tuning direction was predicted by swapping the functions of the lasing and the tuning section.

Coupled cavity devices were fabricated from a monolithic long THz QCL ridge with a single plasmon waveguide. An air gap separation was etched using a FIB milling system

after device packaging and initial characterisation. Due to the limitation imposed by the FIB workstation a narrow air gap was sculpted.

Discrete tuning of 50 and 80 GHz with a blue shift of frequency has been demonstrated from the fabricated devices. A red shift of around 20 and 30 GHz have been observed from the same devices by swapping lasing and tuning sections. The mode-spacings in the two devices were measured to be ~ 15 GHz and 27 GHz respectively, thus demonstrating frequency selectivity between adjacent or alternate FP modes in the lasing section. Additionally, power emission from lasing cavity was unaffected by the tuning. The flexible design methodology can be optimised further to extend the tuning range. A QCL active region with a wide bandwidth, such as the design reported in [85], could be used to obtain a larger tuning range.

The coupled cavity design also offers the possibility of further optimisation to obtain continuous tuning. An effort in this direction is discussed in the following chapter.

Chapter 6

Continuous tuning using coupled cavity QCLs

6.1 Introduction

Continuous tuning of terahertz (THz) quantum cascade lasers (QCLs) is an essential requirement for applications such as gas spectroscopy and heterodyne mixing [196–199]. Continuously tunable THz QCLs with a tuning range of around 25 GHz have been demonstrated by a combination of nitrogen condensation and deposition of dielectric materials on a third order DFB THz QCL [173]. However, a major limitation of this technique is the slow condensation/evaporation of nitrogen gas. Also, the deposition of dielectric material on the QCL ridge is an irreversible process. An electrically-controlled continuously tunable THz QCL is more suited to real world applications. An alternative approach based on an electrically-controlled discrete mode hopping of a THz QCL has been demonstrated using aperiodic photonic gratings in ref. [174]. These devices also allow fine continuous tuning of around 2-3 GHz. A similar range of continuous tuning of frequency was observed in THz QCLs with PLs by varying the heat sink temperature [Figure 3.18 (b)].

This chapter describes continuous tuning of frequency using coupled cavity THz QCLs. This technique is a modification of the discrete Vernier tuning mechanism described

in Chapter 5. The underlying design principle used in this study is identical to that described for discrete Vernier tuning. However, the devices were designed to reduce complete alignment of longitudinal modes between the lasing and tuning sections. These ‘*detuned*’ cavities operate on the partial alignment of longitudinal modes at the lasing and the tuning sections, allowing quasi-continuous frequency tunability between discrete Vernier modes.

In a second approach, devices were also fabricated featuring frequency selective structures like photonic lattices (PLs) to suppress discrete mode transitions. The PLs were patterned in the longer lasing section after packaging using focussed ion beam (FIB) milling. This post-packaging milling allowed device characterisation after each stage of processing. This allowed better evaluation of device performance and imparted flexibility in the designing of the PLs.

The PLs were designed to suppress multiple-mode hopping by introducing a stop band. Continuous tuning in this case was expected at modes at the edges of the stop band. Additionally, PLs with a central $\lambda/4$ -shifted element were also investigated. The $\lambda/4$ -shifted PL introduced a lasing mode at the centre of the stop band, at the Bragg frequency. Thus, a PL with a Bragg frequency at one of the Fabry–Pérot modes in the lasing section would exhibit an enhanced continuous tuning compared with that of a uniform PL.

Continuous frequency tuning using a detuned coupled cavity is described first. The premise for a detuned coupled cavity optimised for quasi-continuous tuning is discussed, followed by designing of two detuned coupled cavity designs. The experimental results obtained from the devices were compared with the simulated result.

In the second design, PLs were designed following identical procedure described in section 3.2. PLs with uniformly spaced gratings and with a central $\lambda/4$ element were designed. The stopband in the PLs were calculated from dispersion relation of the grating as well as a transfer matrix based network model. The effect of the PLs on the discrete mode hopping was modelled to predict frequency tuning. PLs were fabricated on coupled cavity devices, which were previously characterised to study discrete hopping. A focussed ion beam (FIB) milling system was used to pattern the PL gratings on the longer cavity section. Devices were subsequently characterised and their results compared with the simulation.

6.2 Quasi–continuous tuning using detuned coupled cavity QCLs

6.2.1 Theory of detuned coupled cavity QCLs

The coupled cavity designs discussed in the previous chapter were optimised to obtain a complete alignment of longitudinal modes in the lasing and the tuning sections at a resonant frequency. Emission was favoured in this resonant frequency due to the lower lasing threshold. A current induced perturbation of the refractive index resulted in a change in the longitudinal modes in the tuning section. The cavity lengths were chosen such that this index perturbation resulted in a progressive shift in the resonant frequency analogous to a Vernier tuning. This tuning mechanism is illustrated in Figure 6.1, where the longitudinal modes in the lasing and the tuning sections are plotted as the tuning current is increased.

A closer inspection of the longitudinal modes in Figure 6.1 reveals that increasing the tuning current shifts the longitudinal modes in the tuning section. This detunes the initial resonance at 2.755 THz and results in partial alignment of modes (Figure 6.1, red coloured box region). In fact, this transition from a complete alignment to a misaligned state and vice versa exists at all modes (Figure 6.1, blue, green and black coloured box regions for discrete modes at 2.78, 2.805 and 2.825 THz respectively).

The detuned coupled cavity design aims to disrupt this step–wise shift in resonance that facilitated the discrete Vernier tuning. Instead, the cavity lengths are modified to attain ‘*partial alignment*’ of longitudinal modes at the two cavities. In the absence of complete alignment, the lasing threshold is lowered where there is a greater overlap between the modes. Quasi-continuous tuning is then obtained from such designs by changing the frequency at which this partial alignment of the longitudinal modes occurs by varying both the lasing and tuning current.

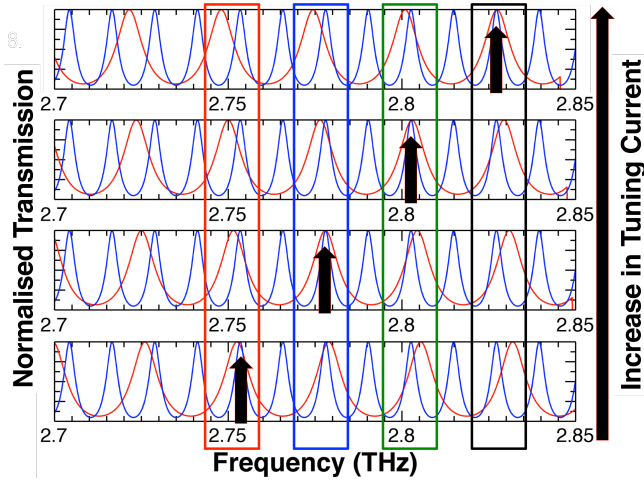


Figure 6.1: Normalised transmission in a coupled cavity device with a 3.4-mm long lasing section (red), 1.5-mm long tuning section (blue) and a 16- μm wide air gap (design 2, Chapter 5). The coupled cavity has a resonant frequency of 2.755 THz when no tuning current is applied (bottom panel). Increasing the tuning current changes refractive index of the tuning section and shifts the alignment as indicated by arrows (top three panels, tuning current is increased to a maximum bias in the top panel). The shift of alignment results in partially aligned detuned states. The misalignments of the longitudinal modes are highlighted in coloured rectangle boxes.

The longitudinal modes at the lasing and the tuning section in such a detuned device are simulated using the cascaded transfer matrix model discussed in section 5.3. The normalised transmission in such a device is shown in Figure 6.2. A change in the longitudinal mode of the tuning section is simulated by varying the heating current. However, the shift in the alignment does not follow the progressive shift in resonance as observed in devices for discrete Vernier tuning. In such detuned coupled cavity devices, greater control over alignment can be achieved by perturbing the refractive index in both lasing and tuning sections. In this study the longitudinal modes at the two sections were controlled simultaneously by varying the drive currents as well as the heat sink temperature. Two detuned coupled cavity devices were designed following this principle, and are discussed next.

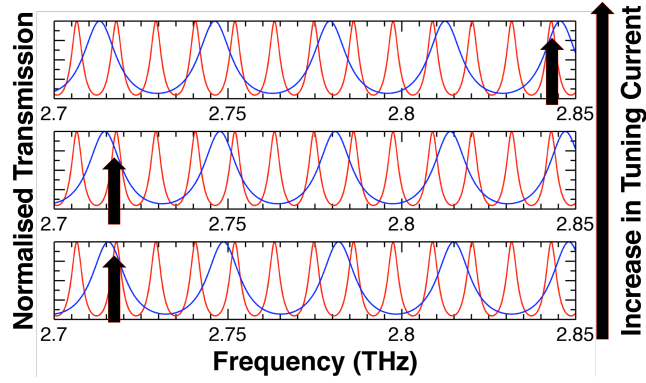


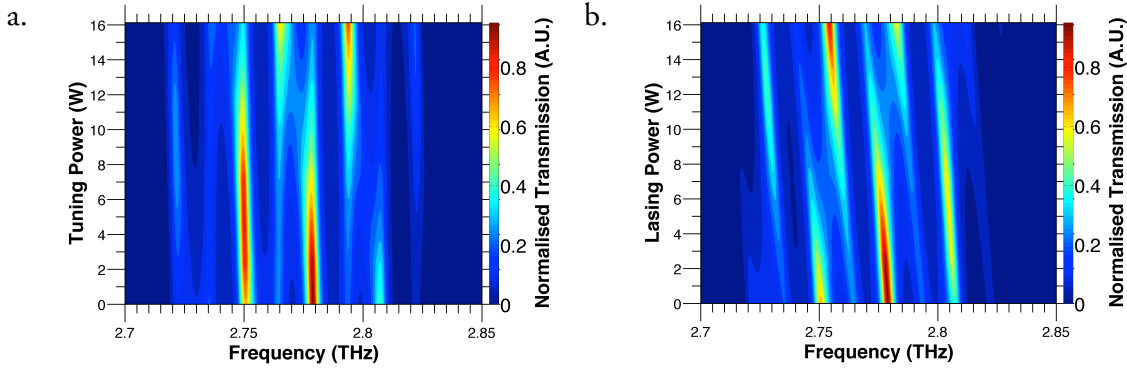
Figure 6.2: Normalised transmission in a detuned coupled cavity device with a 3.6 mm long lasing section (red) and 1.3 mm long tuning section (blue). The longitudinal modes at the lasing and tuning sections are partially aligned. The modes with maximum longitudinal mode overlap are marked with arrows. Increasing tuning current does not result in a monotonic shift in resonance.

6.2.1.1 Detuned coupled cavity design

Cavity lengths were chosen such that the longitudinal mode spacing at the tuning section was more than twice as much as that in the lasing section, as is evident from longitudinal modes in Figure 6.2. Initially, the alignment of longitudinal modes was simulated, as a function of the change in the tuning section current (with a constant lasing section current) and the lasing section current (with constant tuning section current), at constant heat sink temperature.

A detuned coupled cavity device from L701 (Design 1) was designed with a 2.96-mm long lasing section and a 1.65-mm long tuning section. The two sections were separated by a 13.73- μm wide air gap. A complete alignment of longitudinal modes was observed at ~ 2.75 and 2.78 THz when the current was varied at the tuning section only, [Figure 6.3 (a)]. Partial alignment of longitudinal modes is evident where the amplitude of the transmission intensity is less than unity but greater than zero. The salient feature of this design was the possibility of selecting different frequencies, where the alignment of longitudinal modes from lasing and tuning sections were comparable. For example, heating the tuning section with input power of $\sim 10\text{--}12$ W results in identical alignment of longitudinal modes at 2.75, 2.765, 2.78 and 2.795 THz. By carefully controlling the current in the tuning section, each mode can be selected.

A similar behaviour was observed when the current was varied at the lasing section only, with a constant tuning section current [Figure 6.3 (b)]. In this case, complete alignment of longitudinal modes was observed at ~ 2.78 and 2.76 THz. With a lasing section heating of ~ 6 – 8 W, longitudinal modes with identical alignment were observed at ~ 2.725 , 2.75 , 2.76 , 2.79 and 2.81 THz.



Detuned Design 1

Figure 6.3: Normalised product of transmission at lasing and tuning section as a function of heating power. Results from a detuned coupled cavity design with a 3.0-mm long lasing section, 1.6-mm long tuning section and a $16\text{-}\mu\text{m}$ wide air gap: (a) Heating power varied at the tuning section only. (b) Heating power varied at the lasing section only. Distribution of alignment is represented as a colour contour with red being complete alignment and dark blue being misalignment.

In addition to the variation of the current (or conversely the heating power) at the lasing and the tuning sections, the possibility of obtaining quasi-continuous tuning from these detuned devices was studied by varying heat sink temperature to ~ 60 K. Schematic diagram of the variation of these three parameters used to simulate quasi-continuous tuning is shown in Figure 6.4. The combined effect of these three factors on the alignment of longitudinal modes is presented in Figure 6.5. It can be observed that through careful selection of these three parameters frequency tuning from ~ 2.75 – 2.80 THz is possible. The nature of the frequency tuning is essentially discrete mode hopping amongst closely spaced modes, where longitudinal modes at the lasing and the tuning sections attain maximal relative alignment. A careful examination of the alignment would also reveal that there exists certain frequencies where no alignment of longitudinal modes is achieved, for e.g. at ~ 2.765 and 2.795 THz. Thus, the predicted tuning in these devices is essentially quasi-

continuous in nature. It is also worth noting that the variation of current at the lasing section would imply a variation in the emitted power. Increasing the heat sink temperature would also decrease the emitted power further.

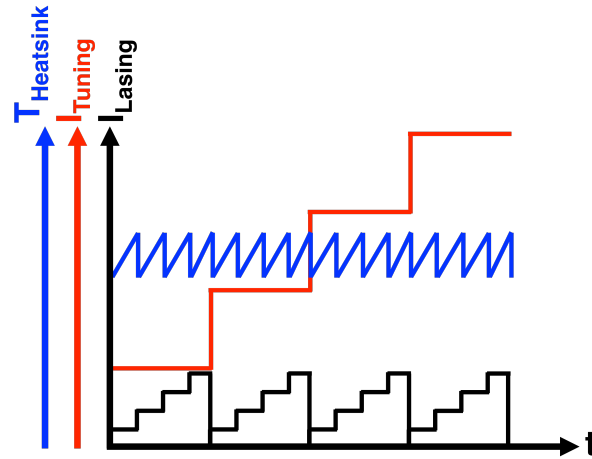
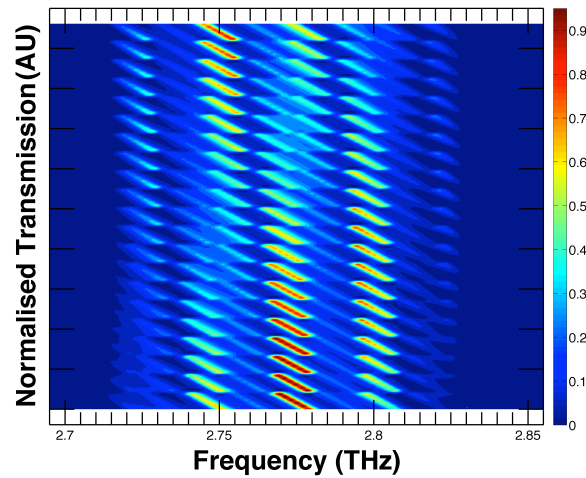


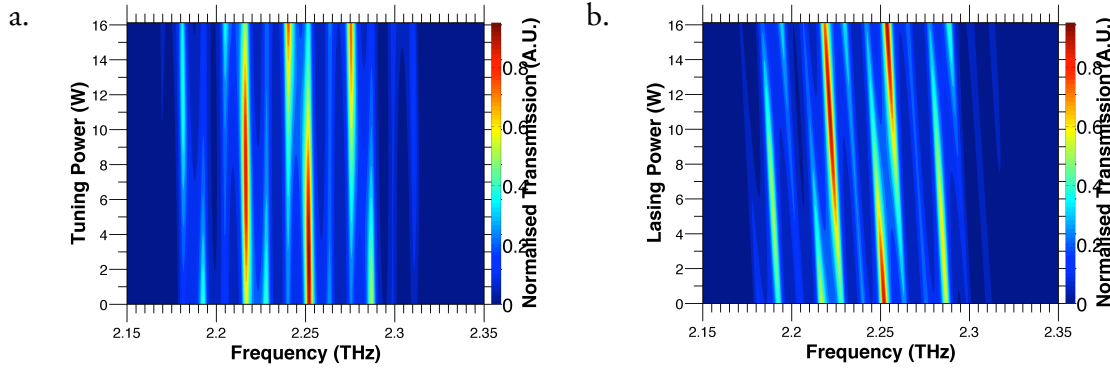
Figure 6.4: Schematic diagram of the variation of the current at the lasing and tuning section and the heat sink temperature used to simulate quasi-continuous tuning.



Detuned Design 1

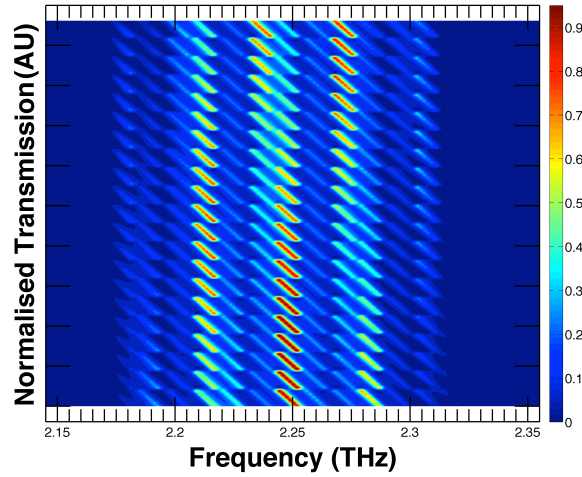
Figure 6.5: Normalised product of transmission at the lasing and the tuning section. Results from a detuned coupled cavity from L701 with a 3.0-mm long lasing section, 1.6-mm long tuning section and a 16- μm wide air gap. Current at both the lasing and the tuning sections, and heat sink temperature are varied. Distribution of alignment is represented as a colour contour with red being complete alignment and dark blue being misalignment.

A similar design was adopted for a device from wafer L1007 (Design 2). A detuned coupled cavity device was designed with a 3.52-mm long lasing cavity, 1.29-mm long tuning cavity and an air gap separation of 16.96 μm . This device exhibited complete alignment of longitudinal modes at ~ 2.225 and 2.250 THz when the current was varied at the tuning section only, as shown in Figure 6.6 (a). Similarly, complete alignment was observed at 2.225 and 2.260 THz when the current was varied at the lasing section only with a constant tuning section current [Figure 6.6 (b)]. Quasi-continuous frequency tuning in the range of 2.21–2.29 THz was predicted, when all three tuning parameters (current to the lasing and tuning sections, and heat sink temperature) were varied [Figure 6.7]. A complete misalignment of longitudinal modes was observed at ~ 2.23 and 2.265 THz, similar to the design shown in Figure 6.5.



Detuned Design 2

Figure 6.6: Normalised product of transmission at lasing and tuning section as a function of heating power. Results from a detuned coupled cavity design from L1007 with a 3.5-mm long lasing section, 1.2-mm long tuning section and a 16- μm wide air gap: (a) Heating power varied at the tuning section only. (b) Heating power varied at the lasing section only. Distribution of alignment is represented as a colour contour with red being complete alignment and dark blue being misalignment.



Detuned Design 2

Figure 6.7: Normalised product of transmission at lasing and tuning section from a detuned coupled cavity from L1007 with a 3.5 mm long lasing section, 1.2 mm long tuning section and a 16 μm air gap. Current at both lasing and tuning sections, and heat sink temperature are varied. Distribution of alignment is represented as a colour contour with red being complete alignment and dark blue being misalignment.

6.2.2 Fabrication

The detuned coupled cavity devices were fabricated following identical processing steps discussed in the previous chapter. The following table tabulates the device specification.

Table 6.1: List of processed detuned coupled cavity THz QCLs.

Device Number	Device Unique ID	Lasing Cavity (mm)	Tuning Cavity (mm)	Air Gap (μm)
6A	L701-S21-D2	3.117	1.495	10.00
6B	L1007-S1-D2	3.527	1.288	16.57

The experimental setup used for the characterisation is discussed next.

6.2.3 Experimental setup

Coupled cavity devices were characterised following identical characterisation techniques, as described in section 5.5. Spectra were acquired at different current applied to the tuning

section. Wider current pulses (10, 20, 30 and 95 μs) were applied to the tuning section. The narrow lasing current pulses were synchronised with the tuning pulses and were delayed by 8, 17, 27 and 90 μs delay respectively. Devices were also characterised with a DC current applied to the tuning section. In order to increase current-induced Joule heating in the tuning section, it was biased with high current with negative polarity from -2 A to 0.9 A. The reversal of polarity of the bias allowed higher current without causing the tuning section to lase. The experimental setup for DC tuning section characterisation is shown in Figure 6.8.

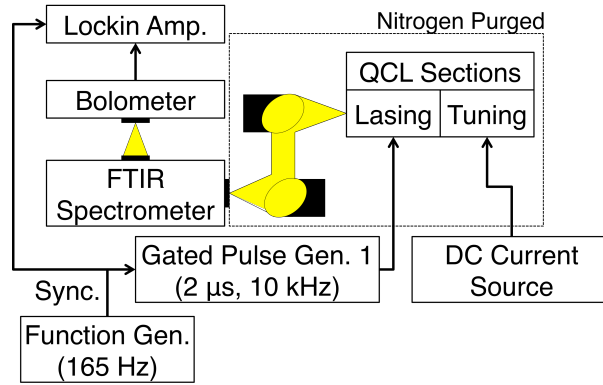


Figure 6.8: Schematic diagram of experimental setup for measuring spectra from detuned coupled cavity QCLs.

The fabricated devices were characterised to study the spectral characteristics and is discussed next.

6.2.4 Experimental results

Spectra from the detuned coupled cavity devices were recorded as the current to the lasing section was varied. The current applied to the tuning section was varied in the following configurations:

1. Pulse mode operation:
 - a. Varying the amplitude of the tuning current pulses.
 - b. Varying the width of the tuning current pulses between 10–95 μs .
2. DC operation:
 - a. Varying the amplitude of the tuning current.

The recorded spectra, collected with different tuning current configuration (noted above), were collated and compared with the simulated results.

6.2.4.1 Design 1: Device 6A

Spectra from the detuned device 6A were acquired with the lasing section current at 1.73 A and 2.29 A. First, tuning pulse widths of 10 and 95 μ s were applied to the tuning section. This was followed by characterisation with a DC tuning current. To evaluate the continuous tuning from the detuned devices, the weighted mean of the spectral power density (SPD) of the emission was also calculated.

A single mode (SM) emission was observed at ~ 2.785 THz, when the lasing section was driven at 1.73 A with no applied current on the tuning section [Figure 6.9 (a)]. For the same lasing section current, varying the amplitude of the tuning pulses resulted in a continuous tuning of ~ 1 GHz [Figure 6.9]. This continuous tuning is evident from the weighted mean of the SPD [Figure 6.9 (b, d, f)]. At higher pulsed tuning currents, discrete hopping to ~ 2.763 THz was observed [Figure 6.9 (a–d)], while with a DC tuning current discrete hopping to ~ 2.817 THz became possible [Figure 6.9 (e, f)].

A similar SM emission at ~ 2.785 THz was observed when the lasing drive current was increased to 2.29 A [Figure 6.10 (a)]. With pulsed current applied to the tuning section, additional peaks appeared at ~ 2.763 and ~ 2.817 THz [Figure 6.10 (c, e)]. Applying a DC current from -1.90 – 0.90 A resulted in a continuous tuning of ~ 3 – 4 GHz, at ~ 2.773 and ~ 2.785 THz [Figure 6.10 (e, f)]. Additional modes at ~ 2.75 and ~ 2.761 THz was also observed. The increase in Joule heating at the tuning section, due to the DC bias with negative polarity, resulted in the continuous tuning at the two frequency peaks. Thus, a greater control over localised Joule heating within the tuning section was possible by using a DC current with negative polarity. However, a high DC of 2 A shorted the electrical contacts and damaged the device [Figure 6.11], preventing further characterisation.

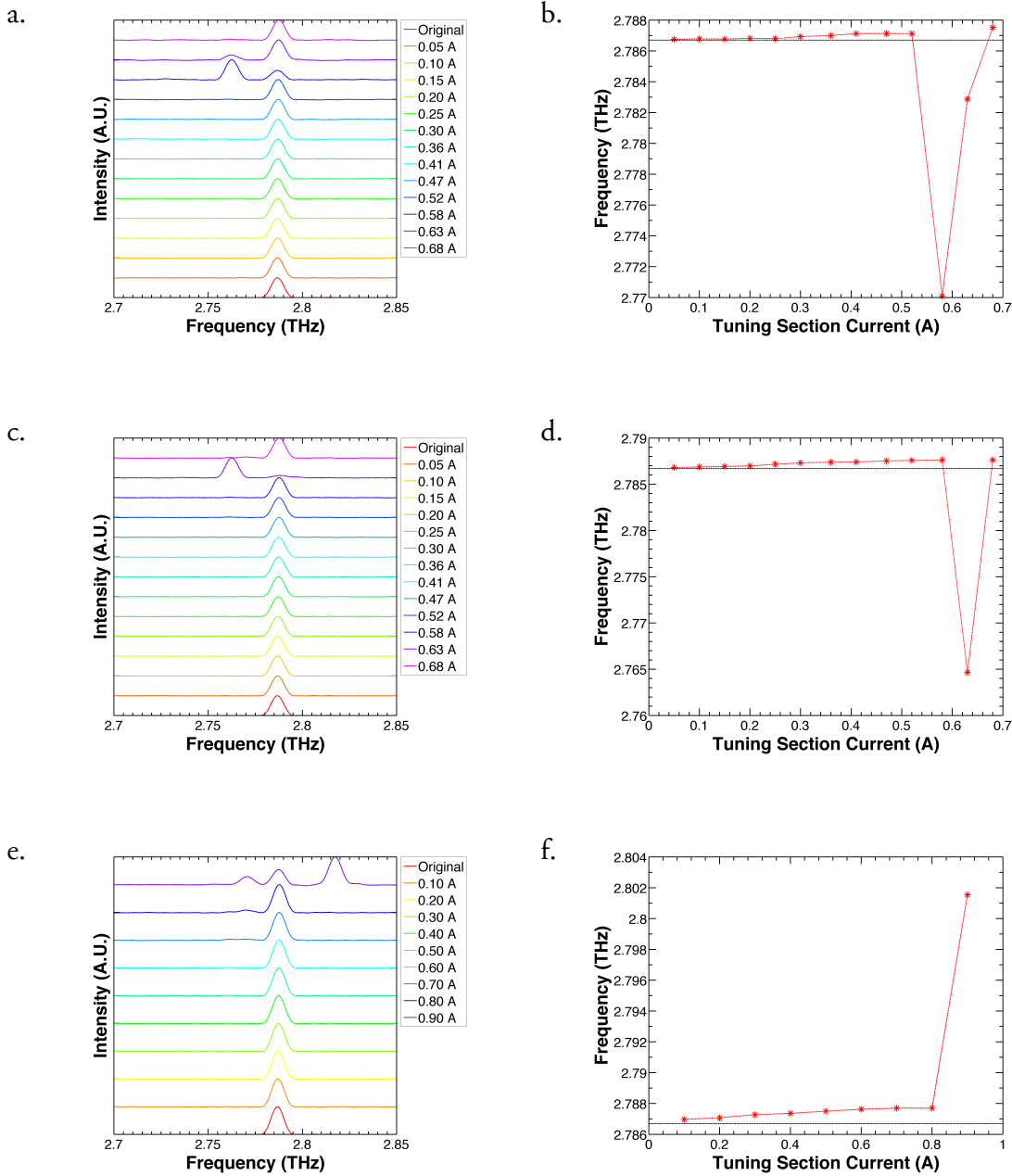


Figure 6.9: Spectra and the corresponding weighted mean of the SPD from de-tuned coupled cavity device 6A. Lasing section current of 1.73 A. Tuning section heated with: (a) 10 μ s and (b) 95 μ s wide pulses, and (c) with DC current. SPD is plotted as a function of the tuning section current is shown (b, d, f). The horizontal line shows the mean SPD when no current is applied to the tuning section, and serves as a reference.

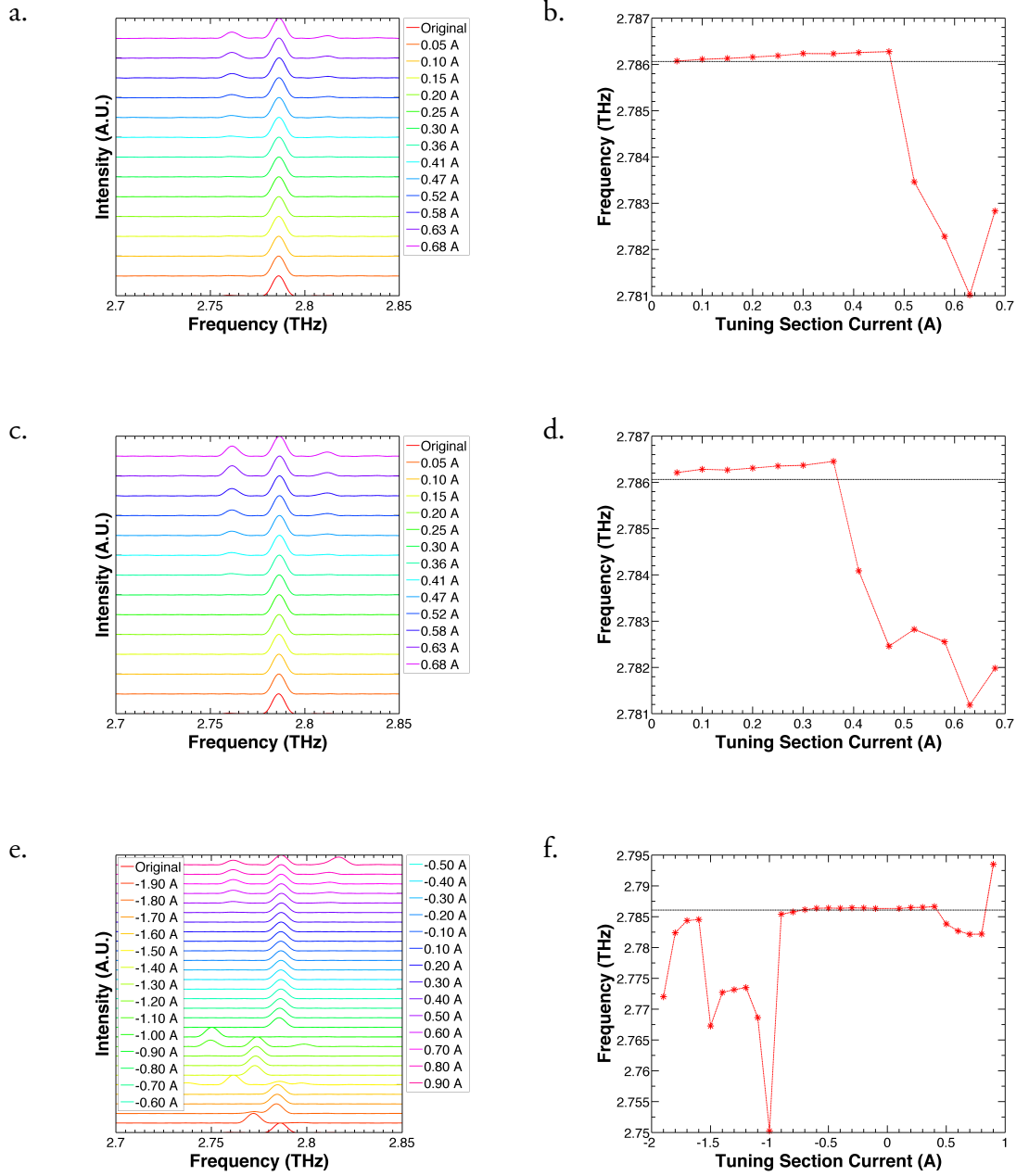


Figure 6.10: Spectra and the corresponding weighted mean of the SPD from detuned coupled cavity device 6A. Lasing section current of 2.29 A. Tuning section heated with: (a) 10 μ s and (b) 95 μ s wide pulses, and (c) with DC current. SPD is plotted as a function of the tuning section current is shown (b, d, f). The horizontal line shows the mean SPD when no current is applied to the tuning section, and serves as a reference.

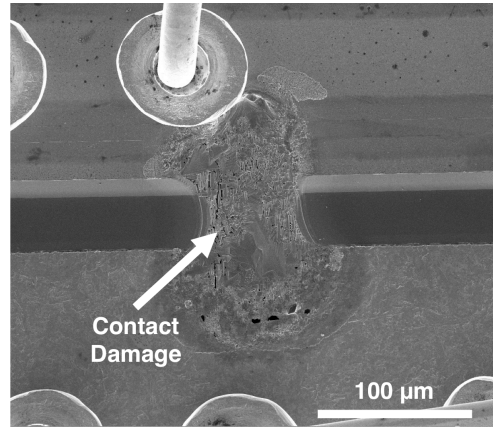


Figure 6.11: Scanning electron microscopy of damage to device 6A after high DC negative current operation. The electrical contacts to the device were shorted.

A cumulative tuning range of ~ 67 GHz was observed from device 6A. A continuous tuning of ~ 5 GHz and ~ 3 -4 GHz was observed at 2.785 and 2.773 THz from the collated data [Figure 6.12]. The observed discrete transitions correspond well to the simulated results [Figure 6.3]. The continuous tuning observed experimentally agrees well with the simulated data shown in Figure 6.5. However, the simulated continuous tuning range is greater than 5 GHz, as the simulation assumed a change in heat sink temperature of ~ 60 K. In the experiments, the heat sink temperature was varied by a maximum of 10 K.

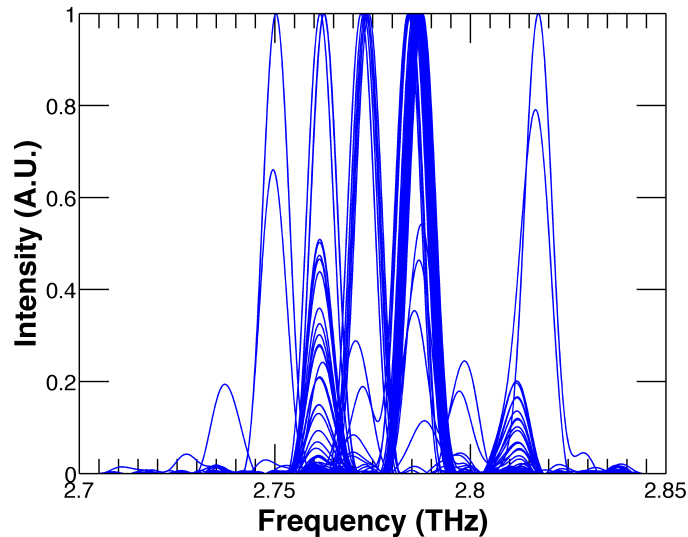


Figure 6.12: Collated spectra from detuned coupled cavity device 6A.

6.2.4.2 Design 2: Device 6B

Spectra from device 6B was characterised with the tuning section biased in pulsed mode only. DC operation of the tuning section was avoided to prevent damage to device.

Emission was recorded at different lasing drive currents [Figure 6.13]. Without any tuning current, SM emission was observed at 2.217 and 2.25 THz. This corresponds well with the results obtained from simulation, where maximal alignment was predicted at these frequencies [Figure 6.6 (a)]. The amplitude and the pulse width of the tuning pulses were varied and the corresponding change in spectra was recorded [Figure 6.13].

The collated spectral data from the device is shown in Figure 6.14. A tuning range of ~ 100 GHz is observed, with continuous tuning of ~ 6 GHz is evident at 2.25 THz. The range of emission peaks recorded from this device exceeds the maximum discrete tuning of ~ 80 GHz (device 5B in the previous chapter). The experimental result agrees well with the simulated data shown in Figure 6.7. The density of the emission peaks were higher than that observed for discrete Vernier devices. Eight frequency peaks were observed over a 50 GHz range from 2.21–2.26 THz, which can be attributed to the cavity dimensions and the detuned alignment. The results could be improved further by increasing the heat sink temperature, as is predicted in Figure 6.7, which assumes an increase in heat sink temperature by ~ 60 K. However, the poor dynamic range of the wafer L1007 at higher temperatures (Figure 2.20, compared to a similar dynamic range from wafer L701 shown in Figure 3.12) limited such attempts.

The closely spaced discrete tuning observed in device 6B shows great improvement over the detuned design 1 (device 6A). The former had a greater density of emission peaks. This is due to the smaller longitudinal mode spacing at the lasing section in device 6B. The detuned cavity designs can be improved further by including a longer lasing cavity. Continuous tuning over a large range of frequencies can be obtained, when the longitudinal mode spacing in the lasing section is comparable to the maximum current induced shift of longitudinal modes in the tuning section. In such a cavity, a perturbation to the longitudinal modes at the tuning section would favour a neighbouring longitudinal mode at the lasing section. Design and implementation of such detuned cavity devices has been left as a future work.

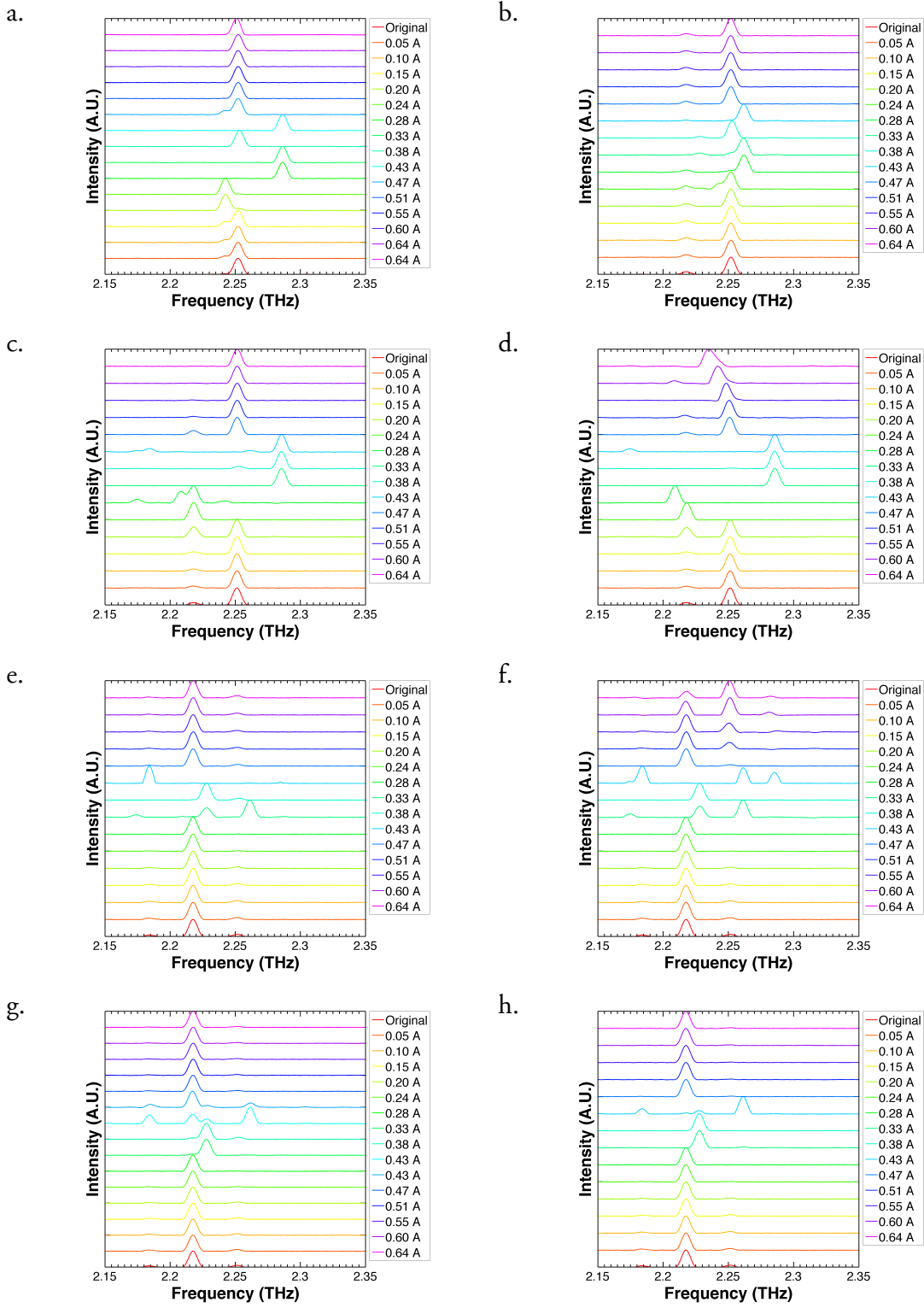


Figure 6.13: Spectra from detuned design 6B: at different lasing section bias and (tuning section pulse width): (a) 0.83 A (20 μ s), (b) 1.20 A (20 μ s), (c) 0.95 A (20 μ s), (d) 0.95 A (95 μ s), (e) 1.06 A (20 μ s), (f) 1.06 A (95 μ s), (g) 1.13 A (20 μ s), (h) 1.13 A (95 μ s).

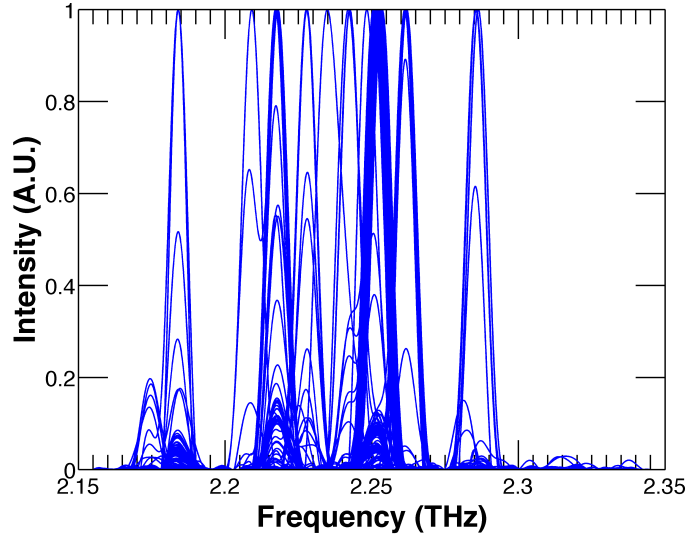


Figure 6.14: Collated spectra from detuned coupled cavity device 6B.

6.2.5 Discussion

It can be concluded from Figure 6.12 and Figure 6.14 that detuned coupled cavity designs have greater capability of selecting a larger number of longitudinal modes at the lasing cavity, than those designed for monotonic Vernier tuning. The closely spaced discrete hopping along with the continuous tuning observed at the lasing modes, yield quasi-continuous or narrow spaced discrete tuning.

The device designs can be improved further to enhance the continuous tuning range. The tuning range can be extended further by using a wide band QCL active region. Continuous tuning in THz QCLs was also investigated from coupled cavity devices by integrating frequency selective periodic structures, such as PLs into the lasing cavity. This is discussed in greater detail in the following section.

6.3 Continuous frequency tuning using photonic lattice

The underlying principle for this second design approach was to use a PL to introduce a stop band in the transmission spectra. The coupled cavity device 5B discussed in the previous chapter and the device 6B discussed in section 6.2.4.2, were used to investigate iteratively the effect of PLs. A schematic of a coupled cavity device with a PL is shown in Fig-

ure 6.15. The following section describes the theory and modelling of coupled cavity devices with a PL.

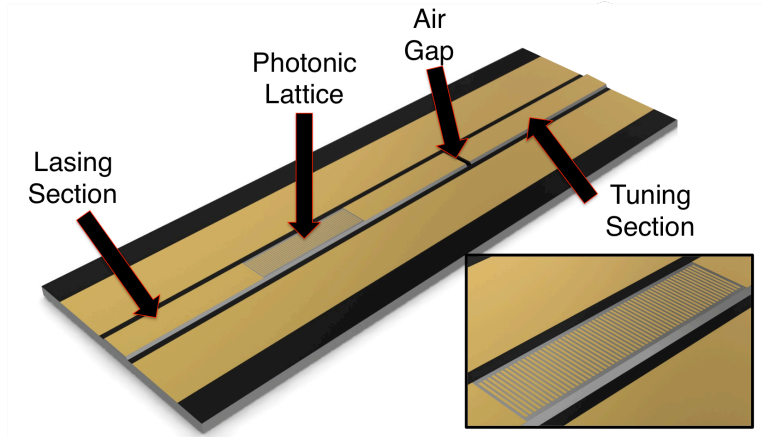


Figure 6.15: Schematic illustration of a coupled cavity device with photonic lattice. Inset: Photonic lattice.

6.3.1 Theory and modelling of coupled cavity QCLs with PL

Partial alignment of longitudinal modes has been discussed in section 6.2.1. It is evident from Figure 6.1 that the transition from a maximal alignment to a gradual misalignment is exhibited at all frequencies where the longitudinal modes of the lasing and tuning section are in close proximity (coloured boxed regions in Figure 6.1). In designs discussed so far the effect of this subtle transition is superseded by the discrete Vernier selection rule. However, this effect of the gradual transition can be studied if a PL is introduced in the lasing cavity, such that all but one of the discrete transition modes are suppressed. For e.g. in Figure 6.1, if a PL supports the mode at 2.755 THz only, then the tuning current induced transition from a maximal alignment to a gradual misaligned state would be dominant. This would manifest as continuous tuning around 2.755 THz.

The bandwidth of the continuous tuning, in this case, depends on the current induced change in refractive index at the tuning section. As noted in section 5.2.1.3, a maximum current induced shift in longitudinal modes of around 3–4 GHz was observed for ~5–6 W of input power in the tuning section. As a result, a maximum continuous tuning of an equivalent range, i.e. 3–4 GHz was predicted from THz QCLs with PLs.

The following section describes the modelling technique used to simulate the coupled cavity geometry with an integrated PL in the lasing section.

6.3.1.1 Modelling of coupled cavity QCLs with PL

PLs were designed following identical design procedure described in section 3.2. PLs with a duty cycle of 50% were used for this study and were fabricated after device packaging using FIB milling. Due to limitations imposed by FIB milling, only a finite number of grating sites (8 to 28) could be milled. This post packaging patterning of PLs allowed controlling the etch depth of the PL unmetallised section. This also allowed controlling the effective refractive index of the PL by varying the etch depth, and consequently the bandwidth of the stopband. ‘*Shallow*’ and ‘*deep*’ profiles with etch depths of 0.2 μm and 2 μm were used in the unmetallised section of the PL. The former corresponded to etching of the metal cladding only. In this case, the grating profile was identical to the EBL deposited PL described in Chapter 3. A deeper etch profile was also investigated that entailed etching of active material in the unmetallised section of the PL.

The refractive index of the PL sections (with an active region based on L701) was simulated using a similar finite element modelling (FEM) technique to that discussed in section 3.2.1.1. The refractive index of the unmetallised section was computed as $3.48 - j0.0325$ and $3.28 - j0.0628$ from FEM simulations for an etch depth of 0.2 μm and 2 μm respectively. The refractive index of the metallised section was calculated as $3.62 - j0.0064$. A stopband with a bandwidth of 90 GHz and ~ 230 GHz was predicted using the same dispersion relation described in section 3.2.2, for the shallow and deep etching profiles respectively.

The coupled cavity model based on scattering and transmission matrices, described in the previous chapter, was modified to include the PL gratings in the lasing cavity. The transmission characteristics of a single unit of PL pitch were modelled as [106]

$$\begin{aligned}
T_{11} &= \frac{1}{t^2} [\exp(j\phi_+) - r^2 \exp(-j\phi_-)] \\
T_{12} &= \frac{r}{t^2} [\exp(-j\phi_+) - \exp(j\phi_-)] \\
T_{21} &= \frac{r}{t^2} [\exp(j\phi_+) - \exp(-j\phi_-)] \\
T_{22} &= \frac{1}{t^2} [\exp(-j\phi_+) - r^2 \exp(j\phi_-)]
\end{aligned} \tag{6.1}$$

where

$$\begin{aligned}
\phi_+ &= \beta_{met} L_{met} + \beta_{gap} L_{gap} \\
\phi_- &= \beta_{met} L_{met} - \beta_{gap} L_{gap}
\end{aligned} \tag{6.2}$$

β_{met} and β_{gap} are complex propagation constants in the metallised and unmetallised section of the PL of length L_{met} and L_{gap} respectively. The reflectivity of the PL was calculated by cascading several repetitions of the unit PL pitch as given below

$$T = \left(\begin{bmatrix} T_{11} & T_{12} \\ T_{21} & T_{22} \end{bmatrix} \right)^N \tag{6.3}$$

where N is the number of grating pitch repetition in the PL.

The reflectivity in the lasing cavity with PL, as illustrated in Figure 6.15, have been calculated by multiplying the T matrices of the individual cavity components:

- Lasing cavity extending from the collection facet to the start of PL
- PL
- Lasing cavity extending from end of the PL to the air gap

Two configurations of PLs were designed featuring a uniform grating and a grating with a central $\lambda/4$ -shifted element [109]. While a uniform PL introduces a stop band centred at the Bragg frequency, a $\lambda/4$ -shifted PL supports a lasing mode at the Bragg frequency [109]. A schematic of a $\lambda/4$ -shifted PL is shown in Figure 6.16. The $\lambda/4$ -shifted element perturbs the phase of the forward and backward scattering waves in a PL and constructively interferes at the Bragg frequency. Thus, a mode is supported at the centre of the stop band. A $\lambda/4$ -shifted element is incorporated in a PL by introducing a break in the

periodicity of the grating [109]. This is accomplished by incorporation of an additional grating feature, either a metal cladding or an etched feature. In the designed PLs, the $\lambda/4$ -shifted element was added at the PL section with an extra cladding material.

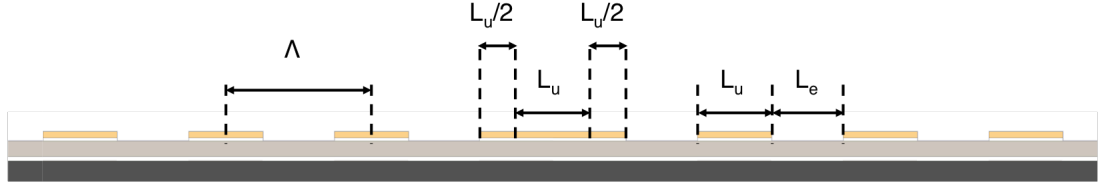


Figure 6.16: A schematic diagram of longitudinal cross-section of a PL with a central $\lambda/4$ -shifted element. PL grating pitch Λ comprise of a metallised section of length L_u (with cladding metal and n^+ -doped contact), and an unmetallised section of length L_e (without cladding metal and n -doped contact). The central $\lambda/4$ -shifted element is realised by breaking the PL periodicity and by inserting an additional element of length L_u into the PL feature with cladding material.

A PL with a uniformly spaced grating was used to design a wide stop band. However, the frequency tuning in this case would depend on the mode at the edge of the stop band. Such uniform gratings are not ideal to investigate narrow band continuous tuning and might support discrete mode hopping. Instead, a PL with a central $\lambda/4$ -shifted element provides flexibility in frequency selectivity as emission is supported at the Bragg frequency. This was verified by simulating a transfer matrix based model to investigate the normalised transmission in a 2- μm deep etched PL with 100 grating sites [Figure 6.17]. The stopband observed in a uniform PL corresponds well with the stopband simulated from the dispersion relation [Figure 3.1 (b)]. A similar PL with a central $\lambda/4$ -shifted element exhibited considerable transmission in the Bragg frequency.

The transfer matrix based network model was used to design two coupled cavity devices with an integrated PL. The first design used a shallow etched uniform PL, while the second design used a deep etched PL with a central $\lambda/4$ -shifted element. Merits of both the designs are discussed next.

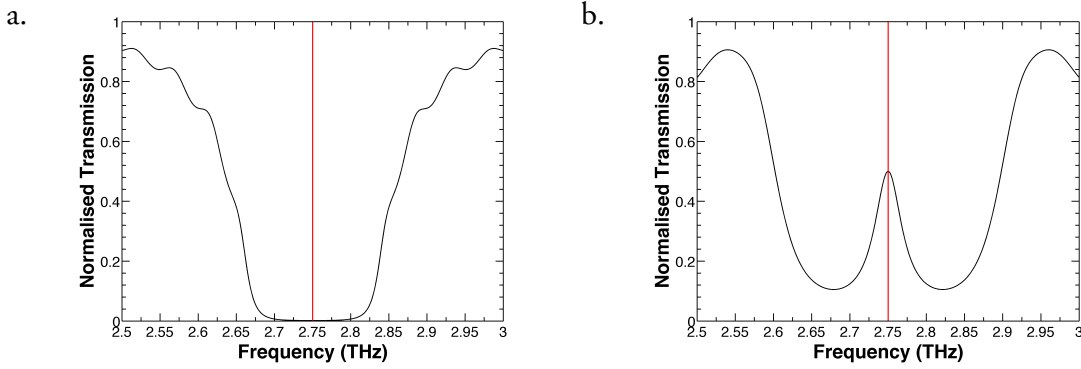


Figure 6.17: Normalised transmission (black) in a: (a) uniform PL and (b) PL with a $\lambda/4$ -shifted element. The uniform PL introduces a stop band centred at Bragg frequency, whereas the $\lambda/4$ -shifted PL introduces a stop band with an additional peak at the Bragg frequency. Both the PLs have a same Bragg frequency (red) at 2.75 THz and have 2- μm deep etched unmetallised sections.

6.3.1.2 Design 3: Coupled cavity devices with a uniform PL

This design evaluates the premise that a PL can selectively suppress discrete Vernier hopping. Coupled cavity device 5B, as described in the previous chapter, was used for this study. In fact, the Bragg frequency of the PL was designed after characterising the Vernier transitions.

A uniform PL was designed with a Bragg frequency at 2.73 THz and a narrow bandwidth sufficient to suppress the mode at 2.755 THz only. A PL with only 14 grating sites and shallow etched unmetallised regions was designed.

Alignment of longitudinal modes in the coupled cavity with the PL was calculated using the modified transfer matrix model at various tuning powers, and is shown in Figure 6.18. A comparison with the results from Figure 5.14 (a) would reveal that the PL changed the nature of discrete Vernier hopping with transitions permitted between modes at 2.78, 2.805 and 2.825 THz only.

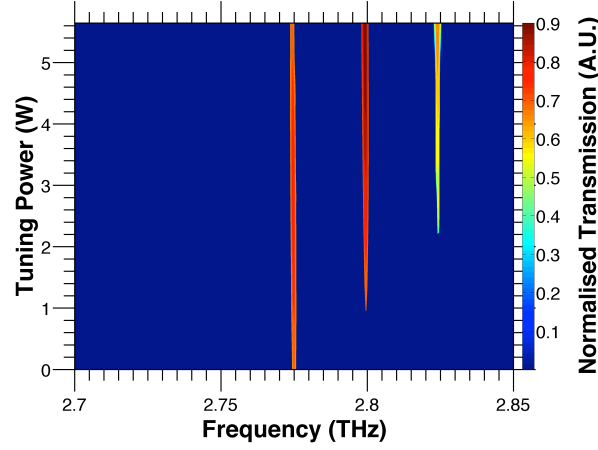


Figure 6.18: Normalised transmission in the coupled cavity device 5B, with a PL centred at 2.73 THz. Distribution of alignment is represented as a colour contour with red being complete alignment and dark blue being misalignment.

6.3.1.3 Design 4: Coupled cavity devices with $\lambda/4$ -shifted PL

A major advantage of $\lambda/4$ -shifted PL is that lasing is favoured at the Bragg frequency. Thus, a careful selection of the grating pitch of a $\lambda/4$ -shifted PL can suppress all Vernier transitions, forcing lasing at one of the misaligned states to obtain continuous tuning.

A $\lambda/4$ -shifted PL with the Bragg frequency at 2.205 THz was designed for the de-tuned design 2 (see section 6.2.1.1). High index contrast PLs with deep etched gratings were used in the design. The ~ 230 GHz wide stop band selected only frequencies at the Bragg frequency, i.e. 2.205 THz and suppressed at other lasing mode. The continuous tuning range of ~ 3 –4 GHz was predicted when both lasing and tuning currents were varied simultaneously, as shown in Figure 6.19.

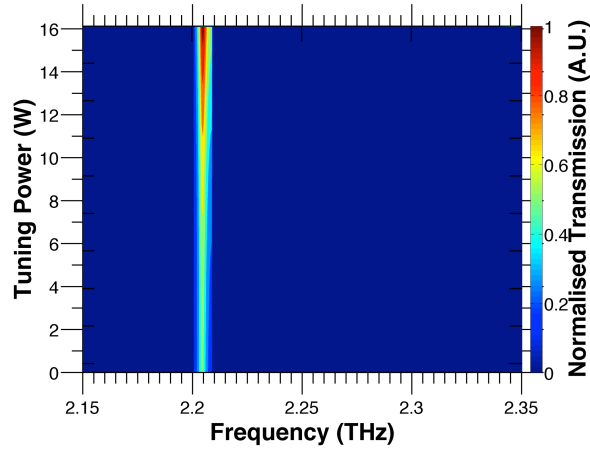


Figure 6.19: Normalised transmission from detuned cavity design 2 (device 6B) with a $\lambda/4$ -shifted PL centred at 2.205 THz as a function of heating power at the tuning section.

6.3.2 Fabrication

Coupled cavity devices, which had been packaged and characterised, were etched in a second FIB milling process to pattern the PL grating. The PL grating regions were located at the centre of the long lasing cavity, as shown in Figure 6.20.

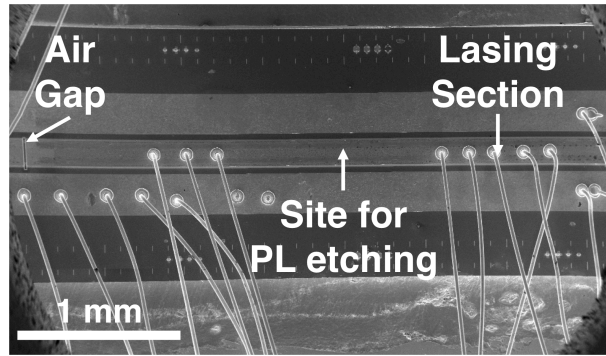


Figure 6.20: Scanning electron microscopy of a coupled cavity device before FIB milling to etch PL. Devices were wire bonded on either side of a central region where PL would be milled at the lasing section.

Device 5B was etched to a depth of ~ 200 nm to form a uniformly spaced PL [Figure 6.21 (a, b)]. This shallow etching process left residual material on the etched surface, as shown in Figure 6.21 (b). This device is re-labelled as ‘5B-PL’ after the PL patterning.

The device 6B (discussed in section 6.2.4.2) was patterned with a 2- μm deep etched $\lambda/4$ -shifted PL in a single FIB milling process [Figure 6.21 (c)]. Unlike the shallow etching process, no residual material was deposited on etched surface during the deep etching process. This device is relabelled as ‘6B-PL’ after the PL patterning.

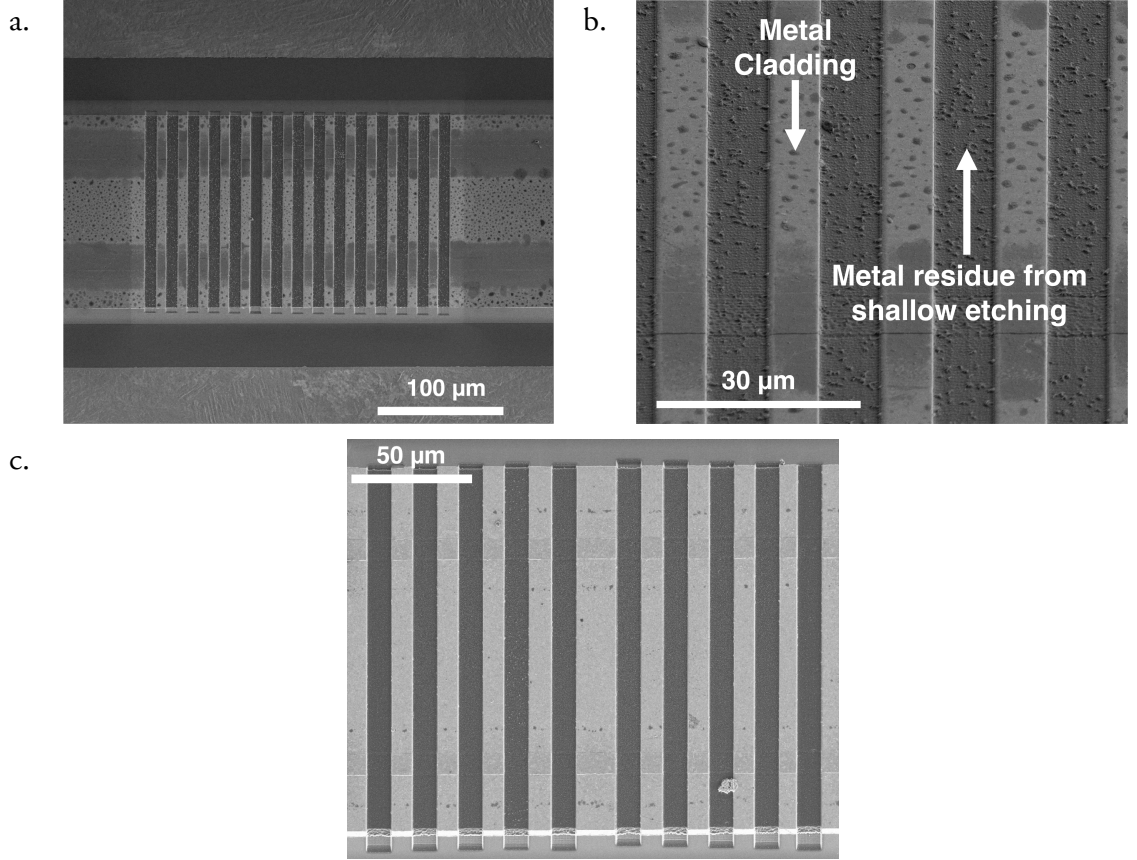


Figure 6.21: Scanning electron microscopy after FIB milling of PL in device 5B-PL: (a) a shallow etched uniform PL, (b) shallow etch profile, (c) Deep etched $\lambda/4$ -shifted PL in device 6B-PL.

A list of devices fabricated for this study is tabulated in Table 6.2.

Table 6.2: List of processed coupled cavity THz QCLs with a PL.

Device Number	Device Unique ID	Lasing Cavity (mm)	Tuning Cavity (mm)	Air Gap (μm)	Specification
5B-PL	L701-S21-D3	3.380	1.570	16.67	Uniform PL
6B-PL	L1007-S1-D2	3.527	1.288	16.57	π - shifted PL

Devices were characterised using an identical setup as described in section 6.2.3. The spectral data recorded from the devices are discussed next.

6.3.3 Experimental results

6.3.3.1 Uniform PL: Device 5B-PL

Emission at the edge of the stopband edge (2.775 THz) was observed from the device 5B-PL, after milling of a uniformly spaced PL with Bragg frequency at 2.73 THz [Figure 6.22]. Discrete transition between lasing modes at ~2.775, 2.795 and 2.825 THz was observed, when current at the tuning section is varied. Discrete Vernier tuning between lasing modes at ~2.740, 2.770, 2.80 and 2.825 THz was observed from the same device prior to PL milling [Figure 5.24 (a)]. The narrow band PL has suppressed the mode at 2.74 THz. The spectral evolution seen here corroborates the theoretical premise that discrete transitions could be selectively suppressed using a PL. The observed tuning behaviour is similar to the simulated result shown in Figure 6.18. Continuous tuning predicted from the detuned states, however, was not observed from this device.

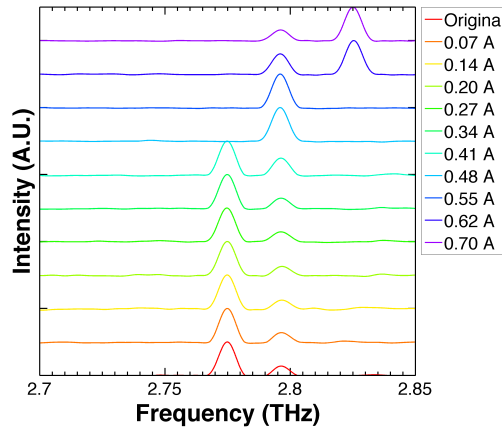


Figure 6.22: Spectra from device 5B-PL after uniform PL milling.

The devices were also characterised to obtain light–current–voltage (LIV) characteristics at different tuning currents [Figure 6.23]. An increase in threshold current density was observed due to the increase in waveguide losses after PL patterning. Power emission from the lasing section remains unaffected by changes in the tuning section current and agrees with similar observation made in coupled cavity QCLs [Figure 5.21].

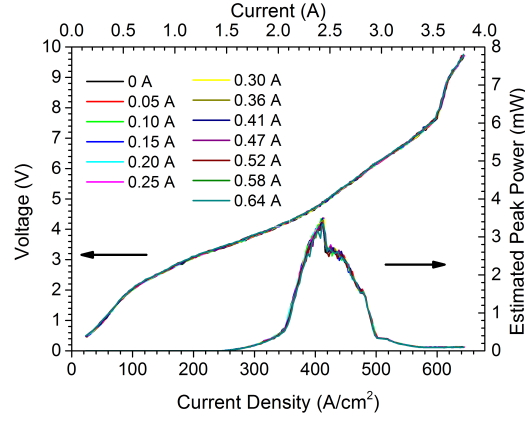


Figure 6.23: LIV characteristics obtained from device 5B-PL after $\lambda/4$ -shifted PL patterning. Emission from lasing section is obtained at different current at tuning section.

6.3.3.2 $\lambda/4$ -shifted PL: Device 6B-PL

An improved single mode emission was obtained from the device 6B-PL with a $\lambda/4$ -shifted PL. Emission at ~ 2.21 THz was observed and was close to the Bragg frequency 2.205 THz. Spectra were acquired at different lasing drive currents, while the amplitude and the pulse width of the tuning section current were varied between 0.05–0.65 A and 20–95 μ s respectively. The tuning section was also driven with DC current from 0.10–0.60 A.

The collated spectra under different configurations are shown in Figure 6.24. The wide stopband obtained from the deep etched PL had suppressed all discrete transitions observed in Figure 6.14, except the mode at the Bragg frequency. A SM emission with a side mode suppression ratio (SMSR) of 20 dB was also observed [Figure 6.24 (a)]. A maximum continuous tuning of ~ 3 GHz was observed as the current at both the lasing and the tuning sections were varied [Figure 6.24 (b)]. The experimental results substantiate the premise that the maximum continuous tuning from a coupled cavity PL devices is limited by the maximum perturbation to longitudinal modes at the tuning section. Furthermore, this continuous tuning range is comparable to that obtained from QCLs with PL by varying heat sink temperature [Figure 3.18 (b)]. Increasing, the heat sink temperature could widen the tuning range by ~ 1 -2 GHz. However, such attempts were impeded by a low output power and narrow dynamic range of operation in L1007 [Figure 2.20 (a)]. Thus, continuous tuning range of a PL enhanced coupled cavity device is limited to a maximum

of around 5-6 GHz. An enhanced continuous tuning range is possible from optimised de-tuned coupled cavity designs. Some design aspects of these devices are discussed in Chapter 7.

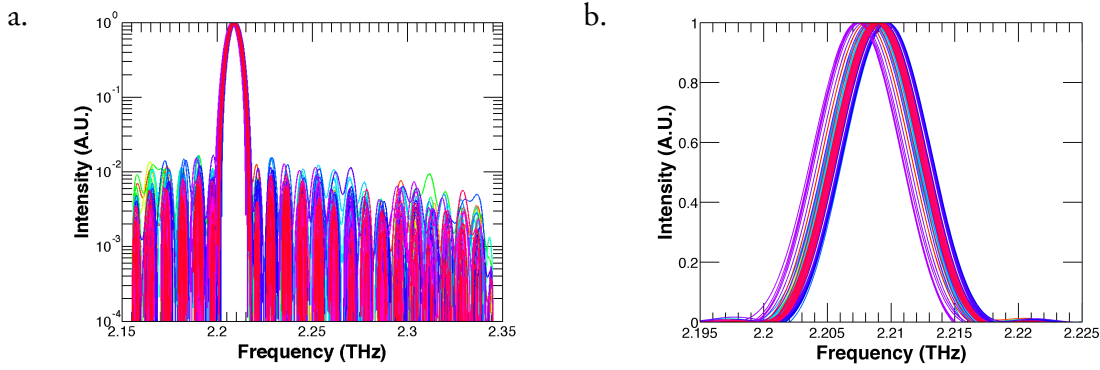


Figure 6.24: Collated spectra from device 6B-PL with a $\lambda/4$ -shifted PL at different lasing and tuning currents. (a) SM emission at 2.21 THz with an SMSR of 20 dB and (b) a continuous tuning of ~ 3 GHz.

6.4 Summary

Continuous tuning of THz QCLs has been investigated using coupled cavity QCLs. Two different design approaches were adopted. The first set of devices, the ‘*detuned*’ coupled cavity devices, aimed to obtain quasi-continuous or closely spaced discrete hopping using optimised coupled cavity designs. A tuning range of ~ 67 GHz and 100 GHz was observed from two detuned coupled cavity devices. Continuous tuning of around ~ 5 GHz was observed at certain modes within the overall quasi-continuous tuning range. The results can be improved further by using longer lasing cavities with closely spaced longitudinal modes.

The second set of devices, coupled cavity QCLs with PLs, were studied to investigate the possibility of selectively suppressing discrete Vernier tuning transitions in coupled cavity devices. Continuous tuning of ~ 3 GHz has been detected from devices with a $\lambda/4$ -shifted PL. An increase to the continuous range, in devices with PLs, is limited by the maximum perturbation that can be induced at the tuning section.

Chapter 7

Conclusion and future work

This project investigated single-mode (SM) emission and frequency tunable terahertz (THz) quantum cascade lasers (QCLs). SM emission was obtained using one-dimensional photonic lattices (PLs). Frequency tunability in THz QCLs was investigated by means of carrier depletion in PL structures and by using a two-section coupled cavity geometry. Various aspects of a device development lifecycle, including theoretical design and computer simulations, fabrication and characterisation, were discussed in the relevant chapters. The following sections summarise the results obtained and the possibility of improving frequency tunability in new design iterations, which could be investigated in future.

7.1 SM emission from THz QCLs with PLs

THz QCLs with PLs patterned by electron-beam lithography (EBL) were used to obtain SM emission, and was discussed in Chapter 3. The lithography based processing allows easier fabrication compared to subtractive techniques like focussed ion beam (FIB) milling, which is used to process devices after packaging.

Optical mode profile in the metallised and unmetallised sections of the PL were computed using a finite element modelling (FEM) technique. The spectral behaviour of the PL was subsequently simulated using the coupled mode theory. The PL introduces a stop-

band centred at the characteristic Bragg frequency. The bandwidth of this stopband was calculated as ~ 90 GHz from the coupled mode theory. Emission was predicted at the edge of the stopband. The observed behaviour corresponded well with a stopband simulated from the dispersion relation of the PL.

THz QCLs with single metal waveguides were fabricated with the top n -doped epilayer was etched away in a $530\text{-}\mu\text{m}$ central section using wet chemicals. PLs were subsequently deposited using EBL and thin-film deposition technique. SM emission outside the stopband was observed from all devices. The bandwidth of the stopband was experimentally determined to be $\sim 86\text{--}89$ GHz, and agreed well with the simulated value. The devices also exhibited a higher threshold current; lower emitted power and reduced temperature of operation, due to an increased waveguide losses arising from the 40% metal coverage in the PLs. This degradation in device performance can be improved by increasing the duty cycle of the PL pitch, and is left as a future work.

The spectral response from such devices can be improved further by increasing the refractive index contrast between the metallised and non-metallised sections of the PL. This can be achieved by an additional etching step to remove active region material under the non-metallised parts of the grating. Additionally, engineered defects such as a central $\lambda/4$ -shifted element can allow emission at the Bragg frequency.

The device geometry used in this study was modified to allow an external electrical bias to be applied to the PLs to investigate frequency tunability through carrier depletion under the PL metallised sections.

7.2 Frequency tunable THz QCL through carrier depletion

Tunability from THz QCLs with PLs was investigated through depletion of carriers under the PL metallised section, and was discussed in Chapter 4. The variation of refractive index of a THz QCL active region was simulated as a function of carrier concentration using a bulk Drude model. The refractive index exhibited a sharp non-linearity as the doping was varied between $10^{15} - 2 \times 10^{16} \text{ cm}^{-3}$. A PL based tuning scheme was designed to vary the

refractive index in this non-linear region by varying the carriers under the metallised section.

A single-metal waveguide was modified to form a THz QCL with three electrically isolated sections. The PL was deposited in a central section, with the two outer sections on either side of the PL left unpatterened. The three sections were electrically isolated by chemically etching the top conducting MBE grown layer in the central segment before the PL patterning. Deposition of the PL cladding metal directly on the active material (after etching away the top contact epilayer) formed a Schottky junction at the metal-semiconductor interface resulting in a thin depletion layer under the metallised section of the PL. A reverse bias was applied to the PL to increase the width of this depletion layer and deplete carriers under the metallised section.

The devices were initially characterised to study the electrical properties of the three-section THz QCLs. An electrical model of the three-section device was developed. The simulated data from this model agreed well with the experimental data. The width of the depletion layer was calculated from the electrical model. The resulting variation in carrier profile in the PL metallised section was calculated analytically and the corresponding change in the refractive index was calculated from a FEM simulation. A maximum tuning of ~ 15 – 20 GHz was predicted from the Drude model corresponding to the variation in carrier density in the PL. The bandwidth of the stopband was simulated using the coupled mode theory. A reduction in the bandwidth of the stopband from 90 GHz to 77 GHz was calculated as a bias was applied to the PL. This reduction in the bandwidth, along with the shift in Bragg frequency, results in a net mode shift of ~ 5 – 6 GHz.

In an exemplar device, a 15 GHz mode hopping was observed as the bias was applied to the PL. Emission from this device was observed at the centre of the stopband, i.e. at the characteristic Bragg frequency, implying a greater loss modulation. However, in all other devices emission was observed beyond the edge of the stopband. It was observed that by applying a bias to the PL, the spectral power density (SPD) amongst lasing modes was changed.

It was concluded that with the present design, the variation of refractive index through carrier depletion manifests as a very small observable change in frequency. This small perturbation in the refractive index made it imperative to modify the device design.

Instead of relying on the small index perturbation to directly tune the lasing modes, a Vernier selection scheme based on a two-section coupled cavity design was adopted.

7.3 THz QCLs using a coupled cavity

Discrete frequency hopping using a coupled-cavity geometry and following a Vernier selection rule was discussed in Chapter 5. The coupled-cavity THz QCLs comprised two cavities of precise lengths separated by an air gap. The devices were fabricated post-packaging using FIB milling. While one of the two cavities formed the lasing section and was driven above threshold, the second cavity acted as a tuning control element and was operated below the lasing threshold. In such coupled cavities, a lower lasing threshold is observed where the longitudinal modes at the lasing and the tuning sections overlap.

The coupled cavity geometry was modelled with a transfer-function-based model on cascaded network components. The thermal behaviour in the tuning section was modelled using a bulk thermal model. The device designs were optimised such that a blue-shift and a red-shift in frequency is obtained from the same device by simply swapping the functions of the cavities attributed to lasing and tuning.

Two coupled cavity designs were investigated, where the lengths of the lasing section and the tuning section were in approximate ratios of either 1:1 or 2:1. A monotonic frequency tuning of ~ 50 and 85 GHz, respectively, with a blue shift in frequency was observed from the devices. A red shift of ~ 20 and 30 GHz was also observed from the same devices by swapping the operating segments. Additionally, the power emission from such coupled cavity designs did not exhibit a significant degradation upon tuning.

This design was further modified to disrupt the monotonic shift in frequency by changing the cavity lengths, and was discussed in Chapter 6. A closely spaced discrete tuning or quasi-continuous frequency tuning was predicted as the lasing drive current, the heating tuning current and the heat sink temperature were varied simultaneously. This resulted in a closely spaced discrete tuning over a range of around ~ 50 GHz. The same device also exhibited a broad frequency tuning over around 100 GHz.

Continuous frequency tunability was also investigated by patterning laser cavities with PLs using FIB. Continuous frequency tuning over a maximum range of $3\text{--}4$ GHz was

predicted using the same transfer matrix–model, with continuous tuning of ~ 3 GHz was subsequently observed experimentally.

The coupled cavity design discussed in this work has a tremendous scope for optimisation. Some of these optimisations, which can be investigated in future are described in the following section.

7.4 Future Work

The performance of the coupled cavity devices can be improved by further optimisation of reflectivity of the tuning section with the lasing section. Continuous tuning of frequency is possible from detuned coupled–cavity devices if the mode spacing in the lasing section is comparable to the tuning current or heat induced shift in the mode spacing. This is possible in ~ 6 mm long lasing cavities and ~ 3 mm long tuning sections. Such long cavities were not investigated in the present project and are left for future work.

The design used in this study comprised simple cascaded-cavities of identical ridge-widths, coupled through their end facets. This design can be optimised further to improve coupling between the lasing and tuning sections by using, for example, a wide aperture tuning section. A schematic diagram of such a design is shown in Figure 7.1. The wide aperture in the tuning section can couple diffracted radiation from the edges of the lasing cavity to the tuning section and increase the coupling.

Coupling between QCL ridges can also be investigated in evanescent field coupled cavities. In such a design, the lasing and tuning sections would not be cascaded sequentially and coupled via the end facets. Instead, cavities would be coupled along the length of the cavity through evanescent field coupling, analogous to optical couplers [106]. Schematic diagram of such a device is shown in Figure 7.2.

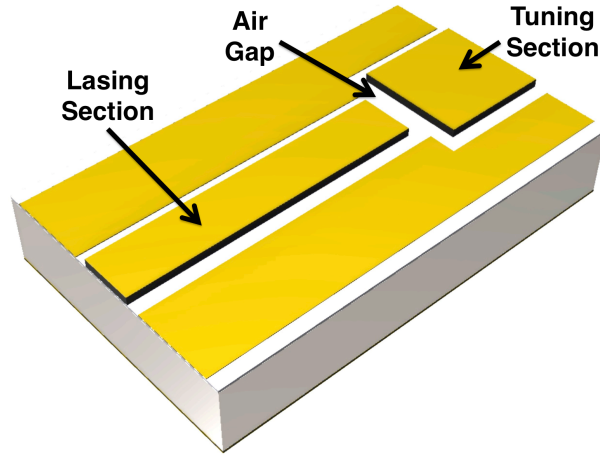


Figure 7.1: Illustration of a coupled cavity THz QCL with a wide aperture tuning section.

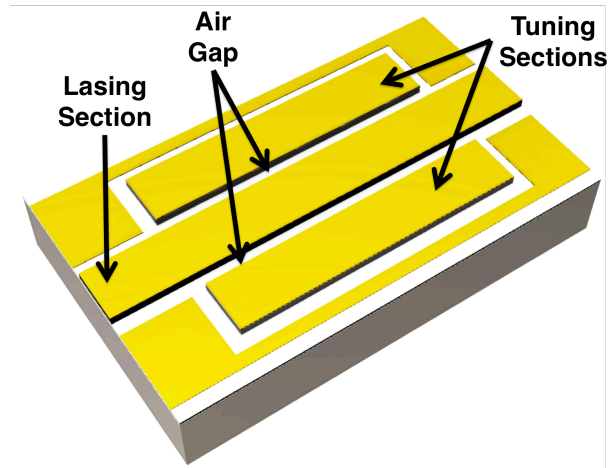


Figure 7.2: Illustration of a coupled cavity THz QCL with evanescent field coupled tuning sections.

Evanescent field coupled THz QCLs would be crucial towards realisation of THz QCL integrated photonic systems. In optical photonic integrated circuits, various components such as sampled distributed Bragg reflectors (SG-DBR), phase matching sections and semiconductor optical amplifiers are cascaded sequentially [106]. While such cascaded designs are ideal for short wavelength optical systems, the longer wavelength in the THz spectrum dictates that such systems be several centimetres long. Fabrication and thermal extraction from such long devices put a practical limit towards such realisation. On the other hand, a successful demonstration of evanescent field coupled THz QCL cavities could lead to integration of additional photonic components. One such simple implementation is

shown in Figure 7.3. In this design, the central gain section is coupled to two external cavities, which are patterned with sampled grating distributed feedback gratings (SG-DFB). Such SG-DBRs are used to design frequency tunable optical lasers, and similar frequency tunability is estimated from an optimised SG-DFB based design. A successful demonstration of frequency tuning in such devices could lead to development of integrated THz QCL photonic circuits.

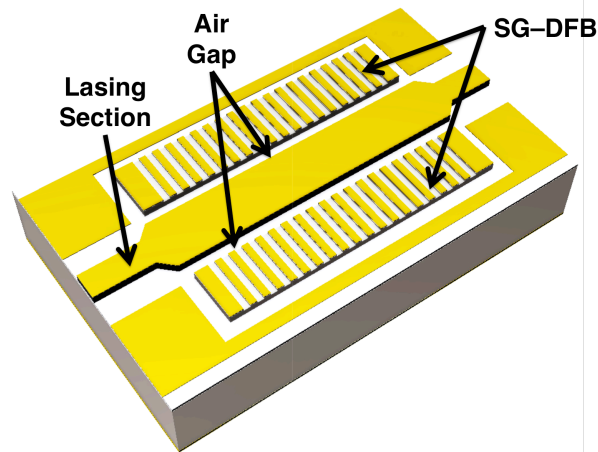


Figure 7.3: Illustration of a coupled cavity THz QCL with evanescent field coupled SG-DFBs. The central section is tapered near the coupled sections to increase coupling.

References

1. C. Sirtori, "Applied physics: Bridge for the terahertz gap," *Nature* **417**, 132–133 (2002).
 2. G. Davies and E. Linfield, "Bridging the terahertz gap," *Phys. World* **17**, 37–41 (2004).
 3. B. B. Hu and M. C. Nuss, "Imaging with terahertz waves," *Opt. Lett.* **20**, 1716–1718 (1995).
 4. P. H. Siegel, "Terahertz technology," *IEEE Trans. Microw. Theory Tech.* **50**, 910 – 928 (2002).
 5. A. G. Davies, A. D. Burnett, W. Fan, E. H. Linfield, and J. E. Cunningham, "Terahertz spectroscopy of explosives and drugs," *Mater. Today* **11**, 18 – 26 (2008).
 6. S. M. Kim, F. Hatami, J. S. Harris, A. W. Kurian, J. Ford, D. King, G. Scalari, M. Giovannini, N. Hoyler, and J. Faist, "Biomedical terahertz imaging with a quantum cascade laser," *Appl. Phys. Lett.* **88**, 153903 (2006).
 7. D. D. Arnone, C. M. Ciesla, A. Corchia, S. Egusa, M. Pepper, J. M. Chamberlain, C. Bezant, E. H. Linfield, R. Clothier, and N. Khammo, "Applications of terahertz (THz) technology to medical imaging," in *Industrial Lasers and Inspection (EUROPTO Series)* (International Society for Optics and Photonics, 1999), pp. 209–219.
 8. M. Shur, "Terahertz technology: devices and applications," in *Solid-State Circuits Conference, 2005. ESSCIRC 2005. Proceedings of the 31st European* (IEEE, 2005), pp. 13–21.
 9. T. G. Phillips and J. Keene, "Submillimeter astronomy [heterodyne spectroscopy]," *Proc. IEEE* **80**, 1662–1678 (1992).
 10. D. T. Leisawitz, W. C. Danchi, M. J. DiPirro, L. D. Feinberg, D. Y. Gezari, M. Hagopian, W. D. Langer, J. C. Mather, S. H. Moseley Jr, and M. Shao, "Scientific motivation and technology requirements for the SPIRIT and SPECS far-
-

- infrared/submillimeter space interferometers," in *Astronomical Telescopes and Instrumentation* (International Society for Optics and Photonics, 2000), pp. 36–46.
11. D. Woolard, "Terahertz electronic research for defense: Novel technology and science," in *11th Int. Space Terahertz Tech. Symp* (2000), pp. 1–3.
 12. A. Dobroiu, M. Yamashita, Y. N. Ohshima, Y. Morita, C. Otani, and K. Kawase, "Terahertz Imaging System Based on a Backward-Wave Oscillator," *Appl. Opt.* **43**, 5637–5646 (2004).
 13. X.-C. Zhang, B. B. Hu, J. T. Darrow, and D. H. Auston, "Generation of femto-second electromagnetic pulses from semiconductor surfaces," *Appl. Phys. Lett.* **56**, 1011–1013 (1990).
 14. J. Cunningham, M. Byrne, P. Upadhy, M. Lachab, E. H. Linfield, and A. G. Davies, "Terahertz evanescent field microscopy of dielectric materials using on-chip waveguides," *Appl. Phys. Lett.* **92**, 032903 (2008).
 15. R. Köhler, A. Tredicucci, F. Beltram, H. E. Beere, E. H. Linfield, A. G. Davies, D. A. Ritchie, R. C. Iotti, and F. Rossi, "Terahertz semiconductor-heterostructure laser," *Nature* **417**, 156–159 (2002).
 16. Safa O. Kasap, *Optoelectronics and Photonics: Principles and Practices*, First Edition (Prentice Hall, 2001).
 17. Paul Harrison, *Quantum Wells, Wires and Dots - Theoretical and Computational Physics of Semiconductor Nanostructures*, Second Edition (John Wiley & Sons, 2005).
 18. Peter S. Zory, ed., *Quantum Well Lasers (Quantum Electronics - Principles and Applications)* (Academic Press Inc., 1993).
 19. Roberto Paiella, *Intersubband Transitions in Quantum Structures* (The McGraw-Hill Companies, 2006).
 20. C. Gmachl, F. Capasso, D. L. Sivco, and A. Y. Cho, "Recent progress in quantum cascade lasers and applications," *Rep. Prog. Phys.* **64**, 1533 (2001).
 21. J. Alton, "Bound-to-Continuum THz Quantum Cascade Lasers," PhD Thesis, University of Cambridge (2005).
 22. R. Kazarinov and R. Suris, "Amplification of electromagnetic waves in a semiconductor superlattice," *Sov. Phys. Semicond.* **5**, 707–709 (1971).
 23. A. Y. Cho and M. B. Panish, "Magnesium-doped GaAs and $\text{Al}_x\text{Ga}_{1-x}\text{As}$ by molecular beam epitaxy," *J. Appl. Phys.* **43**, 5118–5123 (1972).
 24. A. Y. Cho and F. K. Reinhart, "Interface and doping profile characteristics with molecular-beam epitaxy of GaAs: GaAs voltage varactor," *J. Appl. Phys.* **45**, 1812–1817 (1974).
-

25. A. Y. Cho and J. R. Arthur, "Molecular beam epitaxy," *Prog. Solid State Chem.* **10**, Part 3, 157–191 (1975).
 26. J. Faist, F. Capasso, D. L. Sivco, C. Sirtori, A. L. Hutchinson, and A. Y. Cho, "Quantum Cascade Laser," *Science* **264**, 553–556 (1994).
 27. M. C. Wanke, F. Capasso, C. Gmachl, A. Tredicucci, D. L. Sivco, A. L. Hutchinson, S.-N. G. Chu, and A. Y. Cho, "Injectorless quantum-cascade lasers," *Appl. Phys. Lett.* **78**, 3950–3952 (2001).
 28. A. Friedrich, G. Boehm, M. C. Amann, and G. Scarpa, "Quantum-cascade lasers without injector regions operating above room temperature," *Appl. Phys. Lett.* **86**, - (2005).
 29. A. Straub, T. S. Mosely, C. Gmachl, R. Colombelli, M. Troccoli, F. Capasso, D. L. Sivco, and A. Y. Cho, "Threshold reduction in quantum cascade lasers with partially undoped, dual-wavelength interdigitated cascades," *Appl. Phys. Lett.* **80**, 2845–2847 (2002).
 30. J. Faist, F. Capasso, C. Sirtori, D. L. Sivco, A. L. Hutchinson, and A. Y. Cho, "Vertical transition quantum cascade laser with Bragg confined excited state," *Appl. Phys. Lett.* **66**, 538–540 (1995).
 31. F. Capasso, A. Y. Cho, J. Faist, A. L. Hutchinson, C. Sirtori, and D. L. Sivco, "Unipolar semiconductor laser," U.S. patent US5509025 A (April 1996).
 32. J. Faist, F. Capasso, C. Sirtori, D. L. Sivco, A. L. Hutchinson, and A. Y. Cho, "Continuous wave operation of a vertical transition quantum cascade laser above $T=80$ K," *Appl. Phys. Lett.* **67**, 3057–3059 (1995).
 33. C. Sirtori, J. Faist, F. Capasso, D. L. Sivco, A. L. Hutchinson, S. N. G. Chu, and A. Y. Cho, "Continuous wave operation of midinfrared ($7.4\text{--}8.6\text{ }\mu\text{m}$) quantum cascade lasers up to 110 K temperature," *Appl. Phys. Lett.* **68**, 1745–1747 (1996).
 34. C. Sirtori, J. Faist, F. Capasso, D. L. Sivco, A. L. Hutchinson, and A. Y. Cho, "Mid-infrared ($8.5\text{ }\mu\text{m}$) semiconductor lasers operating at room temperature," *IEEE Photonics Technol. Lett.* **9**, 294–296 (1997).
 35. J. Faist, F. Capasso, C. Sirtori, D. L. Sivco, A. L. Hutchinson, M. S. Hybertsen, and A. Y. Cho, "Quantum cascade lasers without intersubband population inversion," *Phys. Rev. Lett.* **76**, 411 (1996).
 36. J. Faist, F. Capasso, C. Sirtori, D. L. Sivco, J. N. Baillargeon, A. L. Hutchinson, S.-N. G. Chu, and A. Y. Cho, "High power mid-infrared ($\lambda\sim 5\text{ }\mu\text{m}$) quantum cascade lasers operating above room temperature," *Appl. Phys. Lett.* **68**, 3680–3682 (1996).
 37. F. Capasso, J. Faist, C. Sirtori, D. L. Sivco, J. N. Baillargeon, A. L. Hutchinson, and A. Y. Cho, "Quantum cascade lasers: new resonant tunnelling light sources for the mid-infrared," *Philos. Trans. R. Soc. Lond. Ser. Math. Phys. Eng. Sci.* **354**, 2463–2467 (1996).
-

38. G. Scamarcio, F. Capasso, C. Sirtori, J. Faist, A. L. Hutchinson, D. L. Sivco, and A. Y. Cho, "High-power infrared (8-micrometer wavelength) superlattice lasers," *Science* **276**, 773–776 (1997).
 39. F. Capasso, A. Tredicucci, C. Gmachl, D. L. Sivco, A. L. Hutchinson, A. Y. Cho, and G. Scamarcio, "High-performance superlattice quantum cascade lasers," *IEEE J. Sel. Top. Quantum Electron.* **5**, 792–807 (1999).
 40. A. Tredicucci, F. Capasso, C. Gmachl, D. L. Sivco, A. L. Hutchinson, A. Y. Cho, J. Faist, and G. Scamarcio, "High-power inter-miniband lasing in intrinsic superlattices," *Appl. Phys. Lett.* **72**, 2388–2390 (1998).
 41. A. Tredicucci, F. Capasso, C. Gmachl, D. L. Sivco, A. L. Hutchinson, and A. Y. Cho, "High performance interminiband quantum cascade lasers with graded superlattices," *Appl. Phys. Lett.* **73**, 2101–2103 (1998).
 42. C. Sirtori, P. Kruck, S. Barbieri, P. Collot, J. Nagle, M. Beck, J. Faist, and U. Oesterle, "GaAs/Al_xGa_{1-x}As quantum cascade lasers," *Appl. Phys. Lett.* **73**, 3486–3488 (1998).
 43. B. S. Williams, "Terahertz quantum cascade lasers," PhD Thesis, Massachusetts Institute of Technology (2003).
 44. S. Slivken, A. Matlis, C. Jelen, A. Rybaltowski, J. Diaz, and M. Razeghi, "High-temperature continuous-wave operation of $\lambda \sim 8 \mu\text{m}$ quantum cascade lasers," *Appl. Phys. Lett.* **74**, 173–175 (1999).
 45. C. Sirtori, H. Page, C. Becker, and V. Ortiz, "GaAs-AlGaAs quantum cascade lasers: physics, technology, and prospects," *IEEE J. Quantum Electron.* **38**, 547–558 (2002).
 46. C. Sirtori, H. Page, and C. Becker, "GaAs-based quantum cascade lasers," *Philos. Trans. Math. Phys. Eng. Sci.* 505–522 (2001).
 47. M. J. W. Rodwell, ed., *High Speed Integrated Circuit Technology, Towards 100GHz Logic*, Selected Topics in Electronics and Systems (World Scientific Publishing Co. Pte. Ltd, 2001), Vol. 21.
 48. J. Faist, F. Capasso, D. L. Sivco, A. L. Hutchinson, C. Sirtori, S. N. G. Chu, and A. Y. Cho, "Quantum cascade laser: Temperature dependence of the performance characteristics and high T_0 operation," *Appl. Phys. Lett.* **65**, 2901–2903 (1994).
 49. C. Sirtori, C. Gmachl, F. Capasso, J. Faist, D. L. Sivco, A. L. Hutchinson, and A. Y. Cho, "Long-wavelength ($\lambda \approx 8 - 11.5 \mu\text{m}$) semiconductor lasers with waveguides based on surface plasmons," *Opt. Lett.* **23**, 1366–1368 (1998).
 50. C. Sirtori, J. Faist, F. Capasso, D. L. Sivco, A. L. Hutchinson, and A. Y. Cho, "Quantum cascade laser with plasmon-enhanced waveguide operating at $8.4 \mu\text{m}$ wavelength," *Appl. Phys. Lett.* **66**, 3242–3244 (1995).
-

51. W. L. Barnes, A. Dereux, and T. W. Ebbesen, "Surface plasmon subwavelength optics," *Nature* **424**, 824–830 (2003).
 52. C. Gmachl, A. Tredicucci, F. Capasso, A. L. Hutchinson, D. L. Sivco, J. N. Baillargeon, and A. Y. Cho, "High-power $\lambda \approx 8 \mu\text{m}$ quantum cascade lasers with near optimum performance," *Appl. Phys. Lett.* **72**, 3130–3132 (1998).
 53. A. Tredicucci, C. Gmachl, F. Capasso, A. L. Hutchinson, D. L. Sivco, and A. Y. Cho, "Single-mode surface-plasmon laser," *Appl. Phys. Lett.* **76**, 2164–2166 (2000).
 54. A. Tredicucci, C. Gmachl, F. Capasso, D. L. Sivco, A. L. Hutchinson, and A. Y. Cho, "Long wavelength superlattice quantum cascade lasers at $\lambda \approx 17 \mu\text{m}$," *Appl. Phys. Lett.* **74**, 638–640 (1999).
 55. K. Unterrainer, R. Colombelli, C. Gmachl, F. Capasso, H. Y. Hwang, A. M. Sergent, D. L. Sivco, and A. Y. Cho, "Quantum cascade lasers with double metal-semiconductor waveguide resonators," *Appl. Phys. Lett.* **80**, 3060–3062 (2002).
 56. C. Sirtori, S. Barbieri, P. Kruck, V. Piazza, M. Beck, J. Faist, U. Oesterle, P. Collot, and J. Nagle, "Influence of DX centers on the performance of unipolar semiconductor lasers based on $\text{GaAs-Al}_x\text{Ga}_{1-x}\text{As}$," *IEEE Photonics Technol. Lett.* **11**, 1090–1092 (1999).
 57. C. Sirtori, P. Kruck, S. Barbieri, H. Page, J. Nagle, M. Beck, J. Faist, and U. Oesterle, "Low-loss Al-free waveguides for unipolar semiconductor lasers," *Appl. Phys. Lett.* **75**, 3911–3913 (1999).
 58. D. Indjin, P. Harrison, R. W. Kelsall, and Z. Ikonić, "Mechanisms of temperature performance degradation in terahertz quantum-cascade lasers," *Appl. Phys. Lett.* **82**, 1347–1349 (2003).
 59. H. Callebaut, S. Kumar, B. S. Williams, Q. Hu, and J. L. Reno, "Analysis of transport properties of terahertz quantum cascade lasers," *Appl. Phys. Lett.* **83**, 207–209 (2003).
 60. B. S. Williams, S. Kumar, H. Callebaut, Q. Hu, and J. L. Reno, "Terahertz quantum-cascade laser operating up to 137 K," *Appl. Phys. Lett.* **83**, 5142–5144 (2003).
 61. L. Ajili, G. Scalari, D. Hofstetter, M. Beck, J. Faist, H. Beere, G. Davies, E. Linfield, and D. Ritchie, "Continuous-wave operation of far-infrared quantum cascade lasers," *Electron. Lett.* **38**, 1675 – 1676 (2002).
 62. R. Köhler, A. Tredicucci, F. Beltram, H. E. Beere, E. H. Linfield, A. G. Davies, D. A. Ritchie, S. S. Dhillon, and C. Sirtori, "High-performance continuous-wave operation of superlattice terahertz quantum-cascade lasers," *Appl. Phys. Lett.* **82**, 1518–1520 (2003).
 63. R. Köhler, A. Tredicucci, F. Beltram, H. E. Beere, E. H. Linfield, A. G. Davies, and D. A. Ritchie, "Low-threshold quantum-cascade lasers at 3.5 THz ($\lambda = 85 \mu\text{m}$)," *Opt. Lett.* **28**, 810–812 (2003).
-

-
64. C. Worrall, J. Alton, M. Houghton, S. Barbieri, H. E. Beere, D. Ritchie, and C. Sirtori, "Continuous wave operation of a superlattice quantum cascade laser emitting at 2 THz," *Opt. Express* **14**, 171–181 (2006).
 65. G. Scalari, L. Ajili, J. Faist, H. Beere, E. Linfield, D. Ritchie, and G. Davies, "Far-infrared ($\lambda \approx 87 \mu\text{m}$) bound-to-continuum quantum-cascade lasers operating up to 90 K," *Appl. Phys. Lett.* **82**, 3165–3167 (2003).
 66. B. S. Williams, "Terahertz quantum-cascade lasers," *Nat. Photonics* **1**, 517–525 (2007).
 67. S. Barbieri, J. Alton, H. E. Beere, J. Fowler, E. H. Linfield, and D. A. Ritchie, "2.9 THz quantum cascade lasers operating up to 70 K in continuous wave," *Appl. Phys. Lett.* **85**, 1674–1676 (2004).
 68. S. P. Khanna, S. Chakraborty, M. Lachab, N. M. Hinchcliffe, E. H. Linfield, and A. G. Davies, "The growth and measurement of terahertz quantum cascade lasers," *Phys. E Low-Dimens. Syst. Nanostructures* **40**, 1859–1861 (2008).
 69. C. Walther, G. Scalari, J. Faist, H. Beere, and D. Ritchie, "Low frequency terahertz quantum cascade laser operating from 1.6 to 1.8 THz," *Appl. Phys. Lett.* **89**, 231121 (2006).
 70. C. Walther, M. Fischer, G. Scalari, R. Terazzi, N. Hoyler, and J. Faist, "Quantum cascade lasers operating from 1.2 to 1.6 THz," *Appl. Phys. Lett.* **91**, 131122 (2007).
 71. J. R. Freeman, O. Marshall, H. E. Beere, and D. A. Ritchie, "Improved wall plug efficiency of a 1.9 THz quantum cascade laser by an automated design approach," *Appl. Phys. Lett.* **93**, 191119 (2008).
 72. B. S. Williams, H. Callebaut, S. Kumar, Q. Hu, and J. L. Reno, "3.4-THz quantum cascade laser based on longitudinal-optical-phonon scattering for depopulation," *Appl. Phys. Lett.* **82**, 1015–1017 (2003).
 73. Q. Hu, B. S. Williams, S. Kumar, H. Callebaut, S. Kohen, and J. L. Reno, "Resonant-phonon-assisted THz quantum-cascade lasers with metal-metal waveguides," *Semicond. Sci. Technol.* **20**, S228 (2005).
 74. H. Luo, S. R. Laframboise, Z. R. Wasilewski, G. C. Aers, H. C. Liu, and J. C. Cao, "Terahertz quantum-cascade lasers based on a three-well active module," *Appl. Phys. Lett.* **90**, 041112 (2007).
 75. R. W. Adams, K. Vijayraghavan, Q. J. Wang, J. Fan, F. Capasso, S. P. Khanna, A. G. Davies, E. H. Linfield, and M. A. Belkin, "GaAs/Al_{0.15}Ga_{0.85}As terahertz quantum cascade lasers with double-phonon resonant depopulation operating up to 172 K," *Appl. Phys. Lett.* **97**, 131111 (2010).
 76. S. Kumar, B. S. Williams, S. Kohen, Q. Hu, and J. L. Reno, "Continuous-wave operation of terahertz quantum-cascade lasers above liquid-nitrogen temperature," *Appl. Phys. Lett.* **84**, 2494–2496 (2004).
-

77. B. Williams, S. Kumar, Q. Hu, and J. Reno, "Operation of terahertz quantum-cascade lasers at 164 K in pulsed mode and at 117 K in continuous-wave mode," *Opt. Express* **13**, 3331–3339 (2005).
 78. B. S. Williams, S. Kumar, Q. Hu, and J. L. Reno, "Resonant-phonon terahertz quantum-cascade laser operating at 2.1 THz ($\lambda \approx 141 \mu\text{m}$)," *Electron. Lett.* **40**, 431–433 (2004).
 79. S. Kumar, B. S. Williams, Q. Hu, and J. L. Reno, "1.9 THz quantum-cascade lasers with one-well injector," *Appl. Phys. Lett.* **88**, 121123 (2006).
 80. S. Kumar, "Recent Progress in Terahertz Quantum Cascade Lasers," *IEEE J. Sel. Top. Quantum Electron.* **17**, 38–47 (2011).
 81. M. I. Amanti, G. Scalari, R. Terazzi, M. Fischer, M. Beck, J. Faist, A. Rudra, P. Gallo, and E. Kapon, "Bound-to-continuum terahertz quantum cascade laser with a single-quantum-well phonon extraction/injection stage," *New J. Phys.* **11**, 125022 (2009).
 82. L. Li, L. Chen, J. Zhu, J. Freeman, P. Dean, A. Valavanis, A. G. Davies, and E. H. Linfield, "Terahertz quantum cascade lasers with $>1 \text{ W}$ output powers," *Electron. Lett.* **50**, 309–311 (2014).
 83. L. Lever, N. M. Hinchcliffe, S. P. Khanna, P. Dean, Z. Ikonić, C. A. Evans, A. G. Davies, P. Harrison, E. H. Linfield, and R. W. Kelsall, "Terahertz ambipolar dual-wavelength quantum cascade laser," *Opt. Express* **17**, 19926–19932 (2009).
 84. J. R. Freeman, O. P. Marshall, H. E. Beere, and D. A. Ritchie, "Electrically switchable emission in terahertz quantum cascade lasers," *Opt. Express* **16**, 19830–19835 (2008).
 85. D. Turčinková, G. Scalari, F. Castellano, M. I. Amanti, M. Beck, and J. Faist, "Ultra-broadband heterogeneous quantum cascade laser emitting from 2.2 to 3.2 THz," *Appl. Phys. Lett.* **99**, 191104 (2011).
 86. J. R. Freeman, C. Worrall, V. Apostolopoulos, J. Alton, H. Beere, and D. A. Ritchie, "Frequency Manipulation of THz Bound-to-Continuum Quantum-Cascade Lasers," *IEEE Photonics Technol. Lett.* **20**, 303–305 (2008).
 87. S. P. Khanna, M. Salih, P. Dean, A. G. Davies, and E. H. Linfield, "Electrically tunable terahertz quantum-cascade laser with a heterogeneous active region," *Appl. Phys. Lett.* **95**, 181101–3 (2009).
 88. L. Ajili, G. Scalari, N. Hoyler, M. Giovannini, and J. Faist, "InGaAs–AlInAs/InP terahertz quantum cascade laser," *Appl. Phys. Lett.* **87**, 141107 (2005).
 89. C. Deutsch, M. Krall, M. Brandstetter, H. Detz, A. M. Andrews, P. Klang, W. Schrenk, G. Strasser, and K. Unterrainer, "High performance InGaAs/GaAsSb terahertz quantum cascade lasers operating up to 142 K," *Appl. Phys. Lett.* **101**, 211117 (2012).
-

90. K. Ohtani, M. Fischer, G. Scalari, M. Beck, and J. Faist, "Terahertz intersubband electroluminescence from InAs quantum cascade light emitting structures," *Appl. Phys. Lett.* **102**, 141113 (2013).
 91. M. A. Belkin, J. A. Fan, S. Hormoz, F. Capasso, S. P. Khanna, M. Lachab, A. G. Davies, and E. H. Linfield, "Terahertz quantum cascade lasers with copper metal-metal waveguides operating up to 178 K," *Opt. Express* **16**, 3242–3248 (2008).
 92. S. Fatholouloumi, E. Dupont, S. G. Razavipour, S. R. Laframboise, G. Parent, Z. Wasilewski, H. C. Liu, and D. Ban, "On metal contacts of terahertz quantum cascade lasers with a metal–metal waveguide," *Semicond. Sci. Technol.* **26**, 105021 (2011).
 93. S. Kumar, C. W. I. Chan, Q. Hu, and J. L. Reno, "A 1.8-THz quantum cascade laser operating significantly above the temperature of $\hbar\omega/k_B$," *Nat. Phys.* **7**, 166–171 (2011).
 94. S. Kumar, Q. Hu, and J. L. Reno, "186 K operation of terahertz quantum-cascade lasers based on a diagonal design," *Appl. Phys. Lett.* **94**, 131105 (2009).
 95. S. Fatholouloumi, E. Dupont, C. W. I. Chan, Z. R. Wasilewski, S. R. Laframboise, D. Ban, A. Mátyás, C. Jirauschek, Q. Hu, and H. C. Liu, "Terahertz quantum cascade lasers operating up to ~200 K with optimized oscillator strength and improved injection tunneling," *Opt. Express* **20**, 3866–3876 (2012).
 96. A. J. L. Adam, I. Kašalynas, J. N. Hovenier, T. O. Klaassen, J. R. Gao, E. E. Orlova, B. S. Williams, S. Kumar, Q. Hu, and J. L. Reno, "Beam patterns of terahertz quantum cascade lasers with subwavelength cavity dimensions," *Appl. Phys. Lett.* **88**, 151105 (2006).
 97. J. A. Fan, M. A. Belkin, F. Capasso, S. Khanna, M. Lachab, A. G. Davies, and E. H. Linfield, "Surface emitting terahertz quantum cascade laser with a double-metal waveguide," *Opt. Express* **14**, 11672–11680 (2006).
 98. S. Kumar, B. S. Williams, Q. Qin, A. W. Lee, Q. Hu, and J. L. Reno, "Surface-emitting distributed feedback terahertz quantum-cascade lasers in metal-metal waveguides," *Opt. Express* **15**, 113–128 (2007).
 99. M. I. Amanti, M. Fischer, G. Scalari, M. Beck, and J. Faist, "Low-divergence single-mode terahertz quantum cascade laser," *Nat. Photonics* **3**, 586–590 (2009).
 100. J. Lloyd-Hughes, G. Scalari, A. van Kolck, M. Fischer, M. Beck, and J. Faist, "Coupling terahertz radiation between sub-wavelength metal-metal waveguides and free space using monolithically integrated horn antennae," *Opt. Express* **17**, 18387–18393 (2009).
 101. A. W. M. Lee, Q. Qin, S. Kumar, B. S. Williams, Q. Hu, and J. L. Reno, "High-power and high-temperature THz quantum-cascade lasers based on lens-coupled metal-metal waveguides," *Opt. Lett.* **32**, 2840–2842 (2007).
-

102. N. Yu, Q. J. Wang, M. A. Kats, J. A. Fan, S. P. Khanna, L. Li, A. G. Davies, E. H. Linfield, and F. Capasso, "Designer spoof surface plasmon structures collimate terahertz laser beams," *Nat. Mater.* **9**, 730–735 (2010).
 103. C. Walther, G. Scalari, M. I. Amanti, M. Beck, and J. Faist, "Microcavity Laser Oscillating in a Circuit-Based Resonator," *Science* **327**, 1495–1497 (2010).
 104. A. A. Tavallaei, B. S. Williams, P. W. C. Hon, T. Itoh, and Q.-S. Chen, "Terahertz quantum-cascade laser with active leaky-wave antenna," *Appl. Phys. Lett.* **99**, 141115 (2011).
 105. A. A. Tavallaei, P. W. C. Hon, Q.-S. Chen, T. Itoh, and B. S. Williams, "Active terahertz quantum-cascade composite right/left-handed metamaterial," *Appl. Phys. Lett.* **102**, 021103 (2013).
 106. L. A. Coldren, S. W. Corzine, and M. L. Masanovic, *Diode Lasers and Photonic Integrated Circuits*, Second, Wiley Series in Microwave and Optical Engineering (John Wiley & Sons, 2012).
 107. H. Kogelnik and C. V. Shank, "Stimulated Emission in a Periodic Structure," *Appl. Phys. Lett.* **18**, 152–154 (1971).
 108. H. Kogelnik and C. V. Shank, "Coupled-Wave Theory of Distributed Feedback Lasers," *J. Appl. Phys.* **43**, 2327–2335 (1972).
 109. John Carroll, James Whiteaway, and Dick Plumb, *Distributed Feedback Semiconductor Lasers*, Circuits, Devices and Systems Series No. 10 (The Institution of Electrical Engineers, London, 1998).
 110. T. S. Mansuripur, S. Menzel, R. Blanchard, L. Diehl, C. Pflügl, Y. Huang, J.-H. Ryou, R. D. Dupuis, M. Loncar, and F. Capasso, "Widely tunable mid-infrared quantum cascade lasers using sampled grating reflectors," *Opt. Express* **20**, 23339–23348 (2012).
 111. L. Mahler, R. Köhler, A. Tredicucci, F. Beltram, H. E. Beere, E. H. Linfield, D. A. Ritchie, and A. G. Davies, "Single-mode operation of terahertz quantum cascade lasers with distributed feedback resonators," *Appl. Phys. Lett.* **84**, 5446–5448 (2004).
 112. L. Ajili, J. Faist, H. Beere, D. Ritchie, G. Davies, and E. Linfield, "Loss-coupled distributed feedback far-infrared quantum cascade lasers," *Electron. Lett.* **41**, 419 – 421 (2005).
 113. L. Mahler, A. Tredicucci, R. Köhler, F. Beltram, H. E. Beere, E. H. Linfield, and D. A. Ritchie, "High-performance operation of single-mode terahertz quantum cascade lasers with metallic gratings," *Appl. Phys. Lett.* **87**, 181101 (2005).
 114. O. Demichel, L. Mahler, T. Losco, C. Mauro, R. Green, A. Tredicucci, J. Xu, F. Beltram, H. E. Beere, D. A. Ritchie, and V. Tamošiūnas, "Surface plasmon photonic structures in terahertz quantum cascade lasers," *Opt. Express* **14**, 5335–5345 (2006).
-

-
115. L. Mahler, A. Tredicucci, F. Beltram, C. Walther, H. E. Beere, and D. A. Ritchie, "Finite size effects in surface emitting Terahertz quantum cascade lasers," *Opt. Express* **17**, 6703–6709 (2009).
 116. B. S. Williams, S. Kumar, Q. Hu, and J. L. Reno, "Distributed-feedback terahertz quantum-cascade lasers with laterally corrugated metal waveguides," *Opt. Lett.* **30**, 2909–2911 (2005).
 117. E. Yablonovitch, "Photonic band-gap structures," *J. Opt. Soc. Am. B* **10**, 283–295 (1993).
 118. Y. Chassagneux, R. Colombelli, W. Maineult, S. Barbieri, H. E. Beere, D. A. Ritchie, S. P. Khanna, E. H. Linfield, and A. G. Davies, "Electrically pumped photonic-crystal terahertz lasers controlled by boundary conditions," *Nature* **457**, 174–178 (2009).
 119. Y. Chassagneux, R. Colombelli, W. Maineults, S. Barbieri, S. P. Khanna, E. H. Linfield, and A. G. Davies, "Predictable surface emission patterns in terahertz photonic-crystal quantum cascade lasers," *Opt. Express* **17**, 9491–9502 (2009).
 120. Y. Chassagneux, R. Colombelli, W. Maineult, S. Barbieri, S. P. Khanna, E. H. Linfield, and A. G. Davies, "Graded photonic crystal terahertz quantum cascade lasers," *Appl. Phys. Lett.* **96**, 031104 (2010).
 121. G. Sevin, D. Fowler, G. Xu, F. H. Julien, R. Colombelli, S. P. Khanna, E. H. Linfield, and A. G. Davies, "Optimized surface-emitting photonic-crystal terahertz quantum cascade lasers with reduced resonator dimensions," *Appl. Phys. Lett.* **97**, 131101 (2010).
 122. G. Sevin, G. Xu, N. Isac, R. Colombelli, H. E. Beere, and D. A. Ritchie, "Monolithically integrated two-dimensional arrays of surface-emitting photonic-crystal terahertz lasers," *J. Infrared Millim. Terahertz Waves* **34**, 386–392 (2013).
 123. L. Mahler, A. Tredicucci, F. Beltram, C. Walther, J. Faist, H. E. Beere, and D. A. Ritchie, "High-power surface emission from terahertz distributed feedback lasers with a dual-slit unit cell," *Appl. Phys. Lett.* **96**, 191109 (2010).
 124. D. G. Allen, T. Hargett, J. L. Reno, A. A. Zinn, and M. C. Wanke, "Index Tuning for Precise Frequency Selection of Terahertz Quantum Cascade Lasers," *IEEE Photonics Technol. Lett.* **23**, 30–32 (2011).
 125. M. Bahriz, V. Moreau, R. Colombelli, O. Crisafulli, and O. Painter, "Design of mid-IR and THz quantum cascade laser cavities with complete TM photonic bandgap," *Opt. Express* **15**, 5948–5965 (2007).
 126. S. John, "Strong localization of photons in certain disordered dielectric superlattices," *Phys. Rev. Lett.* **58**, 2486–2489 (1987).
 127. E. Yablonovitch, "Inhibited spontaneous emission in solid-state physics and electronics," *Phys. Rev. Lett.* **58**, 2059 (1987).
 128. J.D. Joannopoulos, S. G. Johnson, J.N. Winn, and R. D. Meade, *Photonic Crystals: Molding the Flow of Light*, Second Edition (Princeton University Press, 2008).
-

129. Marc J. Madou, *Fundamentals of Microfabrication, The Science of Miniaturization*, Second Edition (CRC Press, 2002).
 130. S. Franssila, *Introduction to Microfabrication* (John Wiley & Sons Ltd., 2004).
 131. Dow Chemicals, *Shipley Microposit(R) S100(R) Series Photo Resists* (n.d.).
 132. I. Barycka and I. Zubel, "Chemical etching of (100) GaAs in a sulphuric acid-hydrogen peroxide-water system," *J. Mater. Sci.* **22**, 1299–1304 (1987).
 133. Shigeo Sugawara, Kaichi Saito, Jin Yamauchi, and Masako Shoji, "Chemical Etching of {111} Surfaces of GaAs Crystals in $\text{H}_2\text{SO}_4\text{--H}_2\text{O}_2\text{--H}_2\text{O}$ System," *Jpn. J. Appl. Phys.* **40**, 6792 (2001).
 134. C. R. Tellier, G. Huve, and T. G. Leblois, "Micromachining of GaAs structures with an acidic hydrogen peroxide solution: Experimental and theoretical 3D etching shapes," *Sens. Actuators Phys.* **127**, 179–193 (2006).
 135. A. G. Baca and C. I. H. Ashby, *Fabrication of GaAs Devices*, EMIS Processing Series 6 (The institution of Electrical Engineers, London, 2005), Vol. 6.
 136. Y.-C. Shih, M. Murakami, E. L. Wilkie, and A. C. Callegari, "Effects of interfacial microstructure on uniformity and thermal stability of AuNiGe ohmic contact to *n*-type GaAs," *J. Appl. Phys.* **62**, 582–590 (1987).
 137. D. Jucknischke, H. J. Buhlmann, R. Houdré, M. Ilegems, M. A. Py, B. Jeckelmann, and W. Schwitz, "Properties of alloyed AuGeNi-contacts on GaAs/Ga/AlAs-heterostructures," *IEEE Trans. Instrum. Meas.* **40**, 228–230 (1991).
 138. M. Hatzakis, B. J. Canavello, and J. M. Shaw, "Single-step optical lift-off process," *IBM J. Res. Dev.* **24**, 452–460 (1980).
 139. T. Sands, "Compound semiconductor contact metallurgy," *Mater. Sci. Eng. B* **1**, 289–312 (1988).
 140. A. Messica, U. Meirav, and H. Shtrikman, "Refractory metal-based low-resistance ohmic contacts for submicron GaAs heterostructure devices," *Thin Solid Films* **257**, 54–57 (1995).
 141. A. G. Baca, F. Ren, J. C. Zolper, R. D. Briggs, and S. J. Pearton, "A survey of ohmic contacts to III-V compound semiconductors," *Thin Solid Films* **308–309**, 599–606 (1997).
 142. Q. I. Ltd., *Cryogenic Bolometer System Operating Manual (Model: QGeB/0)* (2009).
 143. Thomas Keating Limited, *TK Absolute Power/Energy Meter System - Installation and Operating Instructions* (2010).
 144. N. M. Hinchcliffe, "Fabrication and measurement of double metal terahertz quantum cascade lasers," PhD Thesis, University of Leeds (2009).
-

145. P. Dean, A. H. Awang, I. Kundu, R. Alhathloul, S. P. Khanna, L. H. Li, A. Burnett, E. H. Linfield, and A. G. Davies, "Detection of terahertz frequency radiation via the photothermoelastic response of zincblende crystals," *J. Opt. Soc. Am. B* **30**, 3151–3160 (2013).
 146. S. Chakraborty, T. Chakraborty, S. P. Khanna, E. H. Linfield, A. G. Davies, J. Fowler, C. H. Worrall, H. E. Beere, and D. A. Ritchie, "Spectral engineering of terahertz quantum cascade lasers using focused ion beam etched photonic lattices," *Electron. Lett.* **42**, 404 – 405 (2006).
 147. J. S. Foresi, P. R. Villeneuve, J. Ferrera, E. R. Thoen, G. Steinmeyer, S. Fan, J. D. Joannopoulos, L. C. Kimerling, H. I. Smith, and E. P. Ippen, "Photonic-bandgap microcavities in optical waveguides," *Nature* **390**, 143–145 (1997).
 148. M. C. Parker, R. J. Mears, and S. D. Walker, "A Fourier transform theory for photon localization and evanescence in photonic bandgap structures," *J. Opt. Pure Appl. Opt.* **3**, S171 (2001).
 149. S. Chakraborty, E. H. Linfield, and A. G. Davies, "Semiconductor Laser with Aperiodic Photonic Lattice," U.S. patent WO 2008/012527 A1 (January 31, 2008).
 150. S. Kohen, B. S. Williams, and Q. Hu, "Electromagnetic modeling of terahertz quantum cascade laser waveguides and resonators," *J. Appl. Phys.* **97**, 053106 (2005).
 151. H. Li, J. C. Cao, Y. J. Han, Z. Y. Tan, and X. G. Guo, "Temperature profile modeling and experimental investigation of thermal resistance of terahertz quantum-cascade lasers," *J. Phys. Appl. Phys.* **42**, 205102 (2009).
 152. C. A. Evans, "The optical and thermal properties of quantum cascade lasers," PhD Thesis, University of Leeds (2008).
 153. Mohamed Shahrizan bin Mohd Ibrahim, "Segmented and patterned single-metal terahertz quantum cascade lasers," PhD Thesis, University of Leeds (2011).
 154. R. Rungsawang, N. Jukam, J. Maysonnave, P. Cavalié, J. Madéo, D. Oustinov, S. S. Dhillon, J. Tignon, P. Gellie, C. Sirtori, S. Barbieri, H. E. Beere, and D. A. Ritchie, "Gain enhancement in a terahertz quantum cascade laser with parylene antireflection coatings," *Appl. Phys. Lett.* **98**, 101102 (2011).
 155. P. Dean, M. Salih, S. P. Khanna, L. H. Li, N. K. Saat, A. Valavanis, A. Burnett, J. E. Cunningham, A. G. Davies, and E. H. Linfield, "Resonant-phonon depopulation terahertz quantum cascade lasers and their application in spectroscopic imaging," *Semicond. Sci. Technol.* **27**, 094004 (2012).
 156. S. Kumar and A. W. M. Lee, "Resonant-Phonon Terahertz Quantum-Cascade Lasers and Video-Rate Terahertz Imaging," *IEEE J. Sel. Top. Quantum Electron.* **14**, 333 – 344 (2008).
 157. P. Dean, Y. L. Lim, A. Valavanis, R. Kliese, M. Nikolić, S. P. Khanna, M. Lachab, D. Indjin, Z. Ikonić, P. Harrison, A. D. Rakić, E. H. Linfield, and A. G. Davies, "Te-
-

- terahertz imaging through self-mixing in a quantum cascade laser," *Opt. Lett.* **36**, 2587–2589 (2011).
158. Y. L. Lim, P. Dean, M. Nikolić, R. Kliese, S. P. Khanna, M. Lachab, A. Valavanis, D. Indjin, Z. Ikonić, P. Harrison, E. H. Linfield, A. G. Davies, S. J. Wilson, and A. D. Rakić, "Demonstration of a self-mixing displacement sensor based on terahertz quantum cascade lasers," *Appl. Phys. Lett.* **99**, 081108 (2011).
159. L. A. Coldren and S. W. Corzine, "Continuously-tunable single-frequency semiconductor lasers," *IEEE J. Quantum Electron.* **23**, 903 – 908 (1987).
160. B. Broberg and S. Nilsson, "Widely tunable active Bragg reflector integrated lasers in InGaAsP-InP," *Appl. Phys. Lett.* **52**, 1285–1287 (1988).
161. K. Kobayashi and I. Mito, "Single frequency and tunable laser diodes," *J. Light. Technol.* **6**, 1623 –1633 (1988).
162. Y. Kotaki and H. Ishikawa, "Spectral characteristics of a three-section wavelength-tunable DBR laser," *IEEE J. Quantum Electron.* **25**, 1340 –1345 (1989).
163. V. Jayaraman, Z.-M. Chuang, and L. A. Coldren, "Theory, design, and performance of extended tuning range semiconductor lasers with sampled gratings," *IEEE J. Quantum Electron.* **29**, 1824 –1834 (1993).
164. L. A. Coldren, "Monolithic tunable diode lasers," *IEEE J. Sel. Top. Quantum Electron.* **6**, 988 –999 (2000).
165. L. A. Coldren, G. A. Fish, Y. Akulova, J. S. Barton, L. Johansson, and C. W. Coldren, "Tunable semiconductor lasers: a tutorial," *J. Light. Technol.* **22**, 193 – 202 (2004).
166. A. J. Ward, D. J. Robbins, G. Busico, E. Barton, L. Ponnampalam, J. P. Duck, N. D. Whitbread, P. J. Williams, D. C. J. Reid, A. C. Carter, and M. J. Wale, "Widely tunable DS-DBR laser with monolithically integrated SOA: design and performance," *IEEE J. Sel. Top. Quantum Electron.* **11**, 149 – 156 (2005).
167. N. Zhuo, J. Zhang, F. Liu, L. Wang, S. Tan, F. Yan, J. Liu, and Z. Wang, "Tunable Distributed Feedback Quantum Cascade Lasers by a Sampled Bragg Grating," *IEEE Photonics Technol. Lett.* **25**, 1039–1042 (2013).
168. M. Pantouvaki, C. C. Renaud, P. Cannard, M. J. Robertson, R. Gwilliam, and A. J. Seeds, "Fast Tuneable InGaAsP DBR Laser Using Quantum-Confined Stark-Effect-Induced Refractive Index Change," *IEEE J. Sel. Top. Quantum Electron.* **13**, 1112 – 1121 (2007).
169. M. S. Vitiello and A. Tredicucci, "Tunable Emission in THz Quantum Cascade Lasers," *IEEE Trans. Terahertz Sci. Technol.* **1**, 76 –84 (2011).
170. J. Xu, J. M. Hensley, D. B. Fenner, R. P. Green, L. Mahler, A. Tredicucci, M. G. Allen, F. Beltram, H. E. Beere, and D. A. Ritchie, "Tunable terahertz quantum cascade lasers with an external cavity," *Appl. Phys. Lett.* **91**, 121104 (2007).
-

171. A. W. M. Lee, B. S. Williams, S. Kumar, Q. Hu, and J. L. Reno, "Tunable terahertz quantum cascade lasers with external gratings," *Opt. Lett.* **35**, 910–912 (2010).
 172. L. Mahler, A. Tredicucci, F. Beltram, H. E. Beere, and D. A. Ritchie, "Tuning a distributed feedback laser with a coupled microcavity," *Opt. Express* **18**, 19185–19191 (2010).
 173. D. Turčinková, M. I. Amanti, F. Castellano, M. Beck, and J. Faist, "Continuous tuning of terahertz distributed feedback quantum cascade laser by gas condensation and dielectric deposition," *Appl. Phys. Lett.* **102**, 181113 (2013).
 174. S. Chakraborty, O. Marshall, C. W. Hsin, M. Khairuzzaman, H. Beere, and D. Ritchie, "Discrete mode tuning in terahertz quantum cascade lasers," *Opt. Express* **20**, B306–B314 (2012).
 175. O. P. Marshall, S. Chakraborty, M. Khairuzzaman, T. Folland, A. Gholinia, H. E. Beere, and D. A. Ritchie, "Electronically tunable aperiodic distributed feedback terahertz lasers," *J. Appl. Phys.* **113**, 203103 (2013).
 176. B. G. Lee, M. A. Belkin, R. Audet, J. MacArthur, L. Diehl, C. Pflügl, F. Capasso, D. C. Oakley, D. Chapman, A. Napoleone, D. Bour, S. Corzine, G. Höfler, and J. Faist, "Widely tunable single-mode quantum cascade laser source for mid-infrared spectroscopy," *Appl. Phys. Lett.* **91**, 231101 (2007).
 177. C. Gmachl, D. L. Sivco, R. Colombelli, F. Capasso, and A. Y. Cho, "Ultra-broadband semiconductor laser," *Nature* **415**, 883–887 (2002).
 178. S. L. Lu, L. Schrottke, S. W. Teitsworth, R. Hey, and H. T. Grahn, "Formation of electric-field domains in $\text{GaAs/Al}_x\text{Ga}_{1-x}\text{As}$ quantum cascade laser structures," *Phys. Rev. B* **73**, 033311 (2006).
 179. C. C. Hu, *Modern Semiconductor Devices for Integrated Circuits* (Pearson, 2009).
 180. Simone Montanari, *Metal Semiconductor Schottky Contact Injector* (n.d.).
 181. K. Ohtani, M. Beck, and J. Faist, "Electrical laser frequency tuning by three terminal terahertz quantum cascade lasers," *Appl. Phys. Lett.* **104**, 011107 (2014).
 182. L. A. Coldren and T. L. Koch, "Analysis and design of coupled-cavity lasers - Part I: Threshold gain analysis and design guidelines," *IEEE J. Quantum Electron.* **20**, 659 – 670 (1984).
 183. L. A. Coldren and T. L. Koch, "Analysis and design of coupled-cavity lasers - Part II: Transient analysis," *IEEE J. Quantum Electron.* **20**, 671–682 (1984).
 184. F. K. Khan and D. T. Cassidy, "Widely tunable coupled-cavity semiconductor laser," *Appl. Opt.* **48**, 3809–3817 (2009).
 185. S. Höfling, J. Heinrich, J. P. Reithmaier, A. Forchel, J. Seufert, M. Fischer, and J. Koeth, "Widely tunable single-mode quantum cascade lasers with two monolithically coupled Fabry-Pérot cavities," *Appl. Phys. Lett.* **89**, 241126 (2006).
-

186. P. Fuchs, J. Seufert, J. Koeth, J. Semmel, S. Höfling, L. Worschech, and A. Forchel, "Widely tunable quantum cascade lasers with coupled cavities for gas detection," *Appl. Phys. Lett.* **97**, 181111 (2010).
 187. I. Kundu, P. Dean, A. Valavanis, L. Chen, L. Li, J. E. Cunningham, E. H. Linfield, and A. G. Davies, "Discrete Vernier tuning in terahertz quantum cascade lasers using coupled cavities," *Opt. Express* **22**, 16595–16605 (2014).
 188. C. Breck Hitz, J. J. Ewing, and Jeff Hecht, *Introduction to Laser Technology*, 4th Edition (John Wiley & Sons, 2012).
 189. L. Ajili, G. Scalari, J. Faist, H. Beere, E. Linfield, D. Ritchie, and G. Davies, "High power quantum cascade lasers operating at $\lambda \simeq 87$ and $130\ \mu\text{m}$," *Appl. Phys. Lett.* **85**, 3986–3988 (2004).
 190. Zhang Yong-Gang, He You-Jun, and Li Ai-Zhen, "Transient Thermal Analysis of InAlAs/InGaAs/InP Mid-Infrared Quantum Cascade Lasers," *Chin. Phys. Lett.* **20**, 678–681 (2003).
 191. C. A. Evans, D. Indjin, Z. Ikonić, P. Harrison, M. S. Vitiello, V. Spagnolo, and G. Scamarcio, "Thermal modeling of terahertz quantum-cascade lasers: comparison of optical waveguides," *IEEE J. Quantum Electron.* **44**, 680–685 (2008).
 192. M. S. Vitiello, G. Scamarcio, and V. Spagnolo, "Time-resolved measurement of the local lattice temperature in terahertz quantum cascade lasers," *Appl. Phys. Lett.* **92**, 101116–3 (2008).
 193. M. S. Vitiello, G. Scamarcio, V. Spagnolo, J. Alton, S. Barbieri, C. Worrall, H. E. Beere, D. A. Ritchie, and C. Sirtori, "Thermal properties of THz quantum cascade lasers based on different optical waveguide configurations," *Appl. Phys. Lett.* **89**, 021111 (2006).
 194. C. A. Evans, V. D. Jovanović, D. Indjin, Z. Ikonić, and P. Harrison, "Investigation of thermal effects in quantum-cascade lasers," *IEEE J. Quantum Electron.* **42**, 859–867 (2006).
 195. R. Sharma, L. Schrottke, M. Wienold, K. Biermann, R. Hey, and H. T. Grahn, "Effect of stimulated emission on the transport characteristics of terahertz quantum-cascade lasers," *Appl. Phys. Lett.* **99**, 151116 (2011).
 196. S. Barbieri, P. Gellie, G. Santarelli, L. Ding, W. Maineult, C. Sirtori, R. Colombelli, H. Beere, and D. Ritchie, "Phase-locking of a 2.7-THz quantum cascade laser to a mode-locked erbium-doped fibre laser," *Nat. Photonics* **4**, 636–640 (2010).
 197. D. Rabanus, U. U. Graf, M. Philipp, O. Ricken, J. Stutzki, B. Vowinkel, M. C. Wiedner, C. Walther, M. Fischer, and J. Faist, "Phase locking of a 1.5 Terahertz quantum cascade laser and use as a local oscillator in a heterodyne HEB receiver," *Opt. Express* **17**, 1159–1168 (2009).
 198. F. Friederich, G. Schuricht, A. Deninger, F. Lison, G. Spickermann, P. H. Bolívar, and H. G. Roskos, "Phase-locking of the beat signal of two distributed-feedback di-
-

-
- ode lasers to oscillators working in the MHz to THz range," *Opt. Express* **18**, 8621–8629 (2010).
199. P. Khosropanah, A. Baryshev, W. Zhang, W. Jellema, J. N. Hovenier, J. R. Gao, T. M. Klapwijk, D. G. Paveliev, B. S. Williams, S. Kumar, Q. Hu, J. L. Reno, B. Klein, and J. L. Hesler, "Phase locking of a 2.7 THz quantum cascade laser to a microwave reference," *Opt. Lett.* **34**, 2958–2960 (2009).
-